REPORT DOCUMENTATION PAGE

The public reporting burden for this collection of information is estimated to average 1 hour per response, including the time for reviewing instructions, searching existing data sources, gathering and maintaining the data needed, and completing and reviewing the collection of information. Send comments regarding this burden estimate or any other aspect of this collection of information, including suggestions for reducing the burden, to Department of Defense, Washington Headquarters Services, Directorate for Information Operations and Reports (0704-0188), 1215 Jefferson Davis Highway, Suite 1204, Arlington, VA 22202-4302. Respondents should be aware that notwithstanding any other provision of law, no person shall be subject to any penalty for failing to comply with a collection of information if it does not display a currently valid OMB control number.
PLEASE DO NOT RETURN YOUR FORM TO THE ABOVE ADDRESS.

1. REPORT DATE (DD-MM-YYYY)	2. REPORT TYPE	3. DATES COVERED (From - To)
08-11-2001	Conference Proceedings	29-31 Oct 2001

4. TITLE AND SUBTITLE

2001 JSASS International Session

5a. CONTRACT NUMBER
F6256201M9123

5b. GRANT NUMBER

5c. PROGRAM ELEMENT NUMBER

6. AUTHOR(S)

Conference Committee

5d. PROJECT NUMBER

5e. TASK NUMBER

5f. WORK UNIT NUMBER

7. PERFORMING ORGANIZATION NAME(S) AND ADDRESS(ES)
National Aerospace Laboratory
7-44-1 Jindaji Higashi-machi
Chofu, Tokyo 182-8522
Japan

8. PERFORMING ORGANIZATION REPORT NUMBER
N/A

9. SPONSORING/MONITORING AGENCY NAME(S) AND ADDRESS(ES)

AOARD
UNIT 45002
APO AP 96337-5002

10. SPONSOR/MONITOR'S ACRONYM(S)
AOARD

11. SPONSOR/MONITOR'S REPORT NUMBER(S)
CSP-011017

12. DISTRIBUTUION/AVAILABILITY STATEMENT

Approved for public release; distribution is unlimited.

20011120 100

13 SUPPLEMENTARY NOTES

14. ABSTRACT

The 15th International Session of the Japan Society of Aeronautical and Space Sciences was held 29-31 Oct 2001 in Gifu Japan. It incorporated the 2nd Japan-Korea Aerospace Technology Symposium. Thirty-none papers are included in the proceedings. Topical sessions included: Guidance Navigation and Control, Development, Fluid Dynamics and Propulsion, Fluid Dynamics, Guidance and Control, Structure, Structure and Aeroelasticity.

15. SUBJECT TERMS

Aerodynamics, Flight Control, Wind Tunnels, Computational Fluid Dynamics, Navigation, Comunications & Guidance

16. SECURITY CLASSIFICATION OF:			17. LIMITATION OF ABSTRACT	18. NUMBER OF PAGES	19a. NAME OF RESPONSIBLE PERSON
a. REPORT	b. ABSTRACT	c. THIS PAGE			Mark L. Nowack, Lt Col, USAF
U	U	U	UU	182	

19b. TELEPHONE NUMBER (Include area code)
+81-3-5410-4409

JSASS 15TH INTERNATIONAL SESSIONS IN 39TH AIRCRAFT SYMPOSIUM

Incorporating
2nd JAPAN-KOREA AEROSPACE TECHNOLOGY SYMPOSIUM

October 29-31, 2001

Nagaragawa Convention Center
Gifu, Japan

The Japan Society for Aeronautical and Space Sciences (JSASS)

Proceedings of
JSASS 15th International Sessions
in 39th Aircraft Symposium

Incorporating
2nd Japan-Korea Aerospace
Technology Symposium

October 29-31, 2001

Nagaragawa Convention Center
Gifu, Japan

The Japan Society for Aeronautical and Space Sciences
(JSASS)

Chairperson
Akira Umemura
Professor, Department of Aerospace,
Nagoya University
Furo-cho,Chikusa-ku,Nagoya City,
Aichi Prefecture, 464-8603 JAPAN

Organizing Committee
Masahiko Ikuta   Mitsubishi Heavy Industry
Takuji Kurotaki   National Aerospace Laboratory
Keiichi Murakami   Nagoya University
Masahiro Obukata   Fuji Heavy Industry
Norihiko Shishido   Kawasaki Heavy Industry
Makoto Ueno   National Aerospace Laboratory

Acknowledgement

The organizing committee of the 15th International Sessions in the 39th Aircraft Symposium wishes to thank the following for their contribution to the success of this conference:

Table of Contents

1F1 PROMOTING AUTONOMOUS CONTROL IN CIVIL TRANSPORTS

– PROPOSAL FOR THE FLIGHT COMMAND SYSTEM

Junichiro Sumita

Nishinippon Institute of Technology

Key Words: Aircraft,　Aircraft Operation,　Air Traffic Control, Guidance and Control

ABSTRACT

Reflecting the recent tends in the accidents in the civil transport type of aircraft, to minimize the pilot-interface with the system of automation is taken a proper approach to counter the problem area. And the Flight Command System (FCS) is proposed to be applied to eliminate or reduce the accidents.

The FCS is a central autonomous logic to control the Flight Management System, Auto-Pilot, and Fundamental Flight Control, which have a hierarchy in structure with the human centered cockpit. Those are designed in a high reliability as high as 10^{-9} under the concept of the Fault Tolerant System. Although the automation level would become high to integrate with the Air Traffic Control System, it is stressed that the autonomous control could contribute to reduce the interface area between the system and the pilot. And the pilot can be aware the situation of the aircraft intuitively, through the devices at the cockpit.

In the proposed system, the pilot plays a role of a final authority in the aircraft control by overriding or disconnecting the system in needs and in case.

1. INTRODUCTION

It is very controversial these days that the rate of the aircraft accidents is not decreasing even in the most advanced type of transports. According to the recent analysis for the accident reports, the interface between the automation of the aircraft and the operating pilot could cause the accidents in most of the cases as a main factor.[1] The automation surprise, mode confusions, human-factors are the terminology to express the phenomena.[2]

The author proposed to apply the flight command system (FCS) to the aircraft to cope with the problem area at the Japanese session of the symposium in last year.[3] The FCS has the autonomous control capabilities in the flight control of the aircraft to generate and modify the flight plans under the Air Traffic Control (ATC) by the advanced Flight Management System (FMS). The pilot supervises the flight in a normal flight condition and commands the

flight in the abnormal conditions, with the assistance by the human centered cockpit, equipped with the 3 dimensional displays, etc. by which the pilot easily can enhance the　situation awareness of the aircraft.

This paper augments the importance of the autonomous control in the aircraft system to achieve the flight safety, especially from the point of the integration of Air Traffic Control with the FCS. The autonomous characteristics and the pilot existence are contradictory, however, the pilot integrity is very important to manage the system in every corner of flights in the aircraft operation.

2. AUTONOMOUS FLIGHT CONTROL

As the related problems are mainly caused from the man-machine interface, the interface area should be minimized to seek the air safety for the direct countermeasures, with a care of smoothness in pilot controls of the system. The concrete method for the direction is to promote the autonomous control capabilities in a flight control system of an aircraft.

The recent advancement in an automation system in the flight control of the transport is magnificent. The FMS could be a substitute of a pilot in maneuvering, and controlling an aircraft under the optimum law of the flight operation. Even the flight plan of the aircraft is generated and modified by the current system under the pilot inputs of the required conditions. However, the system became very complicated in the modes and the work-loads of the pilot to handle the conveniences are getting higher and higher.[4] This is another reason to push to be applied the autonomous system.

The next step for developing the system is to integrate with the Air Traffic Control System to get the negotiated modification of the plan ,[5] and to make it possible by the autonomous control to avoid the complications of the system of the automation, and make it simple from the operator's point of view, and to reduce the work-loads.

The autonomous control requires the system to judge the situation of the aircraft and determine the action to take by the system itself. The study for the Intelligent Flight Control System employing a neural

network software is under way.[6] The author suggested that the sequential control by the expert system expressed by the predetermined pilot-procedures can structure the autonomous control laws without applying the advanced concepts, like an artificial brain.[7] Although this is required to be complete in the expression of the law and be verified in the flight test, the method is already within our reach.

It is also true that the expert system above mentioned cannot cope with a completely new situation, so the pilot is required to exist in the system as a final flight commander. The pilot could be a supervisor in a normal operation and a manipulator in an abnormal condition of the aircraft. It is considered that the highest automation level by Sheridan [8] is not proper to be applied for now due to the technology immaturity.

The current discussion for the pilot of the aircraft is to seek the possibilities of the one-man crew. The pilot and the autonomous system could conform a dual redundant high reliability system with a self-detection capability in the fault tolerant sense.

And we have to consider the frictionless operation in the man-machine of the aircraft, as long as we have the pilot in the system.

However, the autonomous control of the system can reduce a necessity of a pilot by reducing the interface area between the two, and reduces the pilot work-loads, and let the pilot concentrate to keep his alertness to control the aircraft. Those are lead to a reduction of the possibilities of the related accidents for certain.

Naturally the FCS has to have the fault tolerant characteristics to give the system very high operational reliability to be sure of safety in the flight.

3. PROPOSAL FOR FLIGHT COMMAND SYSTEM

The general idea for the Flight Command System is expressed in Fig.1.
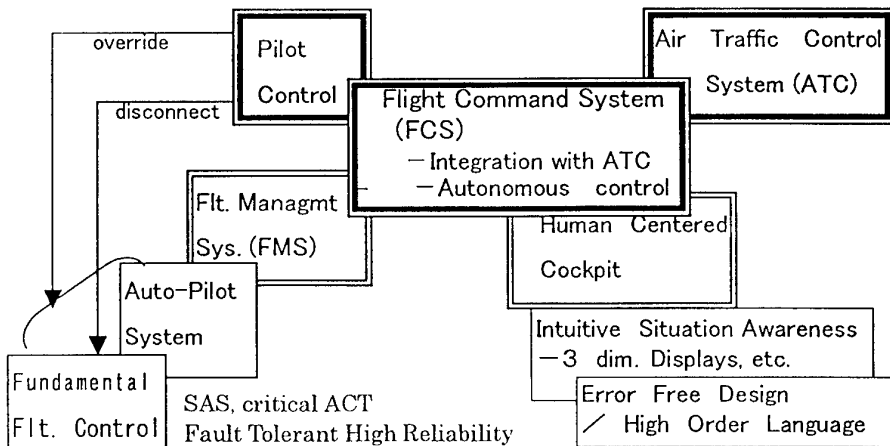
1) ADVANCED FMS

The FMS enables the aircraft to be operated in the optimum flight-time or fuel-consumption from a take-off to landing, and automatically control the aircraft in the flight segments with the Auto-Pilot system. There would be no critical problem to get the autonomous control version of FMS, if we could add the judging process for the aircraft situation. We may be able to change the control and regain the proper approach pattern autonomously through the system, for example, after stopping the landing procedures in the midst of the landing by a waiting order from the ATC or some weather hazards, etc..

The autonomous control modes in the FMS should be limited superficially to avoid a pilot's confusion in the situation awareness to, say, Take-off, Cruise, Landing. The take-off mode, for example, includes a heading hold on a runway, rotation, gear and flaps up procedures, take-off abort, speed-hold, mach-hold, holding the taking-off pattern, etc.

The Auto-Pilot system supports the FMS in controlling the aircraft in an automatic ways. This is also simplified in the modes in the case of the pilot's manual inputs.

The fundamental flight control devices control directly the control surfaces of the aircraft, with SAS (Stability Augmentation System), and the critical ACT (Active Control Technology), such as Gust Load Alleviation, Flutter Suppression, etc.

These of FCS, FMS, Auto-Pilot, and The fundamental Flight Control should be structured in a hierarchy in a very clear-cut way to simplify the flight control system and modes, and to make it easy to add the autonomous function in control.

2) AIR TRAFFIC CONTROL SYSTEM

On the last day of January, this year, two JAL's aircrafts equipped with TCAS made a near-miss accident over Yaizu, caused from the miss-control by the traffic controllers, and the insufficient communication among the pilots and the controllers.

Reflecting the results, several improvements in the ATC system are

Figure 1.   The Concept of Flight Command System

reported, in the format changes of the display at the controller, etc. Those kinds of improvements reflected from the each accident are very important to eliminate further accidents of the same kind, without doubts.

The author suggests that much more innovative measures should be taken to cope with the problem area in the ATC system, by shifting it to the autonomous control system.

The basic concept for the improvement is to have the digital interfaces between the aircrafts and the ATC system, and make it possible to communicate each other by the digital dialogue as the first step.

a) VIEW POINT FROM AIRCRAFT

The aircraft should be able to request the change or modification of the flight plan due to the needs of itself, and to check and judge the acceptability of the responses suggested from the ATC system, until a satisfactory solution is obtained, and to carry out the change autonomously, after getting an approval from the ATC in digital way.

The necessary capability of the system for the above function is developed by the advanced FMS.

Furthermore, the contact method by the aircraft with the specific controller should be simplified. The focal point for the aircraft in the ATC system is to be single, and the radio frequency for dialogues between the two systems is also to be one kind. The focal point will distributes the dialogue to the related controller with the frequency changes, if necessary.

It is also important to collect the information through the link about weather, and traffic condition for seeking the necessity to change the flight profile autonomously.

b) VIEW POINTS FROM ATC SYSTEM

The basic requirements for the traffic control by the system are to have the data to identify the aircraft, and to grasp the navigation information of each aircraft with some forecast by the digital way.

The autonomous control in this system also has a significant meaning to eliminate the human interfaces among the pilot, the controller, and the system. The control law could be built up by an expert system, basing upon a way of sequential controls.

Although we have to study further the autonomous level and the software creative way, the controller should have the roll of the supervisor at normal condition and final decision maker at the abnormal lone, same as the pilot plays in the aircraft system.

The system should be controlled under the general controller, which is the one representative of the system, in order to control one aircraft throughout the flight time from its take-off to the landing, and to grasp the position and the dynamic vectors for many aircrafts at the same time, without confusions among the controllers in various control sectors. The representative should not necessarily be a person or an organization. One network server could play the role. And the current ATC systems of each sector are networked under the boss with the autonomous control policy for each sector.

The general concept for the network to keep the consistencies of the control is shown in Fig.2.

AGC : Airport Gnd. Controller, GCA : Ground Control Approach
TRC : Terminal Radar Control, AC : Approach Control
ARC : Air Route Control
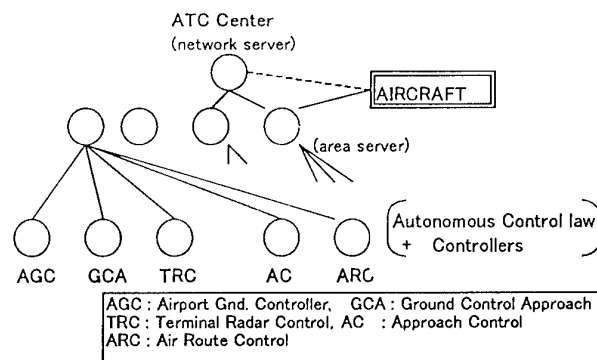
Figure 2. The concept of ATC network

3) PILOTS POSITION IN THE SYSTEM

The autonomous control system and the pilot are contradictory in existence by the sense of dual commanders in one system.

We have to place the role for each in definit way in order not to generate another interface problems.

At the normal condition of the system, the FCS commands the aircraft, and the pilot only supervises and monitors the aircraft condition. But at the system failure or degradation of the function, the pilot commands the aircraft. The pilot can take over the control any time, however, with only activation of the fundamental flight control, and the Auto-Pilot system. So, the monitoring devices for the pilot are to be very important.

4) HUMAN CENTERED COCKPIT
   a) Intuitive Situation Awareness

The monitoring technique to grasp the aircraft situation is very important, all the more the pilot is expected to participate in maneuvering the aircraft in needs. It is considered to be best to offer the devices by which the pilots can instantly do Situation Awareness without confusions, i.e. intuitively. It may be natural to have the 3 dimensional description of the aircraft situation

be required to have multi-displays to cover limitation of the field of sight, with a simulation of a sound, feeling, and so forth.

The holographic display system and the windowless cockpit will require a little more time to be applied. The current effective alternative for the above seems to have the X-Z plane display with a terrain mapping just like the Enhanced GPWS has. [9] In order to be intuitive for grasping the situation through the devices, the format of the displays and other devices should be designed by those of figures, images, patterns, icons, etc.

b) The Human Engineering for the Design

The most of the current practices are to improve the cockpit design from the points of the human engineering, to avoid the human mistakes, by reflecting the reports of the accidents in past. And those kinds of activities in pursuing the flight safety are very important.

It is also very effective to apply the higher order language in the FMS to minimize the input errors.[10] And the analogy to check the pilot inputs should be developed, such as by pre-plays of the planned flight on the 3-D displays in a very short time, for example.

4. OPERATION CONCEPT OF FCS

1) AT NORMAL CONDITION

The FCS has a control of the aircraft. But the pilot has a final authority in the command by the way of saying that he can take over the control anytime. The pilot controls the aircraft through the fundamental flight control and the Auto-Pilot, with the advisory assistance by the FCS and FMS.

2) FAILURE MANAGEMENT

When something happened in the condition of the system, the pilot takes over the control by overriding, or disconnecting the system

By the override, the pilot controls the aircraft using the Auto-Pilot, so which should be constituted of the simplified modes, at one failure.

By the disconnection, the pilot manipulates the aircraft through the fundamental flight control, with the SAS, and the critical ACT at the second failure.

The FCS, and FMS are designed under the one-fail operation, and Fundamental Flight Control is designed under the two-fail operation both in the fault tolerant ways.

The pilot's alertness should be discussed for that the FCS and FMS have the same level of redundancy to increase the reliability as the fundamental system.

5. CONCLUSION

Reflecting the recent tends in the aircraft accidents, the approach to minimize the pilot- interface with the system of automation is discussed, and the autonomous Flight Command System is proposed to be applied to eliminate the causes of the accidents.

The FCS is constituted from the autonomous flight control system, and the human centered cockpit. The autonomous control has the FCS, FMS, Auto-Pilot, and Fundamental Flight Control in a hierarchy in the structure, and is designed under the concept of the Fault Tolerant System and goes beyond to be integrated with ATC.

The pilot plays a role of a final authority in the aircraft control by overriding or disconnecting the system in needs and in case. So, it is very important for the system that the pilot can be intuitively aware the situation of the aircraft, through the devices of 3 dimensional displays with a mapping information, for example, at the advanced cockpit.

The author hopes that these kinds of idea are refined by many people of the related area and verified through the flight simulation tests and the flight tests, to prove the actual airworthiness of these kinds of thought to realize the real air safety in the aircraft operation.

We should share the target with the USA in this area to reduce the accidents to 1/10 until 2023.[11]

REFERENCES

1) P.D.Arbuckle,K.H.Abbott,et.al. "Future Flight Decks" ICAO 21st Congress PN98-1.9.3 (NASA,larc), 1998
2) "Automation" AW&ST Jan.30, 1995
3) J.Sumita, "Proposal on Flight Command System" JSASS 38th Aircraft Symposium, pp157-160,2000
4) K.K.Lee, B.D.Sanford, "The Human Factors of FMS Usage in the Terminal Area" AIAA CTAS internet, 1997
5) ""Flight Crew Factors for CTAS/FMS Integration in the Terminal Airspace", http://human-factor.arc.gov, 1998
6) "Safety Flight Control Software Tested " Innovation, Vol.7,No.3, 5/6 1999
7) J.Sumita, "Large Scale UAV System Operation Concept" JSASS 14th International Session in Aircraft Symposium, pp.731-734, 2000
8) Billing, "Aviation Automation " NASA larc. Internet 1997
9) Allied Signal catalogue, "EGPWS" , 1999
10).P.Proctor, "Honeywell Simplifies FMS Programming", AW&ST Nov.24, 1997
11) http://www.aero-space.nasa.gov,1997

1F2

AN IMPROVED NEURAL NETWORK GUIDANCE LAW USING A NETWORK PRUNING TECHNIQUE

Ki-Hoon Lee*, Han-Lim Choi*, Min-Jea Tahk†, and Hyo-Choong Bang**

Division of Aerospace Engineering, Korea Advanced Institute of Science and Technology,
373-1, Kusong-dong, Yusung-gu, Taejon, 305-701, Korea.
E-mail : {khlee, hlchoi, mjtahk, hcbang}@fdcl.kaist.ac.kr

Key Words: Guidance and Control, Neural network, Pruning technique

ABSTRACT

Recently, a neural network has been frequently employed in designing a feedback guidance law form open-loop solutions of optimization problems because of its function approximation characteristic. The performance of the resultant guidance law greatly depends on the network structure. Unfortunately, we cannot say confidently about the guidance performance with only the smallest network training error, since a complex network usually leads to small training error but results in overfitting phenomenon.

This paper proposes an improved neural network guidance law by using a network pruning to overcome the overfitting of the neural network. A neural network guidance law is based on open-loop solutions of two-dimensional pursuit-evasion games. Computer simulations are performed for the validation of performance enhancement achieved by the pruning technique.

I. INTRODUCTION

Pursuit-evasion game is a representative minimax problem, and recently it becomes an attractive concept in design of missile guidance law against an intelligently maneuvering target, since it guarantees a worst-case performance. This game problem can be solved by several numerical methods that provide open-loop-type solutions. However, open loop solutions are not appropriate for practical implementation, since missile's on-board computer has limitations on memory capacity as well as it is not fast enough to solve pursuit-evasion games in real-time.

These problems can be overcome by training a neural network with pre-computed open-loop solutions under various scenarios. Through the training, the guidance law can be expressed as a simple functional form of connection weight matrices that contains information of a large amount of open-loop solutions. Many researchers have studied the validity of application of neural networks to conversion of open loop solutions into the feedback form. Song et al. [1] introduced sub-optimal midcourse guidance laws using neural networks. Choi et al. [2] constructed a neural network guidance law using open loop solution s of three-dimensional pursuit-evasion games.

However, the neural network structure is determined thru of trials and errors, since there is no indicator that can definitely says if a certain network structure guarantees the best guidance performance. The neural network

training error cannot be a good indicator, since a complicated network results in low training error but leads to overfitting phenomena.

This problem can be resolved to some extend by pruning techniques. By eliminating useless weight connections and nodes, the pruning technique lower a redundant degree of freedom resulting from too many weight connections and excessive training of neural network. Many papers on pruning techniques have reported that the methods yield better generalization performance avoiding overfitting phenomena.

This study adopts a pruning technique to enhance the guidance performance of the neural network guidance law based on pursuit-evasion games. The effects of the pruning on the guidance performance are investigated thru the numerical simulations.

II. NEURAL NETWORK GUIDANCE LAW FROM PURSUIT-EVASION GAME

The pursuit-evasion game is an important class of two-players zero-sum differential games. Considered in the view of missile/target dynamics, the pursuit-evasion game is a minimax optimization situation in which the missile minimizes a prescribed payoff and the target maximizes it. The payoff is usually represented as the final capture time, the final miss distance, or a combination of both of them. That is, when the final capture time, denoted as t_f, is employed as the payoff, the pursuit-evasion game is expressed as the following minimax optimization problem:

$$\min_{u_p} \quad \max_{u_e} \quad t_f \tag{1}$$

which is subject to the dynamics of the pursuer and the evader, and u_p, u_e denote the pursuer and evader control input histories, respectively. The solution of the problem can be obtained by several numerical methods. A gradient method introduced in Tahk et. al[3] provides good solutions during reasonable computing time. However, since just open-loop solutions are available from the numerical solver above, it is not easy to use the solutions for the real application in the missile guidance. A feedback law is preferable for the real implementation than a large size of open-loop solution sets. A multi-layer feedforward neural network (NN) can resolve this difficulty. An approximate functional relationship between state variables and guidance commands can be obtained by training a NN whose inputs are states variables and outputs are guidance commands. The key idea is to train a neural network to learn the optimal guidance command in feedback form.
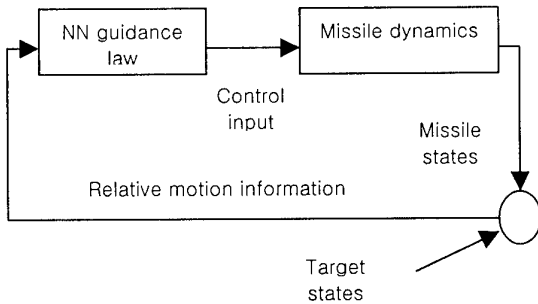
Figure 1. Implementation of the NN guidance law

In constructing a NN guidance law, it is important to include key state variables into the NN input variables to get an effective NN guidance law. Although there may be many candidates for the NN inputs, we use four variables of range, range rate, line-of-sight (LOS), and LOS rate for inputs of the NN, since with these inputs, the relative motions between the missile and the target can be described reasonably. Figure 1 illustrates a brief diagram of implementation of the NN guidance law.

III. NEURAL NETWORK PRUNING TECHNIQUE

If a neural network is trained on the smallest size that fits the data of a system, good generalization performance can be obtained. However, there is no way of determining the best size for good performance. For this reason, a neural network is usually trained on a larger size than necessary, which may cause overfitting problems with unsatisfying effects on the generalization performance. As the number of weight connections and nodes in the system increases, this problem becomes more critical. With pruning techniques, a neural network with a compact size not causing the overfitting problem can be acquired. Pruning is the process of reducing the complexity of a neural net system by deleting superfluous weights and nodes of a system based on the magnitude and/or the sensitivity of the parameters. The key strategies of pruning are to estimate the saliency of the weights and the nodes of a system, and to eliminate the parameter with low saliency. The saliency can be simply calculated based on the magnitude under the assumption that the saliency is proportional to the magnitude of parameters. The change of the error with respect to the change or deletion of parameters is also a good criterion for more reasonable pruning.

Some pruning techniques have been suggested with the philosophies above. Le Cun et. al [4] introduced the optimal brain damage (OBD) that uses the minimal increase in training error as the criterion for weight elimination. Hassibi et. al [5] suggested a more mathematical and refined method, the optimal brain surgeon (OBS), which shares the same basic idea with OBD except that the latter considers the best changes of the other weights too when deleting a weight. Thus, the retraining after pruning is not required in OBS.

In this paper, we employ OBS strategy to improve the performance of the neural net guidance law. The OBS is derived from the following mathematical logic. The change in error with respect to the weights (or parameters) for the well-trained system can be expressed as:

$$\delta E = \frac{1}{2}\delta w^T H \delta w \qquad (H \equiv \frac{\partial^2 E}{\partial w^2}) \qquad (2)$$

where H is the Hessian matrix. The elimination of w_i is equivalent to the following equation:

$$e_i \delta w + w_i = 0 \qquad (3)$$

where e_i is a unit vector in weight space corresponding to w_i. By using a Lagrange multiplier λ, the change in error (2) can be minimized under the constraint of the equation (3).

$$L = \frac{1}{2}\delta w^T H \delta w + \lambda(e_i^T \delta w + w_i) \qquad (4)$$

Here, our goal is to find δw minimizing the equation (4). The functional derivative of (4) gives the following results:

$$\delta w = -\frac{w_i}{[H^{-1}]_{ii}} H^{-1} e_i \qquad (5)$$

$$\delta E_i = \frac{1}{2}\frac{w_i^2}{[H^{-1}]_{ii}} \qquad (6)$$

The weight with the smallest δE is deleted and the other weights are updated by (5).

The algorithm of OBS is summarized as follows:
1. Train a network until the minimum error is reached.
2. Calculate the inverse of H.
3. Select the weight providing the lowest change in error.
4. Update all the weights in the network by (5).
5. Go to step 2 and repeat the above procedure until stopping criteria are satisfied.

IV. SIMULATION RESULTS

We consider two-dimensional pursuit-evasion games shown in the figure 2. The equations of motion of the pursuer or the evader are expressed as follows:

$$\dot{x} = v\cos\gamma$$
$$\dot{y} = v\sin\gamma$$
$$\dot{\gamma} = \frac{v}{R}u \quad , \quad |u| \leq 1 \qquad (7)$$
$$\dot{v} = -\frac{v^2}{R}(a + bu^2)$$

where x, y are the pursuer or the evader's position and v is the speed and γ the flight path angle, respectively. u is the control input and R is the minimum turn radius. a, b are related to the lift and/or drag coefficients. The values of R, a, b for each player are given as follows: a_p=0.0875, b_p=0.40, R_p=1515.15, a_e=0, b_e=0.40, and R_e=600.

Pursuit-evasion games are solved for 16 engagement situations in which the path angle of the pursuer varies from 0° to 30° by 10° and that of the evader, from 0° to 90° by 30°, while the initial positions and the speeds are fixed as (x_p, y_p, v_p) = (0m, 0m, 600m/s), and (x_e, y_e, v_e) = (0m, 0m, 200m/s). Game solutions are obtained using gradient
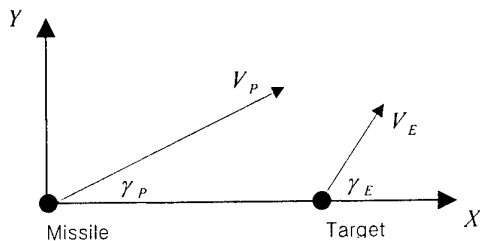
Figure 2. Two-dimensional pursuit-evasion game

method proposed by Tahk et. al [3].

The NN guidance law is organized using the obtained solutions. As stated in section II, range, range rate, LOS angle, and LOS rate are selected as network inputs that generate the normalized control input of the missile throughout the network. The original network has 301 weight connections resulting from one fully connected hidden layer of 50 processing nodes with biases. The network is trained until the final training error criterion - less than 10^{-8} of mean-squared error (MSE) - is reached, by using Levenberg-Marquardt method [6].

By applying OBS algorithm, we pruned 80 weights from the original NN. Consequently, we obtain the network system with 221 weights that provides 10^{-6} of MSE. Since there is no obvious criterion about how many weights should be pruned to satisfy our purpose, we determine the number of deletions on the observation of the change in the training error.

Since the value of MSE cannot say about the performance of the NN guidance law, we need to reconstruct the trajectory using NN feedback guidance law to examine the NN guidance law. We reconstruct the trajectories for 40 scenarios, 16 of trained scenarios and 24 of off-trained scenarios. The off-trained scenarios are selected by changing the evader's initial path angle six times - $10°$, $20°$, $40°$, $50°$, $70°$, $80°$ - with the same configuration of the initial position, speed, and missile path angle as in the trained scenarios.

We compare the results of trajectory reconstruction by two NN guidance laws - original NN and pruned NN respectively, by adopting two performance-indicating parameters, the miss distance (r_f) and the final time error (e_f), respectively. Table 1 and 2 contains the number of scenarios corresponding to a prescribed performance level, as to r_f and e_f respectively. We can find that the original NN fails in interception more than half of the scenarios, even for the trained scenarios. Meanwhile, the pruned NN guarantees interception for almost all scenarios. One interesting point is that the performance of guidance law using the pruned NN is robust to the scenario variation. For most scenarios, a few meters miss distance and a few tenth percent final time error is guaranteed.

Figure 4 illustrates the trajectories and control histories for one scenario. The histories of four neural network input variables, that is range, range rate, LOS angle, and LOS rate, are depicted in figure 5. We can observe that before 12 sec, the original NN generates almost same control input values as the optimal solutions. However, small LOS error arisen at about 13 sec causes control value to diverge, and leads the missile to fail to intercept the target in the sequel. On the other hand, although the pruned NN generates an erroneous control initially, it makes control inputs that compensate the LOS error during the engagement, and finally succeed in capturing the target.

Although we neglect the attitude dynamics when solving the pursuit-evasion games, the autopilot delay caused attitude dynamics cannot be neglected in real implementation. We compare the interception performance of two NN guidance laws in the existence of the autopilot delay. The dynamics of the actual control values is assumed first order. Table 3 shows the miss distances for two guidance laws with autopilot delay 0.1 sec or 0.5 sec. For the original NN guidance, the interception performance is seriously degraded as the autopilot delay increases, while the pruned NN guidance is insensitive to the autopilot delay. The trajectories in figure 6 and control histories in figure 7 also demonstrate this feature.

V. CONCLUSIONS

This paper proposes an improved neural network guidance law using optimal brain surgeon, one of network pruning techniques. A feedback guidance law based on pursuit-evasion games is constructed by using neural network approximation. Optimal brain surgeon is employed to prune the neural network for the sake of avoiding the overfitting phenomena and improving the guidance performance. Computer simulations are performed to validate the performance enhancement achieved by pruning. Consequently, it is found that the pruned neural network guarantees good interception performance robust to the scenario variation and to the missile autopilot delay.

ACKNOWLEDGEMENT

REFERENCES

[1] E.J.Song and M.J.Tahk, "Real-time midcourse guidance with intercept point prediction," *Control Engineering Practice*, Vol.6, No.8, p.957-967, November 1998.

[2] H.L.Choi, Y.Park, H.G.Lee, and M.J.Tahk, "A Three-dimensional differential game missile guidance law using neural networks," *AIAA Guidance, Navigation, and Control Conference*, Montreal, Canada, August 2001.

[3] M.J.Tahk, H.Ryu, and J.G.Kim, "An iterative numerical method for a class of quantitative pursuit-evasion games," *AIAA Guidance, Navigation, and Control Conference*, Boston, Mass., USA, August 1998.

[4] Y.Le Cun, J.S.Denker, and S.A.Solla, "Optimal brain damage," in *Advances in Neural Information Processing Systems 2*, D.S.Touretzky, Ed., p.598-605. Morgan Kaufmann, San Mateo, CA, 1990.

[5] B.Hassibi, D.G.Stork, "Second order derivatives for network pruning: optimal brain surgeon," *NIPS92*, 1992.

[6] M.Hagan and M.Menhaj, "Training feedforward networks with the Marquardt algorithm," *IEEE Transactions on Neural Networks*, Vol. 5, No. 6, November 1994.

Table 1. Results of miss distance without autopilot delay
(number of corresponding scenarios)

Miss Distance (m)	Original NN		Pruned NN	
	Trained	Off-trained	Trained	Off-trained
< 1.0	7	4	3	7
1.0 - 10.0	0	4	11	13
10.0 - 30.0	2	1	1	2
Fail	7	15	1	2

Table 2. Results of final time error without autopilot delay
(number of corresponding scenarios)

Final Time Error (%)	Original NN		Pruned NN	
	Trained	Off-trained	Trained	Off-trained
< 0.1	9	6	1	0
0.1 - 1.0	0	2	14	21
1.0 - 2.0	0	1	1	1
Fail	7	15	1	2
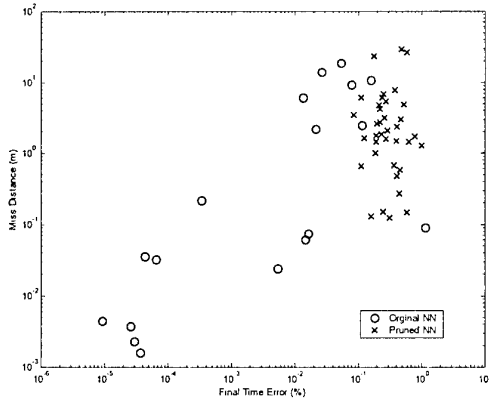
Figure 3. Distribution of performance parameters
(miss distance, final time error)
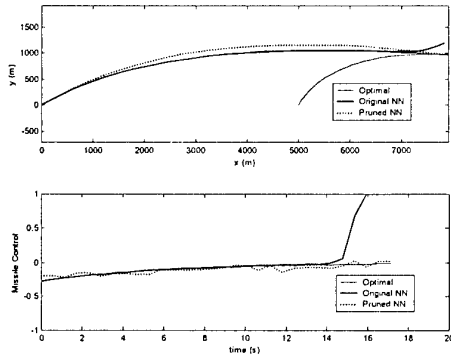
Figure 4. Trajectories and missile control histories without autopilot delay (γ_p=30°, γ_c=60°)
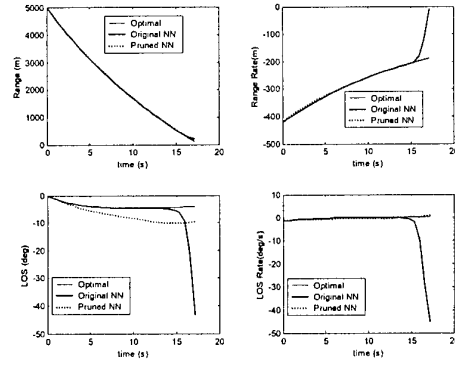
Figure 5. Neural network input variable histories without autopilot delay (γ_p=30°, γ_c=60°)

Table 3. Results of miss distance with autopilot delay
(number of corresponding scenarios)

Miss Distance (m)	Original NN			Pruned NN		
	No delay	Delay 0.1 s	Delay 0.5 s	No delay	Delay 0.1 s	Delay 0.5 s
< 1.0	11	10	8	10	21	14
1.0 - 10.0	4	1	0	24	16	19
10.0 - 30.0	3	0	0	3	0	2
Fail	22	29	32	3	3	5
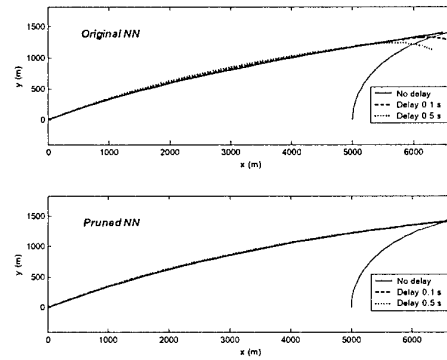
Figure 6. Trajectories with autopilot delay (γ_p=20°, γ_c=90°)
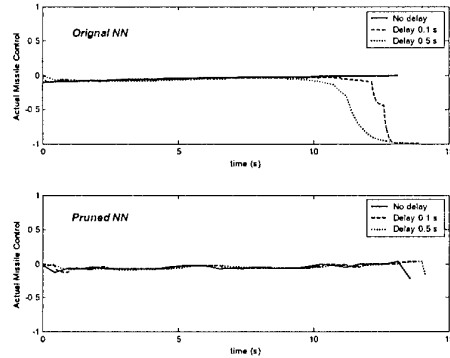
Figure 7. Missile control history with autopilot delay (γ_p=20°, γ_c=90°)

IL1

Research and Future Directions on Smart Structures and Materials in Aerospace Vehicles

Anna-Maria Rivas McGowan
NASA Langley Research Center
Hampton, Virginia

Keywords: Aircraft, Helicopters, Aerodynamics, Fluid Dynamics, Aerodynamic Characteristics, Unsteady Flows, Wings and Airfoil Sections, Turbulent Flows, Flight Dynamics

Abstract

Smart material based sensors and actuators, and their associated support hardware and electronics have been the subject of considerable research activities including demonstration efforts and development of some critical enabling technologies. This research has led to a series of breakthroughs in a variety of disciplines. Integration of smart materials and structures into aerospace vehicles shows the promise of significant benefits if the appropriate application issues are addressed and if the vehicle is designed to effectively use the technology. When fully realized, smart materials and structures have the potential to produce considerable increments in flight vehicle system safety, affordability, environmental compatibility, and efficiency. This paper will highlight some research efforts and technical challenges in applying smart materials and structures to aerospace vehicles.

Introduction

The exceptional capabilities of smart materials and structures have inspired numerous innovative concepts that may enable substantial improvements in the adaptability and efficiency of future aerospace vehicles. These concepts include using active flow control to enable simpler high-lift systems and active aeroelastic control to attenuate undesired vibratory response. In this context, smart is defined as the ability to respond to a stimulus in a predictable and reproducible manner. Smart materials are also known as adaptive materials, active materials, or multifunctional materials. This class of unusual materials has been available and used effectively for considerable time. However, application of these materials to aerospace vehicles for large-scale sensing and actuation has only received attention over the past two decades.

Often called a disruptive technology, the application of smart materials and structures to aerospace vehicles brings much promise and controversy to the aerospace community. This dichotomy is not unusual for new technologies. Typically, there is an initial over-selling of new technologies, quickly followed by controversy as to the real benefits provided by the new ideas. In reference [1] Weisshaar represents this trend graphically as shown in Figure 1, to describe the cycles of optimism and pessimism for new technologies. As mentioned in reference 1, two important issues arise in the attempts to apply new technical discoveries: (1) the first use of a new technology often leads to focusing research on the newfound issues in using the technology, and (2) simply replacing existing systems with the new technology often results in sub-optimal performance. In reference 1, Weisshaar describes an example:

Historically, new design uses of a new material are more important than simply using the new materials as replacements for existing materials. An example is aluminum, which became available for aircraft use about 1915. It was a limited success and in some cases a failure when it was only applied as a substitute for wood and canvas on biplanes. However, the development and acceptance of stressed skin construction in the late 1920 s allowed aluminum to revolutionize aircraft design by fostering the introduction of high speed, light weight monoplanes. These issues are prevalent today in the application of smart materials and structures to aerospace vehicles. Likewise, the opportunity for positive, sweeping change in the aerospace industry is also possible if a systems-level, multidisciplinary design approach is used to take advantage of the unique characteristics of smart materials and structures in an optimal fashion.
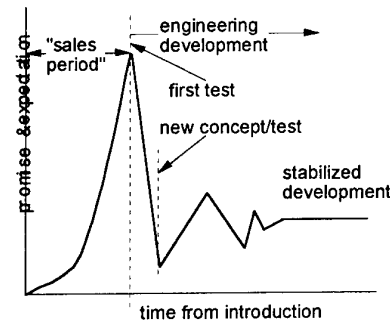
Figure 1 Promise and expectation of new technologies

Today, innumerable universities, government agencies and industries have conducted research in the area of smart materials and structures and their application to aerospace vehicles as well as other mechanical systems. Though much research has been conducted, including some significant experimental demonstrations, the opportunity for far-reaching improvement in vehicle capability remains unbounded. This paper will summarize some significant results and benefits in

using smart materials and structures in aerospace vehicles, identify a few of the enabling technologies and technical challenges, and discuss the future potential of this technical area. Selected studies are also presented to highlight the current work in the smart structures applications to vehicles.

Research on Smart Structures Applications to Aerospace Vehicles

References 1-3 provide overviews of work on applying smart materials-based actuators to flight vehicles. Reference 4 provides a summary of demonstrations of space applications. Some examples of significant experimental demonstrations on applying smart materials and structures to aerospace vehicles have incorporated a variable area nozzle, variable configuration inlet, hingeless control surfaces, wing twist, buffet load alleviation, and individual blade control on rotorcraft. Several large diverse programs have also been formed to address a variety of multidisciplinary technical issues in using smart materials and structures. Note that all of the research efforts mentioned herein include collaborators from various organizations due to the inherently multidisciplinary nature of smart structural concepts.

A team led by United Technologies Research Center designed and tested an innovative concept to enable a simple and effective variable area fan nozzle for high bypass ratio engines.[5] The team used a bundled cable actuation system to optimize strength and packaging of a wire-based shape memory alloy (SMA) actuator. This approach capitalized on the wealth of knowledge available on wire ropes and resulted in a flexible, yet strong SMA actuator with a gradual failure mode. The actuation system was tested in a full-scale component under full-scale aerodynamic loads demonstrating the required 20% nozzle exit area change. The full-scale sector model (testing 2 flaps out of 30) is shown in Figure 2 at the National Aeronautics and Space Administration (NASA) Langley Jet Exit Test Facility. The actuation system was only half of the weight of a conventional mechanical system and the required power (300-400 watts for the component) is reasonable, even when calculated for a full annular system. System studies performed for this effort show a potential 5-6% increase in range and 2-3% savings in aircraft direct operating cost as compared with a fixed-geometry nozzle geared turbofan.[5]
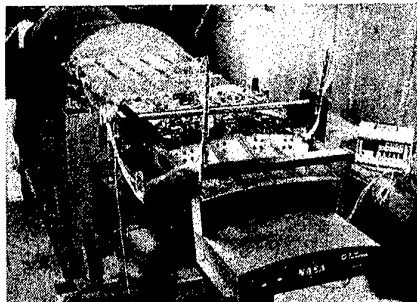
Figure 2 Model tested in variable area nozzle study

The Smart Aircraft and Marine Project System Demonstration (SAMPSON) was conducted by a team led by the Boeing Company, funded by the Defense Advanced Research Projects Agency (DARPA) and managed by NASA Langley Research Center and the US Navy s Office of Naval Research.[6] The SAMPSON program was focused on demonstrating that smart materials can be used to significantly enhance vehicle performance and enable new missions and/or expand current missions. This effort designed and tested SMA actuators at full scale under full-scale aerodynamic loads using an F-15 inlet to validate control of tactical aircraft inlet geometry and internal flows. The inlet configurations being investigated consist of capture area control, compression ramp generation, leading edge blunting, and porosity control. For capture area control, the hydraulic actuator normally used for cowl rotation on the full-scale inlet was replaced with a wire-based, agonist-antagonistic SMA linear actuation system for variation of the inlet capture area. Figure 3 shows the inlet in the 16-foot Transonic Tunnel at NASA Langley for testing. Two hydraulic cylinders were used as braking devices to hold the cowl in place when the SMA wire bundles were not powered. During the first phase of wind tunnel testing, the SMA cowl actuator operated successfully at a Mach range of M=0.0 to M=0.8 rotating the cowl up to 9 degrees. The power required for actuation was 1700 watts per bundle. A second phase of testing was completed in early 2001, and will be documented in future reports.

Figure 3 Inlet in the NASA Langley 16-foot Transonic Tunnel

The DARPA/Air Force Research Laboratory (AFRL)/NASA Smart Wing program was conducted by a team led by the Northrop Grumman Corporation (NGC) to develop and demonstrate smart material-based concepts to improve the aerodynamic performance of military aircraft. This program was divided into two phases during which four wind-tunnel tests were conducted using a variety of actuation mechanisms.[7] During Phase 1 of this program, a 16% scale, semi-span wind-tunnel model, representative of an advanced military aircraft wing, was designed and fabricated by NGC. The model was wind-tunnel tested at NASA Langley s Transonic Dynamics Tunnel (TDT) in May 1996 and June-July 1998. The smart wing model incorporated contoured, hingeless flap and aileron designs actuated using built-in

SMA tendons. Control surface deflections of up to 10¡ were obtained. Variable spanwise twist of the smart wing was achieved using mechanically simple SMA torque tubes that employed novel connection mechanisms to effect a high degree of torque transfer to the structure; 3200 in-lbs. of torque was generated by the SMA tubes. Up to 5¡ of spanwise twist at the wing tip was demonstrated. Under steady-state conditions, 8% to 12% improvements in lift, pitching and rolling moments were achieved over a broad range of wind tunnel and model configurations, in comparison to a conventional design incorporating hinged control surfaces. During Phase 2 a larger, full-span model representative of an uninhabited combat air vehicle (shown in Figure 4) configuration was tested with a conventionally-actuated wing and a smart material-actuated wing. The Phase 2 effort incorporated leading and trailing edge smart control surfaces, higher bandwidth actuation systems and testing at transonic Mach numbers and high dynamic pressures. Additionally, the smart material actuation system was developed to meet the challenging goals of smoothly contoured control surfaces with both chord-wise and span-wise shape variability at high actuation rate. Reference 8 documents the development of the actuation system. The first test in Phase 2 successfully demonstrated increased aileron reversal speed and variable spanwise shape.[9] The second wind-tunnel test in the Phase 2 program was completed in early 2001, and will be documented in future reports.

Figure 4 Phase 2 smart wing model in the TDT at NASA Langley

Numerous analytical and experimental studies demonstrate that piezoelectric materials (piezoelectrics) can be used as actuators to actively control vibratory response. One important study successfully demonstrated using piezoelectric actuators to control buffeting on the vertical tails of twin-tail, high-performance military aircraft. This international effort includes wind-tunnel testing of a 1/6 scale F/A-18 model experiencing aerodynamic buffet[10] and ground testing of a full-scale F/A-18 airplane using simulated buffet input.[11] In addition, recent wind-tunnel tests have been completed that examined the performance of new piezoelectric actuators for buffet load alleviation.[12] Previous studies have also demonstrated active flutter suppression and gust load alleviation using piezoelectric actuators.[13,14] Piezoelectric actuators also have shown to be effective in active noise suppression.[15] One potential alternative for vibration suppression is damping augmentation using shunted

piezoelectrics. This approach allows for active or passive damping augmentation, yet cannot cause instability. Furthermore, shunted piezoelectrics use little to no power and are simple to apply; the only necessary hardware is the piezoelectrics themselves and simple electric circuitry using resistors and inductors. References 16 and 17 discuss the results of some studies using shunted piezoelectrics.

Smart materials and structures have also been considered for rotorcraft applications. Two current efforts are the NASA/Army/MIT Active Twist Rotor program and the DARPA SMART Rotor program. The Active Twist Rotor program is a collaboration between NASA Langley Research Center, the Army Research Laboratory and Massachusetts Institute of Technology. The program is investigating helicopter rotor blades embedded with interdigitated-electrode poled, piezoelectric fiber composite layers (active fiber composites) to enable individual blade control.[18] This technology may reduce rotorcraft vibrations and increase rotor performance. During the program a four-bladed, aeroelastically-scaled, active-twist model rotor was designed with embedded piezoelectric actuators and tested in Transonic Dynamics Tunnel at NASA Langley. Sixty to 95% reductions in the fixed system loads were demonstrated during testing.

The DARPA-funded SMART Rotor program is monitored by the Army Research Office and led by the Boeing Company.[19] The program is focused on developing actuator capability to enable helicopter rotor control using smart materials. Several actuator concepts have been designed and evaluated in the program including SMA torsion tubes. The biaxial SMA tubes work in concert with an SMA-activated lock for powered off conditions. This actuation system enables in-flight, real-time adjustment of rotor blade-tracking tabs to reduce vibration and increase performance.

The Leitprojekt ADAPTRONIK encompasses 24 partners from research institutes and industry in Europe and is led by the German Aerospace Center (DLR). The project is described in reference 20. The objectives of this project are the development and integration of piezoelectric patches and fibers into structures to enable lightweight construction. A variety of applications from the industrial partners is being considered including: active noise and vibration reduction, contour deformation, and micro-positioning. The diversity of industrial applications included in the project is unique. It includes automobiles, rail vehicles, medical engineering and aerospace. Research activities in the project range of from materials development to large-scale demonstration. Another collaboration on smart structures in Europe is the Applications for Smart Structures in Engineering and Technology (ASSET).[21] ASSET is funded under the European Union s Industrial Materials and Technologies research program and includes approximately 50 organizations. The collaboration seeks to encourage exploitation of smart technologies within the European framework.

NASA s Morphing project in the Aerospace Vehicle Systems Technology Office at NASA Langley Research Center develops and matures smart technologies and addresses the

multidisciplinary issues associated with applying these technologies to provide cost-effective system benefits to aircraft and spacecraft.[22] These benefits include enabling self-adaptive flight with significant improvements in efficiency and safety. Integration of smart materials and structures and active flow control research across many disciplines is an important element in the project. Some of the research efforts include: synthetic jet characterization, separation control using oscillatory blowing, fluidic thrust vectoring, new materials and actuator development, shape memory alloys for noise suppression, and shape change for performance enhancement. Analytical studies, laboratory and wind-tunnel tests are currently underway in the Morphing project to assess and further develop these technologies. The Morphing project ultimately strives to assure the usability of adaptive vehicle technologies and, thus, have a major impact on air and space travel and the way in which aircraft and spacecraft are manufactured and flown.

Active Flow Control

Smart materials and advances in fluidics are enabling technologies for advanced active flow control. Recent discoveries in material science and fluidics have been used to create a variety of aerodynamic control devices that have great potential to enable entirely new approaches to aerospace vehicle flight control. In active flow control, the global flowfield is dynamically altered by interacting with and controlling localized flow instabilities and flow structures[23] Thus, for many flow control applications, smart technologies are used to modify local phenomena to support a macroscopic strategy, such as flow separation control for advanced high lift systems. Some of the potential benefits of flow control include reduced weight, part count, operating cost, emissions, and noise, as well as, increased safety and vehicle performance.[24] Two active flow control efforts are summarized herein: the DARPA-funded active flow control effort at the Boeing Company and NASA Langley Research Center s research in this area.

Boeing Active Flow Control System (BAFCS) is sponsored by DARPA and is seeks to develop active flow control technologies to increase the payload on rotorcraft. The focus of this program is reducing download for the V-22 tiltrotor aircraft. The BAFCS is described in reference [25]. For the V-22 in hover mode, AFC may be used to mitigate the download by reducing flow separation on the trailing edge flap resulting in a 20% increase in payload for some missions. There are two phases in the program; the first phase includes 2-D wind-tunnel testing, actuator development, and an assessment of the practicality of the actuation system for the V-22. Phase 2 includes 3-D wind-tunnel testing and continued AFC hardware development. The actuator development in this program incorporates investigating the use of PVDF materials to create zero-net mass flux synthetic jets for separation control. To increase the performance of the synthetic jet actuators, two smart materials are being developed: stretched and electron irradiated polyvinylidene flouride-trifluorethylene copolymer and single crystal piezoelectric materials. Though this program focuses on application of active flow control to the V-22, much of the research is applicable to other rotary and

fixed wing applications including the Bell/Boeing Quad Tiltrotor, the Advanced Tactical Transport, and the XV-15 tiltrotor.

Active flow control research at NASA Langley Research Center focuses on developing cost-effective advanced technologies that may lead to substantial advances in aerodynamic performance and flight vehicle control for a broad range of vehicles. References 26 and 23 provide overviews of the research in active flow control at Langley Research Center. Reference 24 describes the development of design tools for active flow control applications. A number of flow control actuation concepts have been considered including piezoelectric actuators and other fluidic control devices which can produce forces and moments by creating small flow distortions over the surface of an airfoil. Fluidic control devices have also been used to alter the degree of separated flow over specifically-designed portions of an airfoil as described in reference [27]. An advanced aerospace vehicle might use several strategically placed actuators or distributed arrays of hundreds of such devices on its surface to generate forces and moments for stabilization and maneuver control. This approach may reduce or potentially eliminate the need for conventional, hydraulically-actuated ailerons, flaps or rudders.[28]

The high pay off, high risk programs described above were instrumental in not only demonstrating the benefits of using smart materials and structures on flight vehicles, but also in addressing some of the many realistic issues associated with applying this technology to large- and full-scale vehicle components. These programs also provide crucial feedback to the technical community on areas for further development of the enabling technologies such as materials development, actuator design, electronics, modeling, etc.

Enabling Technologies

High performance piezoelectric polymers are also of interest to the aerospace community as they may be useful for a variety of sensor applications including acoustic, flow, and strain sensors. Over the past few years, research on piezoelectric polymers has led to the development of promising high temperature piezoelectric responses in some novel polyimides.[29] Fiber optic sensors are also being considered as a crucial enabling technology for future vehicle health monitoring systems. Actuation technology focused on smart materials includes research on materials processing and packaging. Two examples of widely used actuators include the THUNDER actuator and fiber-based piezoelectric actuators.

Researchers at NASA Langley Research Center developed the high-displacement piezoelectric actuator, THUNDER (THin layer composite UNimorph ferroelectric DrivER and sensor) to meet high displacement actuator requirements. THUNDER actuators are unimorph-type actuators, which consist of a piezoelectric ceramic layer bonded to one or more non-piezoelectric secondary layers. References [31]-[34] contain more information on THUNDER devices and their application. Developed in the mid 1990 s, the THUNDER

actuator is now considered commercial off-the shelf technology.

Additionally, flat, in-plane piezoelectric actuators have been studied extensively for strain actuation applications for over a decade. Research on increasing the performance of in-plane actuation has focused on investigating a variety of characteristics including material selection, actuator geometry and packaging. Although the simplest actuator concept includes using a monolithic patch of piezoelectric material actuated in the 3-1 mode with simple electrodes (using the d_{31}-coupling coefficient), exploitation of the much higher d_{33} coefficient yields significantly larger actuation effectiveness. For actuation in the 3-3 mode, interdigitated electrode (IDE) patterns of electrodes are often used for poling and actuation.[35,36] References 37-42 describe some actuation concepts that use the d_{33} coefficient with IDE electrodes. Some of these actuation concepts are composite piezoceramic fiber devices (as shown in Figure 5) that are very effective, flexible and durable. However, processing and handling the costly piezoceramic fibers during fabrication can be difficult and actuation voltages are typically high.
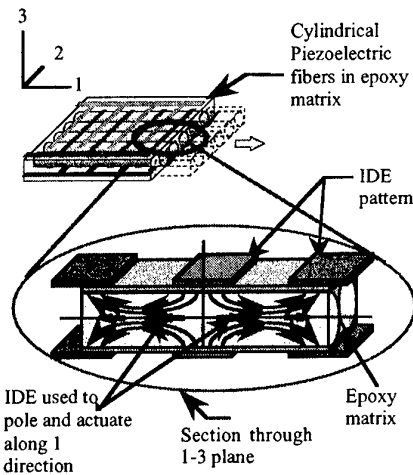

Figure 5 Active Fiber Composite (AFC) actuator concept

At NASA Langley Research Center, a composite device has been recently developed that addresses many of the disadvantages of piezocomposite actuators while retaining the salient features of the actuation concept. Called the LaRC-MFC™ (Langley Research Center — Macro-Fiber Composite™), this actuation concept has high strain energy density, directional actuation, conformability and durability and, most importantly, low cost, uniform manufacturing processes.[43,44] The actuator is shown in Figure 6.

Figure 6 The LaRC-MFC™

The LaRC-MFC™ is already being tested in several applications including large, lightweight, deployable space structures and for buffeting alleviation on fighter airplanes[12] The actuator has produced a factor of 20 increase in the vibration damping capability of lightweight, inflatable space structures.

Adaptive and/or active methods of controlling the structural acoustic response and flutter of panels to reduce the transmitted noise and avoid panel destruction may be accomplished with the use of SMA hybrid composite (SMAHC) panels. These panels have the potential to offer improved thermal buckling/post buckling behavior, dynamic response, fatigue life, and structural acoustic response.[45-46] At NASA LaRC, fabrication of SMAHC structures has focused on embedding ribbon-type Nitinol actuators into a glass/epoxy material system. Quasi-isotropic panels with SMAs prestrained 4% and embedded in the zero degree direction have been successfully fabricated and dynamically tested.[47] In reference 47, Turner shows experimental validation results for a constitutive model and finite element formulation for analyzing such active structures.

Innovative design has led to several novel actuation concepts using smart material. In reference 48, a compact rotary motor driven by piezoelectric bimorph actuators is described. This actuator uses a roller wedge as a rotary clutch to rectify the motion of the actuation system enabling lip-blunting shapes for engine inlets. In reference 49, a piezoelectrically actuated elastodynamic aerodynamic surface was developed to create a meso-scale hovering aerial vehicle.

Technical Challenges and Future Potential

Considerable research has been conducted on smart materials and structures and their application to aerospace vehicles. A few examples of this work are summarized in this report; but this is in no way a just representation of the breadth of excellent research on the subject. Much research remains to address the numerous issues in applying smart structures to vehicles. These issues include: modeling, control, electronics, power requirements, structural integrity, manufacturability, reliability, maintainability, cost, and many others. Improving the efficiency and reducing the size of the actuation electronics is imperative for realistic application of smart materials and structures. An additional complicating factor in the maturation of smart materials and structures applications to flight vehicles is the lack of scaling laws.

Since scaling issues have not been resolved for most applications, it is difficult to quantitatively ascertain full-scale performance from smaller scale lab studies even though bench and lab tests are crucial to increasing technology maturity. Additionally, since smart materials are multifunctional materials (i.e., electro-mechanical, thermo-mechanical, etc.), their performance varies widely depending on how it is integrated into the application and the electrical, thermal, or magnetic system used to actuate them. Hence, although validated analytical tools are currently available for many smart materials and structures, these tools must be carefully re-examined and, at times, redefined for each application.

Though much research has been conducted, including some significant experimental demonstrations, the opportunity for far-reaching improvement in vehicle capability remains unbounded. To date, much of the large or full-scale demonstrations have used piezoelectric-based or SMA-based actuation mechanisms. However, as other smart materials mature, the ability to create actuation systems with other types of smart materials and the ability to combine different materials may yield additional and improved capabilities. To fully exploit the unique capabilities of smart materials and structures in aerospace vehicles, the basic design of the vehicle must be re-evaluated using a systems-level, multidisciplinary, optimal design approach. If the relevant technological issues are addressed and vehicles can be designed to exploit the exceptional capabilities of smart materials and structures, this unusual class of materials will continue to inspire numerous innovative concepts that may enable substantial improvements in future aerospace vehicles.

Acknowledgements

References

[1] Weisshaar, T. A., Aeroservoelastic Control with Active Materials- Progress and Promise, CEAS International Forum on Aeroelasticity and Structural Dynamics, Manchester UK, June 1995.

[2] Crowe, C. R. and Sater, J. M., Smart Aircraft Structures, Future Aerospace Technology in the Service of the Alliance, Vol. 1: Affordable Combat Aircraft, AGARD Conference Proceedings 600, pp. A20-1 to A20-15, Paris, France, 1997.

[3] Loewy, R. G., Recent Developments in Smart Structures with Aeronautical Applications, Journal of Smart Materials and Structures, Vol. 5, October 1997, pp. 11-41.

[4] Henderson, K. and Denoyer, K. K., Recent Transitions of Smart Structures Technologies Through Flight Experiments,

Proceedings of SPIE Smart Structures and Materials 2001, Industrial and Commercial Applications of Smart Structures Technologies, March 5-8, 2001, Newport Beach, California, Paper No. 4332-19.

[5] Rey, N. M., Tillman, G., Miller, R. M., Wynosky, T., Larken, M. J., Flamm, J. D., and Bangert, L. S., Shape Memory Alloy Actuation for a Variable Area Fan Nozzle, Proceedings of SPIE Smart Structures and Materials 2001, Industrial and Commercial Applications of Smart Structures Technologies, March 5-8, 2001, Newport Beach, California, Paper No. 4332-46.

[6] Pitt, D. M., Dunne, J. P., White, E. V., and Garcia, E., Wind Tunnel Demonstration of the SAMPSON Smart Inlet, Proceedings of SPIE Smart Structures and Materials 2001, Industrial and Commercial Applications of Smart Structures Technologies, March 5-8, 2001, Newport Beach, California, Paper No. 4332-43.

[7] Kudva, J. N., Sanders, B. P., Pinkerton-Florance, J. L., and Garcia, E., Overview of the DARPA/AFRL/NASA Smart Wing Phase II Program, Proceedings of SPIE Smart Structures and Materials 2001, Industrial and Commercial Applications of Smart Structures Technologies, March 5-8, 2001, Newport Beach, California, Paper No. 4332-48.

[8] Wang, D. P., Bartley-Cho, J. D., Martin,, C. A., and Hallam, B. J., Development of High-Rate, Lare Deflection, Hingeless Trailing Edge Contro Surface for the Smart Wing Wind Tunnel Model, Proceedings of SPIE Smart Structures and Materials 2001, Industrial and Commercial Applications of Smart Structures Technologies, March 5-8, 2001, Newport Beach, California, Paper No. 4332-51.

[9] Martin, C. A., Scherer, L. B., Flanagan, J. S., Carpenter, B. F., Design, Fabrication, and testing of Scaled Wind Tunnel Model for the Smart Wing Phase II Program, Proceedings of SPIE Smart Structures and Materials 2001, Industrial and Commercial Applications of Smart Structures Technologies, March 5-8, 2001, Newport Beach, California, Paper No. 4332-50.

[10] Moses, R. W., Contributions to Active Buffeting Alleviation Programs by the NASA Langley Research Center, Proceedings of the Proceedings of the 40th AIAA/ASME/ASCE/AHS/ASC Structures, Structural Dynamics and Materials Conference, AIAA 99-1318, St. Louis, MO, April 1999.

[11] Hopkins, M.A., Henderson, D.A., Moses, R.W., Findlay, D., Voracek, D.F., Spangler, R.L., Ryall, T., and Zimcik, D., Active Vibration Suppression Systems Applied to Twin Tail Buffeting, Proceedings of SPIE s 5th Annual Symposium on Smart Structures and Materials, Paper No. 3326-05, San Diego, CA, March 1-5, 1998.

[12] Moses, R. W., Wiesman C. D., Bent, A. A., and Pizzochero, A. E., Evaluation of New Actuators in a Buffet Loads Environment, Proceedings of SPIE Smart Structures

and Materials 2001, Industrial and Commercial Applications of Smart Structures Technologies, March 5-8, 2001, Newport Beach, California, Paper No. 4332-02.

[13] McGowan, A. R., Heeg, J., and Lake, R.C., Results of Wind-Tunnel Testing From the Piezoelectric Aeroelastic Response Tailoring Investigation, Proceedings of the 37th AIAA/ASME/ASCE/AHS/ASC Structures, Structural Dynamics and Materials Conference, Salt Lake City, UT, April 1996.

[14] Costa, P., Moniz, P. A., and Suleman, A., Experimental Aeroelastic Control Using Adaptive Wing Model Concepts. Proceedings of SPIE Smart Structures and Materials 2001, Industrial and Commercial Applications of Smart Structures Technologies, March 5-8, 2001, Newport Beach, California, Paper No. 4332-05.

[15] Gibbs, G. P, Eure, K. W., and Lloyd, J. W., Active Control of Turbulent Boundary Layer Induced Sound Radiation from Aircraft Style Panels, Proceedings of Active 99, Ft. Lauderdale, FL, December 2-4, 1999.

[16] McGowan, A. R., A Feasibility Study of Using Shunted Piezoelectric Piezoelectrics to Reduce Aeroelastic, SPIE s 6th Annual Symposium on Smart Structures and Materials, Industrial and Commercial Applications Conference, Newport Beach, CA Paper number 3674-20, March 1999.

[17] Shu-yau Wu, Travis L. Turner and Stephen A. Rizzi, Piezoelectric Shunt VibrationDamping of an F-15 Panel Under High Acoustic Excitation, SPIE Paper No. 3989-27, SPIE's 7th Annual International Symposium on Smart Structures and Materials, Newport Beach, California, March 5-9, 2000.

[18] Wilbur, M. L., Mirick, P. H., Yeager, W. T., Langston, C. W., Vibratory Loads Reduction Testing of the NASA/Army/MIT Active Twist Rotor, American Helicopter Society 57th Annual Forum, Washington, D.C., May 2001.

[19] Kennedy, Development of an SMA Actuator for Inflight Rotor Blade Tracking, SPIE Paper No. 3985-6.

[20] Hanselka, H. and Sachau, D., German Industrial Research Project ADAPTRONIK: Content, Results, and Outlook, Proceedings of SPIE Smart Structures and Materials 2001, Industrial and Commercial Applications of Smart Structures Technologies, March 5-8, 2001, Newport Beach, California, Paper No. 4332-04.

[21] Culshaw, B., ASSET: Collaboration in Europe on Smart Structures, Proceedings of SPIE Smart Structures and Materials 2001, Industrial and Commercial Applications of Smart Structures Technologies, March 5-8, 2001, Newport Beach, California, Paper No. 4332-03.

[22] McGowan, A. R., Horta, L. G., Harrison, J. S., and Raney, D. L., Research Activities within NASA s Morphing Program, NATO-RTO Workshop on Structural Aspects of

Flexible Aircraft Control, RTO MP-36, Paper 13, October 1999.

23 Washburn, A. E., NASA Micro-Aero-Adaptive Control, SPIE s 8th Annual International Symposium on Smart Structures and Materials, SPIE paper 4332-39, March 2001.

24 Joslin, R.D., Horta, L.G., Chen, F-J., Transitioning Active Flow Control to Applications, Proceedings of the 30th AIAA Fluid Dynamics Conference, AIAA 99-3575, Norfolk, VA, 1999.

[25] Jacot, A. D., Calkins, F. T., and Mabe, J. H., Boeing Active Flow Control System (BAFCS)-11, Proceedings of SPIE Smart Structures and Materials 2001, Industrial and Commercial Applications of Smart Structures Technologies, March 5-8, 2001, Newport Beach, California, Paper No. 4332-38.

26 Pack, L. G., Joslin, R. D., Overview of Active Flow Control at NASA Langley Research Center , SPIE 1998 International Symposium on Smart Structures and Materials, paper 3326-22.

27 Seifert, A., Pack, L.: Separation Control at Flight Reynolds Numbers: Lessons Learned and Future Directions, AIAA Paper 2000-2542, Fluids 2000, June 2000.

[28] Raney, David L., Montgomery, Raymond C., Park, Michael A., and Green, Lawrence L.,: Flight Control Using Distributed Shape-Change Effector Arrays, AIAA paper 2000-1560, April 2000.

[29] Ounaies, Z., Park, C., Harrison, J. S., Smith, J. G., and Hinkley, J. A., Structure-Property Study of Piezoelectricity in Polyimides, Proceedings of Society for Photo-Optical Instrumentation Engineers, Ed. Y. Bar-Cohen, Vol 3669, 171-178 (1999).

[30] Ounaies, Z., Young, J. A., and Harrison, J. S., An Overview of Piezoelectric Phenomenon in Amorphous Polymers in Field Responsive Polymers: Electroresponsive, Photoresponsive, and Responsive Polymers in Chemistry and Biology, Ed. Khan, I. and Harrison, J.S., ACS Symposium Series 726, Washington, DC, (1999).

[31] Hellbaum, R. F., Bryant, R. G., Fox, R. L., Janlink, A. , Rohrbach, W. W., and Simpson, J. O., Thin Layer Composite Unimorph and Ferroelectric Driver and Sensor, U.S. Patent 5,632,840, May 27, 1997.

[32] Bryant, R., Fox, R., Lachowicz, J., Chen, F., Proceedings of Society for Photo-Optical Instrumentation Engineers, Vol 3674, 220-227 (1999).

[33] Mossi, K., Selby, F., and Bryant, R., Materials Letters, 35,29 (1998).

[34] Bryant, R. G. Thunder Actuators , 5th Annual Workshop: Enabling Technologies for Smart Aircraft Systems, NASA Langley Research Center, May 14-16, 1996.

[35] Hagood, N. W., Kindel, R., Ghandi, R., Gaudenzi, P., Improving Transverse Actuation of Piezoelectrics Using Interdigitated Surface Electrodes, SPIE Paper No. 1975-25, Proceedings of the 1993 North American Conference on Smart Structures and Materials, Albuquerque, NM, 1993.

[36] Yoshikawa, S., Farrell, M., Warkentin, D., Jacques, R., Saarmaa, E., Monolithic Piezoelectric Actuators and Vibration Dampers with Interdigitated Electrodes, Proceedings, SPIE s 6 th International Symposium on Smart Structures and Materials, Newport Beach, CA, March 1-5, 1999.

[37] Active Control eXperts, Inc., Product Information, 1999.

[38] Mide Technology Corporation, Product Information, 1999.

[39] Hagood, N. W., Bent, A. A., Development of Piezoelectric Fiber Composites for Structural Actuation, AIAA/ASME Structures, Structural Dynamics, and Materials Conference, La Jolla, CA, April 19-22, 1993.

[40] Bent, A. A. and Hagood, N. W., Improved Performance in Piezoelectric Fiber Composites Using Interdigitated Electrodes , SPIE s 1995 Symposium on Smart Structures and Materials, San Diego, CA, Feb 27-28, 1995.

[41] Bent, A. A., Active Fiber Composite Material Systems for Structural Control Applications, Proceedings, SPIE s 6 th International Symposium on Smart Structures and Materials, Newport Beach, CA, March 1-5, 1999.

[42] AFC Properties Summary, Continuum Control Corporation, 1999.

[43] Wilkie, W. K., et al, NASA Invention Disclosure LAR 15816-1, 1998.

[44] Wilkie, W. K., Bryant, R. G., High, J. W., Fox, R. L., Hellbaum, R. F., Jalink, A., Little, B. D, and Mirick, P. H.: Low-Cost Piezocomposite Actuator for Structural Control Applications, SPIE s 7 th Annual International Symposium on Smart Structures and Materials, March 2000.

[45] Turner, T. L.: SMA Hybrid Composites for Dynamic Response Abatement Applications, Proceedings of the 7th International Conference on Recent Advances in Structural Dynamics, N. S. Ferguson et al. (Editors), The Institute for Sound and Vibration Research, University of Southampton, England, 24-27 July 2000, Vol. 1, pp.453-465.

[46] Turner, T. L., Thermomechanical Response of Shape Memory Alloy Hybrid Composites, NASA/TM-2001-210656.

[47] Turner, T. L.: Experimental Validation of a Thermoelastic Model for SMA Hybrid Composites, SPIE s 8th International Symposium on Smart Structures and Materials; Modeling, Signal Processing, and Control in Smart Structures; Paper 4326-24; Newport Beach, CA; March 2001.

[48] Frank, J., Koopman, G., Chen, W., Mockensturm, E., and Lesieutre, G., Design and Performance of a Resonant Roller Wedge Actuator, SPIE Paper No. 3985-23.

[49] Cox, A., Monopoli, D., Goldfard, M., Garcia, E., Development of Peizoelectrically Actuated Elastodynamic Flapping Micro-Aerial Vehicles, ImechE.

A GAME-THEORETIC APPROACH TO ROBUST OPTIMAL ATTITUDE STABILIZATION OF A SPACECRAFT WITH EXTERNAL DISTURBANCES

Yonmook Park,* Min-Jea Tahk,** and Hyochoong Bang***

Division of Aerospace Engineering
Korea Advanced Institute of Science and Technology
373-1 Kusong, Yusung, Taejon 305-701, Korea

Key Words: Stability and Control, Guidance and Control

ABSTRACT

This paper considers robust, optimal, three-axis attitude stabilization of a rigid spacecraft with external disturbances by a game-theoretic approach, in which a worst-case design, that the external disturbances maximize the performance index that the control inputs minimize, is assumed. The attitude motion of a rigid spacecraft described in terms of the quaternion is considered, and a robust, optimal control law using the angular velocities and quaternion is proposed for attitude stabilization of the rigid spacecraft with external disturbances based on the nonlinear game-theoretic Hamilton-Jacobi equation. Global asymptotic stability of the proposed control law is shown by using the Lasalle Invariance Principle. A numerical example is given to illustrate the theoretical results.

1. INTRODUCTION

The optimal attitude control of a rigid body motion has been addressed by many researchers for the purpose of the optimal attitude control of the spacecraft [1]-[5]. These studies have mainly addressed the optimal regulation problem for the angular velocity subsystem with some quadratic costs. Recently, the optimal attitude control problems of the complete rigid body system including the dynamics as well as the kinematics have been investigated by many researchers: Carrington and Junkins have used a polynomial expansion approach in order to approximate the solution to the Hamilton-Jacobi(HJ) equation for the optimal attitude control problem of the spacecraft [6]. Tsiotras has derived a class of globally asymptotically stabilizing control laws for the complete attitude motion of a nonsymmetric rigid body [7]. Bharadwaj et al. have derived a couple of globally stabilizing attitude control laws using minimal, exponential kinematic parameters [8]. Krstić and Tsiotras have presented an inverse optimal control approach for constructing the optimal control law for regulation of the rigid spacecraft [9]. Especially, Park et al. have first proposed the optimal fuzzy control law for regulation of the rigid spacecraft [10].

On the robustness issues, since a spacecraft is subject to parameter variations and uncertainties mainly due to poorly known space environments in space application, the robust control problems of the spacecraft have also been extensively studied [11]-[14]. These results have mainly been focused on the system parametric uncertainties of the spacecraft. However, robust control schemes considering external disturbances have been seldom addressed.

In this paper, we first address the robust, optimal attitude control problem of a rigid spacecraft subject to external disturbances as well as inertia uncertainties. To solve this problem, we adopt the optimal game-theoretic approach [15], in which the control law and the external disturbance signal are regarded as two players that compete each other for finding the minimax solution of the optimal game problem. One of the efficient numerical methods to solve this kind of minimax problem can be found by Tahk and Sun [16], where a novel coevolution method based on the augmented Lagrangian formulation is proposed for solving constrained optimization problems.

In this paper, we consider the complete (i.e. dynamics and kinematics) attitude motion of a rigid spacecraft described in terms of the quaternion. The quaternion consists of four-dimensional parameters subject to the unity length, and is a widely used kinematic parameter set to represent the global, nonsingular orientation of a body. Instead of using a numerical method to solve the minimax problem, the proposed approach provides the analytic solution of the optimal attitude control problem coincided with the disturbance attenuation problem by investigating a Lyapunov function candidate. The optimality condition proposed in this paper is derived from the nonlinear game-theoretic HJ equation, and global asymptotic stability of the proposed optimal control law is shown by using the Lasalle Invariance Principle [17].

This paper is organized as follows: In Section 2, a rigid spacecraft model with inertia uncertainties and external disturbances is given. In Section 3, we present the robust, optimal attitude control law for the attitude motion of a rigid spacecraft considered in Section 2, and show global asymptotic stability for the proposed control law. Section 4 presents a numerical example to illustrate the theoretical results. Finally, conclusions are given in Section 5.

2. THE RIGID SPACECRAFT MODEL

A. Dynamics

This section briefly introduces the dynamics and kinematics of the rigid body orientation [18]. The dynamics of the rotational motion of a rigid body with external disturbances and inertia uncertainties are described by

---

* Graduate Student, Division of Aerospace Engineering
** Professor, Division of Aerospace Engineering
*** Assistant Professor, Division of Aerospace Engineering

the following set of differential equations:

$$(J_n + \triangle J)\dot{\omega} = S(\omega)(J_n + \triangle J)\omega + u + G\xi, \ \omega(0) = \omega_0 \quad (1)$$

where $J_n \in \Re^{3\times3}$ and $\triangle J \in \Re^{3\times3}$ denote the nominal value of the inertia matrix and the inertia matrix uncertainty of the body, respectively, $\omega \in \Re^3$ is the angular velocity vector of the body in the body-fixed frame, $u \in \Re^3$ is the control torque vector, $\xi \in \Re^3$ is the external disturbance vector, and $G \in \Re^{3\times3}$ is the input matrix for ξ. Note that, throughout this paper we define $J \triangleq J_n + \triangle J$. The matrix $S(\omega)$ denotes a 3×3 skew symmetric matrix given by

$$S(\omega) \triangleq \begin{bmatrix} 0 & \omega_3 & -\omega_2 \\ -\omega_3 & 0 & \omega_1 \\ \omega_2 & -\omega_1 & 0 \end{bmatrix}. \quad (2)$$

B. Kinematics

In this paper, the orientation of the body with respect to the inertia frame is given in terms of the quaternion. Let $\hat{e}$ and ϕ denote the Euler axis and the Euler angle, respectively. Then, the quaternion, q, is defined by

$$q^T = \begin{bmatrix} q_1 & q_2 & q_3 & q_4 \end{bmatrix} = \begin{bmatrix} q_1 & q_v^T \end{bmatrix} \quad (3)$$

where $q_1 = \cos(\phi/2)$ and $q_v = \hat{e}\sin(\phi/2)$. The kinematic equations in terms of the quaternion take the form

$$\dot{q} = \frac{1}{2}E(q)\omega, \ q(0) = q_0 \quad (4)$$

where the matrix-valued function $E(q) : \Re^4 \to \Re^{4\times3}$ denotes the kinematics Jacobian matrix given by

$$E(q) \triangleq \begin{bmatrix} -q_v^T \\ q_1 I_3 + S(q_v) \end{bmatrix} \quad (5)$$

where I_3 implies the 3×3 identity matrix.

3. MAIN RESULTS

In this section, the robust, optimal attitude control law is developed for the complete attitude motion of a rigid spacecraft with inertia uncertainties and external disturbances by adopting the optimal game-theoretic approach.

The optimal game-theoretic approach for *linear* systems is introduced by Dorato *et al* [15]. However, the complete attitude motion of the rigid spacecraft considered in this paper has a *nonlinear* nature and, thus, one may not directly apply the optimal game-theoretic approach of [15] to the optimal control problem for the systems in (1) and (4).

In the following, we present the nonlinear optimal control problem for the systems in (1) and (4) and provide the analytic solution to this problem by investigating a Lyapunov function candidate.

Theorem 1: Consider the systems in (1) and (4) and let

$$x = \begin{bmatrix} \omega^T & q_v^T \end{bmatrix}^T. \quad (6)$$

Then, the control law

$$u = -k_{q_v}q_v - K_\omega\omega \quad (7)$$

with a positive scalar k_{q_v} and positive definite matrix K_ω, and the disturbance signal

$$\xi = W^{-1}G^T\omega \quad (8)$$

with a positive definite matrix W, are optimal with respect to the cost function

$$V = \frac{1}{2}\int_0^\infty (x^TQx + 2u^TNx + u^TRu - \xi^TW\xi) \ dt \quad (9)$$

where

$$\begin{aligned} Q &= \begin{bmatrix} K_\omega - GW^{-1}G^T & 0_3 \\ 0_3 & k_{q_v}^2 K_\omega^{-1} \end{bmatrix}, \\ N &= \begin{bmatrix} 0_3 & k_{q_v} K_\omega^{-1} \end{bmatrix}, \\ R &= K_\omega^{-1}, \end{aligned} \quad (10)$$

0_3 denotes the 3×3 zero matrix, and K_ω satisfies

$$K_\omega > GW^{-1}G^T. \quad (11)$$

Proof: The proof consists of showing that Eqs. (7) and (8) are solutions to the following nonlinear game-theoretic HJ equation

$$\begin{aligned} -\tfrac{\partial V}{\partial t} = \ & \min_u \max_\xi \Big\{ \tfrac{1}{2}x^TQx + u^TNx + \tfrac{1}{2}u^TRu \\ & -\tfrac{1}{2}\xi^TW\xi + \tfrac{\partial V}{\partial \omega}[J^{-1}S(\omega)J\omega + J^{-1}u \\ & + J^{-1}G\xi] + \tfrac{\partial V}{\partial q}\left[\tfrac{1}{2}E(q)\omega\right] \Big\} \end{aligned} \quad (12)$$

with the Lyapunov function candidate

$$V = \frac{1}{2}\omega^T J\omega + k_{q_v}[(q_1 - 1)^2 + q_v^T q_v]. \quad (13)$$

Now, let the condition given in (11) holds. Taking the time derivative of V in (13) along the trajectories of the closed-loop system with (7) and (8) yields

$$\begin{aligned} \dot{V} = \ & \omega^T J\dot{\omega} + k_{q_v}[2(q_1 - 1)\dot{q}_1 + 2q_v^T\dot{q}_v] \\ = \ & \omega^T[S(\omega)J\omega - k_{q_v}q_v - K_\omega\omega + GW^{-1}G^T\omega] \\ & + 2k_{q_v}(q_1 - 1)\left(-\tfrac{1}{2}q_v^T\omega\right) \\ & + 2k_{q_v}q_v^T\left[\tfrac{1}{2}q_1\omega + \tfrac{1}{2}S(q_v)\omega\right] \\ = \ & -\omega^T(K_\omega - GW^{-1}G^T)\omega \le 0. \end{aligned} \quad (14)$$

Then, global asymptotic stability follows from the LaSalle Invariance Principle [17] and the radially unboundedness of V in (13). This completes the proof. ∎

Remark 1: Theorem 1 shows that global asymptotic stability of the closed-loop system is guaranteed even in the presence of the inertia uncertainties. Thus, the optimal control law u (7) also has robustness with respect to the inertia uncertainties of the rigid spacecraft.

Remark 2: Setting $G = 0_3$ in (1) and $W = 0_3$ in (9) and applying Theorem 1 give the optimal *nonlinear* quadratic regulator problem of the rigid spacecraft in the absence of the external disturbances. Hence, the proposed approach can be regarded as the generalization of the optimal attitude control problem of the rigid spacecraft.
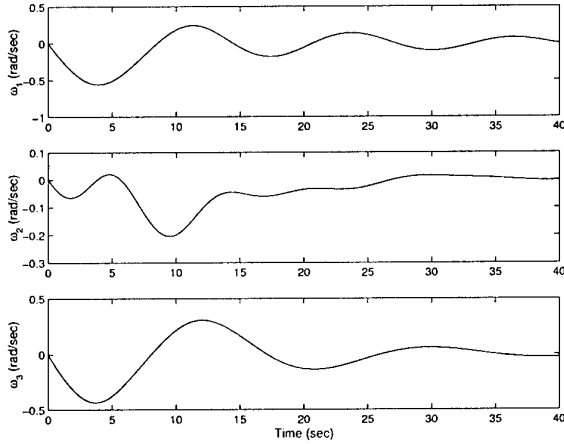
Fig. 1. Time histories of angular velocities.)

Fig. 2. Time histories of quaternions.

4. A NUMERICAL EXAMPLE

A. Numerical Simulation

In this section, we present a numerical example to illustrate the theoretical results in Section 3.

In simulation, a rigid spacecraft with inertia matrix $J = \mathrm{diag}\,[10, 15, 20]\,(kg \cdot m^2)$ is considered. We consider a rest-to-rest maneuver, thus $\omega_0 = 0$. The initial orientation conditions corresponding to the Euler axis and Euler angle pair are given by $\hat{e} = [\ 0.4896\quad 0.2032\quad 0.8480\ ]^T$ and $\phi = 2.4648\,(rad)$.

We set $G = I_3$ in (1) and $W = \mathrm{diag}\,[1, 2, 3]$ in (9). The values for the controller gains were chosen as $k_{q_v} = 5$ and $K_\omega = \mathrm{diag}\,[2, 3, 4]$ to meet the condition (11).

B. Results

The simulation results for the systems in (1) and (4) with the control law (7) and the external disturbance signal (8) are shown in Figures 1-4. As shown in Figures 1-4, the control inputs (7) try to stabilize the closed-loop system with overcoming the external disturbances (8), and the closed-loop system is eventually stabilized, since K_ω satisfies the condition (11).

5. CONCLUSIONS

The robust, optimal, three-axis attitude stabilization problem of a rigid spacecraft with inertia uncertainties and external disturbances is addressed by using the game-theoretic approach. In this approach, the control law and the external disturbance signal are regarded as two players that compete each other with opposite objectives for finding the minimax solution of the optimal game problem. The attitude motion of a rigid spacecraft described in terms of the quaternion is considered, and the robust, optimal control law of a rigid spacecraft is derived from the nonlinear game-theoretic Hamilton-Jacobi equation by investigating a Lyapunov function candidate. Global asymptotic stability of the proposed control law is shown by using the Lasalle Invariance Principle. A numerical example is then considered to illustrate the theoretical results, and the simulation results show the validity of the proposed method.
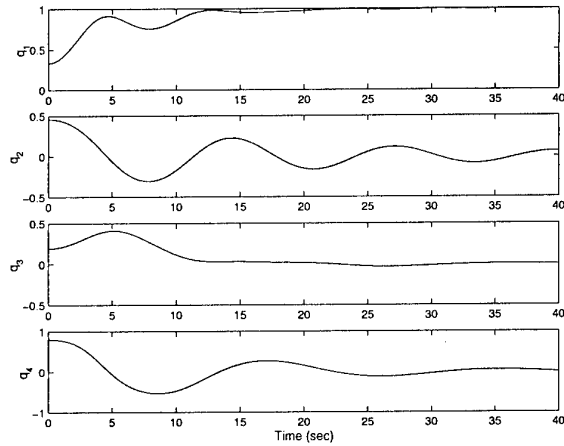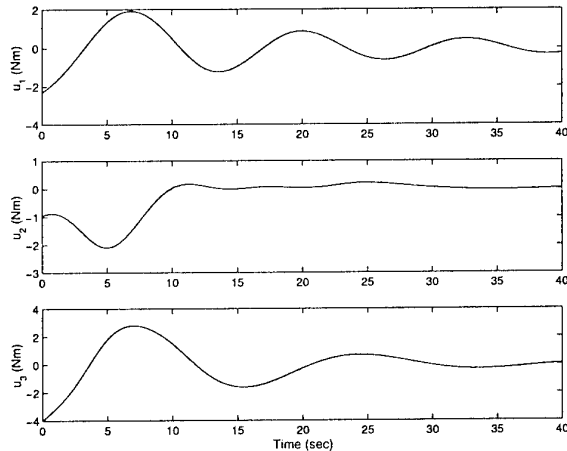

Fig. 3. Time histories of control inputs.
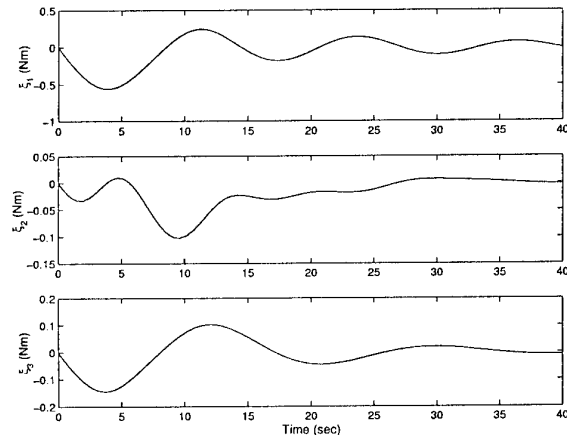

Fig. 4. Time histories of external disturbances.

REFERENCES

[1] Debs, A. S. and Athans, M., "On the optimal angular velocity control of asymmetrical space vehicles," *IEEE Trans. Automat. Contr.*, vol. 14, no. 1, pp. 80–83, 1969.

[2] Dabbous, T. E. and Ahmed, N. U., "Nonlinear optimal feedback regulation of satellite angular momenta," *IEEE Trans. Aerosp. Electr. Syst.*, vol. 18, no. 1, pp. 2–10, 1982.

[3] Vadali, S. R., Kraige, L. G. and Junkins, J. L., "New results on the optimal spacecraft attitude maneuver problem," *J. Guidance, Contr., Dynam.*, vol. 7, no. 3, pp. 378–380, 1984.

[4] Kumar, K. S. P., "On the optimum stabilization of a satellite," *IEEE Trans. Aerosp. Electr. Syst.*, vol. 1, no. 2, pp. 82–83, 1965.

[5] Tsiotras, P., Corless, M. and Rotea, M., "Optimal control of rigid body angular velocity with quadratic cost," in *Proc. 35th IEEE Conf. Decision Contr.*, Kobe, Japan, Dec. 1996, pp. 1630–1635.

[6] Carrington, C. K. and Junkins, J. L., "Optimal nonlinear feedback control for spacecraft attitude maneuvers," *J. Guidance, Contr., Dynam.*, vol. 9, no. 1, pp. 99–107, 1986.

[7] Tsiotras, P., "Stabilization and optimality results for the attitude control problem," *J. Guidance, Contr., Dynam.*, vol. 19, no. 4, pp. 772–779, 1996.

[8] Bharadwaj, S., Osipchuk, M., Mease, K. D. and Park, F. C. "Geometry and inverse optimality in global attitude stabilization," *J. Guidance, Contr., Dynam.*, vol. 21, no. 6, pp. 930–939, 1998.

[9] Krstić, M. and Tsiotras, P., "Inverse optimal stabilization of a rigid spacecraft," *IEEE Trans. Automat. Contr.*, vol. 44, no. 5, pp. 1042–1049, 1999.

[10] Park, Y., Tahk, M. J. and Park, J., "Optimal stabilization of Takagi-Sugeno fuzzy systems with application to spacecraft control," to appear in *J. Guidance, Contr., Dynam.*, vol. 24, no. 4, July-Aug. 2001.

[11] Wie, B., Weiss, H. and Arapostathis, A., "Quaternion feedback regulator for spacecraft eigenaxis rotations," *J. Guidance, Contr., Dynam.*, vol. 12, no. 3, pp. 375–380, 1989.

[12] Joshi, S. M., Kelkar, A. G. and Wen, J. T.-Y., "Robust attitude stabilization of spacecraft using nonlinear quaternion feedback," *IEEE Trans. Automat. Contr.*, vol. 40, no. 10, pp. 1800–1803, 1995.

[13] Karray, F. and Modi, V., "On the pointing robustness issue of a class of new generation spacecraft," *IEEE Trans. Automat. Contr.*, vol. 40, no. 12, pp. 2132–2137, 1995.

[14] Park, Y. and Tahk, M. J., "Robust attitude stabilization of spacecraft using minimal kinematic parameters," in *Proc. 2001 IEEE Int. Conf. Robotics Automation*, Seoul, Korea, May 2001, pp. 1621–1626.

[15] Dorato, P., Abdallah, C. and Cerone, V., *Linear-Quadratic Control: An Introduction*. Englewood Cliffs, NJ: Prentice-Hall, 1995.

[16] Tahk, M. J. and Sun, B. C., "Coevolutionary augmented Lagrangian methods for constrained optimization," *IEEE Trans. Evol. Comput.*, vol. 4, no. 2, pp. 114–124, 2000.

[17] Khalil, H. K., *Nonlinear Systems*, 2nd ed. Englewood Cliffs, NJ: Prentice-Hall, 1996.

[18] Junkins, J. L. and Turner, J. D., *Optimal Spacecraft Rotational Maneuvers*. New York: Elsevier, 1986.

1F4 # Aircraft Control System Design Using Evolutionary Algorithm For Noisy Function

Chang-Su Park*, Hyo-Choong Bang** and Min-Jea Tahk***

Division of Aerospace Engineering
Korea Advanced Institute of Science and Technology(KAIST)
373-1 Kusong-dong, Yusung-gu, Taejon, 305-701, Korea

Key Words: Stability and Control, Guidance and Control

ABSTRACT

Developing a robust controller for an aircraft with uncertain dynamics is an on-going research topic for much of the aerospace control community. Evolutionary computation method has provided the control designer with a more simple approach to these design problems. This paper proposes an evolutionary algorithm for noisy functions with good convergence properties. Thresholding method is also used for improved convergence. The proposed method is applied to aircraft acceleration control problem.

1. INTRODUCTION

To design a controller for an aircraft, various aerodynamic coefficients are required for exact analysis. Since these coefficients are usually obtained from wind tunnel tests or CFD the given coefficients have some uncertainties. Also disturbance is always present in a flying aircraft. So a robust controller must be design to compensate these effects. Designing the controller with the assist of evolutionary algorithm(EA) provides a convenient approach. Applying the evolutionary algorithm consist of selecting a cost function and evolving the parameters to minimize or maximize the cost.

Simple EA optimizes the cost function but does not guarantee any robustness to the solution. Coevolutionary algorithm(CEA) models the controller and the plant into two evolving groups with different objectives[1][2]. Each group evolves by obtaining the best of the worst possibilities, min-max or max-min solutions. CEA solution is a saddle point solution obtained by competing with the opponent. It assumes the plant is intelligent to oppose the controller. In real world, the plant does not show any intelligent behavior. It just shows random behavior. Worst-case evolutionary algorithm(WEA) considers the plant group to be a random population group[3].

In this paper we propose an evolution strategies(ES) based algorithm for noisy function optimization. In the proposed algorithm the cost is accumulated for long lasting parents. This has the effect of evaluating the same position multiple times without much computation effort. The proposed method optimizes to find the mean noise result. It shows good convergence properties. Thresholding method is also used in selection.[4]

* Graduate Student, Division of Aerospace Engineering
**Assistant Professor , Division of Aerospace Engineering
***Professor , Division of Aerospace Engineering
'01 第39回飛行機シンポジウム ©日本航空宇宙学会

In the next section, $(\mu + \mu)$-ES for noisy function is introduced. The effects of the proposed algorithm is verified by simple functions. This method is applied to aircraft control problem.

2. $(\mu + \mu)$-EVOLUTION STRATEGIES FOR NOISY FUNCTION

Generally, evolutionary algorithms are used on optimizing static functions. To use it on more realistic problems, optimization on noisy functions should be addressed. In this section an evolutionary algorithm for optimizing noisy functions is proposed. It is mainly based on $(\mu+\mu)$-ES. $(\mu+\mu)$-ES has the same number of parents(μ) and offsprings(μ) while evolving and the parents for the next generation is selected from the parent and offspring group together. $(\mu+\mu)$-ES has better convergence properties than $(\mu, \mu$ or $\lambda)$-ES which selects the next generation parent from the offspring only[5]. The notation used in the following algorithm is based on [4]

Algorithm

Step 1: Create initial parent population , $y_i^{(g)}, (i = 1, 2, ..., k)$

Step 2: Evaluate noisy cost function, $Q(y_i^{(g)})$, for the parent population. Parent cost functions are calculated as

$$Q'(y_i^{(g)}) = \frac{Q'(y_i^{(g-1)}) * n + Q(y_i^{(g)})}{n+1} . \qquad (1)$$

Step 3: Generate same number of offspring from the parent by mutation. Mutation is applied as $y_i^{(g)} + z_i^{(g)}$, where $z_i^{(g)} \sim \sigma N(0,1)$.

Step 4: Evaluate noisy cost function, $Q(y_i^{(g)} + z_i^{(g)})$, for the offspring population.

Step 5: Selection of the next generation parent from the parent and the offspring population.

Step 6: Check termination conditions. Goto **Step 2**.

In step 2 of the above algorithm, $Q'(y_i^{(g)})$ is the accumulated cost function for the gth generation. n is the number of generation the parent was continuously selected. This kind of parent cost evaluation is useful for noisy function. The effect will be shown in the next section. Different from general ES, the above algorithm uses only random gaussian noise to mutate the parent population. The strength of the gaussian noise is controlled adaptively for better convergence. In the selection process, thresholding is implemented. The offspring

that have better cost than the worst cost parent individual is exchanged with the parent. Threshold level is controlled by lowering the worst cost (in minimization case). The higher the threshold, the less likely the offspring will become the new parent.

3. OPTIMIZATION OF SIMPLE FUNCTIONS

The proposed algorithm is used to optimize simple 2-dimension sphere function, f_1, and Rosenbrock function, f_2, each with random noise.

$$f_1 = x^2 + y^2 + rand * 0.01 \qquad (2)$$
$$f_2 = 100 * (y - x^2)^2 + (1 - x)^2 + rand * 0.01 \qquad (3)$$

where $-6 \le x \le 6, -6 \le y \le 6$.

The results of the optimization are shown from Figure 2 to Figure 9. Each figure is the result of 10 simulation in one plot. Conventional ES finds exact solutions for functions without noise, $(x, y) = (0, 0)$ for f_1 and $(x, y) = (1, 1)$ for f_2. We assume noisy environment by adding uniform random numbers from 0 to 0.01. Thus the mean minimum value will be 0.005 for both f_1 and f_2. Figure 2 shows that after 50 generations the cost is constantly changing in the while in Figure 6 the solution is almost almost stabilized. Table 1 compares the actual costs and parameter values. The proposed ES method gives more accurate cost for the solution and has smaller standard deviation. The propose method is easier for the designer to choose a solution. Same kind of property is observed for the Rosenbrock function case also.

Table 1. Optimization Results for Sphere Function (Conventional vs. Proposed ES)

	Mean	Std.Dev.	Mean	Std.Dev
Cost	0.0021	0.0012	0.0053	0.0003
X	0.0005	0.0190	-0.0040	0.0114
Y	0.0003	0.0204	-0.0031	0.0125

Table 2. Optimization Results for Rosenbrock Function (Conventional vs. Proposed ES)

	Mean	Std.Dev.	Mean	Std.Dev
Cost	0.0018	0.0010	0.0055	0.0007
X	0.9948	0.0162	0.9912	0.0210
Y	0.9962	0.0371	0.9828	0.0413

4. APPLICATION TO AIRCRAFT CONTROL DESIGN

The proposed ES optimization method is applied to aircraft(F-15) acceleration control design problem. The basic data were obtained from the appendix of [6]. The first flight condition was used in this paper. The acceleration control transfer functions are given in [1][3].

The cost function is the integral of power of error between a reference model and the response of the linear system for step input.

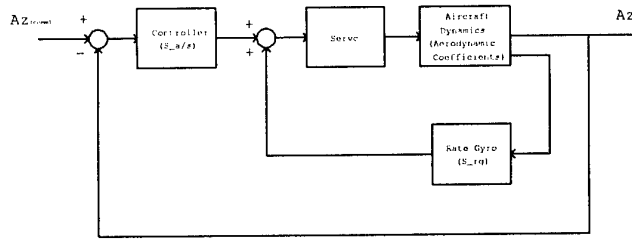$$J = \int_{t_i}^{t_f} (a_z - a_{z_{ref}})^2 dt \qquad (4)$$

Fig. 1. Block Diagram

$t_i = 0 \ sec, t_f = 5 \ sec, dt = 0.1 \ sec$ are used. The reference model is a typical second-order linear system with the following transfer function.

$$\frac{a_{z_{ref}}(s)}{a_{z_{com}}(s)} = \frac{\omega_n^2}{s^2 + 2\zeta\omega_n s + \omega_n^2} \qquad (5)$$

$\zeta = 0.9$ and $\omega_n = 2 \ rad/sec$ for our case.

Aerodynamic coefficient C_{z_α} and C_{m_α} are both perturbed 10% of the nominal value. Gains S_{rg} and S_a are evolved to minimize the cost. Figure 10 and 11 show the evolution history of ES finding the exact solution for the problem. Figure 12 and 13 are the oscillating solution to the noisy aerodynamic coefficient problem by conventional ES. Figure 14 and 15 are the result for the proposed ES method which shows stable convergence.

5. CONCLUSIONS

$(\mu + \mu)$-ES for noisy function has been proposed. The proposed method is verified by optimization of sphere function and Rosenbrock function. It is also applied to aircraft control design problem.

REFERENCES

[1] Park, C.S. and Tahk, M.J., "A numerical solver based on evolutionary computation for minimax problems," *Proceedings of JSASS 11th International Sessions in 35th Aircraft Symposium*, Tokyo, Japan,pp 535-538, Oct. 1997.

[2] Park, C.S. and Tahk, M.J., "A coevolutionary minimax solver and its application to autopilot design," *AIAA Conference on Guidance, Navigation, and Control*, Boston, Mass., USA, pp408-415, Aug., 1998.

[3] Park, C.S., Hur, J. and Tahk, M.J.,"Aircraft Control System Design Using Evolutionary Algorithm", *KSASS*, vol. 27, no.4, pp 104-114, 1999.

[4] Markon, S., Arnold, D., Bäck T., Beielstein, T., and Beyer, H.G, "Thresholding - a Selection Operator for Noisy ES", *Proceedings of the 2001 IEEE Congress on Evolutionary Computation*, pp 465-472, May,2001.

[5] Bäck, T., *Evolutionary Algorithms in Theory and Practice* ,Oxford University Press,1996

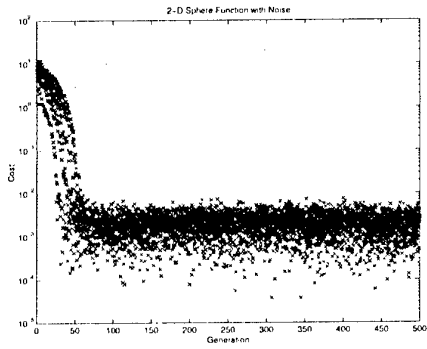[6] Blakelock, J., *Automatic Control of Aircraft and Missiles 2nd Edition* , John Wiley & Sons,Inc.,1991
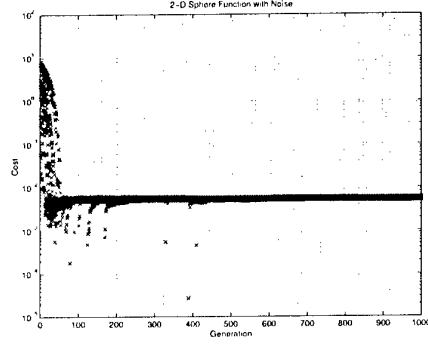
Fig. 2. 2-D Sphere function with noise (Conventional ES)

Fig. 3. 2-D Sphere function with noise (Conventional ES)
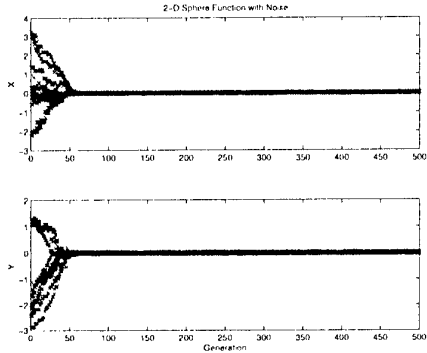

Fig. 4. Rosenbrock function with noise (Conventional ES)

Fig. 5. Rosenbrock function with noise (Conventional ES)

Fig. 6. 2-D Sphere function with noise (Proposed ES)

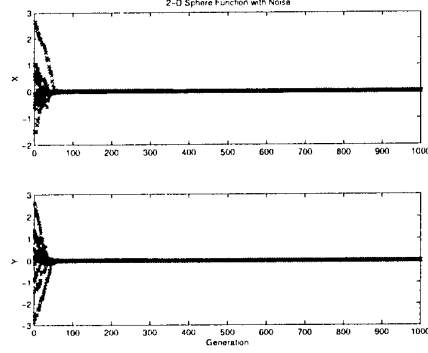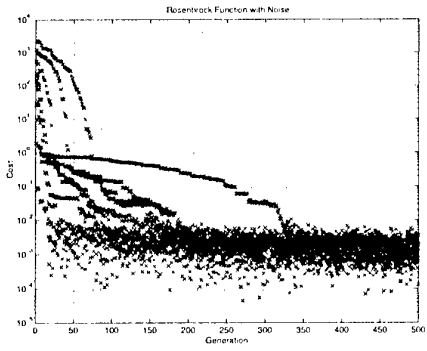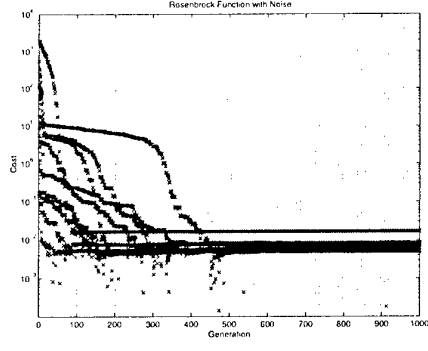Fig. 7. 2-D Sphere function with noise (Proposed ES)

Fig. 8. Rosenbrock function with noise (Proposed ES)
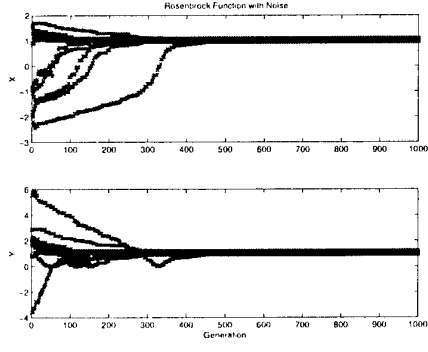
Fig. 9. Rosenbrock function with noise (Proposed ES)
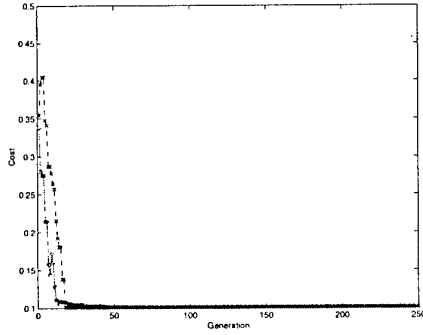
Fig. 10. ES Solution for F-15 Acceleration Control Design (Cost)

Fig. 11. ES Solution for F-15 Acceleration Control Design (Parameters)

Fig. 12. Conventional ES Solution for F-15 Acceleration Control Design (Cost)

Fig. 13. Conventional ES Solution for F-15 Acceleration Control Design (Cost)

Fig. 14. Proposed ES Solution for F-15 Acceleration Control Design (Cost)

Fig. 15. Proposed ES Solution for F-15 Acceleration Control Design (Parameter)

Robust Control Design for Nonlinear Flight Control System with Parameter Uncertainties

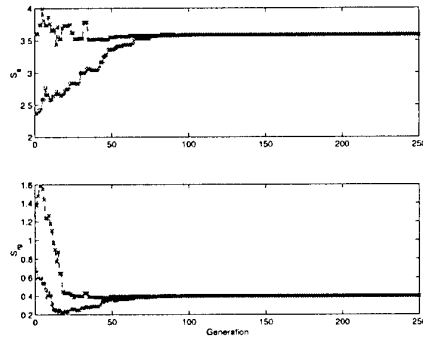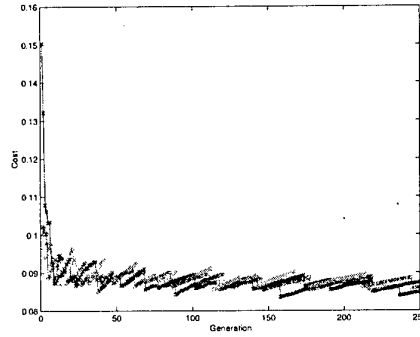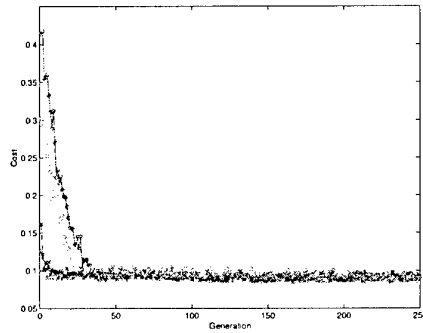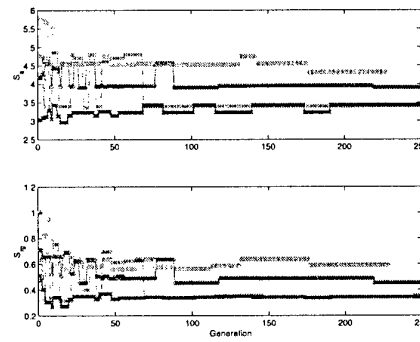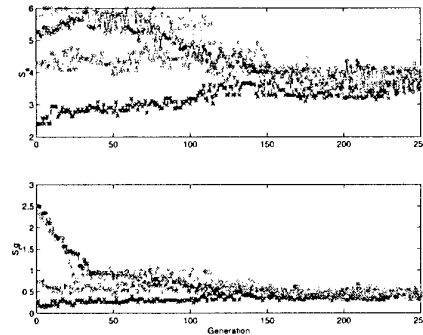*Ari Legowo*, Hiroshi Okubo**, Eiichi Muramatsu***, Hiroshi Tokutake*****

Department of Aerospace Engineering, Osaka Prefecture University, 1-1 Gakuen-cho, Sakai, Osaka 599-8531

ABSTRACT

This paper presents a method of robust control system design for aircraft flight control systems with the existence of uncertainty parameters resulted by parameter identification process of stability and control derivatives from real flight test data. A nonlinear model of aircraft turn coordination system is considered where the problem is to find optimal controller using H_∞ optimal control method. A quasi-Newton optimization method is used for achieving 'nonlinear' gain of the cross pass channel for the aileron and rudder interconnect which causes nonlinearity of the system. Determining controller qualifies as H_∞ optimal control under given value of 'nonlinear' gain, and simultaneously determines the optimal 'nonlinear' gain subject to minimize error performance of turn coordination system using quasi-Newton method. The perturbations of uncertainties model have structured uncertainties constructed by difference between aerodynamic coefficients derived by parameter identification process and wind tunnel result. The proposed method is applied to real flight test data of N250 PA-1 aircraft.

1. INTRODUCTION

The purpose of turn coordination system of an aircraft is to design control laws that determine controller such that the augmented system will allow roll command to perform steady bank angle while keep lateral acceleration and yawing moment are small. For a modern aircraft, the effect of yaw angle due to aileron deflection is adverse and cannot be neglected. It can be analyzed in control derivative $C_{n_{\delta_A}}$, the rate of change of yawing moment coefficient with aileron deflection, is more than 10% of the rate of change of rolling moment coefficient with aileron deflection $C_{l_{\delta_A}}$. In designing of an automatic control system, a cross pass channel from aileron command to rudder is necessary for minimizing effort on feedback input of rudder to counter the effect of adverse yaw. This channel is called as aileron rudder interconnect (ARI), which purposes to provide the component of yaw rate necessary to achieve a stability-axis roll.

The robust system model of turn coordination includes linear model of aircraft lateral/directional modes, actuators model, parameter uncertainties in aerodynamics, and

controller is linear time invariant. However the existence of cross pass channel ARI causes closed loop of turn coordination system is nonlinear. Then to design the optimal ARI gain and other controllers, more complex method is necessary.

In order to determine optimal gain of augmented robust system, application of H_∞ optimal control method is most familiar in recent. Where this method addresses stability and sensitivity, produces a stable closed loop and also need a simply direct one-step procedure. This paper proposes an iterative algorithm to determine controller using H_∞ optimal control method while to optimize value of ARI gain using quasi-Newton optimization subject to minimize sensitivity matrix of closed loop system.

An overview of application is presented to design robust flight control for turn coordination system particularly when there exists an uncertainty in the stability and control derivatives.

2. NOMINAL MODEL for NONLINEAR FLIGHT CONTROL

Consider the nominal model of aircraft turn coordination system as shown in block diagram in Fig. 1. The model of aircraft lateral/directional dynamics is linearized by using small perturbation technique, and for getting a linear model suitable for control law design, the fourth-order model is given as follows:

$$\dot{x} = Ax + Bu$$
$$y = Cx \qquad (1)$$

where $x = [\beta\ p\ r\ \phi]^T$, $u = [\delta_A\ \delta_R]^T$, $y = [\phi\ \beta\ p\ r\ a_y]^T$ are states, input and output/observation respectively.

Output feedback control is applied in the closed loop system, where it takes measurement of roll rate as an element feedback for aileron command and takes lateral acceleration combined with different between yaw rate and roll rate as elements feedback for rudder command. To minimize the contribution of element feedback for rudder on countering adverse yaw effect, feed forward of cross pass channel ARI gain (K_{ARI}) is engaged.

The actuator models for the aileron and rudder are assumed as first order transfer functions with time constant of 0.1 second. A low pass filter or washout filter model is put on the feedback channel of yaw and roll rate for rudder

*) Graduate Student
**) Professor
***) Lecturer
****) Research Associate

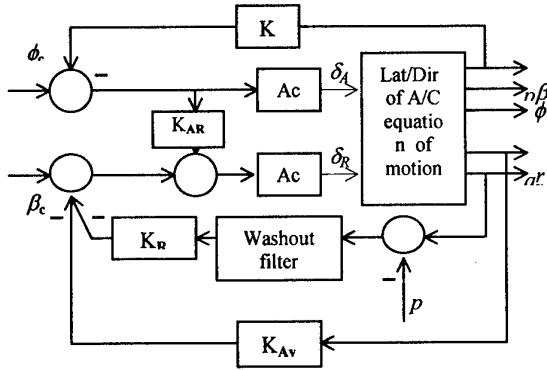input, and it has a first order model with time constant of 0.25 second.

Figure 1. Block diagram of turn coordination system.

3. ROBUST MODEL

Since the value of ARI gain is not known, or it will be determined, the nominal turn coordination system illustrated by Fig. 1 is nonlinear. Because the input element of rudder is also contaminated by the aileron input, input matrix B is not a constant matrix anymore.

In order to utilize the method of H_∞ optimal control, it is assumed that the value of ARI gain is known. Then, the input matrix B becomes

$$B^* = B \begin{bmatrix} 1 & K_{ARI} \\ 0 & 1 \end{bmatrix} \qquad (2)$$

The block diagram of augmented robust system of turn coordination with uncertainty is shown in Fig. 2 where the model of augmented system is given by

$$\dot{x} = Ax + B_1 w + B_2 u$$
$$z = C_1 x + D_{11} w + D_{12} u \qquad (3)$$
$$y = C_2 x + D_{21} w + D_{22} u$$

where z and w are output error and plant's disturbance respectively, and input matrix $B_2 = B^*$. In this model it is assumed that the perturbations are included only in the plant and caused by uncertainty in the coefficient of aerodynamics.
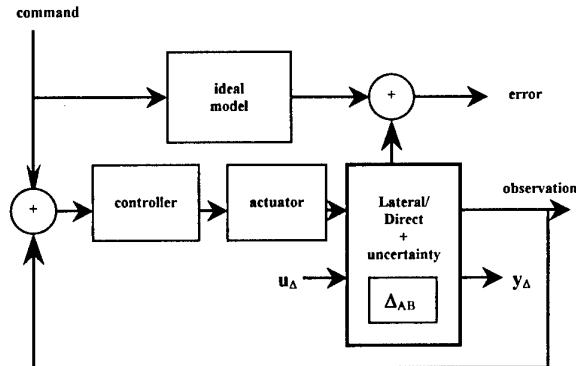
command

Figure 2. Block diagram of augmented robust system.

The robustness to parameter uncertainties is accomplished by modeling the uncertainties in the aerodynamic coefficients as perturbations of the nominal model. Where the uncertainties model is defined as the nominal turn coordination system (Eq. 1) plus uncertainty in the coefficients of aerodynamics and controls contained in matrices A and B. The uncertainty is a structured uncertainty, Δ_{AB}, and it is defined by

$$\Delta_{AB} = B_1 \Delta \Delta_{yu} \qquad (4)$$

where $\Delta_{AB} = [\Delta_A \ \Delta_B]$ is uncertainty in the aerodynamics coefficients corresponding to the elements of matrices A and B respectively, and matrix Δ contents distinguish between aerodynamics coefficients that resulted by wind tunnel with parameter identification process, and has term as follows

$$\Delta = \text{diag} \ [\ \Delta \{ C_{y_\beta} C_{y_p} C_{y_r} C_{y_{\delta_A}} C_{y_{\delta_R}} C_{l_\beta} C_{l_p} C_{l_r} C_{l_{\delta_A}} C_{l_{\delta_R}}$$

$$C_{n_\beta} C_{n_p} C_{n_r} C_{n_{\delta_A}} C_{n_{\delta_R}} \ \}] \qquad (5)$$

and matrix Δ_{yu} is an output model of uncertainties.

Plant perturbation w is defined as combination of roll and yaw rate command with δ_Δ, a perturbation of Δ_{AB} that satisfies $\|\delta_\Delta\|_\infty \leq 1$.

Thus

$$w = [\ \delta_{A_{com}} \ \delta_{R_{com}} \ \delta_\Delta]^T . \qquad (6)$$

The output error to be kept small in the face of perturbation is error between ideal model of aircraft performance and output resulted by system. In this system, bank angle response on steady state of turn due to aileron deflection and sideslip angle are taken as an ideal model

$$\phi = \frac{-C_{l_{\delta_A}} K_1}{C_L K_2} \delta_A$$

$$\phi = \frac{K_1}{C_L K_3} \beta \qquad (7)$$

where

$$K_1 = (C_{y_\beta} C_{l_r} + 4\mu C_{l_\beta})k - (C_{n_r} C_{y_\beta} + 4\mu C_{n_\beta})$$
$$K_2 = C_{l_\beta} C_{n_r} - C_{n_\beta} C_{l_r}$$
$$K_3 = C_{n_r} - kC_{l_r}$$
$$k = \frac{C_{n_\beta}}{C_{l_\beta}}$$

And also ideal model of the estimated adverse yawing moment due to the rolling wing is given by

$$C_n = -\frac{C_L}{8} \frac{pb_w}{2V}, \quad b_w : \text{wing span} \qquad (8)$$

The output to be feedback are

$$y = [p \ r - p \ a_y]^T \qquad (9)$$

and gain to be achieved corresponding to this output control has a structure as follows:

$$K = \begin{bmatrix} K_p & 0 & 0 \\ 0 & K_r & K_{a_y} \end{bmatrix} \qquad (10)$$

4. OPTIMIZATION METHOD

The method of H_∞ optimal control is used for designing robust control, when the control law is assumed to be an output feedback having a constant gain matrix K :

$$u = Ky \qquad (11)$$

Thus, the augmented closed-loop system of Eq. 3 corresponding to output feedback with the control law in Eq. 11 is

$$\dot{x} = A_c x + B_c w \qquad (12)$$
$$z = C_c x + D_c w$$

$$A_c = A + B_2 K C_2$$
$$B_c = B_1 + B_2 K D_{21}$$
$$C_c = C_1 + D_{12} K C_2$$
$$D_c = D_{11} + D_{12} K D_{21}$$

where the closed-loop system in Eq. 12 is assumed that $D_{22} = 0$. Then, this optimization is subjected to minimize singular values of transfer function of closed loop $\|G_{zw}\|_\infty$.

For computing H_∞ norm of the closed loop system in Eq. 12, consider the following fact that [1]

$\|G_{zw}\|_\infty < \gamma$ if only if the right spectral factorization of Hamiltonian matrix

$$\begin{bmatrix} A_c + B_c R^{-1} D_c^T C_c & -B_c R^{-1} B_c^T \\ C_c^T (I + D_c R^{-1} D_c^T) C_c & -(A_c + B_c R^{-1} D_c^T C_c)^T \end{bmatrix} \qquad (13)$$

has no imaginary eigenvalues, where

$$R = \gamma^2 I - D_c D_c^T > 0 . \qquad (14)$$

As a consequence of implementation facts above, if the perturbations matrix in Eq. 6 is under scaled to be less than one, then K is representation of an optimal controller of augmented closed loop system.

In order to determine optimum gain K, quasi-Newton method is taking at its advantage and can be formulated as a recursive algorithm [2]:

$$\hat{K}(i+1) = \hat{K}(i) - H_f(i).G_f(i) \qquad (15)$$

where

$$\hat{K} = [K_p \ K_r \ K_{a_y} K_{ARI}]^T \qquad (16)$$

The cost function to be minimized is given by

$$f(\hat{K}) = \|G_{zw}\|_\infty \qquad (17)$$

where $G_f(i)$ and $H_f(i)$ are first differential and second differential of cost function f with respect to $\hat{K}$ corresponding to iteration number i, respectively. The existence of optimal solution of matrix $\hat{K}$ is depending on given initial values, also continuity of G_f, and invertibility of H_f.

5. EXAMPLE DESIGN

A design was simulated for a turboprop N250 PA-1 aircraft, which is being producted by Indonesia Aircraft Industries. And model of turn coordination in Eq. 3 is taking for 150 Knots on airspeed trim 10000 Feet altitude on cruise flight condition The parameter uncertainties are contained in the difference between elements of matrix A and B, that resulted from wind tunnel test and from aerodynamics parameter identification test (Ari, L. and Okubo, H., et al [4]).

A numerical algorithm has been developed in MATLAB code, which utilizes some routines of the robust control toolbox. The initial value of aileron rudder interconnect gain can be determined by using data of rudder-aileron deflections ratio on trim condition and utilizing aerodynamics and derivatives data from wind tunnel test result, and it depends on aircraft trim speed or angle of attack [3]. For N250 PA-1 aircraft, the initial value of ARI gain have been modeled as linear form as follows [5]

$$K_{ARI} = 0.0212\alpha - 0.3858$$
or $\qquad (18)$
$$K_{ARI} = -0.0021V_E + 0.1260$$

where α is angle of attack in Degrees and V_E is equivalent airspeed in Knots. Then initial values of gain matrix as in Eq. 10 also utilized the stability and control trim data collected by flight test data engineering report [5].

By solving the recursive equation in Eq. 15, optimum gain $\hat{K}$ has been achieved as follows:

$$\hat{K} = [-1.7526 \ -0.0459 \ -0.0476 \ -0.1774]^T$$

It can be shown that, the result of optimal K_{ARI} above is closed enough with predicted value of K_{ARI} corresponding with trim speed of 150 Knots as given by Eq. 18. The cost function history by iteration number is shown in Fig. 3. The plots of singular values, with given disturbance on aileron command, are shown in Fig. 4. The robustness is indicated good for yaw rate response to the parameter uncertainties entire the frequencies range. On the other hand, the robustness for roll reponse is good for the high frequency, but is not good enough for the low frequency. It indicates that some disturbances of parameter uncertainties reject the robustness characteristic. Or the other possibility is that single contribution of element feedback for roll command to handle turn coordination problem is not sufficient, and it

needs some information for elements feedback, i.e. yaw rate or sideslip angle. This reason is supported by the fact that on the full state feedback model for turn coordination resulted the robust system on the entire frequency range for both responses.

6. CONCLUSION

The control laws have been designed for aircraft flight control in turn coordination system including parameter uncertainties on aerodynamics using H_∞ optimal control method and taking advantage of quasi-Newton optimization for optimizing ARI gain. The results show that proposed method is satisfactory regarding robustness of performance and control. This proposed method has a potential for application to the other robust control problems.

References:

1. Doyle, J.C., Glover, K., Khargonekar, P., and Francis, B.,"*State Space Solutions to Standard H_2 and H_∞ Control Problems*", IEEE Transactions on Automatic Control, Vol. 34, No. 8, pp. 831-847, 1989.
2. Polak, E., "*Optimization : Algorithms and Consistent Approximations*", Springer – Verlag, New York, 1997.
3. Stevens, B.L and Lewis, F.L.,"*Aircraft Control and Simulation*", John Wiley & Sons, New York, 1992.
4. Ari, L., Okubo, H., Muramatsu, E., and Tokutake, H.,"*One-Step Parameter Identification Using Moving Horizon States Estimation Method*", Preceedings of 15th IFAC Symposium on Automatic Control in Aerospace, Bologna-Italy, 2001.
5. Indonesia Aircraft Industries, Division of Flight Test Center, Flight Test Data Engineering Group," *N250 PA-1 Flight Testing Data on Aerodynamics Parameter Identification*", 1996.
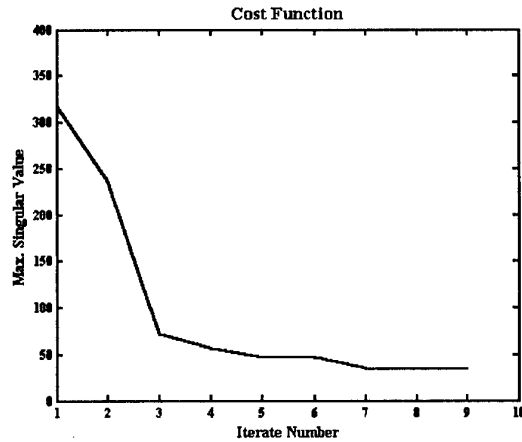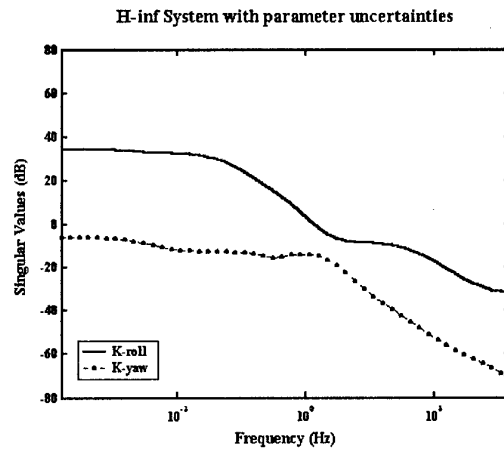
Cost Function

Fig.3. Iterate number history of $\left\|G_{zw}\right\|_\infty$.

H-inf System with parameter uncertainties

Fig.4. Singular values of transfer function $\left\|G_{zw}\right\|_\infty$.

1F6   **THE ASPECT OF SUBJECTIVITY IN FLIGHT MECHANICS**

Prof. M. R. Ananthasayanam
Department of Aerospace Engineering, Indian Institute of Science, Bangalore, INDIA, 560 012
Key Words: Aircraft, Aerodynamics, Flight Mechanics, Subjectivity

ABSTRACT

There are many perspectives of viewing any subject and each provide a different kind of insight and Flight Mechanics is no exception. Earlier Flight Mechanics was viewed by the author from the point of probability, statistics, and random processes as well as optimality. The present paper discusses it from the point of view of subjectivity. It turns out that subjectivity exists in almost every topic of Flight Mechanics. This view provides another systematization for students learning this subject.

1.TOPICS IN FLIGHT MECHANICS

Flight Mechanics is and can be treated objectively but the occurrence of subjectivity is not easily apparent and also not generally discussed in text books or by the instructors. One reason for this could be due to lack of time. In fact the subjective view is best appreciated after studying some topics in Flight Mechanics and then look for the above feature in them. The author having taught the above subject for many years feels that it provides a refreshing way to understand and appreciate the subject. Table 1 lists the topics that are generally dealt with regarding airplanes in the Flight Mechanics course in the Department of Aerospace Engineering at the Indian Institute of Science, Bangalore. It also provides the coverage in the topics and the examples of subjectivity in them which are discussed below.

2.AVIATION HISTORY

In aviation history during appropriate periods the growth rate of various quantities such as speed, passenger capacity, cruise altitude, weight, wing loading, and many more are generally obtained from the data by fitting a straight line by the least squares technique. However the eventual growth rates are specified subjectively in terms of nearly round numbers. There are two reasons for the above. The first one is that with some changes in the data the final numbers would change thus indicating the result to be not unique. Secondly even the least squares is a subjective criterion cast in an objective mathematical form. One could have used other possible criteria like minimising the absolute sum of the departures from the fitted line.

3.ATMOSPHERE

The different atmospheric characteristics like temperature, pressure, density, wind, and humidity vary randomly over various scales of space and time. For aerospace applications the description consists of describing their statistics based on the available meteorological data over suitable range of altitude, latitude, and longitude. In almost every atmosphere such as the International Standard Atmosphere (ISA) or the proposed International Tropical Reference Atmosphere (ITRA) or other reference atmospheres the temperature distribution is specified in terms of constant lapse rate segments between specified

altitudes. Subjectively the temperature as well as the lapse rate is chosen to be close to a round and the altitude ranges to be round numbers as shown in Figure 1 for ISA. It is not desirable to keep changing such values often based on subsequent data and it should be done only at longer intervals with more compelling data. However some values are frozen due historical reasons.

4.FLIGHT REGIMES

The aerospace vehicles operating at various altitude and speed ranges experience different forces due to the varying physical nature of flow over them. The various flight regimes are characterised as free molecular, transition, slip, and continuum flows in terms of the Knudsen number K (which is the ratio of the mean free path λ of the gas in the free stream to the characteristic size L of the body) varying from ∞ to 0. This Knudsen number is of the order of the ratio of Mach number M to the Reynolds number R. The various forces and moments change continuously from free molecular to the continuum flow and one could have had any number of divisions. It has been subjectively found sufficient to have the above four divisions of the flight regimes. Too few would not have smoothly described the changing features and too large would have been cumbersome. Also even the numerical value of the partitioning in terms of functions of M and R is flexible in terms of round numbers. The various divisions of M and R from low to high as it exists is a similar subjective characterisation.

5.FLIGHT LIMITATIONS

There are many well known aerodynamic, structural, propulsive, operational, and other limitations to the flight of an aerospace vehicle constraining it to fly within some regions of the altitude-speed plane. Some of these are such as the stall speed, maximum level flight speed, maximum g loads, peak pressure at the compressor face, noise, or the sonic boom. There is nothing in flight mechanics that can provide such limits. Given the various inputs to the equations of motion and additional ones it can work out the trajectory or the desired performance quantity. These various limits will have to be chosen subjectively by a designer from other extra-flight mechanical considerations.

6.AERODYNAMICS OF BODIES, DRAG AND THRUST

There exists a large number of theoretical approaches or statistical regression relations based on earlier data available for an aerodynamicist to estimate the forces and moments acting on a component or the complex shape of a complete vehicle. These could be from theoretical analysis, or from wind tunnel or flight tests all of which are generally not exact due to varying approximations and limitations of the experimental set up. From among these a designer has to subjectively choose suitable ones for his use. The many proprietary data, relations, or computer codes among the various designers are indicative of the prevailing subjectivity in the evaluation of the aerodynamic characteristics!

Any designer would like to have optimally shaped components for his vehicle design. However many performance, manufacturing, maintenance, operational considerations can compel him to choose shapes that is not optimal. Further even the shapes used in their earlier designs would be subjectively more comfortable for them than others.

The drag and thrust form very crucial inputs for any aerospace vehicle and in particular for an airplane. Right from the conceptual/preliminary, wind tunnel testing/computational, to the flight testing/fleet service of an airplane a continuous improvement in the estimation accuracy of the above inputs takes place due to more definitive geometry, experimental or theoretical methods employed and the flight conditions. The above are based on less and less subjective estimates from increasing amount of data corresponding to the various stages of an airplane design from conceptual to fleet service. Even modelling the structure of the drag polar or the variation of thrust with altitude/density, and speed/Mach number are plenty in the literature so also their eventual wide range of accuracy reflecting the subjectivity introduced and existing in the studies by the analyst. With theory being difficult, in particular the extrapolation from wind tunnel to flight condition as shown in Figure 2 is subjective due to some components of drag being more accurate and some less accurate.

7.AIRPLANE PERFORMANCE

An airplane's performance calculations can be carried out or understood with increasing level of accuracy. These are for (i) obtaining an insight into the airplane performance characteristics (ii) airplane design sizing to meet a given set of specifications (iii) airplane design sizing to meet airworthiness criteria (iv) operational analysis of a given airplane and (iv) accident analysis. The first one is the main purpose in a classroom. Here in specifying the main aerodynamic and propulsive inputs it is a balance between simplicity for mathematical tractability to get closed form solutions as against the complex and physically more realistic situation. It is the simplicity that is sought which leads to many subjective case studies be it in climb, turn, range, endurance, takeoff, or landing performance studies. After a detailed study for optimum climb for a fighter is carried out, for practical use combinations of constant dynamic pressure and constant Mach number schedules are generally specified. The various programs for range and endurance calculations also reflect subjectivity for the advantage of mathematical tractability. In the takeoff and landing studies, in particular the circular arc, constant lift coefficient flare or constant pitch rate during airborne phase are once again subjective approximations for ease of analysis.

8.SAFETY, AIRWORTHINESS, AND DESIGN

The different measures of activity and safety of different forms of transport are all subjective. For airplanes these are for example the fatalities or the fatal accidents in terms of passenger kilometers, or the number of flights or hours flown. Later based on a mathematical study these help to provide insight into where the effort must be put in to improve the achieved safety levels.

The acceptable safety level of air transport by the public is a subjective probabilistic quantity chosen based on a balance between safety and economy. This is reflected in the implied range of acceptable incident rate between 2×10^{-6} and 7×10^{-6} per hour or flight in the ICAO airworthiness codes. In fact society at large in general subjectively (consciously or unconsciously) accepts varying safety levels for different activities. Even the acceptable safety levels are quite different for civil and military airplanes.

There are many components in an airplane and their implications for their aerodynamic, structural, propulsive and other features is very difficult to accurately quantify or carry out a detailed mathematical analysis. Under such circumstances the designer has to necessarily provide his subjective inputs to the design of an airplane and this could affect its success in fleet service!

9.REMARKS ON THE SUBJECTIVITY

The above discussion should not provide the reader with an impression that almost everything in Flight Mechanics is subjective and has no objective treatment. What is implied is that some small or large amount of subjectivity almost always exists which is unavoidable and useful as well. Such an existence of subjectivity should inspire confidence in one to try the consequences of intuitive approaches to handle various problems. It is generally the intuitive beginning that leads to the formulation of logical mathematical framework whose implications are to be compared with observations to provide eventually a good physical theory.

10.CONCLUSIONS

One can sum up to state that so long as there is some change that could occur in a quantity a certain amount of subjectivity is used to specify it stably and easily. The various flight regimes are subjectively partitioned in a few and simple way. The large number of approaches from theory or experiments for estimating the aerodynamic properties reflect the subjectivity that exists due to the prevailing uncertainties which are more than what one would desire. The mathematical tractability necessary to obtain insight into airplane performance in classroom studies leads to subjectivity in mathematically modelling the various inputs. The different measures of flying activity and safety, as well as the acceptable level of safety implied in airworthiness codes are subjective. The airplane design also has many unavoidable subjectivity due to many specialties, components, and their implications for the final product that are difficult to estimate or forecast during the early phases of design. To summarise whenever there are approximations, specifications, partitioning, limitations, many possible approaches and modelling, analysis, different measures and uncertain implications which encompass a large number of common features in any study of this nature exists can lead to small or large amount of subjectivity in any subject for that matter. Thus the subjectivity provides a refreshing insight and enables one a better appreciation of Flight Mechanics.

REFERENCES

1. Diehl W.S., "Notes on the Standard Atmosphere". NACA TN 99, (1922).
2. Gregg W.R., "Standard Atmosphere". NACA Report 147, (1922).
3. ICAO Final Report of the Standing Committee on Performance. ICAO Document 740-AIR/OPS/613. (1953).
4. Narasimha R., ``Flight Safety and National Economy", Report 77 FM 1 Department of Aerospace Engineering, Indian Institute of Science, Bangalore, India (1977).
5. Wolowicz C.H., Bowman J.S. and Gilbert W.P., "Similitude Requirements and Scaling Relationships as Applied to Model Testing", NASA TP-1435, August (1979).
6. Covert E. E., (Editor) "Thrust and Drag: Its Prediction and Verification". Volume 98, Progress in Astronautics and Aeronautics, November (1985).
7. Anderson, Jr J. D., "Introduction to Flight". McGraw-Hill International Editions, (1989).

8. Roskam J., Airplane Design Part I, ``Preliminary Sizing of Airplanes", and Part II, ``Preliminary Configuration Design and Integration of the Propulsion System", Roskam Aviation and Engineering Corporation, Kansas (1989).
9. Ananthasayanam M.R., "Teaching of Flight Performance at the Indian Institute of Science, Bangalore". Proc. of AIAA Flight Mechanics Conference. AIAA-98-4524 (1998).
10. Ananthasayanam M.R., "A Dozen ways of Looking at Aerospace Vehicle Design". Proc. of AIAA Flight Mechanics Conference. AIAA-99-4263 (1999).
11. Ananthasayanam M.R., "Flight Mechanics from the Viewpoint of Probability, Statistics, and Random Process", Proceedings of the Third APCATS, October 4-8, 2000, Kunming China, (2000).
12. Ananthasayanam M.R., "Flight Mechanics from a Viewpoint of Optimal Parameters, Variables, and Approaches", Proc. of AIAA Flight Mechanics Conference at Montreal, AIAA-2001-4315 (2001).
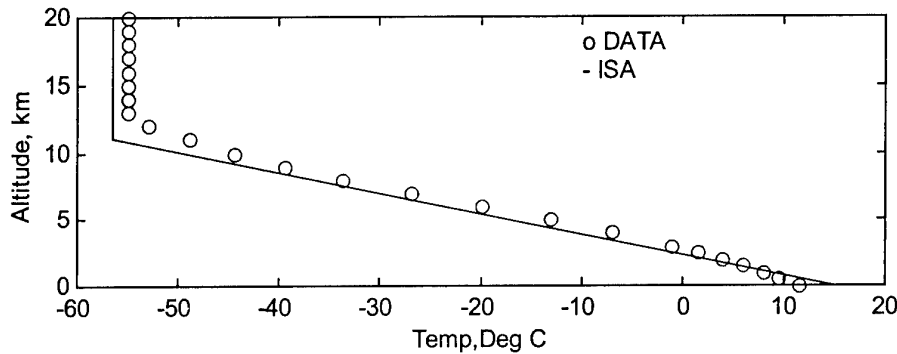
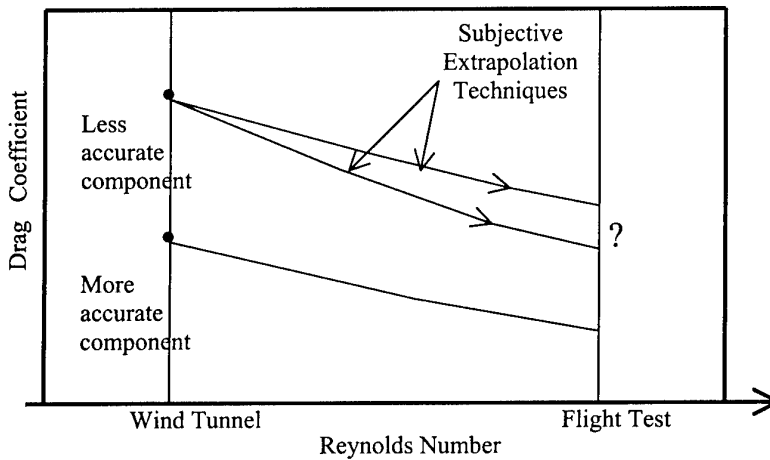Figure 1. Comparison of ISA with Meteorological DATA (Gregg 1922).

Figure 2. Extrapolation of Drag from Wind Tunnel to Flight Condition.

TABLE 1. TOPICS IN FLIGHT MECHANICS AND THE ASPECT OF SUBJECTIVITY.

No.	TOPIC	CONSIDERS	EXAMPLES RELATED TO SUBJECTIVITY
1	Aviation History	Evolution of airplane and its characteristics.	The growth of various quantities as given by least squares fit is rounded off.
2	Atmosphere	Characterization of various atmospheres and their properties over useful scales of space and time.	The standard and reference atmospheres usually consists of straight line variation of temperature. The lapse rate and the altitude at which the lapse rate changes as well as the temperatures are close to round numbers.
3	Flight / Flow Regimes	Interaction of flow with body flying at various altitudes and speed. Specification of forces, moments and heat transfer.	The flight regimes are four in numbers. Their limits in terms of K = M/R is specified in a simple way.
4	Flight Limitations	Limitations in the altitude-velocity plane due to aerodynamic forces, heating, structure, engine, materials and noise considerations.	The limitations of flight in the altitude-speed plane are obtained from extra-flight mechanical namely aerodynamic, structural, propulsive, operational or other considerations.
5	Aerodynamics of Bodies	Forces and moments experienced by bodies at various M and R.	The existence of a large amount of information is an indication of the prevailing subjectivity in the theoretical and experimental approaches to estimate the inputs for flight mechanical performance calculations.
6	Airplane Drag	Estimation of the drag of a vehicle in terms of various components at different R and M.	
7	Thrust or Power and specific fuel consumption	Specification of the thrust or power and specific fuel consumption of power plants with altitude and speed.	
8	Introduction to Airplane Performance	Performance for the purpose of teaching, design, airworthiness, operational and accident analysis. The above need increasing detail but provide higher accuracy.	In a classroom study to obtain an insight into airplane performance the many climb and cruise programs are subjective approaches. Among the different phases of takeoff and landing, in particular the airborne phases lead to many subjective approximations.
9	Climb and Turn	Climb and turn characteristics, their optimums for jets and piston props.	
10	Range and Endurance	Range and endurance calculations for a variety of programs and their optimum for jets and piston props. Effect of Wind.	
11	Takeoff and Landing	Takeoff and landing field length calculations.	
12	Flying activity, Safety and Economy	Measures of flying activity, safety and economy and their correlations.	The different measures of flying activity and safety, as well as the acceptable level of safety implied in airworthiness codes are subjective.
13	Airworthiness Codes	Acceptable level of safety. Specification of appropriate climb gradients and field lengths in various flight stages.	The airplane design also has some unavoidable subjectivity due a large number of specializations, physical components, and other aspects whose implications for the fleet performance of the final product are difficult to estimate or forecast during the early phases of design.
14	Preliminary Airplane Design	Sizing of an airplane for a given specification and meeting airworthiness standards.	

Adaptive Reconfigurable Flight Control System Based on Recursive System Identification

Sungpil Kim[*], Youdan Kim[†], Hee-Seob Kim[‡] and Changho Nam[¶]

* Department of Aerospace Engineering, Seoul National University, Seoul 151-742, Korea
† Department of Aerospace Engineering, Seoul National University, Seoul 151-742, Korea
‡ Korea Aerospace Research Institute, Daejon 305-606, Korea
¶ Department of Manufacturing and Aeronautical Engineering Technology, Arizona State University, MESA, AZ 85212, USA

Key Words: System Identification, Fault Tolerant Control, Adaptive Control, Reconfiguration

Abstract

An adaptive reconfigurable control algorithm is proposed for aircraft fault tolerant control. An input-output model is derived from a discrete state-space model. The formulated model has the same structure as the ARX model, and therefore any recursive system identification method can be used. Model following control schemes are applied for reconfigurable control system design. The reference outputs for the system to be followed are generated via the linear optimal control theory. During the recursive adaptive control process, the reference system model is updated periodically. The proposed algorithm is very robust and applicable on real time. To validate the proposed adaptive fault tolerant control algorithm, numerical simulation is performed.

1. Introduction

A reconfigurable flight control system(RFCS) is a control system that can accommodate faults by redesigning the control system. A RFCS provides a significant enhancement to flight safety and performance in the event of system fault. Recently, reconfiguration control has been widely studied due to its clear benefits. Previously proposed approaches include model following technique,[1] eigenstructure assignment method,[2] variable structure control scheme,[3] and neural network based adaptive control.[4]

In this study, an input-output model is developed for identification of faulty system. This model has the same structure as ARX(Auto Regressive eXternal) model. Hence, any recursive system identification methods are applicable. We present a recursive identification method that is adequate to the input-output model. And an adaptive reconfigurable control method combined with model following schemes is proposed. An adaptive reconfiguration control with an estimator is also presented. The noise effects can be excluded from the output signals through the estimator. The numerical simulation is performed to validate the proposed control method.

2. Input-output Model and Identification

In this section, we first derive an input-output model from state-space model. This model will be used to describe the real system. Then, a recursive system identification method is developed using input-output signals. The recursive identification method is adequate to identify the proposed input-output model.

A. Input-output model

Consider the discrete-time model of a system in a state-space form

$$x(k+1) = Ax(k) + Bu(k) \qquad (1)$$
$$y(k) = Cx(k) \qquad (2)$$

where $x(k) \in R^n$, $u(k) \in R^m$, $y(k) \in R^p$, and A, B, C are system, input influence, and output influence matrices, respectively. The discrete system matrix A is a state transition matrix, and is always nonsingular. Therefore, the output variables can be described using the state variables and inputs as follows:

$$y(k-j) = CA^{-j}x(k) - \sum_{i=0}^{j-1} CA^{-j+i}Bu(k-i-1) \qquad (3)$$

where $j = 0, \cdots, q-1$. In the matrix form, the above equation can be expressed as

$$Y(k) = Hx(k) + PU(k) \qquad (4)$$

where

$$Y(k) = \begin{bmatrix} y(k) \\ y(k-1) \\ \vdots \\ y(k-q+1) \end{bmatrix}, \quad H = \begin{bmatrix} C \\ CA^{-1} \\ \vdots \\ CA^{-q+1} \end{bmatrix}, \quad U(k) = \begin{bmatrix} u(k-1) \\ u(k-2) \\ \vdots \\ u(k-q+1) \end{bmatrix},$$

$$P = \begin{bmatrix} 0 & 0 & 0 & 0 \\ -CA^{-1}B & 0 & 0 & 0 \\ \vdots & & \ddots & \vdots \\ -CA^{-q+1}B & -CA^{-q+2}B & & -CA^{-1}B \end{bmatrix}$$

Note from Eq. (4) that the state variable $x(k)$ can be obtained from the given input and output signals. If the size of matrix H is $n \times n$ and the rank of matrix A is n, then $x(k)$ can be uniquely determined by using $Y(k)$ and $U(k)$. Using Eq. (1) and Eq. (4), the following equation can be obtained.

$$Y(k+1) = H\,x(k+1) + P\,U(k+1)$$
$$= HAH^+[Y(k) - P\,U(k)] + HB\,u(k) + PU(k+1) \qquad (5)$$

where H^+ is the pseudo-inverse of matrix H. If the rank of matrix H^+ equals the system order n, then the solution $x(k)$ satisfying Eq. (4) is uniquely determined. However, too many parameters are required to represent the system using Eq. (5).

* Graduate Student
† Associate Professor
‡ Research Engineer
¶ Associate Professor

Therefore, simple manipulation is performed to reduce the number of parameters.

Using the definition of $U(k)$, the following input history equation can be constructed.

$$U(k+1) = I_m u(k) + J_m U(k) \quad (6)$$

where

$$I_m = \begin{bmatrix} I_{m \times m} & 0 & \cdots & 0 \end{bmatrix}^T, \quad J_m = \begin{bmatrix} 0 & 0 & 0 & 0 \\ I_{m \times m} & 0 & 0 & 0 \\ 0 & \ddots & 0 & 0 \\ 0 & 0 & I_{m \times m} & 0 \end{bmatrix}$$

and $I_{m \times m}$ is an $m \times m$ identity matrix.

Substituting Eq. (6) into Eq. (5) yields

$$Y(k+1) = HAH^+[Y(k) - PU(k)] + \begin{bmatrix} CB u(k) \\ 0 \\ \vdots \\ 0 \end{bmatrix} + P J_m U(k) \quad (7)$$

$$= HAH^+[Y(k) - PU(k)] + I_p CB u(k) + P J_m U(k)$$

where $I_p = \begin{bmatrix} I_{p \times p} & 0 & \cdots & 0 \end{bmatrix}^T$, and $I_{p \times p}$ is a $p \times p$ identity matrix. Note from Eq. (7) that the matrix HAH^+ plays the same role as a system matrix. Let us define M_Y and M_U as

$$M_Y H = HA, \quad M_U = PJ_m - M_Y P \quad (8)$$

Then, Eq. (7) can be rewritten as follows.

$$Y(k+1) = M_Y Y(k) + M_U U(k) + I_p CB u(k) \quad (9)$$

Note from Eq. (8) that matrix M_Y has the following structure.

$$M_Y = HAH^+ + UZ \quad (10)$$

where $ZH = 0$. The matrix U is a design parameter computed in consideration of the structure of matrix H. If the size of matrix H is $n \times n$, and the rank of matrix H is n, then the solution is uniquely determined. By selecting the matrix U appropriately, the matrix M_Y can be constructed in the following form.

$$M_Y = HAH^+ + UZ = J_p + I_p \alpha \quad (11)$$

where $\alpha = \begin{bmatrix} \alpha_1 & \cdots & \alpha_q \end{bmatrix}$, and $\alpha_i \in R^{p \times p}$. From Eq. (8) and Eq. (11), M_U is given by

$$M_U = PJ_m - (J_p + I_p \alpha)P$$
$$= (PJ_m - J_p P) - I_p \alpha P \quad (12)$$

In consideration of the structures of P, J_m, and I_p, we have

$$PJ_m - J_p P = 0 \quad (13)$$

Therefore, we have

$$M_U = -I_p \alpha P \quad (14)$$

Substituting Eqs. (8), (11), and (14) into Eq. (7), we have

$$Y(k+1) = (J_p + I_p \alpha)Y(k) - I_p \alpha P U(k) + I_p CB u(k) \quad (15)$$

In the consideration of the structure of matrix P, the output variable $y(k+1)$ can be obtained by pre-multiplying I_p^T to Eq. (15) as follows:

$$y(k+1) = \alpha Y(k) - \alpha P U(k) + CB u(k) \quad (16)$$

Equation (16) is used to identify the real system for the adaptive control system. It has the same structure as the ARX model. Therefore, any recursive numerical method for conventional system identification can be used.

B. Recursive Identification Algorithm

Equation (16) can be rewritten as

$$y(k+1) = \begin{bmatrix} \alpha & CB & -\alpha P \end{bmatrix} \begin{bmatrix} Y(k) \\ u(k) \\ W(k) \end{bmatrix} = \theta \, \phi(k) \quad (17)$$

where θ is a parameter matrix to be identified. In Eq. (17), the number of parameters to represent α is $p \times pq$, $p \times m$ for CB, and $p \times (q-1)m$ for αP. Therefore, the total number of parameters in Eq. (17) is $p \times (pq + qm)$. If pq is equal to the system order n, then the total number of parameters becomes the same as the number of parameters required for system identification.

To identify the parameters, s-sets of data can be used. The chosen data sets satisfy the following equation.

$$Y = \begin{bmatrix} y(k+1) & y(k+2) & \cdots & y(k+s) \end{bmatrix}$$
$$= \theta \begin{bmatrix} \phi(k) & \phi(k+1) & \cdots & \phi(k+s-1) \end{bmatrix} \quad (18)$$
$$= \theta \, \Phi$$

Equation (18) consists of $p \times s$ constraint equations, and the number of parameters is $p \times (p+m)q$. To obtain the better solution, s should be greater than $(p+m)q$. If not, there exists a uniqueness problem, and the identified model may not represent the real system appropriately.

Consider the system that has the time-varying parameters. In this case, there may exist an estimation error between the identified parameter matrix $\theta(k-1)$ in the $(k-1)$ step and the current parameter matrix $\theta(k)$; that is

$$Y - \theta(k-1)\Phi = \delta\theta \, \Phi \quad (19)$$

where $\delta\theta = \theta(k) - \theta(k-1)$. The least square solution of $\delta\theta$ can be obtained as follows.

$$\delta\theta = [Y - \theta(k-1)\Phi] \Phi^T [\Phi\Phi^T]^{-1} \quad (20)$$

By using Eq. (20), the current parameter matrix can be updated by using the following recursive equation.

$$\theta(k) = \theta(k-1) + \kappa \, \delta\theta$$
$$= \theta(k-1) + \kappa [Y - \theta(k-1)\Phi] \Phi^T [\Phi\Phi^T]^{-1} \quad (21)$$

where the positive scalar $\kappa < 1$ is the step-size for the parameter identification.

3. Adaptive Control System Design

A mathematical model for an adaptive control system is usually obtained by on-line system identification based on input-output signals. The on-line recursive identification method uses the limited input signals to excite the system in a finite time. For this reason, the identified model by the on-line recursive identification method is less accurate than that obtained by the off-line identification method. Therefore, in this paper, the model following control scheme is adopted to compensate the effects of the identification errors.

A. Adaptive Model Following Controller without Estimator

In this section, the key procedures to design the adaptive model following controller are described as follows.

Step 1. Determine the system model in the form of Eq. (16). The initial model can be identified using input-output signals or obtained by mathematical modeling methods. During the recursive adaptive control process, however, the system model is updated periodically via the on-line identification method addressed in Sec. 2.B.

Step 2. Generate reference outputs for the system to be followed. To design a stabilizing control law for the system model, Eq. (16), let us rewrite Eq. (6) and Eq. (15) in matrix form as follows.

$$\begin{bmatrix} Y(k+1) \\ U(k+1) \end{bmatrix} = \begin{bmatrix} J_p + I_p\alpha & -I_p\alpha P \\ 0 & J_m \end{bmatrix} \begin{bmatrix} Y(k) \\ U(k) \end{bmatrix} + \begin{bmatrix} I_p CB \\ I_m \end{bmatrix} u(k) \quad (22)$$

Note that the above equation has the same form as state-space model. Therefore, a control law stabilizing Eq. (22) can be easily designed as follows:

$$u^*(k) = -K_1 Y(k) - K_2 U(k) = -K \begin{bmatrix} Y(k) \\ U(k) \end{bmatrix} \quad (23)$$

The gain matrices of the above controller can be determined by applying LQR theory. It is obvious from Eq. (4) that the above control law also stabilizes $y(k+1)$. Therefore, substituting Eq. (23) into Eq. (16) yields the desired model responses as

$$y^*(k+1) = \alpha Y(k) - \alpha P U(k) + CB u^*(k) \quad (24)$$

Step 3. Design the model following controller. The objective of the model following control scheme is to make the system output follow the desired responses; that is

$$y^*(k+1) = y(k+1) \\ = \alpha Y(k) - \alpha P U(k) + CB u(k) \quad (25)$$

The control input can be determined using the pseudo-inverse as follows

$$u(k) = (CB)^+ (y^*(k+1) - \alpha Y(k) + \alpha P U(k)) \quad (26)$$

Note that the existence of $u(k)$ is dependent on the structure of matrix CB. When the number of outputs is greater than the number of inputs, the model following can be achieved in the least square sense, thereby the control input can be over-designed. On the other hand, when the number of outputs is less than the number of inputs, there exist several solutions for the input to make the system outputs follow the desired outputs. In this case, the control inputs can be designed such that the magnitude of control inputs may be minimized. Consider the following objective function.

$$J = [y^*(k+1) - y(k+1)]^T Q [y^*(k+1) - y(k+1)] \\ + u^T(k) R u(k) \quad (27)$$

where Q and R are positive definite weighting matrices. The first term is related to the model following performance, and the second term is related to the control energy minimization. By applying the optimality condition, the control input can be obtained as

$$u(k) = G[y^*(k+1) - \alpha Y(k) + \alpha P U(k)] \quad (28)$$

where $G = [R + B^T C^T QCB]^{-1} B^T C^T Q$.

Step 4. Go to 1 or 2. The model following control procedure is iterated at every time step. However, the system model is updated periodically at $n(>1)$ time steps instead of every time step to reduce the computation time.

B. Adaptive Model Following Controller with Estimator

In general, the output signals include some measurement noise. To accommodate the noise effects from the output signals, an estimator can be used. The estimator for the system shown in Eq. (15) can be constructed as follows:

$$\hat{Y}(k+1) = (J_p + I_p \alpha)\hat{Y}(k) - I_p \alpha PU(k) + I_p CB u(k) \\ + L (Y(k) - \hat{Y}(k)) \quad (29)$$

Let us introduce the estimation error, $E(k) = Y(k) - \hat{Y}(k)$. Then, the estimator error equation can be obtained by using Eq. (15) and Eq. (29) as

$$E(k+1) = (J_p + I_p\alpha - L)E(k) \quad (30)$$

Assume that the estimator gain L_0 stabilizes the system matrix $(J_p + I_p\alpha_0)$ where α_0 is an identified parameter matrix using the initial model, and L_0 is the estimator gain matrix designed by using the initial model. Then, the state estimator gain L at the current step can be designed as

$$L = I_p\alpha - I_p\alpha_0 + L_0 \quad (31)$$

The above equation provides an efficient algorithm for designing the estimator gain matrix.

Consider the following objective function.

$$J = [y^*(k+1) - \bar{y}(k+1)]^T Q [y^*(k+1) - \bar{y}(k+1)] \\ + u^T(k) R u(k) \quad (32)$$

where the estimated output $\bar{y}(k+1)$ is defined as follows:

$$\bar{y}(k+1) = \alpha \hat{Y}(k) - \alpha PU(k) + CB u(k) \quad (33)$$

Note from the above equation that the estimated output from Eq. (29) is used instead of using the identified model, Eq. (15). Substituting Eq. (33) into Eq. (32), and by applying the optimality condition to the resulting equation, the control input can be obtained as follows

$$u(k) = G[y^*(k+1) - \alpha\hat{Y}(k) + \alpha PU(k)] \quad (34)$$

where $G = [R + B^T C^T QCB]^{-1} B^T C^T Q$.

4. Numerical Examples

In this section, a numerical example is presented to verify the adaptive RFCS developed in the Sec. 3. For a damaged system model, a high performance aircraft with a critical damage on the wing surface is considered. Proper orthogonal decomposition (POD) technique is applied to reduce the size of the system matrix down to three. Reduced order system matrices can then be used to predict the initial parameter quickly and accurately in the adaptive reconfigurable control system. Figures 1 and 2 show the sensor signal of the open loop and closed loop system for the critical damage model. The control input histories of the closed loop system is shown in Figure 3. Figures show that after a short period of time for system identification, the developed reconfigurable controller suppresses the aeroelastic instability.

Conclusions

An adaptive reconfigurable control algorithm is proposed for aircraft fault tolerant control. An input-output model is developed to describe the real system. This model has the same structure as an ARX model that can be easily identified by recursive algorithms. To identify the system model, a recursive method is presented that is adequate to the proposed input-output model. For the control system, adaptive control schemes are proposed with the combination of model following control scheme. The reference outputs for the system to be followed were generated using the LQR theory. Also, an adaptive reconfiguration control with an estimator is presented. The proposed reconfigurable control is very robust and applicable on real time. To demonstrate the proposed adaptive fault tolerant control algorithm, numerical simulation is performed.

Acknowledgement

References

1. Morse, W. E. and Ossman, K. A., "Model Following Reconfigurable Flight Control System for the AFTI/F-16," Journal of Guidance, Control, and Dynamics, Vol. 13, No. 6, 1990, No. 969-976.

2. Jiang, J., "Design of Reconfigurable Control System Using Eigenstructure Assignment," International Journal of Control, Vol. 59, No. 2, 1994, pp. 395-410.

3. Calise, A. J., Lee, S., and Sharma, M., "Development of a Reconfigurable Flight Control Law for the X-36 Tailless Fighter Aircraft," Proceedings of the AIAA Guidance, Navigation, and Control Conference, Denver, CO, 2000.

4. Kim, D. and Kim, Y., "Robust Variable Structure Controller Design for Fault Tolerant Flight Control," Journal of Guidance, Control, and Dynamics, Vol. 23, No. 3, 2000, pp. 430-437.
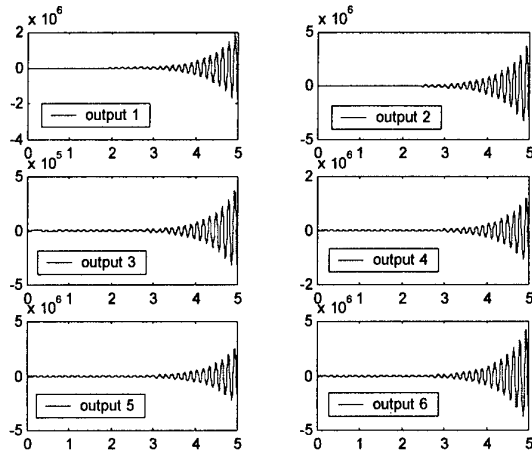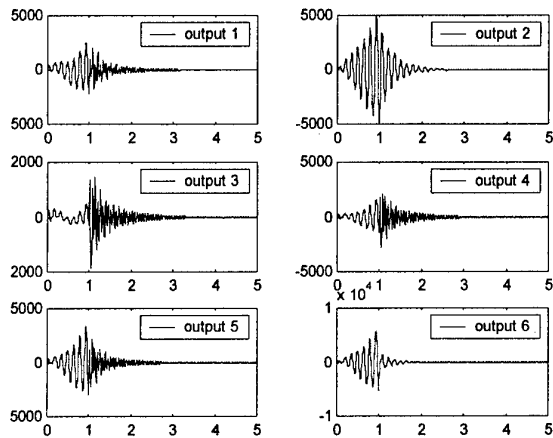
Figure 1. Open loop sensor signals of the damaged model

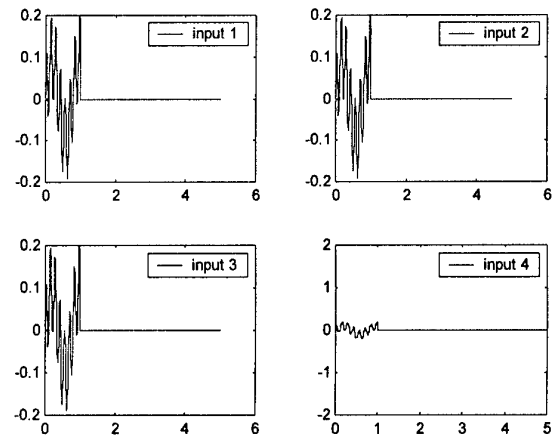Figure 2. Closed loop sensor signals of the damaged model

Figure 3. Control input histories

1F8   Robust Fault Tolerant Control systems Using Adaptive Schemes

Chungil Ahn * and Youdan Kim **

Department of Aerospace Engineering, Seoul National University, Seoul 151-742, Korea

Key Words: Aircraft, Guidance and Control, Fault Tolerant Control

ABSTRACT

In this paper, robust fault detection and isolation algorithm is proposed using the adaptive scheme. The proposed fault detection and isolation scheme is robust with respect to the unstructured uncertainties such as signal noise, parameter variation, and modeling errors. The time-varying uncertainty is considered, and it is assumed that the characteristics of the uncertainty are unknown. The fault tolerant control system is designed to make the failed system follow the model outputs updated by the adaptive rule to minimize the effects of the faults. The robust analysis of the proposed control system is performed via Lyapunov approach. To validate the proposed adaptive fault tolerant control algorithm, numerical simulation is performed using VTOL aircraft.

1. INTRODUCTION

Recently, fault tolerant control has received much attention in the aerospace fields.[1] Fault tolerant control procedure includes all or parts of the following processes: fault detection and isolation(FDI), on-line identification of failed system, and reconfiguration process for the failed system to enhance the reliability and survivability while guaranteeing the stability.[2] In the complicated systems such as aircraft systems, there exist lots of various fault sources as well as the internal/external uncertainties including parameter variations and external disturbances.[3] Therefore, robust algorithms for fault detection/isolation, and reconfigurable control system are required.

In this paper, a fault tolerant control system based on adaptive scheme possessing FDI capability as well as fault tolerance property is proposed. With the scheme, pre-determined model for reconfigurable control is not required. The proposed algorithm is shown to be very useful for the aircraft systems having unstructured uncertainties, which results in unexpected performances. Numerical result shows the applicability of the proposed algorithm in this paper.

2. FDI BASED ADAPTIVE SCHEMES

Consider a system described by

---

* Graduate Student
** Associate Professor

$$\dot{x} = Ax + \Delta Ax + Bu + \Delta Bu + f \tag{1}$$
$$y = Cx + w \tag{2}$$

where $x(t) \in R^n$ is a state vector, $u(t) \in R^m$ is a control input vector, $y(t) \in R^p$ is an output vector, and $f(t) \in R^r$ ($r \le m$) represents possible added-form actuator fault. The matrices A, B, and C are real matrices with appropriate dimensions, and variations ΔA and ΔB denote uncertainty and nonlinearity in the system and input parameters whose characteristics and distribution are unknown. The following assumptions are used in the design and analysis processes.

Assumption 1
The pairs (A, B) and (A, C) are controllable and observable, respectively.

Assumption 2
The uncertainty, input, and disturbance are all bounded.

The following adaptive diagnostic observer is proposed for FDI.

$$\dot{\hat{x}} = A\hat{x} + Bu + \hat{f} + L(y - \hat{y}) \tag{3}$$
$$\hat{y} = C\hat{x} \tag{4}$$

where the initial value of $\hat{f}$ is set to zero for the healthy system (no fault), and L is the observer gain matrix such that $A - LC$ is a stable matrix.

Let us define the estimation errors as follows.

$$e_x = x - \hat{x} \tag{5}$$

$$e_y = y - \hat{y} \tag{6}$$

Then, the observation error equation can be obtained as follows.

$$\dot{e}_x = (A - LC)e_x + f - \hat{f} + \Delta Ax + \Delta Bu - Lw \tag{7}$$

$$e_x = (sI - A_c)^{-1}\tilde{f} + (sI - A_c)^{-1}\Delta(s)u - (sI - A_c)^{-1}Lw \tag{8}$$

$$e_y = Ce_x + w \tag{9}$$

where $\tilde{f} = f - \hat{f}$, $A_c = A - LC$. The modeling error can be expressed by the following input-output expression in Laplace domain. Let us define $\Delta(s) = (sI - \Delta A)^{-1}\Delta B$.

Consider the following fault free system.

$$\dot{x} = Ax + \Delta Ax + Bu + \Delta Bu + v \tag{10}$$
$$y = Cx + w \tag{11}$$

where v denotes the possible input disturbance and is assumed to be uniformly bounded. For the healthy system, a threshold value, the criterion to pick out the fault from system variation, should be determined. From the assumption, the

threshold value is defined as follows.

$$\left\| e_y \right\| \le \max_{w \ge 0} \left\| C(jwI - A_c)^{-1} \right\| \delta_1 + \max_{w \ge 0} \left\| I - C(jwI - A_c)^{-1} L \right\| \delta_0$$
$$+ \max_{w \ge 0} \left\| C(jwI - A_c)^{-1} \Delta(jw) \right\| \delta_2 = \lambda \quad (12)$$

To isolate the fault after detecting the fault, the error dynamics of adaptive diagnostic observer is further expressed as

$$e_y = W_1 \tilde{f}(t) + W_2 w(t) + W_3 u(t) \quad (13)$$

The above equation gives the relationship between the observation error e_y and the fault estimation errors $\tilde{f}$. In this study, fault detection and isolation scheme is proposed to use the available e_y, u, and y to construct a adaptive law for $\hat{f}$ such that $\lim_{t \to \infty} \hat{f} = f$. To use the parameter adjustment rule, the stability or SPR(Strictly Positive Real) property of the transfer functions should be guaranteed.

1) W_1: Transfer function W_1 applied to adaptive law should be SPR. According to Kalman Yakubovich Lemma, the transfer function $W_1(s) = C(sI - A_c)^{-1}l$ is SPR and stable if and only if there exists positive definite matrices P and Q such that $A_c{}^T P + P A_c = -Q$, $l^T P = C$. Therefore, the SPR property W_1 is guaranteed since P and Q exits.

2) W_2: Since the poles of transfer function W_2 is the same as those of W_1, the SPR property of W_2 is up to the property of W_1. Therefore, W_1 and W_2 is SPR.

3) W_3: Compared to W_1, transfer function W_3 consists of the combination of modeling errors, thereby can be formulated as $W_3 = W_1 \Delta$. By the properties of additive uncertainties, the closed-loop system is well-posed and stable for $\left\| \Delta \right\|_\infty < 1$, if and only if $\left\| W_1 \right\|_\infty \le 1$. By the small gain theorem and the assumptions, this is true for all $\Delta \in RH_\infty$ with $\left\| \Delta \right\|_\infty < 1$, if and only if $\left\| W_1 \right\|_\infty \le 1$. More detailed proof can be found in Ref. [4].

It can be shown, using the augmented error technique of Narendra and Annaswamy, that

$$\varepsilon_y = \theta^T \zeta + [W_1(s)\tilde{f}(t) - \tilde{f}(t)W_1(s)u(t)] + W_2 w(t) + W_3 u(t) + \delta(t)$$
$$\theta = \tilde{f}, \zeta = W_1(s)u(t)$$
$$(14)$$

where $\delta(t)$ decays exponentially and is negligible. Since the second term of Eq.(14) is measurable, the augmented error dynamics for the system can be defined as

$$\varepsilon(t) = \varepsilon_y - [W_1(s)\tilde{f}(t) - \tilde{f}(t)W_1(s)u(t)] \quad (15)$$

Thus, it can be shown that

$$\varepsilon(t) = \theta^T \zeta + \eta_0 \quad (16)$$

where $\eta_0 = W_2(s)w(t) + W_3(s)u(t)$. The deadzone value of η_0 is bounded as

$$\left\| \eta_0 \right\| \le \max_{w \ge 0} \left\| W_2(jw) \right\| \delta_1 + \max_{w \ge 0} \left\| W_3(jw) \right\| \delta_2 = \lambda_1 \quad (17)$$

After determining the value of λ_1, it can be used to construct dead zone for an adaptive law. The adaptive update law can therefore be applied to adjust θ as follows, to estimate the fault.

$$\dot{\theta} = \begin{cases} -\Gamma \dfrac{\varepsilon(t)\zeta(t)}{1 + \zeta^T(t)\zeta(t)} & \left\| \varepsilon(t) \right\| > \lambda_1 \\ 0 & \left\| \varepsilon(t) \right\| \le \lambda_1 \end{cases} \quad (18)$$

Now, let us analyze the robustness performance for FDI using the Lyapunov approach. Using Eqs.(15) and (17), we have

$$\dot{\theta} = -\Gamma \frac{\zeta \zeta^T}{1 + \zeta^T \zeta} \theta - \Gamma \frac{\zeta \eta_0}{1 + \zeta^T \zeta} \quad (19)$$

where the error term $\eta_0(t)$ can be expressed as

$$\dot{\phi} = A_\eta \phi \quad (20)$$
$$v_0 = C_\eta \phi \quad (21)$$

Consider a following Lyapunov function candidate

$$V = \frac{\theta^T \Gamma^{-1} \theta}{2} + \frac{\phi^T P_\eta \phi}{4} \quad (22)$$

where P_η is positive definite matrix that satisfies the following equation.

$$P_\eta A_\eta + A_\eta{}^T P_\eta = -Q_\eta - C_\eta{}^T C_\eta \quad (23)$$

The time derivative of V along the trajectories of Eqs.(19)~(22) can be expressed as

$$\dot{V} = \theta^T \Gamma^{-1} \dot{\theta} + \frac{\dot{\phi}^T P_\eta \phi}{4} + \frac{\phi^T P_\eta \dot{\phi}}{4}$$
$$= -\left[\frac{\zeta^T \theta + \eta_0/2}{\sqrt{1 + \zeta^T \zeta}} \right]^T \left[\frac{\zeta^T \theta + \eta_0/2}{\sqrt{1 + \zeta^T \zeta}} \right] - \frac{\eta_0{}^T \eta_0}{4(1 + \zeta^T \zeta)} - \frac{\phi^T Q_\eta \phi}{4} \le 0 \quad (24)$$

The condition $\dot{V} \le 0$ implies that $V, \phi, \eta_0, \theta, \zeta \in L_\infty$ and that

$$\lim_{t \to \infty} V(\theta(t), \phi(t)) = V_\infty < \infty.$$

Furthermore, from Eq.(24), we have

$$\int_0^\infty \left[\frac{\zeta^T \theta + \eta_0/2}{\sqrt{1 + \zeta^T \zeta}} \right]^T \left[\frac{\zeta^T \theta + \eta_0/2}{\sqrt{1 + \zeta^T \zeta}} \right] d\tau$$
$$+ \int_0^\infty \frac{\eta_0{}^T \eta_0}{4(1 + \zeta^T \zeta)} d\tau + \int_0^\infty \frac{\phi^T Q_\eta \phi}{4} d\tau \le V(\theta(0), \phi(0)) - V_\infty \quad (25)$$

Because $\lambda_{min}(Q_\eta) \left| \phi \right|^2 \le \phi^T Q_\eta \phi$ and $V(\theta(0), \phi(0))$ is finite for any finte initial condition, Eq.(25) implies that $\eta_0, \phi \in L_2$ and therefore $\varepsilon \in L_2$. From the adaptive law, Eq.(17), we have

$$\left| \dot{\theta} \right| \le \left\| \Gamma \right\| \left\| \varepsilon \right\| \left\| \zeta \right\| \quad (26)$$

Since $\varepsilon \in L_2, |\zeta| \in L_\infty$, we have $\dot{\theta} \in L_2 \cap L_\infty$. Now, Eq. (18) guarantees that $\theta = f - \hat{f} \to 0$ which implies that the estimated faults converge to the real faults. The results show that the robust fault detection and isolation with respect to uncertainties including disturbances and modeling errors is guaranteed. The proof of convergence of fault is summarized in Appendix.

3. RECONFIGURATION

In this section, fault reconfiguration control law is designed to accommodate the effects of fault. The system and adaptive observer considered in the previous section hold. The control law using the observer is given by

$$u(t) = K^T \hat{y} + r \qquad (27)$$

where K is the controller parameter and r is the reference input. This control law has the form of the observer-based controller. To design the control law, the error dynamics of adaptive diagnostic observer can be expressed as

$$e_y = C(sI - A_c)^{-1} \Delta(s)(K^T \hat{y} + r) + (sI - A_c)^{-1} \tilde{f} + [I - (sI - A_c)^{-1}L]w \qquad (28)$$

$$= W_1 K^T \hat{y} + W_2 \tilde{f}(t) + W_3 w(t) + W_1 r(t)$$

Consequently, Eq. (28) gives the relationship between the observation error e_y, the fault estimation errors $\tilde{f}$, and the input term $K^T \hat{y}$. It can be shown using the augmented error technique of Narendra and Annaswamy, that

$$\varepsilon_y = \theta^T \zeta + [W_1(s)\tilde{K}^T \hat{y}(t) - \tilde{K}^T W_1(s)\hat{y}(t)]$$

$$+ [W_2(s)\tilde{f}(t) - \tilde{f}(t)W_2(s)u(t)] + W_3 w(t) + W_1 r(t) + \delta(t) \qquad (29)$$

$$\theta = \tilde{f}, \zeta = W_1(s)u(t)$$

where $\delta(t)$ decays exponentially and is negligible. Since the second term of Eq. (29) is measurable, the augmented error dynamics for the system can be defined as

$$\varepsilon(t) = \varepsilon_y - [W_1(s)\tilde{K}^T \hat{y}(t) - \tilde{K}^T W_1(s)\hat{y}(t)] - [W_2(s)\tilde{f}(t) - \tilde{f}(t)W_2(s)u(t)] \qquad (30)$$

Thus, it can be shown that

$$\varepsilon(t) = \theta^T \zeta + \eta_0 \qquad (31)$$

where $\eta_0 = W_2(s)w(t) + W_1(s)r(t)$ and the deadzone value of η_0 is bounded as

$$\|\eta_0\| \leq \max_{w \geq 0}\|W_2(jw)\| \delta_1 + \max_{w \geq 0}\|W_1(jw)\| \delta_3 = \lambda_2 \qquad (32)$$

After determining the constant value of λ_2, it can be used to construct a dead zone for an adaptive law. The adaptive update law can therefore be applied to adjust θ as follows to estimate the fault and control law.

$$\dot{\theta} = \begin{cases} -\Gamma \dfrac{\varepsilon(t)\zeta(t)}{1 + \zeta^T(t)\zeta(t)} & \|\varepsilon(t)\| > \lambda_2 \\ 0 & \|\varepsilon(t)\| \leq \lambda_2 \end{cases} \qquad (33)$$

Theorem: The control law and adaptive law, Eqs.(27) and (33), guarantee that all signals in the closed-loop system are bounded and the observation error e_y converges to zero.

Proof) the proof of the theorem can be found in Ref [5].

The above theorem represents the design procedure of the estimated fault and controller to follow the fault and to degrade the effect of estimated fault.

4. NUMERICAL SIMULATION

In this section, the performance of fault detection, isolation, and reconfiguration for the system with the unstructured uncertainties and modeling errors is demonstrated via the numerical simulation of VTOL aircraft. The linearized dynamics of VTOL aircraft in the vertical plane is adopted from Narendra and Tripathi.[3] To verify the robustness of the proposed scheme, the airspeed is assumed to vary randomly around the operating point (135kt). As the airspeed changes, the dynamic characteristics of aircraft also change. It is assumed that only the selected significant parameters may change from their nominal values, and all other parameters remain constant. The bias fault of collective control occurs at 10 sec. with the magnitude of 0.8 and another negative bias fault of magnitude of 0.6 acts on the longitudinal pitch control after t=15 sec. The results of the fault detection, isolation, and reconfiguration are shown in Fig. 1~3. Figures show that the satisfied results for the fault detection, isolation, and reconfiguration processes are obtained.

5. CONCLUDING REMARKS

In this paper, fault tolerant control scheme possessing the FDI capability as well as the fault tolerance property is proposed. The algorithm is based on the adaptive scheme, and is designed to make the failed system follow the outputs of the model that is updated by the adaptive rule to minimize the effects of faults. The robustness of the proposed control system is analyzed via Lyapunov approach. Numerical simulation shows that the proposed algorithm is applicable to the fault tolerant flight control system.

Acknowledgement

REFERENCES

[1] R.J. Patton, "Fault Tolerant Control: the 1997 Situation (Survey)," Proceeding of IFAC SAFEPROCESS '97, University of Hull, August 1997, pp.1033~1055.

[2] D. Kim, and Y. Kim, "Robust Variable Structure Controller Design for Fault Tolerant Flight Control", Journal of Guidance, Control, and Dynamics, Vol.23, No.3, 2000, pp.430-437.

[3] L.-C. Shen, S.-K. Chang, and P.-L. Hsu, "Robust Fault Detection and Isolation with Unstructured Uncertainty with Eigenstructure Assignment," Journal of Guidance, Control, and Dynamics, Vol. 21, No. 1, 1998, pp. 50-57.

[4] K. Zhou, and J.C. Doyle, Essentials of Roubust Control, Prentice Hall, 1998.

[5] P.A. Ioannou, and J. Sun, Robust Adpative Control, Prentice Hall, 1996.

APPENDIX

(The proof of $\theta = f - \hat{f} \to 0$):

The error equation (36) can be written as

$$\dot{\theta} = A(t)\theta \qquad (A.1)$$

$$y_0 = C(t)\theta \qquad (A.2)$$

where $A(t) = -\Gamma \dfrac{\zeta\zeta^T}{1+\zeta^T\zeta}$, $C(t) = \dfrac{\zeta^T}{1+\zeta^T\zeta}$, $y_0 = \left[\dfrac{\varepsilon(t)-\eta_0}{1+\zeta^T\zeta}\right]^T$.

Consider the Lyapunov function.

$$V = \frac{\theta^T\Gamma^{-1}\theta}{2} + \frac{\phi^T P_\eta \phi}{4} \qquad (A.3)$$

Let $\Gamma^{-1} = P_\theta$, then the following equation can be obtained

$$\dot{V} = -\frac{\theta^T(P_\theta A_\theta + A^T P_\theta)\theta}{2} + \frac{\phi^T(P_\eta A_\eta + A_\eta^T P_\eta)\phi}{4} \qquad (A.4)$$

$$= -\theta^T CC^T \theta - \phi^T(Q_\eta + C_\eta^T C_\eta)\phi \le 0$$

The first part of above equation implies that

$$\dot{P} + P_\theta A + A^T P_\theta + 2CC^T \le 0 \qquad (A.5)$$

where $\dot{P} = 0$. According to Theorem A, $\theta = f - \hat{f} \to 0$ exponentially as $t \to \infty$.

Theorem A:

A necessary and sufficient condition for the asymptotically stability of the equilibrium of θ_e is that there exists a symmetric matrix $P(t)$ and $N(t, t+v)$ such that

$$\gamma_1 I \le P(t) \le \gamma_2 I, \quad \gamma_1, \gamma_2 > 0 \qquad (A.6)$$

$$\dot{P}(t) + P(t)A(t) + A^T(t)P(t) + vC(t)C^T(t) \le 0 \qquad (A.7)$$

$$\beta_1 I \le N(t_0, t_0 + v) \le \beta_2 I, \quad v > 0 \qquad (A.8)$$

where $N(t_0, t_0 + v) \square \int_{t_0}^{t_0+v} \Phi^T(\tau, t_0)C(\tau)C^T(\tau)\Phi(\tau, t_0)d\tau$ is the observability grammian and $\Phi(t, \tau)$ is the state transition matrix associated with $A(t)$, and v, γ_1, γ_2 are constant.

Proof) the proof of the theorem can be found in Ref [5].
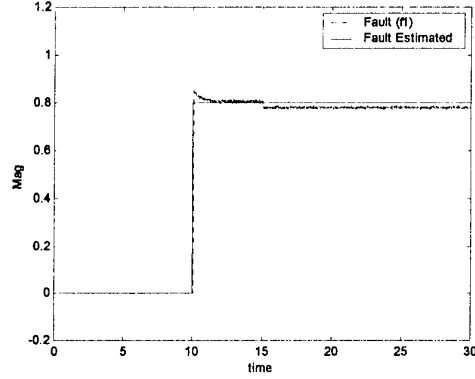
<Fig. 1> FDI (Case of Fault 1)
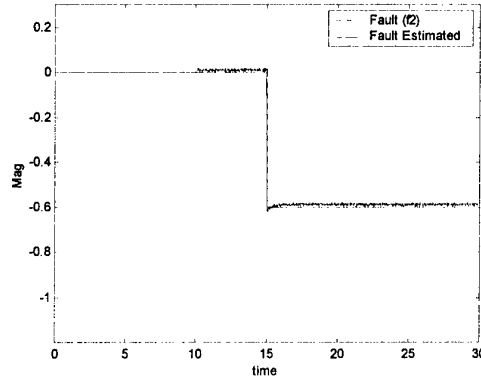
<Fig. 2> FDI (Case of Fault 2)
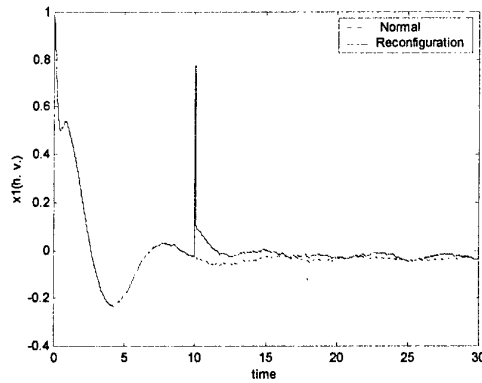
< Fig. 3 > Fault reconfiguration

A new multiple model estimation for systems with switching models

*Sang Jin Shin, **Taek Lyul Song

Hanyang University
Department of Control and Instrumentation Engineering
Sa 1 Dong 1271, Ansan, Kyunggi-do, 425-791, Korea

ABSTRACT

In this paper, a new estimation algorithm with multiple model is suggested. Though the derivation of the proposed algorithm is different from the existing IMM, both algorithms are exactly the same if the dynamic system is linear. However, for nonlinear systems, it appears that the proposed algorithm is different from the IMM algorithm. The proposed algorithm is tested by a series of simulation runs for performance verification.

1. INTRODUCTION

For several decades, filtering algorithms with multiple model have been popular in the field of the estimation and identification [1]-[6]. Multiple model filtering algorithms become explicit and feasible by using the homogeneous Markov chain on the transition between models. Some useful multiple model estimation algorithms are reviewed here briefly. Assuming that the system obeys one of a finite N models, the GPB1 utilizes the scheme that single lumped state and covariance at $t = k - 1$ evolve into N states and covariances in the prediction step and then the N estimates (states and covariances) are updated at k. After that, N estimates are merged into a single estimate. The GPB2 shows that N estimates at $t = k - 1$ evolve into N^2 estimates and become N^2 updates estimates at $t = k$. At the end of each cycle, N^2 update estimates are merged into N estimates. Both the IMM and the MMAE maintain N estimates throughout the prediction and update steps. However, the IMM has an important interacting step for reinitialization of each filter, and it is known that computational effectiveness with superior performance of the IMM over the existing multiple model estimation algorithms results from this procedure.

In this paper, a new multiple model estimation algorithm similar to the IMM is introduced. The proposed algorithm calculates N^2 predicted estimates, and mixes the N^2 predicted estimates into N predicted estimates. It can be shown that if the system dynamics are linear, the proposed algorithm becomes the existing IMM. In other words, the proposed algorithm has same performance as the IMM in linear systems, however it has similar performance to the GPB2 rather than the IMM for estimation of nonlinear systems.

* Graduate student

** Professor

In addition, the computational burden of the proposed algorithm, the extended interacting multiple model(EIMM), is much less than the GPB2. In order to verify the performance of the EIMM, nonlinear target motion dynamics are used in the simulation, and the performance is compared with those of the existing algorithms. Analytic comparison of computational complexities between the EIMM and the GPB2 will also be carried out in this paper.

2. FILTER ALGORITHM

2.1 System Dynamics

Consider the filtering problem for a linear system with a Markov chain taking values in { $H_k = H_k^i, i = 1, 2, \cdots, N$ }.

$$x_{k+1} = \Phi(H_{k+1})x_k + B(H_{k+1})w_k. \tag{1}$$

In the above equation, the state transition matrix $\Phi(H_k)$ is independent of the n-dimensional state x_k, and w_k is a zero-mean white gaussian process noise vector with covariance of Q_k. Generally, if the state transition matrix can not be decoupled with the state, we have a nonlinear system equation as follows:

$$x_{k+1} = f(H_{k+1}, x_k) + B(H_{k+1})w_k. \tag{2}$$

where f is a known function. Also note that the form of (2) is somewhat restrictive in that w_k is assumed to be a separate additive term and is not included in the f. However, to do otherwise complicates the problem cosiderablely, and thus we will stay with this restrictive form in this paper. The associated measurement relationship is assumed to be linear for both cases of (1) and (2).

$$z_{k+1} = Cx_{k+1} + v_{k+1} \tag{3}$$

where v_k is a zero-mean white gaussian noise vector with covariance of R_k.

2.2 IMM AND EIMM

Fig. 1-(a) shows a cycle of recursions for the conditional probability density function of the ith mode states in the EIMM. In Fig. 1-(a), Z_k is a measurement set until time $t = k$, $Z_k = \{z_1, z_2, \cdots z_k\}$. Note that compared to the EIMM, the IMM algorithm separates the prediction step of Fig. 1-(a) into the two steps, 'mixing' or 'interacting' step and 'evolution' step as shown in Fig.1-(b).
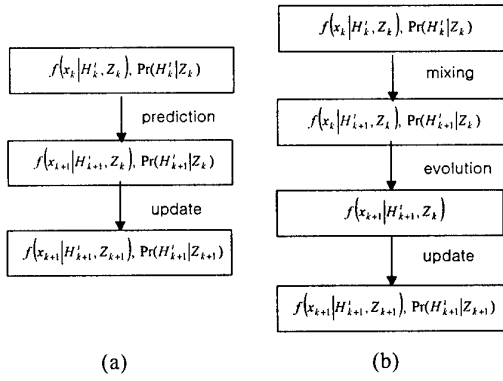
(a)   (b)

Fig. 1 Timing flow ((a) EIMM (b) IMM)

The i th predicted mode probability is obtained by using the mode probability transition matrix $\Pi = \{\pi_{ij}\}$ and the previous updated mode probabilities,

$$\Pr\left(H_{k+1}^i \middle| Z_k\right) = \sum_{j=1}^{N} \pi_{ij} \Pr\left(H_k^j \middle| Z_k\right) . \tag{4}$$

Note that π_{ij} is the transition probability from the mode $\widetilde{H}^j$ at $t = k$ to the mode $\widetilde{H}^i$ at $t = (k+1)$.

The updated steps of the i th mode for both the IMM and the EIMM are the same as

$$\hat{x}_{k+1}^i = \overline{x}_{k+1}^i + K_{k+1}^i (z_{k+1} - C\overline{x}_{k+1}^i) , \tag{5}$$

$$\hat{P}_{k+1}^i = (I - K_{k+1}^i C)\overline{P}_{k+1}^i (I - K_{k+1}^i C)^T + K_{k+1}^i R_{k+1} K_{k+1}^{i}{}^T , \tag{6}$$

$$K_{k+1}^i = \overline{P}_{k+1}^i C^T (C\overline{P}_{k+1}^i C^T + R_{k+1})^{-1} . \tag{7}$$

$\hat{x}_{k+1}^i$ and $\hat{P}_{k+1}^i$ are the updated states and the updated covariance, respectively. Notice that the EIMM procedure to obtain the i th predicted state $\overline{x}_{k+1}^i$ and covariance $\overline{P}_{k+1}^i$ is different from the IMM. According to the reference [6], the i th predicted estimates denoted as the subscript 'IMM' are

$$\overline{x}_{k+1,IMM}^i = \Phi(H_{k+1}^i)\widetilde{x}_k^i , \tag{8}$$

$$\overline{P}_{k+1,IMM}^i = \Phi(H_{k+1}^i)\widetilde{P}_k^i \Phi^T(H_{k+1}^i) + B(H_{k+1}^i)Q_k B^T(H_{k+1}^i) \tag{9}$$

where

$$\widetilde{x}_k^i = \frac{\sum_{j=1}^{N} \hat{x}_k^j \pi_{ij} \Pr(H_k^j|Z_k)}{\sum_{j=1}^{N} \pi_{ij} \Pr(H_k^j|Z_k)} , \tag{10}$$

$$\widetilde{P}_k^i = \frac{\sum_{j=1}^{N} (\hat{P}_k^j + \hat{x}_k^j \hat{x}_k^{j}{}^T) \pi_{ij} \Pr(H_k^j|Z_k)}{\sum_{j=1}^{N} \pi_{ij} \Pr(H_k^j|Z_k)} - \widetilde{x}_k^i \widetilde{x}_k^{i}{}^T . \tag{11}$$

In the nonlinear situation of (2) and (3), a method often used to obtain a practical estimation algorithm is to expand $f(H_{k+1}, x_k)$ in a Taylor series about the current

conditional mean $\widetilde{x}_k^i$, and then an approximate dynamic equation is used in the IMM by dropping all but the first two terms of the expansion $f(H_{k+1}, x_k)$. We can express the i th predicted estimates of the IMM as follows:

$$\overline{x}_{k+1,IMM}^i = f(H_{k+1}^i, \widetilde{x}_k^i) , \tag{12}$$

$$\overline{P}_{k+1,IMM}^i = A_{k+1}^i \widetilde{P}_k^i A_{k+1}^{i}{}^T + B(H_{k+1}^i)Q_{k+1}B^T(H_{k+1}^i) \tag{13}$$

where $A_{k+1}^i = \dfrac{\partial f(H_{k+1}, x)}{\partial x}\bigg|_{x=\widetilde{x}_k^i, H_{k+1}=H_{k+1}^i} . \tag{14}$

In the prediction step of Fig. 1-(a), EIMM uses the conditional probability density function(CPDF) as

$$f(x_{k+1}|H_{k+1}^i, Z_k) = \frac{\sum_{j=1}^{N} f(x_{k+1}|H_k^j, H_{k+1}^i, Z_k)\pi_{ij} \Pr(H_k^j|Z_k)}{\sum_{l=1}^{N} \pi_{il} \Pr(H_k^l|Z_k)} \tag{15}$$

which is different from the CPDF of the IMM. From the appendix at the end of this paper, the conditional mean and covariance of (15) are expressed as

$$\overline{x}_{k+1}^i = \frac{\sum_{j=1}^{N} \overline{x}_{k+1}^{ij} \pi_{ij} \Pr(H_k^j|Z_k)}{\sum_{l=1}^{N} \pi_{il} \Pr(H_k^l|Z_k)} , \tag{16}$$

$$\overline{P}_{k+1}^i = \frac{\sum_{j=1}^{N} (\overline{P}_k^{ij} + (\overline{x}_k^{ij} - \overline{x}_k^i)(\overline{x}_k^{ij} - \overline{x}_k^i)^T)\pi_{ij} \Pr(H_k^j|Z_k)}{\sum_{l=1}^{N} \pi_{il} \Pr(H_k^l|Z_k)} \tag{17}$$

$\overline{x}_{k+1}^{ij}$ is 'evolution-state mean' which is a conditional mean under the condition based on the hypothesis H^j at time $t = k$ and on the hypothesis H^i at time $t = k+1$. If the system dynamics are linear, the evolution-state mean and covariance are

$$\overline{x}_{k+1}^{ij} = \Phi(H_{k+1}^i)\hat{x}_k^j , \tag{18}$$

$$\overline{P}_{k+1}^{ij} = \Phi(H_{k+1}^i)\hat{P}_k^j \Phi^T(H_{k+1}^i) + B(H_{k+1}^i)Q_k B^T(H_{k+1}^i) . \tag{19}$$

After inserting above two equations into (16) and (17), the following two equations are obtained.

$$\overline{x}_{k+1}^i = \Phi(H_{k+1}^i)\widetilde{x}_k^i , \tag{20}$$

$$\overline{P}_{k+1}^i = \Phi(H_{k+1}^i)\widetilde{P}_k^i \Phi^T(H_{k+1}^i) + B(H_{k+1}^i)Q_k B^T(H_{k+1}^i) \tag{21}$$

which are the same filter equations (8)-(11) of the IMM. If the system dynamics are nonlinear, the nonlinear dynamic function is applied to a Taylor series as mentioned early. We can obtain the evolution-state mean and covariance as

$$\overline{x}_{k+1}^{ij} = f(H_{k+1}^i, \hat{x}_k^j) , \tag{22}$$

$$\overline{P}_{k+1}^{ij} = A_{k+1}^i \hat{P}_k^j A_{k+1}^{i}{}^T + B(H_{k+1}^i)Q_k B^T(H_{k+1}^i) , \tag{23}$$

$$A_{k+1}^{i} = \left. \frac{\partial f(H_{k+1}, x)}{\partial x} \right|_{x = \hat{x}_k^i, H_{k+1} = H_{k+1}^i} . \qquad (24)$$

These equations can not be transformed into (12) and (13), so the EIMM becomes different from the IMM for nonlinear systems. The EIMM algorithm compared to the IMM is somewhat complex and it is linked to the computational burden. However, as shown in the next section, the performance of the EIMM is better than the IMM and similar to the GPB2 which has more computational burden than the EIMM. In a cycle of recursions, the EIMM and the GPB2 procedures are the same up to the point of obtaining $\bar{x}_{k+1}^{ij}$ and $\bar{P}_{k+1}^{ij}$. Notice that $\bar{x}_{k+1}^{ij}$ and $\bar{P}_{k+1}^{ij}$ of the GPB2 are directly updated so that N^2 Kalman update equations for the updated states must be calculated while those of the EIMM are merged into N predicted values so that N Kalman update equations are needed similar to the IMM. Table 1, where the results are referred to [7] to illustrate the number of computaions, shows the number of multiplications, summations and exponentials required for the remaining stages of the EIMM and the GPB2. The remaining steps for the EIMM are the merging step of the predicted estimates, the measurement update step and mode probability update step, while the remaining steps for the GPB2 are the measurement update step and mode probability update step. According to the table 1, for $n = 4$ and $N = 3$, the number of computations of the GPB2 is over two times as many as that of the EIMM, and over three times if $N = 6$. The difference of the number of computations increases for larger n.

Table 1 The number of computations
(measurement dimension=2)

Multiplication	$(n^2 + 2n + 2)N^2 + \frac{1}{2}(n^3 + 9n^2 + 22n + 26)N$
Summation	$(n^2 + 3n + 1)N^2 + \frac{1}{2}(n^3 + 7n^2 + 10n + 4)N - 1$
Exponential	N

(a) EIMM

Multiplication	$\frac{1}{2}(n^3 + 11n^2 + 26n + 28)N^2 + N$
Summation	$\frac{1}{2}(n^3 + 10n^2 + 19n + 6)N^2 - \frac{1}{2}(n^2 + 3n)N - 1$
Exponential	N^2

(b) GPB2

3. SIMULATION RESULTS

The EIMM is applied to a planar engagement tracking problem to verify the performance through a series of simulation runs. In this study, filter states are composed of radar-target range, LOS(line of sight) angle, target velocity and target flight path angle as depicted in Fig. 3. It is assumed that the target does not make any accelerating motion in the direction of longitudinal axis and the lateral acceleration is
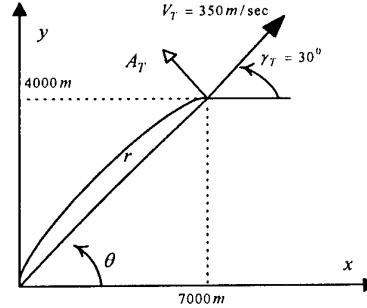
Fig. 3 Engagement geometry

unknown so that $A_T^1 = -10g$ and $A_T^2 = 10g$ are used as the modes in this study. Note that the ' g ' is the gravity acceleration. The system dynamic model is represented as

$$\frac{d}{dt} \begin{pmatrix} r \\ \theta \\ V_T \\ \gamma_T \end{pmatrix} = \begin{pmatrix} V_T \cos(\theta - \gamma_T) \\ -V_T \sin(\theta - \gamma_T)/r \\ 0 \\ A_T \end{pmatrix} + \begin{pmatrix} 0 \\ 0 \\ w_V \\ w_\gamma \end{pmatrix}$$

$$= f(A_T, x) + Bw \qquad (25)$$

where the process noise w_V and w_γ are zero-mean white gaussian noises with standard deviations of $1m/\sec^2$ and $0.1mrad/\sec$, respectively. The measurements from the radar at $t = k$ composed of the noise-corrupted radar-target range and the LOS angle can be expressed as

$$z_k = (I_2, 0_2)x_k + (v_r, v_\theta)^T \qquad (26)$$

where I_2 is a 2×2 identity matrix and 0_2 is a 2×2 zero matrix, and v_r and v_θ are zero-mean white gaussian noises with standard deviations of $12m$ and $3mrad$, respectively. The initial values of the target used in this planar engagement study are depicted in Fig. 3. The sampling frequency is 20Hz and the mode probability transition matrix used in this study is

$$\Pi = \begin{pmatrix} 0.98 & 0.02 \\ 0.02 & 0.98 \end{pmatrix}. \qquad (27)$$

The target lateral acceleration history is set to be $A_T(t) = 7g \cdot u(t) - 14g \cdot u(t - 20)$ where ' $u(t)$ ' is a unit step function. The estimated target lateral acceleration is obtained by using the total probability theorem as

$$\hat{A}_T(k) = \sum_{i=1}^{N} A_T^i \Pr(H_k^i | Z_k). \qquad (28)$$

Figs. 4-5 show the results of 20 runs of Monte Carlo simulation carried out to evaluate the performance of the EIMM. In these figures, after the abrupt target maneuver varying from $7g$ to $-7g$ at 20 sec, the EIMM and GPB2 have fast responses for the reduction of the RMSE(root mean square errors) of the estimation. It can be seen that the EIMM algorithm gives superior estimation performance at the transition of the target motion over the GPB1 and the IMM
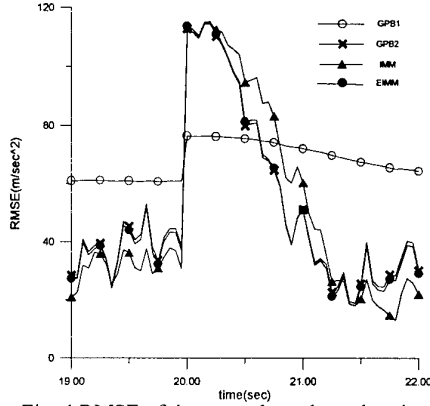
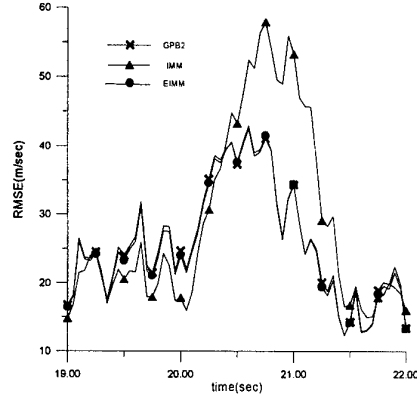Fig. 4 RMSE of the target lateral acceleration

Fig. 5 RMSE of the target $x - axis$ velocity

4. CONCLUSIONS

The EIMM algorithm is proposed here as a useful multiple model estimation algorithm for nonlinear systems. The EIMM algorithm has the same filtering procedure and thus to have the same estimation performance as the IMM in linear systems, however it results in a different form in nonlinear systems. In addition, the EIMM has similar performance to the GPB2 rather than the IMM for estimation performance of nonlinear systems. The EIMM algorithm is tested by a series of Monte Carlo simulation runs along with the IMM, GPB2, and GPB1 to evaluate the estimation performance. The results indicate that the EIMM algorithm gives superior estimation performance over the other filter algorithms in the respects of computational efficiency and RMSE of the estimation.

REFERENCES

[1] Magill, D. T., "Optimal adaptive estimation of sampled stochastic processes," IEEE Transactions on Automatic Control, AC-10, Oct. 1965.

[2] Bruckner, J. M. H., Scott, R. W. and Rea, F. G., "Analysis of multimodal systems," IEEE Transactions on Aerospace and Electronic Systems, AES-9, Nov. 1973, 883-888.

[3] Chang, C. B. and Athans, M., "State estimation for discrete systems with switching parameters," IEEE Transactions on Aerospace and Electronic Systems, AES-14, May. 1978, 418-425.

[4] Mathews, V. J. and Tugnait, J. K., "Detection and estimation with fixed lag for abruptly changing systems," IEEE Transactions on Aerospace and Electronic Systems, AES-19, Sep. 1983, 730-739.

[5] Moose, R. L., "An adaptive state estimation solution to the maneuvering target problem," IEEE Transactions on Automatic Control, AC-20, Jun. 1988, 359-362

[6] Blom, H. A. P. and Bar-Shalom, Y., "The interacting multiple model algorithm for systems with Markovian switching coefficients," IEEE Transactions on Automatic Control, AC-33, Aug. 1988, 780-783.

[7] Daeupour, E. and Bar-Shalom, Y., "IMM tracking of maneuvering targets in the presence of glint," IEEE Transactions on Aerospace and Electronic Systems, AES-34, Jul. 1998, 996 -1003

APPENDIX

Given $f(x_k | H_k^i, Z_k)$, $i = 1, 2, \cdots, N$, $f(x_{k+1} | H_{k+1}^i, Z_k)$ is expressed from the Bayes' formula as

$$f(x_{k+1} | H_{k+1}^i, Z_k) = \frac{\sum_{j=1}^{N} f(x_{k+1} | H_k^j, H_{k+1}^i, Z_k) \pi_{ij} \Pr(H_k^j | Z_k)}{\sum_{l=1}^{N} \pi_{il} \Pr(H_k^l | Z_k)},$$

$$\bar{x}_{k+1}^i = E[x_{k+1} | H_{k+1}^i, Z_k]$$

$$= \frac{\sum_{j=1}^{N} \int x_{k+1} f(x_{k+1} | H_k^j, H_{k+1}^i, Z_k) dx_{k+1} \pi_{ij} \Pr(H_k^j | Z_k)}{\sum_{l=1}^{N} \pi_{il} \Pr(H_k^l | Z_k)}. \quad (29)$$

Let $\bar{x}_{k+1}^{ij} = \int x_{k+1} f(x_{k+1} | H_k^j, H_{k+1}^i, Z_k) dx_{k+1}$ and set the difference between $\bar{x}_{k+1}^{ij}$ and $\bar{x}_{k+1}^i$ to be $\Delta \bar{x}_{k+1}^{ij}$ as follows:

$$\bar{x}_{k+1}^i = \bar{x}_{k+1}^{ij} - \Delta \bar{x}_{k+1}^{ij}. \quad (30)$$

$$\bar{P}_{k+1}^i = E[(x_{k+1} - \bar{x}_{k+1}^i)(x_{k+1} - \bar{x}_{k+1}^i)^T | H_{k+1}^i, Z_k]$$

$$= \sum_{j=1}^{N} \int (x_{k+1} - \bar{x}_{k+1}^{ij})(x_{k+1} - \bar{x}_{k+1}^{ij})^T f(x_{k+1} | H_k^j, H_{k+1}^i, Z_k) dx_{k+1} \mu_{ij}$$

$$+ \sum_{j=1}^{N} \int (x_{k+1} - \bar{x}_{k+1}^{ij}) \Delta \bar{x}_{k+1}^{ij}{}^T f(x_{k+1} | H_k^j, H_{k+1}^i, Z_k) dx_{k+1} \mu_{ij}$$

$$+ \sum_{j=1}^{N} \int \Delta \bar{x}_{k+1}^{ij}(x_{k+1} - \bar{x}_{k+1}^{ij})^T f(x_{k+1} | H_k^j, H_{k+1}^i, Z_k) dx_{k+1} \mu_{ij}$$

$$+ \sum_{j=1}^{N} \int \Delta \bar{x}_{k+1}^{ij} \cdot \Delta \bar{x}_{k+1}^{ij}{}^T f(x_{k+1} | H_k^j, H_{k+1}^i, Z_k) dx_{k+1} \mu_{ij} \quad (31)$$

where $\mu_{ij} = \dfrac{\pi_{ij} \Pr(H_k^j | Z_k)}{\sum_{l=1}^{N} \pi_{il} \Pr(H_k^l | Z_k)}$. $\quad (32)$

In the right hand side of the above equation (31), the second and the third terms become zero, so that we can obtain (17).

The Activation-only VSIMM

Seong Hee Choi* and Taek Lyul Song**

Hanyang University

Department of Control and Instrumentation Engineering

Sa 1 Dong 1271, Ansan, Kyunggi-do, 425-791, Korea

Keyword : FSIMM, VSIMM, Activation, Termination

ABSTRACT

This paper suggests the activation-only VSIMM estimator, applied mainly to target tracking problems. This algorithm is much simpler and easier to implement than the ordinary VSIMM algorithm. Also the activation-only VSIMM algorithm provides a substantial reduction in computation while having identical performance with the ordinary VSIMM estimator and the FSIMM estimator. More importantly, the drawbacks related to the improper termination and activation inherent to the VSIMM algorithm are eliminated in this algorithm.

The performance of this estimator will be shown through a Monte Carlo simulation for target tracking.

1. Introduction

Multiple-Model (MM) estimation has received a great deal of attention in recent years due to its powerful performances in handling problems for estimating structural and parametric uncertainties inherent to system identification such as target tracking and fault detection. This MM estimation was initiated in [1]. After that, the various MM algorithms such as the generalized-pseudo Bayesian of first order and second order (GPB1 and GPB2) estimators in [2] and interacting multiple model (IMM) in [3] were released and used in many fields. Especially the IMM algorithm was popular due to its better performance and more cost-effective aspect than other MM algorithms.

But these MM estimators, including the IMM estimator, are a fixed structure MM (FSMM) in the sense that they use a fixed set of models at all times. These estimators usually perform reasonably well for problems that can be handled with a small set of good models. However, in many practical situations, especially with high-dimensional systems, FSMM estimators need many models to cover the real system variation. At that time, the use of many models in FSMM will increase the computational burden considerably. More importantly, the performance could be deteriorated if too many models are used

due to the excessive unlikely models. Briefly the use of too many models to cover the real situations is inadequate in aspect to the computational burden and to the performances.

The variable structure MM (VSMM) was needed to overcome the FSMM estimator's fundamental limitations. The VSMM was initiated in [5] and continued in [6], [7] and [8] to lay down a theoretical foundation to overcome the limitation of the FSMM. Also [9] presents a VSIMM estimator, equipped with the model-group switching (MGS) algorithm, which is generally applicable to many hybrid estimation problems. Additionally the VSIMM is easy to implement and has the cost-effectiveness in contrast to the FSIMM estimators. The VSIMM algorithm can be decomposed into two separate tasks, activation and termination.

Reference [10] indicates that the VSIMM algorithm is substantially more cost-effective than the FSIMM estimator, especially when the total model-set is large. But one of the drawbacks of the VSIMM is that a computational burden increases abruptly when a new group is activated and continues until one of two groups is terminated. Moreover improper setting of the filter parameters such as group probability ratio threshold and sequential group likelihood ratio threshold in the termination logic makes the performance worse because inadequate thresholds cannot terminate an unnecessary model group of two groups appropriately.

So this paper suggests the activation-only VSIMM method that is composed with activation only to reduce the computational load of the VSIMM and to respond to the change of the system adaptively and quickly.

2. Variable Structure IMM(VSIMM)

The Variable Structure Interacting Multiple Model (VSIMM) estimator is different from the FSIMM because the total model-set is not needed at all times. In this estimator, the model-set in effect is made adaptively by activating and terminating a model group among a number of predetermined model groups, each representing closely related system behaviors. As such, one or two model groups has to be run at any time, and thus substantially computational reduction is achieved if it is compared with a FSIMM estimator based on the total model-set.

---

* Graduate student

**Professor

The key features of the VSIMM algorithm include the following aspects.

First, the switching between model groups is done in two stages : activation and termination. The model-group that is deemed likely to be a good candidate at a time is activated first without forcing the termination of the model-group currently in effect. And then, the VSIMM runs the union sets recursively until sufficient information is gathered to terminate one of them.

Second, the initialization of the newly activated model-group is needed to run the IMM algorithm with the union model groups because the filter status of the newly activated model-group has not been determined yet. The initial filter status of the newly activated model-group can be calculated from the previous estimates through the predetermined mode probability transition matrix.

Third, the decision concerning model group termination is made based on a combination of the model-group probability ratio test and the sequential model-group likelihood ratio test.

Reference [9] and [10] explain the VSIMM algorithm in detail.

A flowchart of the VSIMM algorithm is presented in Fig. 1.
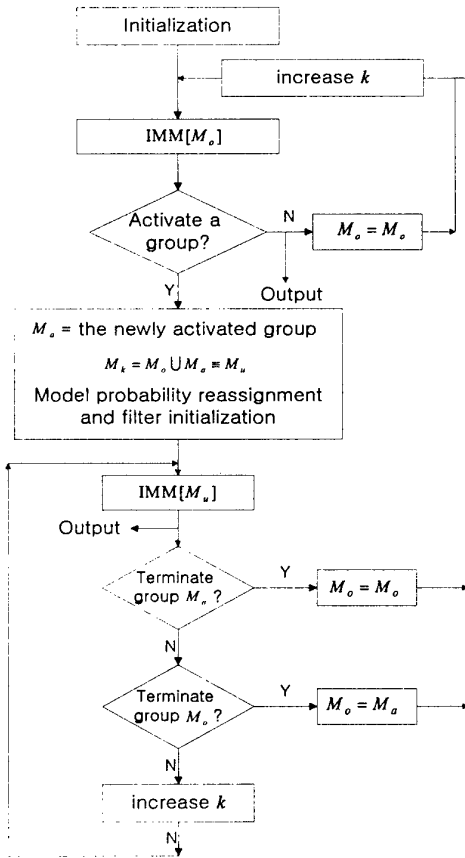
Fig. 1 Flowchart of the VSIMM

3. Activation-only VSIMM

This method does not contain the termination logic that may cause some problems like an inability of termination due to the unsuitable thresholds. In the following section the algorithm of the activation-only VSIMM will be explained and the design for a simulation will be presented.

The decision for model-group activation consists of a model probability and its likelihood function among several model sets in a current activated model-group. It is apparent that the higher thresholds in the activation logic will lead to have a delay in activating the correct model-group while the too lower thresholds will result in a high false activation rate. Therefore suitable thresholds need to reduce the false activation rate, to improve the accuracy and to follow the system variation quickly and correctly. Based on the above considerations, we use the following simple activation rules in the simulation.

1) Activate group M_j while $M_k = M_i$ where $i \neq j$, if both of the following two conditions are satisfied.

Likelihood condition: $L_k^j = max_{m_i \in M_k} L_k^i$

Probability condition: $\mu_k^j > t_a$

Namely, if the model group M_j is deemed true as the above two criteria, then M_j is activated.

2) There is direct switching in only adjacent model groups.

This indicates that the current mode-group and the candidate model-group should have the common models.

After selecting a candidate model-group for activating, the initialization task of the newly activated filters is needed. Above all, it is necessary to assign the probabilities, at one time cycle before, to the newly activated models that do not include the common models of the candidate model-group and the current model-group. For example, if m_k^n is a newly activated model at time k, then its probability of being true at $k-1$ is zero, i.e.,

$$\mu_{k-1}^n = \text{Prob}\{m_{k-1}^n \mid M^{k-1}, Z^{k-1}\} = 0, \quad \forall m_k^n \in M_k^n . \tag{1}$$

The expected probability of m_k^n being true at time k without information in the observation at k (i.e., the predicted mode probability) is calculated through the given mode probability transition matrix.

$$\mu_{k|k-1}^n = \text{Prob}\{ m_k^n \mid M^{k-1}, Z^{k-1}\}$$

$$= \sum_{m_j \in E_n} \text{Prob}\{m_k^n \mid m_{k-1}^j\} \text{Prob}\{m_{k-1}^j \mid M^{k-1}, Z^{k-1}\}$$

$$= \sum_{m_j \in E_n} \pi_{jn} \mu_{k-1}^j \tag{2}$$

where $\pi_{jn} = \text{Prob}\{m_k^n \mid m_{k-1}^j\}$ and E_n is the set of models in $\mathbf{M}_{k-1}$ that are allowed to switch to m_k^n:

$$E_n = \{ m_{k-1}^l : m_{k-1}^l \in M_{k-1}, \ \pi_{ln} \neq 0 \}. \qquad (3)$$

The initial probabilities of common models in the activated model group should be unchanged. That is, the process of initialization probabilities is needed only in the newly activated models. Also the estimates of the newly activated filters in the interacting step for IMM algorithm should be calculated as follows,

$$\tilde{x}_{k-1}^n = E[\, x_{k-1} \mid m_k^n, M^{k-1}, Z^{k-1} \,]$$

$$= \sum_{m_{k-1}^i \in M_{k-1}} \hat{x}_{k-1}^i \mu_{k-1}^{i|n} \qquad (4)$$

$$\mu_{k-1}^{i|n} = \text{Prob}\{m_{k-1}^i \mid m_k^n, M^{k-1}\} = \frac{\pi_{in}\mu_{k-1}^i}{\sum\limits_{m_{k-1}^l \in M_{k-1}} \pi_{jn}\mu_{k-1}^j}. \qquad (5)$$

The associated covariances can be calculated accordingly.

$$\tilde{P}_{k-1}^n = E[\, (x_{k-1} - \tilde{x}_{k-1}^n)(x_{k-1} - \tilde{x}_{k-1}^n)' \mid m_k^n, M^{k-1}, Z^{k-1} \,]$$

$$= \sum_{m_{k-1}^i \in M_{k-1}} [\, \hat{P}_{k-1}^i + (\hat{x}_{k-1}^i - \tilde{x}_{k-1}^n)(\hat{x}_{k-1}^i - \tilde{x}_{k-1}^n)' \,]\mu_{k-1}^{i|n}. \ (6)$$

In other words, if model m_k^n can only be switched from model m_{k-1}^i in $\mathbf{M}_{k-1}$, then $\hat{x}_{k-1}^i$ and $\hat{P}_{k-1}^i$ should be used for the initial estimate and covariance of the filter based on m_k^n at time k. A flowchart of the activation-only VSIMM algorithm is presented in Fig. 2.
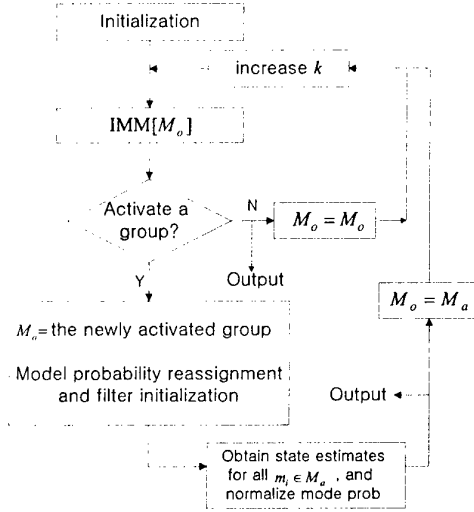
Fig. 2 Flowchart of the activation-only VSIMM

4. Simulation Results

In this paper, the activation-only VSIMM algorithm is compared with the ordinary VSIMM and the FSIMM

simultaneously over 100 Monte Carlo runs. The system dynamic equitation is presented in (7).

$$x_{k+1} = \begin{bmatrix} 1 & \frac{T^2}{2} & 0 & 0 \\ 0 & 1 & 0 & 0 \\ 0 & 0 & 1 & \frac{T^2}{2} \\ 0 & 0 & 0 & 1 \end{bmatrix} x_k + \begin{bmatrix} \frac{T^2}{2} & 0 \\ T & 0 \\ 0 & \frac{T^2}{2} \\ 0 & T \end{bmatrix} w_k$$

$$z_k = \begin{bmatrix} 1 & 0 & 0 & 0 \\ 0 & 0 & 1 & 0 \end{bmatrix} x_k + \begin{bmatrix} 1 & 0 \\ 0 & 1 \end{bmatrix} v_k \qquad (7)$$

where w_k is the process noise with $Q = 10^2 I_2$ and v_k is the measurement noise with $R = 20^2 I_2$. The initial position and velocity are 20km and 340m/sec for each axis. Also the sampling interval T is 1 sec. The mode probability transition matrix $\{\pi_{ij}\}$, for total model-set is the same in reference [4] as illustrated in Appendix .

Fig. 3 represents the total model-set for the simulation, and each model is characterized by the expected acceleration vector $\mathbf{a}$ in (8),
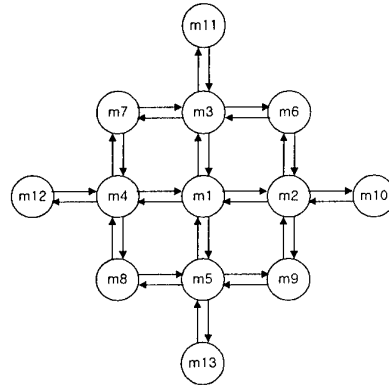
Fig. 3 Graph-representation of the total model-set

$$m_1 : \mathbf{a} = \begin{bmatrix} 0 & 0 \end{bmatrix}' \qquad m_2 : \mathbf{a} = \begin{bmatrix} 20 & 0 \end{bmatrix}'$$
$$m_3 : \mathbf{a} = \begin{bmatrix} 0 & 20 \end{bmatrix}' \qquad m_4 : \mathbf{a} = \begin{bmatrix} -20 & 0 \end{bmatrix}'$$
$$m_5 : \mathbf{a} = \begin{bmatrix} 0 & -20 \end{bmatrix}' \qquad m_6 : \mathbf{a} = \begin{bmatrix} 20 & 20 \end{bmatrix}'$$
$$m_7 : \mathbf{a} = \begin{bmatrix} -20 & 20 \end{bmatrix}' \qquad m_8 : \mathbf{a} = \begin{bmatrix} -20 & -20 \end{bmatrix}' \qquad (8)$$
$$m_9 : \mathbf{a} = \begin{bmatrix} 20 & -20 \end{bmatrix}' \qquad m_{10} : \mathbf{a} = \begin{bmatrix} 40 & 0 \end{bmatrix}'$$
$$m_{11} : \mathbf{a} = \begin{bmatrix} 0 & 40 \end{bmatrix}' \qquad m_{12} : \mathbf{a} = \begin{bmatrix} -40 & 0 \end{bmatrix}'$$
$$m_{13} : \mathbf{a} = \begin{bmatrix} 0 & -40 \end{bmatrix}'.$$

And the model groups are set in (9) for model-group switching,

$$M_1 = \{m_1, m_2, m_3, m_4, m_5\}$$
$$M_2 = \{m_2, m_{10}, m_6, m_1, m_9\}$$
$$M_3 = \{m_3, m_{11}, m_7, m_1, m_6\}$$
$$M_4 = \{m_4, m_{12}, m_8, m_1, m_7\}$$
$$M_5 = \{m_5, m_{13}, m_9, m_1, m_8\}. \qquad (9)$$

The threshold of probability, t_a to activate a candidate group is set to 0.4 for the VSIMM and the activation-only VSIMM. Also model-group probability ratio thresholds and model-group

likelihood ratio thresholds to terminate an activated group or a current group in VSIMM are used by (10).

$$t_1^\mu = 0.85, \quad t_1^L = 0.9$$
$$t_2^\mu = 0.93, \quad t_2^L = 1.0 \quad\quad (10)$$

The system mode sequence for scenario no.1, characterized by the sequence of acceleration $\mathbf{a}_k$, is specified by (11).

$$S1 \; : \; \mathbf{a}_k = \begin{cases} [0 \quad 0]' & 1 \le k \le 30 \\ [18 \quad 3]' & 31 \le k \le 45 \\ [38 \; -2]' & 46 \le k \le 55 \\ [0 \quad 0]' & 56 \le k \le 80 \\ [1 \quad 22]' & 81 \le k \le 98 \\ [3 \quad -1]' & 99 \le k \le 119 \\ [-35 \quad 1]' & 120 \le k \le 139 \\ [-20 \quad 0]' & 140 \le k \le 150 \\ [3 \quad 2]' & 151 \le k \le 200 \end{cases} \quad (11)$$

Fig. 4 and Fig. 5 show the RMSE for estimating the sequence of acceleration for the given S1 through Monte Carlo runs.
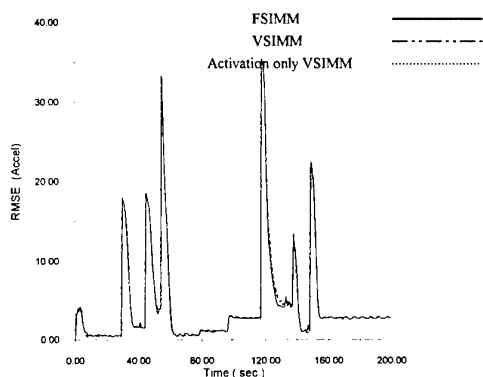
Fig. 4 RMSE for acceleration in S1 (X axis)
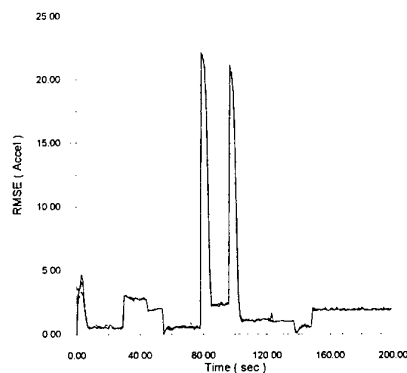
Fig. 5 RMSE for acceleration in S1 (Y axis)

The performances of three estimators used in this scenario are almost same except the computational burden.

Table 1 lists the computational complexity in terms of relative CPU time. Table 1 indicates that the activation-only VSIMM has the least computational burden compared to the ordinary VSIMM and the FSIMM. The computational burden

Table 1 Average CPU time over 100 Monte Carlo runs.

Estimator	Total clock	Percent (%)
FSIMM	25229	100
VSIMM	10632	42.14
Activation-only VSIMM	9504	37.67

of the VSIMM increases abruptly when a candidate model-group is activated and continues until one of two model groups is terminated. More seriously, if a different sequence scenario of $\mathbf{a}_k$ is simulated with the same conditions and thresholds of the parameters mentioned in the above, the estimation performance of the VSIMM becomes worse because of the unmatched thresholds in termination and activation logics. The scenario no.2 is presented in (12).

$$S2 \; : \; \mathbf{a}_k = \begin{cases} [0 \quad 0]' & 1 \le k \le 30 \\ [35 \; -3]' & 31 \le k \le 45 \\ [-2 \quad 15]' & 46 \le k \le 55 \\ [0 \quad 31]' & 56 \le k \le 80 \\ [3 \; -11]' & 81 \le k \le 98 \\ [0 \quad 0]' & 99 \le k \le 119 \\ [-35 \quad 4]' & 120 \le k \le 139 \\ [2 \quad 0]' & 140 \le k \le 150 \\ [2 \; -18]' & 151 \le k \le 200 \end{cases} \quad (12)$$
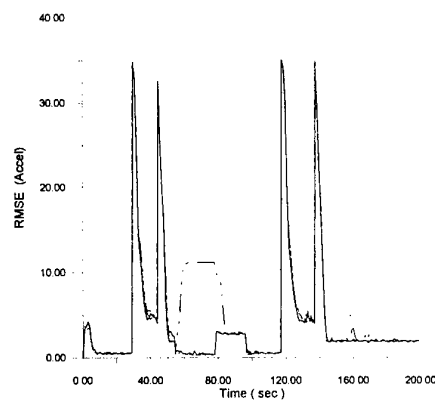
Fig. 6 RMSE for acceleration in S2 (X axis)
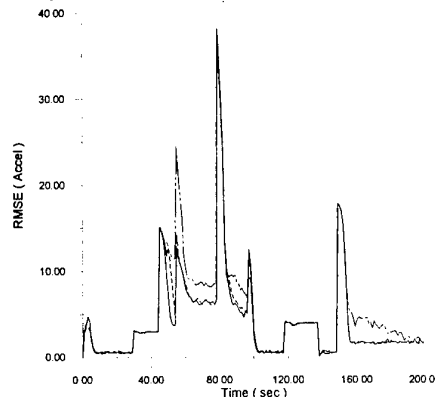
Fig. 7 RMSE for acceleration in S2 (Y axis)

The above Fig. 6 and Fig. 7 indicate that the VSIMM has the worst performance in the S2. For example, the true target switches from M_2 to M_1 at $k=46$ and then goes to M_3 at $k=56$, but the VSIMM can't terminate M_2 of the union-set(i.e., M_1 and M_2) due to the unmatched thresholds while the target stayes in M_1. Finally when the target switches to M_3, the VSIMM can not activate M_3 since the union-set is running still. It is found that performance of the VSIMM estimator becomes so sensitive to thresholds of the termination logic. If the thresholds are not chosen adaptively for each sceanrio, the VSIMM may not terminate the unlikely model-group correctly which results in delayed activation of a new candidate model-group suitable for the true system variation. Also it is hard to find a general rule for the corresponding threshold values to apply to diverse scenarios. Therefore, the thresholds should be tuned in each different scenario to have a good performance. This indicates that the VSIMM method may not be suitable for target tracking problem where the target maneuvers arbitrarily.

The activation-only VSIMM algorithm avoids this drawback since the termination logic is not included in the algorithm.

4. Conclusions

In this paper, the activation-only VSIMM algorithm which is applied mainly to target tracking has been presented and the simulation results in terms of RMSE for acceleration and CPU time have been shown when it is compared with the ordinary VSIMM and the FSIMM for the maneuvering target tracking problem.

The simulation results indicate that the activation-only VSIMM provides a substantial reduction in the computational burden while having identical performance to the FSIMM estimator. Additionally, this estimator is the most cost-effectiveness compared to the VSIMM algorithm and the FSIMM. More importantly, the drawbacks related to the improper termination and activation inherent to the VSIMM algorithm are eliminated in the activation-only VSIMM algorithm, so that the algorithm can be used securely for abruptly maneuvering target tracking problems.

REFERENCES

1. Magill, D.T., "Optimal adaptive estimation of sampled stochastic processes," IEEE Trans. Automat. Contr. Vol 10, pp. 434-439, 1965.
2. Bar-Shalom, Y. and Li, X. R., "Estimation and Tracking : Principles, Techniques and Software," Boston, MA : Artech House 1993.
3. Blom, H.A.P. and Bar-Shalom, Y., "The interacting multiple model algorithm for systems with Markovian switching coefficients," IEEE Trans. Automat. Contr. Vol 33, pp. 780-783, Aug 1988.
4. Li, X. R., "Hybrid estimation techniques," in Control and Dynamic Systems : Advances in Theory and Applications, C.T. Leondes, Ed. New York: Academic, Vol 76, pp. 213-287, 1996.
5. Li, X. R., "Mode-set adaptation in multiple-model estimators for hybrid systems," in Proc. 1992 Amer. Control. Conf, Chicago, IL, pp. 1794-1799, June 1992.
6. Li, X. R., "Multiple-Model estimation with variable structure: some theoretical considerations," In Proc 33rd IEEE Conf. Decision and Control, Orlando, FL, pp. 1199-1204, Dec 1994.
7. Li, X. R. and Bar-shalom, Y., "MM estimation with variable structure," IEEE Trans. Automat. Contr. Vol 41, pp. 478-493, Apr 1996.
8. Li, X. R., "Multiple-model estimation with variable structure-Part II : Model-set Adaptation," IEEE Trans. Automat. Contr. Vol 45, pp. 2047-2060, Nov 2000.
9. Li, X. R. and Zhi, X. R. and Zhang, Y. M., "Multiple-model estimation with variable structure-Part III : Model-group switching algorithm," IEEE Transactions on Aerospace and Electronic Systems, Vol 35, pp.225-241, Jan 1999.
10. Li, X. R. and Zhi, X. R. and Zhang, Y. M., "Multiple-model estimation with variable structure-Part IV : Design and Evaluating of Model-Group Switching Algorithm," IEEE Transactions on Aerospace and Electronic Systems, Vol. 35, pp.242-254, Jan 1999

Appendix

$$\pi_{ij} = \begin{bmatrix}
116/120 & 1/120 & 1/120 & 1/120 & 1/120 & 0 & 0 & 0 & 0 & 0 & 0 & 0 & 0 \\
0.02 & 0.95 & 0 & 0 & 0 & 0.01 & 0 & 0 & 0.01 & 0.01 & 0 & 0 & 0 \\
0.02 & 0 & 0.95 & 0 & 0 & 0.01 & 0.01 & 0 & 0 & 0 & 0.01 & 0 & 0 \\
0.02 & 0 & 0 & 0.95 & 0 & 0 & 0.01 & 0.01 & 0 & 0 & 0 & 0.01 & 0 \\
0.02 & 0 & 0 & 0 & 0.95 & 0 & 0 & 0.01 & 0.01 & 0 & 0 & 0 & 0.01 \\
0 & 1/30 & 1/30 & 0 & 0 & 28/30 & 0 & 0 & 0 & 0 & 0 & 0 & 0 \\
0 & 0 & 1/30 & 1/30 & 0 & 0 & 28/30 & 0 & 0 & 0 & 0 & 0 & 0 \\
0 & 0 & 0 & 1/30 & 1/30 & 0 & 0 & 28/30 & 0 & 0 & 0 & 00 & 0 \\
0 & 1/30 & 0 & 0 & 1/30 & 0 & 0 & 0 & 28/30 & 0 & 0 & 0 & 0 \\
0 & 0.1 & 0 & 0 & 0 & 0 & 0 & 0 & 0 & 0.9 & 0 & 0 & 0 \\
0 & 0 & 0.1 & 0 & 0 & 0 & 0 & 0 & 0 & 0 & 0.9 & 0 & 0 \\
0 & 0 & 0 & 0.1 & 0 & 0 & 0 & 0 & 0 & 0 & 0 & 0.9 & 0 \\
0 & 0 & 0 & 0 & 0.1 & 0 & 0 & 0 & 0 & 0 & 0 & 0 & 0.9
\end{bmatrix}$$
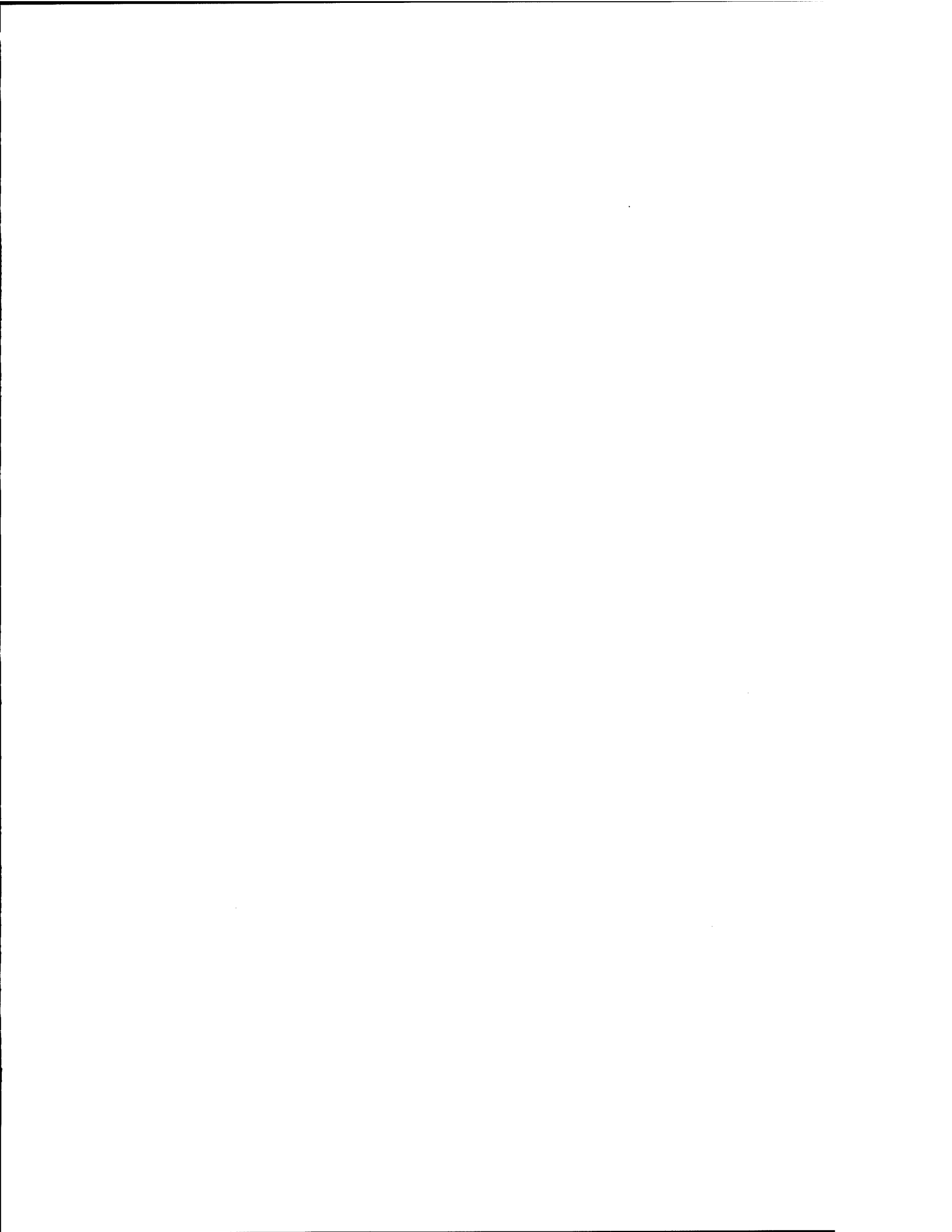
1F11   A PRELIMINARY STUDY ON THE FLIGHT CONTROL SYSTEM OF
THE STRATOSPHERIC PLATFORM

Fumiaki IMADO*, Tsunehisa IWANAMI*, Akira TADA**, Shuichi SASA**, Kenya HARADA**
*Department of Mechanical Systems Engineering, Shinshu University
4-17-1 Wakasato Nagano, Nagano 380-8553 JAPAN
**National Aerospace Laboratory, 6-13-1 Oosawa Mitaka, Tokyo 181-0015 JAPAN

Key Words: Flight Dynamics, Guidance and Control

ABSTRACT

A preliminary study on the guidance and flight control system for a test model of the stratospheric airship is conducted, and the result is briefly explained. The test model is intended to stay at the altitude of 4000m, within 1km distance from the indicated point. As the energy source is limited, the airship is usually supposed to be flying with a very low speed. The longitudinal and lateral flight control systems are designed, and the performance is verified by simulations, which generally show good performances. The design method of the control systems is briefly explained, and some of simulation results are shown.

1.INTRODUCTION

The stratospheric platform airship is currently under development, and the 1/4 scale test model is scheduled to fly in 2004 in order to get basic data for the full scale airship. The model is designed to fly at the altitude of 4000m and to stay within 1km radius of the indicated point. As there was no discussion about the flight control system of the airship at the last aircraft symposium, this paper shows some preliminary study results about it.

SYMBOLS

$C_{L\alpha}$, $C_{L\delta}$: Aerodynamic force coefficients

$C_{m\alpha}$, $C_{m\delta}$, $C_{m\dot\alpha}$, C_{mq} : Aerodynamic
moment coefficients

Q : Dynamic pressure

S : Reference area

C : Reference length

m_t : Mass

I_y : Pitch moment of inertia

$Z_{\dot w}$, $M_{\dot q}$: Apparent mass effects

K : Recovery moment by buoyance

V : Total velocity

2.RATE AND ACCELERATION LOOPS

In this study, the flight control system is designed by the classical pole allocation method. The transfer functions between the elevator angle, pitch rate, and

flight path angle rate are approximately given by the following equations.

$$\frac{\dot\theta(s)}{\delta_e(s)} = \frac{C_1(1+\tau_{\dot\theta}s)}{1+a_1s+a_2s^2} \qquad \frac{\dot\gamma^p(s)}{\delta_e(s)} = \frac{C_1(1+b_1s+b_2s^2)}{1+a_1s+a_2s^2}$$

where

$$C_1 = -\frac{f_\alpha m_\delta - f_\delta m_\alpha}{m_\alpha + f_\alpha m_q} \qquad \tau_{\dot\theta} = \frac{m_\delta - f_\delta m_{\dot\alpha}}{f_\alpha m_\delta - f_\delta m_\alpha}$$

$$a_1 = \frac{m_{\dot\alpha} + m_q - f_\alpha}{m_\alpha + f_\alpha m_q} \qquad a_2 = -\frac{1}{m_\alpha + f_\alpha m_q}$$

$$b_1 = -\frac{f_\delta(m_{\dot\alpha} + m_q)}{f_\alpha m_\delta - f_\delta m_\alpha} \qquad b_2 = \frac{f_\delta}{f_\alpha m_\delta - f_\delta m_\alpha}$$

where

$$f_\alpha = \frac{QSC_{L\alpha}}{(m_t - Z_{\dot w})V} \qquad f_\delta = \frac{QSC_{L\delta}}{(m_t - Z_{\dot w})V}$$

$$m_\alpha = \frac{QScC_{m\alpha} + K}{I_y - M_{\dot q}} \qquad m_\delta = \frac{QScC_{m\delta}}{I_y - M_{\dot q}}$$

$$m_{\dot\alpha} = \frac{QSc^2C_{m\dot\alpha}}{2V(I_y - M_{\dot q})} \qquad m_q = \frac{QSc^2C_{mq}}{2V(I_y - M_{\dot q})}$$

In Fig.1, the control loops between $\dot\gamma_c^p$ to $\dot\gamma_p$ and a_c^p to a^p are called as the "rate loop" and the "acceleration loop", respectively. The rate loop transfer function is given as follows.
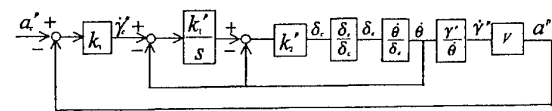
Fig.1 Rate and acceleration loops

$$f_r^P(s) = \frac{\dot{\gamma}^P(s)}{\dot{\gamma}_c^P(s)}$$

$$= \frac{k_1^P k_2^P C_1 (1 + b_1 s + b_2 s^2)}{s(1 + a_1 s + a_2 s^2) + k_2^P C_1 (1 + \tau_\theta s)(s + k_1^P)}$$

$$= \frac{1 + b_1 s + b_2 s^2}{\left[1 + (2\xi_r / \omega_r)s + s^2 / \omega_r^2\right]} \qquad (1)$$

By allocating the three poles of the Eq.(1) appropriately, we can determine the values of k_1^P and k_2^P. The acceleration loop transfer function is given as follows.

$$f_a^P(s) = \frac{a^P(s)}{a_c^P(s)} = \frac{f_r^P(s)}{1/(k_3^P V) + f_r^P(s)} \qquad (2)$$

The denominator of Eq.(2) also has three poles, and we can determine the value of k_3^P so that these poles are allocated appropriately.

3.NORMAL VELOCITY AND ALTITUDE LOOPS

Figure 2 shows the pitch normal velocity and altitude loops. Once the acceleration loop $f_a^P(s)$ is designed, we can easily determine the values of k_{vh} and k_h so that each loop has proper characteristics. The yaw (lateral) loop is designed in the same way, except that there is no recovery moment by the buoyance. Figures 3 and 4 show the resultant pitch and yaw control loops, where the thrust moment cancellation loop is added in the pitch loop. All of these gain parameters are determined as functions of the total velocity V, that is, for the pitch loop, (V =9m/s - 30m/s) and the yaw loop, (V =1m/s - 30m/s). The pitch control loop is employed only for the velocity of greater than 10m/s, as the elevator becomes invalid because of the recovery moment by buoyance when V is less than 8m/s.

4.FORWARD VELOCITY CONTROL LOOP

Figure 5 shows the forward velocity control loop, which is a bang bang type controller with histereses.

5.BUOYANCY CONTROL

In order to sustain the airship structure, the pressure difference between inside and outside the airship must be maintained between 20mmAq - 100mmAq. Within this limitation, the airship buoyance can be controlled by taking in or exhausting the air. As the operation is closely related to the thermal environment, and we can't process it only from the altitude control viewpoint, in this paper, only two cases are considered, that is,

(a) There is no operation about the air control in the airship.

(b) The air in the airship is controlled so that the buoyance is balanced with the gravity force. Nominally, the buoyance is balanced with the gravity force at the altitude of 4000m, therefore in case (a), as the buoyance decreases with an increased altitude, therefore the buoyance acts as the recovery force to maintain the airship at the nominal altitude.

6.SIMULATION RESULTS

Figures 6-8 show step responses for the pitch acceleration loop, velocity loop, and position (altitude) loop, respectively. In order to show the loop characteristics clearly, the buoyance is controlled following to (b) case in the preceding section. Because of the recovery moment by the buoyance, the step acceleration command produces a steady rate of climb, and other two loops show good performances. Figures 9-11 show step responses for the yaw acceleration loop, velocity loop, and position loop, respectively. All of these responses show good performances. Figures 12-17 show simulation examples for the position keeping mode. The airship is cruising with the velocity of 5m/s around the origin of the graph with the radius of 200m. In Fig.12, the guidance is conducted only by
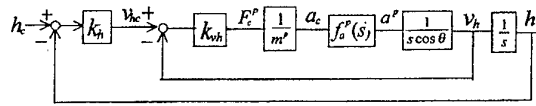
Fig.2 Normal velocity and altitude loops
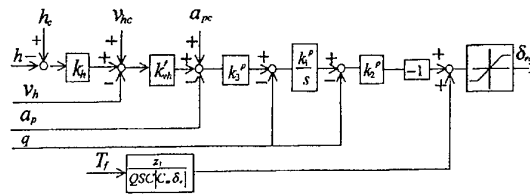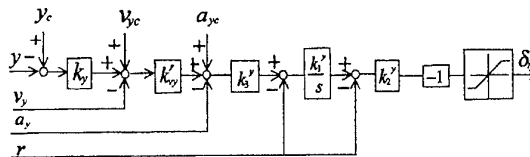

Fig.3 Pitch control loop
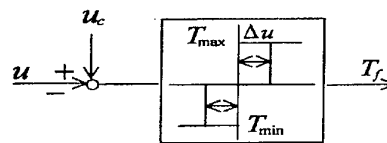

Fig.4 Yaw control loop

Fig.5 Velocity control loop

the acceleration command without any feedback, while in Fig. 13, the guidance is conducted by the acceleration command with the position and velocity feedback loop. Figures 14 and 15 show the cases corresponding to Figs 12 and 13, where there is a wind of 2m/s which is blowing to positive x direction. These results show good performance of the designed control loops. Figures 16 and 17 show the velocity and the altitude histories corresponding to the case of Fig. 15.

7.CONCLUSIONS

The summary of the study is as follows.
1. Because of the buoyance recovery moment, the longitudinal control system by the elevator is employed only at the high velocity of more than 10m/s. Therefore, the altitude should be controlled with the combination of buoyancy control system.
2. The lateral control can be successfully implemented by the rudder throughout the velocity range of 1m/s - 30m/s.
3. The step responses for acceleration, velocity, and position commands showed good performances for both pitch and yaw control loops.
4. Position keeping simulations are conducted, which show good performances.
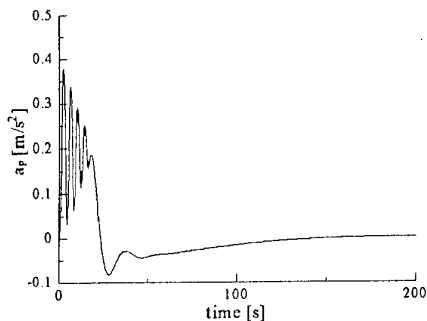
Fig.6 Pitch acceleration loop
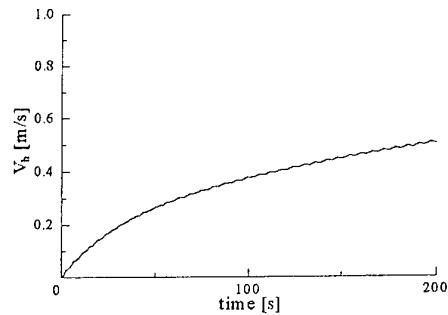
Fig.7 Pitch velocity loop
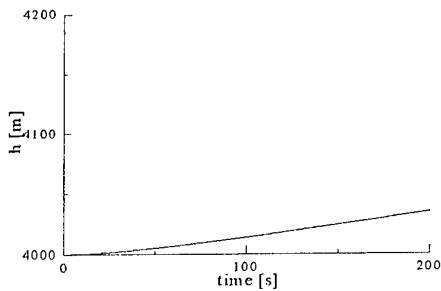
Fig.8 Pitch position (altitude) loop
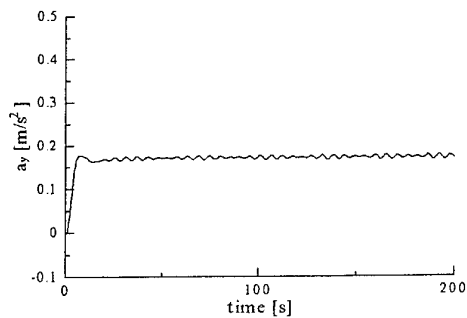
Fig.9 Yaw acceleration loop
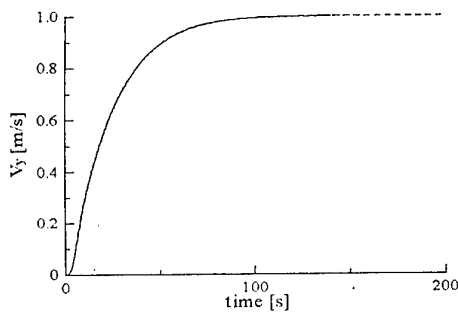
Fig.10 Yaw velocity loop
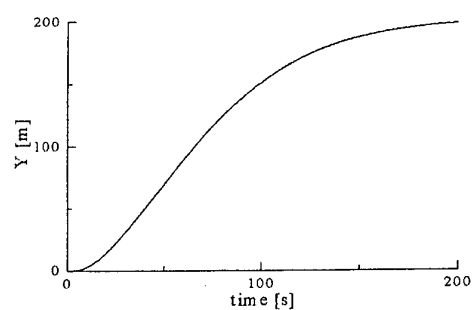
Fig.11 Yaw position loop
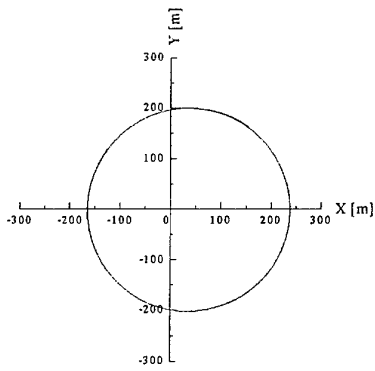
Fig.12 Position keeping without feedback
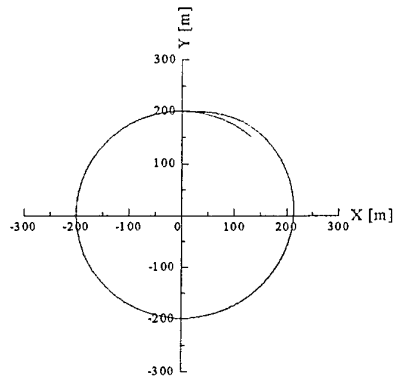
Fig.13 Position keeping with feedback
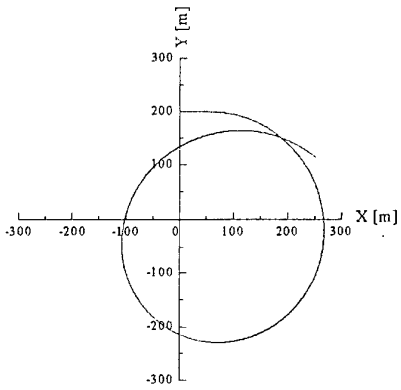
Fig.14 Position keeping without feedback
(with a wind)
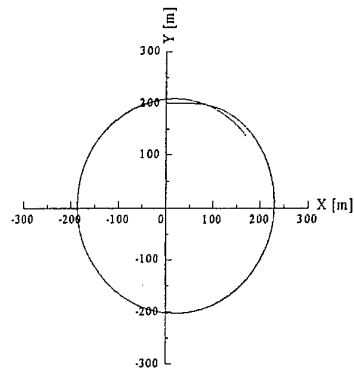
Fig.15 Position keeping with feedback
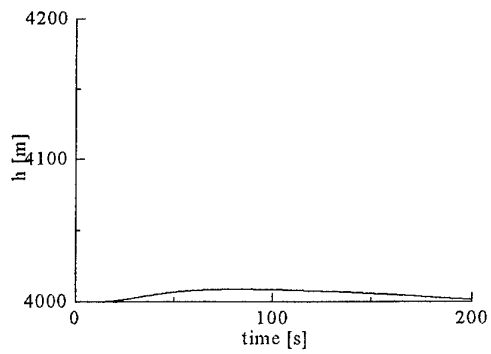(with a wind)
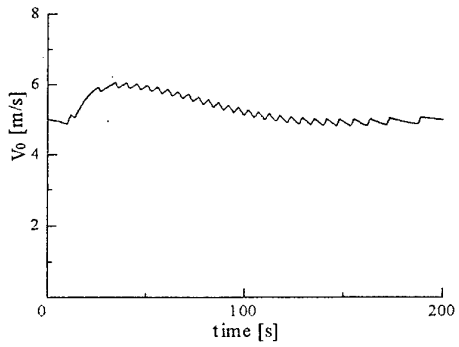
Fig.16 Velocity history in Fig.15

Fig.17 Altitude history in Fig.15

Positioning Accuracy of the Laser Tracking System for Flight Testing

Hamaki INOKUCHI* and Takeshi FUJIWARA**

National Aerospace Laboratory of Japan, 6-13-1 Osawa Mitaka-shi Tokyo 181-0015

Key words: Flight Testing, Laser Tracker, Positioning Accuracy

ABSTRACT

The laser tracking system[1,2] (LT) is a ground equipment for the flight path measurement of aircraft. The positioning accuracy of the LT was evaluated by a high-precise GPS navigation system[3] in flight experiments. The standard deviation and bias of the measured value by LT are approximately 0.6 to 5 meters and 0.7 to 4 meters, respectively. However, they depend on the slant range and meteorological condition. The availability of the LT is inferior to GPS navigation system because the tracking is sometimes impossible by the obstruction.

1. INTRODUCTION

In National Aerospace Laboratory of Japan, a laser tracking system (LT) as a ground tracking system for the flight path measurement of aircraft was developed in 1995. The LT is an equipment to measure Slant Range (SR), Azimuth (AZ) and Elevation (EL) to a target using laser while performing automatic tracking, and it is perfectly separate with onboard navigation and measurement system as a ground equipment. It had already been utilized in flight experiments such as the ALFLEX[4] and the standard flight path for evaluating positioning accuracy of the other system was derived. However, it was not possible to carry out the sufficient inspection as far as the positioning accuracy except for measuring stationary points in spite of fixing the positioning accuracy in the specification in those days. Recently, positioning accuracy of the LT was evaluated by the flight experiment since high-precise navigation and measurement system using the GPS had been developed. The evaluation of the positioning accuracy was carried out using three kinds of flight patterns in 2000. The each measurement error has been confirmed experimentally. The evaluated results are described.

2. LASER TRACKING SYSTEM

The appearance of the LT is shown in Fig. 1. It suitable for tracking a small flying object or the case in which the independence from the onboard equipment is required, because any power supply is not required in the target. The installation only a small retro-reflector on the target is required. The basic specifications of the LT are shown in Table 1.
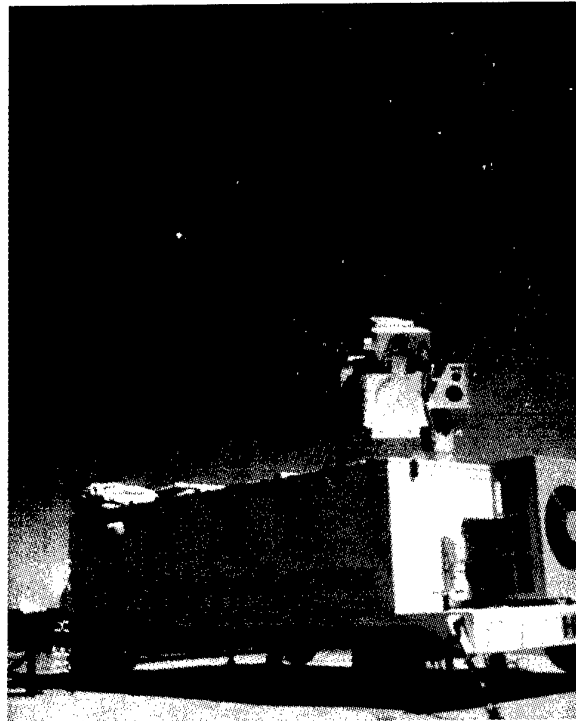

Fig. 1 Laser Tracking System (LT)

Table 1 Specifications of the LT

Measuring Range		300 m ～ 40 km
Accuracy	AZ, EL	20 s (1 σ)≒0.1 mrad
	SR	0.3 m (1 σ)
	Time	1 μ s
Data Sampling		60 Hz
Laser	Type	Nd-YAG
	Wave length	0.532 μ m
	Power	20 mJ/pulse

---

* Senior Researcher, Flight Systems Research Center
** Researcher, Flight Systems Research Center

The measurement principle of the LT is explained as shown in Fig.2. A retro-reflector has been installed on the nose underside of the experimental aircraft. The SR can be obtained at the time when the laser beam shuttles between on the target and the LT. The AZ and EL angle are measured by the image processing of the received laser light, and simultaneously, the automatic tracking is executed.
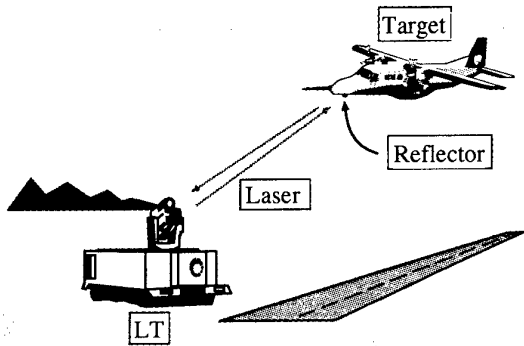

Fig. 2 Positioning Principle

The LT is installed on the position beforehand surveyed, before it is used. The star calibration is conducted after the installation and the calibration of angle measurement is carried out. Next, the range offset is measured using the fixed targets. After the tracking work, compensation of laser delay by atmosphere is carried out on the basis of the meteorological observation, and the more accurate positioning data is obtained. The change of the level is monitored by two levels every tracking work.

3. FLIGHT TESTING

The flight testing for evaluation of the LT was carried out at the Taiki Multipurpose Aviation Park in Hokkaido. The arrangement of the experiment facilities and definition of the coordinates are shown in Fig. 3. The LT was stationed in the side of the runway and three fixed targets for the collimation were installed. The woods have blindfolded some directions from the LT.
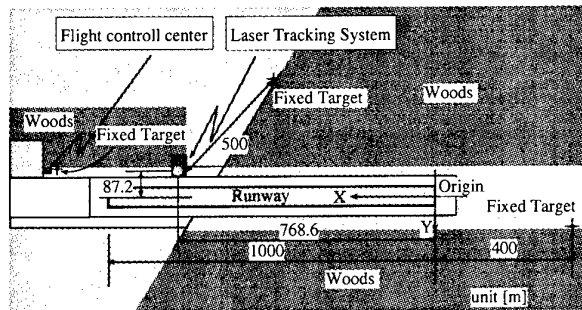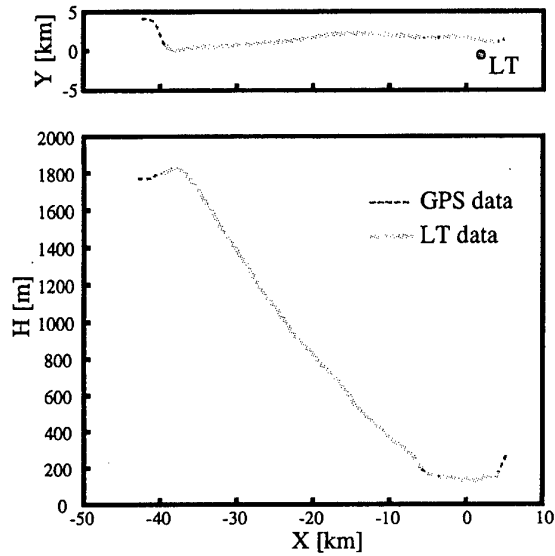

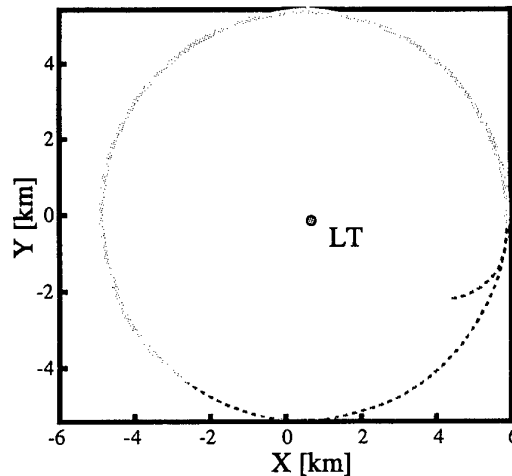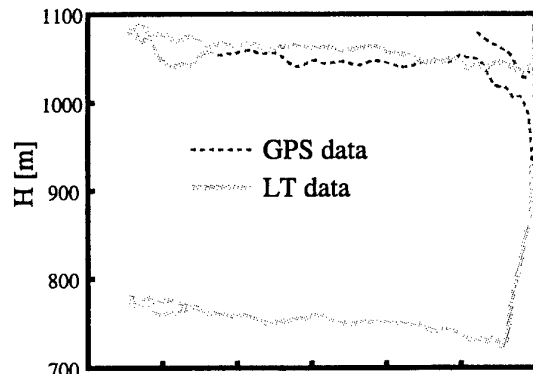Fig. 3 Arrangement

Fig.4 Flight Case 1 (SR)

Fig.5 Flight Case 2 (AZ)

The data by the GPS navigation system with an INS can be utilized as a standard of the positioning and that it measures the position at the accuracy of several centimeters. Following three experimental flight cases were conducted for the evaluation of the LT. The H in the figures is altitude of the target and LT is the installation position of the LT.

1) Flight case 1: Straight approach (see Fig. 4)

The influence of the SR was examined by the change of the SR.

2) Flight case 2: Orbital flight (see Fig. 5)

The influence of the AZ was examined by the change of the AZ.

3) Flight case 3: Cylindrical flight (see Fig. 6)

The influence of the EL was examined by the change of the EL.
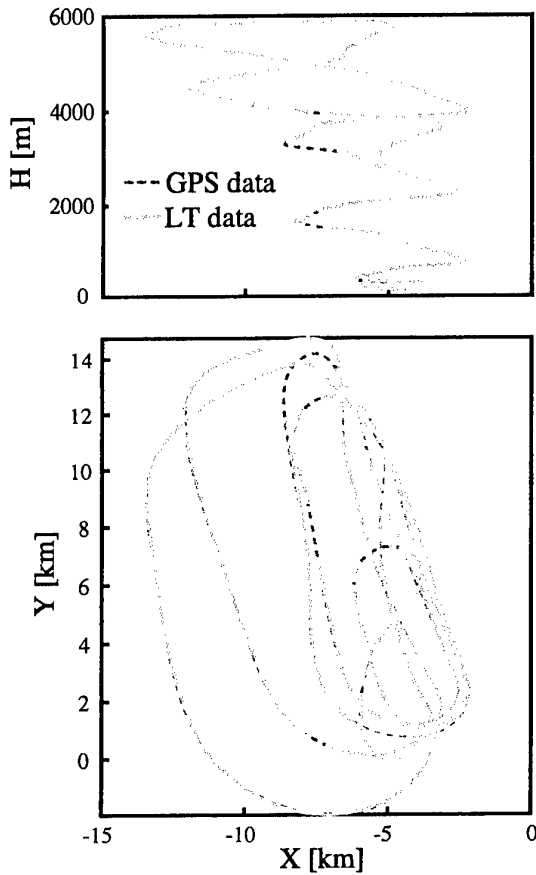
Fig.6 Flight Case 3 (EL)

The parts of the only broken line are the region which the target could not be tracked by the LT. The positioning data of LT and GPS agrees with each other in the other parts. As shown in Fig. 4, the measuring range satisfies the specification. As shown in Fig. 5, the tracking is not possible for the region obstructed in the woods. As shown in Fig. 6, the SR decreases, as the EL increases in case of this flight pattern.

4. POSITIONING ACCURACY

The influence of the SR on positioning accuracy is shown in Fig. 7. The dispersion of the measured value increases, as the SR increases, because the influence of the atmosphere as a long distance is easy to be suffered. There is the abnormality in the characteristic of the AZ error since it changes periodically. The deviation of the SR increases, as the SR increases. Temperature, humidity and atmospheric pressure at a great distance are different from those in the vicinity of the LT, and the laser velocity changes in proportion to the meteorological condition. Thus, it is considered that the deviation increases.
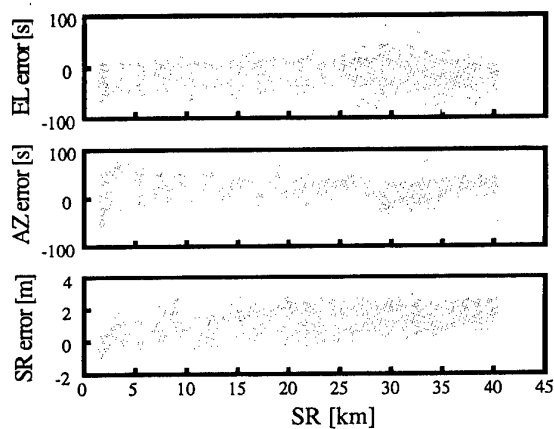

Fig. 7 Positioning Accuracy (SR)

The influence of the AZ on positioning accuracy is shown in Fig. 8. If the base of the LT tilts, the error of the EL is sure to become a sine curve. However, clarified sine curve is not observed in this figure. There is a stepped change in the characteristic of the EL error in spite of a sine curve. It is considered that the characteristic of the AZ encoder is abnormal since the AZ error fluctuates periodically concerning the AZ. The abnormality of the AZ error in case 1 seems to be same problem by the slight change of the AZ.

The influence of the EL on positioning accuracy is shown in Fig. 9. The dispersion of the measured value increases by the atmosphere of the low altitude, as the EL decreases. It is not so extreme change. The deviation of the SR decreases, as the EL increases. It is considered that the influence of the SR increases, as the EL decreases in case of this flight pattern. There is the abnormality in the characteristic of the EL encoder since the EL error fluctuates periodically concerning

the EL. The abnormality of the EL error in case 2 seems to be same problem by the slight change of the EL.
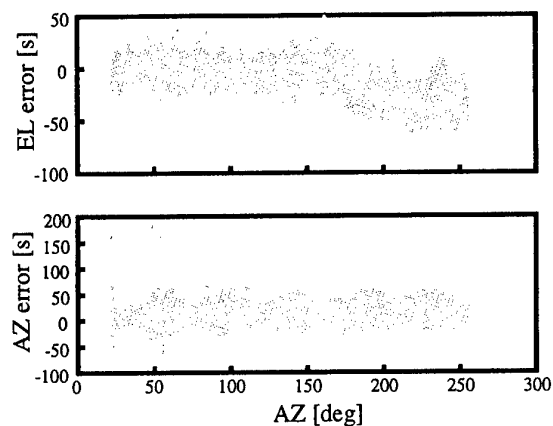
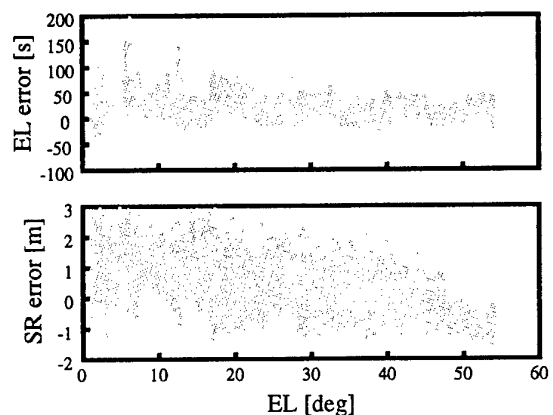

Fig. 8 Positioning Accuracy (AZ)

Fig.9 Positioning Accuracy (EL)

The standard deviation (SD) and bias of measured error by the LT in each case are shown in Table. 2. It appears that the practice accuracy in the flight experiment is inferior to the specifications. It is already established that calibration accuracy of the star calibration of the LT is approximately 12 arc seconds. The calibration error becomes a cause of the angle measurement bias.

Table 2 Positioning Accuracy

Case	SR [m]		AZ [s]		EL [s]	
	SD	bias	SD	bias	SD	bias
1 (SR)	0.66	0.82	16.0	21.4	14.2	-14.5
2 (AZ)	0.33	0.91	16.6	13.7	16.6	-11.2
3 (EL)	0.71	0.46	23.7	10.9	22.1	-1.7
Average	0.57	0.73	18.8	15.3	17.6	-9.1

According to the above, it is possible to show positioning accuracy of the LT by angle measurement accuracy and ranging accuracy. However, the positioning accuracy is defined in following equations since the distance accuracy is important in actual use. The results are shown in Table 3. Judging from the results of the experiment, the standard deviation of the measured value is approximately 0.6 to 5 meters and the bias of the measured value is approximately 0.7 to 4 meters. However, they depend on the SR and meteorological condition.

$$Accracy_{SD} = \{SR_{SD}^2 + (AZ_{SD} \times SR)^2 + (EL_{SD} \times SR)^2\}^{1/2}.$$
$$Accuracy_{bias} = \{SR_{bias}^2 + (AZ_{bias} \times SR)^2 + (EL_{bias} \times SR)^2\}^{1/2}.$$

Table 3 Positioning Accuracy

SR (km)		1	3	10	40
Accuracy	SD	0.58	0.68	1.37	5.02
(m)	bias	0.74	0.77	1.13	3.53

5. CONCLUSIONS

The following conclusions have been confirmed experimentally.

1) The standard deviation and bias of the measured value by LT are approximately 0.6 to 5 meters and 0.7 to 4 meters, respectively. However, they depend on the SR, meteorological condition and calibration accuracy.

2) The angle measurement accuracy and ranging accuracy of the LT are inferior to the specifications. However, they depend on SR, meteorological condition and calibration accuracy.

3) The availability of the LT is inferior to GPS navigation system because sometimes tracking of the target is impossible according to the position.

4) The deviation of the positioning error increases, as the SR increases. It depends on meteorological condition.

5) There is no extreme degradation of accuracy even in the low EL angle.

6) There is the abnormality in the characteristic of the angle measurement encoders.

REFERENCES

1. Ono, T. et al, "Development of a Laser Tracker and its Evaluation by Flight Testing" Technical Report of National Aerospace Laboratory TR-1331, 1997.

2. Kitagawa, K. et al. "Positioning Accuracy of the Laser Tracking System for ALFLEX" Proceedings of the ALFLEX Symposium, pp.133-138, 1997.

3. Tsujii, T. et al, "Development of Kinematic GPS Software, KINGS, and Flight Test Evaluation" Technical Report of National Aerospace Laboratory TR-1357T, 1998.

4. HOPE team ALFLEX Sub Group. "Proceedings of the ALFLEX Symposium" Special Publication of National Aerospace Laboratory SP-39T, 1998.

ISL1   # Development of KTX-1 and its Spin Characteristics

Taehwan Cho

Professor, Gyeongsang National University, Jinju, Korea

Abstract

Development of KTX-1 is reviewed and introduced. Technical approach to solve spin problem of KTX-1 is presented. It was shown that UMRC method, vertical wind tunnel test and model airplane simulation can give quite reliable spin prediction. Real flight test shows good spin characteristics predicted by analysis

1. Introduction

With a few exceptions, developing countries which tried to build up their own aerospace industries seem to have a model of a developing stages(Ref. 1). They usually started with a depot maintenance of their airplanes which is imported from other countries. License production usually followed with additional cost. And as their industrial skills level up, they started part production and localization. Participating international co-development program or independent development program can be the next step. Korea followed these procedure(Fig. 1). After Korean War, starting with a depot maintenance of L-19 reconnaissance airplane in 1955, Korean aerospace industry continued only on maintenance of military aircraft such as C-46, C-54 transport airplanes until the early part of 1970s. But due to the intense national defense environment, it was necessary to increase the number of the military aircraft and to establish national aerospace industry utilizing this demand, Korea started license production of small helicopter, MD-500, with Hughs in the middle of 1970s, and start license production of fighter, F-5, with Northrop in early 1980s. In 1980s, with the assembly and license production of helicopter and fighter, jet engines for that airplanes were assembled and license produced and by contract some airframe parts were fabricated and exported.

The efforts of design and developing Korean ingenious airplane was attempted several times during this period. But was not successful enough for full production. The first true Korean ingenious airplane development was attempted by ADD and Air Force and Daewoo Heavy Industry and that is KTX-1 program, the basic trainer aircraft developmental program for Korean Air Force. Later, the KTX-2 program, an advanced jet trainer developmental program was created in collaboration with Lockheed Aircraft company of the U.S.A. and became a key developmental program for Korean Aerospace Industry. Korean Aerospace Industry had a big organizational restructuring during this period. Initially there were four aerospace companies competing each other, which is Korean Air, Samsung Aerospace Incorporation, Daewoo Heavy Industry and Hyundai Aerospace Incorporation. Out of these four, three companies excluding Korean Air formed a new one big aerospace company which is Korean Aerospace Incorporation.
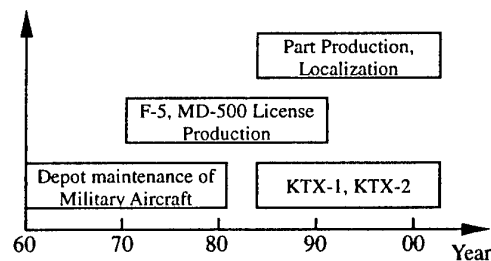

Fig. 1 Korean Aerospace Industry Status

2. Development Schedule of KTX-1

In 1988, The KTX-1 program was granted from the Ministry of National Defense. 4 years was required to build two airplanes designated as KTX-1 No. 1 and No. 2. And they made a successful first flight in Dec. 1991. The airplane was equipped with turboprop engine, 550 hp, manufactured by Pratt & Whitney Canada. Although the development and the flight

looked quite successful at that time, there was a big arguments about the engine power and the flight speed. There was an opinion in the MND which is responsible for funding this program that this airplane should be equipped with stronger engine, say 900 to 1000 hp, that it can be used to train student pilots for next 20 to 30 years. The decision was made after many lengthy discussions and a new development program was issued according to that requirements. This program has 6 years span from 1993 to 1998 consists of 4 years for Advanced Development(for Demonstration and Validation) and 2 years for Full Scale Development(Fig. 2).

‘93	‘94	‘95	‘96	‘97	‘98	‘99	‘00	‘01	‘02
	A. D.			F.S.D		Production			
						Forward Air Controller			
	ITPT	ΦΦPP	Pοχ Pελεασε	Σελεχτιον V	Προδυχτιο				
		#03/04		Παρτ	ΛΑππροδαλ	#1 A/X			
Design					Προδυχτιον Τζστ				
	Manuf								
		Assem	DamVdTest	Mod	FSD Test				
				Des Man Ass Test					
					Dsign&Manuf	T&E & Ballistic Table			
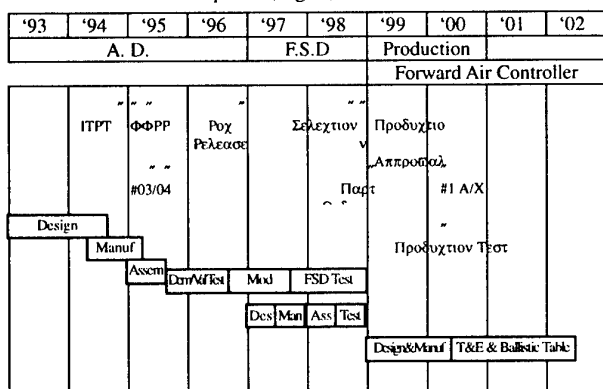
Fig. 2   Overview of KTX-1 Development Schedule

The Air Force issued new updated R.O.C.(Required Operational Capability). The quantitative R.O.C.s are shown in (Fig. 3) along with the final flight test results.

Performance	Requirements	Test Results
Max. Level Speed (kts)	250 or over	256
Stall Speed (kts)	72 or less	70
Climb Rate (fpm)	3,000 or over	3,400
Service Ceiling (ft)	30,000 or over	38,000
TO/LD Distance (ft)	1,500/1,500 or less	1,150 / 1,170
Endurance (hr)	2.5 or over	3.0

Fig. 3   Required Operational Capabilities

The design team were able to find a suitable engine which has 950 hp, manufactured by same company, and started to redesign the airplane based on the No. 1 airplane design and flight test data. The nose section was enlarged to adopt the large engine and to counter the lateral and directional destabilizing effects due to the stronger propeller downstream and the elongated front fuselage, aileron was enlarged and the

rear fuselage shape was changed after painful analysis and discussions. The KTX-1 No. 3 airplane, which is the first airplane equipped with 950 hp engine, made a first flight on Aug. 10th 1995. The result was not a successful one. The test pilots onboard were not satisfied with the flying qualities of the airplane at all. It was pointed out that the lateral-directional stability was not satisfactory so that this airplane was not suitable for training inexperienced student pilots. The analysis from the scratch revealed that the aircraft needed to be redesigned several places. For stability, wing dihedral angle and forward fuselage should be changed. For better spin characteristics and flying performances the wing and the horizontal tail should be changed. It was decided to change airplane No. 3 only on wing dihedral angle and horizontal tail to show an intermediate output in a short time and designate it to be airplane No. 3A and let airplane No. 4 to be changed completely as intended and designated No. 4A(Ref. 2). That decision was a success. The first flight of the airplane No. 3A was made in November 1995 and it shows a good flying qualities as predicted. Airplane No. 4A was prepared as scheduled and made a successful first flight in May 1996. With this result the Advanced development phase could be terminated successfully and the Full Scale Development began from 1997. During these 2 years one more airplane, airplane No. 5 was assembled and made a successful first flight in March 1998. No. 5 airplane had the same configuration with No. 4A airplane except the enlarged rear fuselage cross section to make it structurally stronger(Fig. 4). After finishing all the requirements, the KTX-1 is renamed as KT-1, a true basic trainer for Korean Air Force and now is in production.
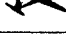
A/C No.	F.F	Major Configuration Change	
#01/#02	’91.12.12	Basic Configuration (550 hp Engine)	
#03	’95. 8.11	950 hp Engine	
#03A	’95.11.22	Increase Wing Dihedral Angle	
#04A	’96. 5. 9	Increase Wing Area Reduce Forward Fuse. Length Move H/T backward	
#05	’98. 3.16	Increase Rear Fuselage Cross Section Area	

Fig.4 Configuration Changes of KTX-1 during Development
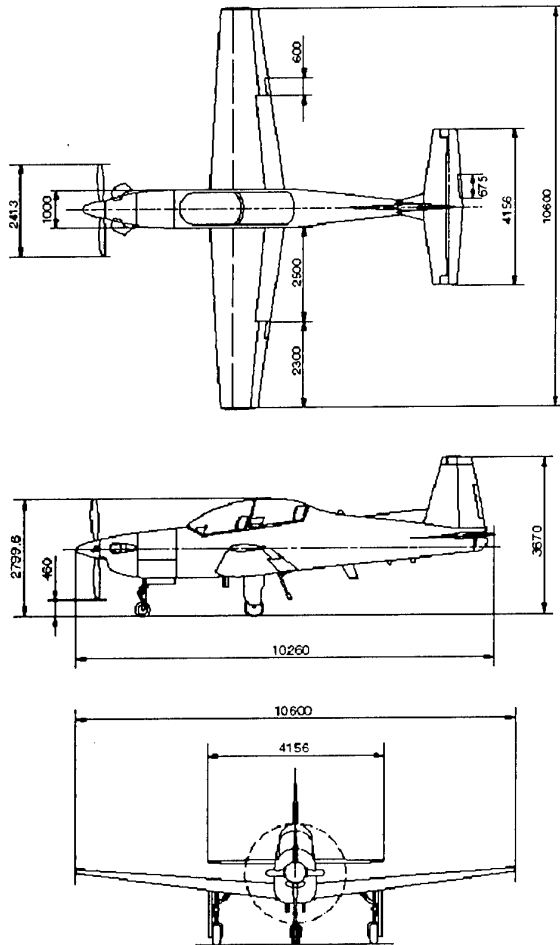
3. Dimensions and Performances

Fig. 5 Dimensions of KTX-1 Aircraft

| Max. Cruise Speed	255 kts
Engine Power	950 hp
Max. Altitude	36,400 ft
Empty Weight	4,210 lbs
Max. Take-off Weight	5,600 lbs
G Limit	+7.0 ~ -3.5
Take-off/Landing Distance	840 ft / 1,340 ft
Design Spec.	MIL Spec.
Operation Temperature	-25°C ~ +45°C

Fig. 6 Performance of KTX-1

Fig. 5 and Fig. 6 shows dimensions and performances of KTX-1(Ref. 3). KTX-1 airframe is designed as semi monocoque structure. Fuselage is consisted of 3 parts, forward fuselage, center fuselage, rear fuselage, forward fuselage

contains engine, nose landing gear, fire wall, and battery, center fuselage contains cockpit, electronic equipment and wing attachment. Rear fuselage includes horizontal/vertical stabilizer, elevator and rudder. Engine of the KTX-1 is PT6A-62 turboprop engine, 950 hp, made by Pratt & Whittney Canada. Engine is attached to fuselage using EMS(Engine Mounting System). Landing Gear System is consisted of main landing gear, nose landing gear, steering system, wheel, tire and rear door. Landing gear is operated by a hydraulic system, and steering angle is ± 22°. Control system is consisted of a main mechanical control system which controls aileron, rudder and elevator and auxiliary control system which controls trim tabs of aileron, rudder and elevator. Fuel system consists of fuel tank, fuel transport system, fuel indicating system. Equipped with acrobatic tank, KTX-1 can maintain 30 sec. inverted flight. Electric system consists of a power supply system and power distribution system. Main power system supplies 9kw, 300A electricity and supplies to each system through generator control unit. Ejection system consists of a front ejection seat (MK MR 16C F-3) and rear ejection seat (MK KL 16CF-4).

4. Technical approach for KTX-1 Spin problem

Stall of an airfoil at high angle of attack is a well known aerodynamic phenomena. Flow around an airfoil usually remains attached when it is in low angle of attack. As angle of attack is increased to get more lift, the flow in the trailing portion of upper surface of the airfoil starts to separate and gradually progress forward with angle of attack due to pressure distribution(Ref. 4). As the angle of attack is increased further, say 13 to 16 degrees, then the gradual progressing of the separated area suddenly jumps to whole upper surface separation(Fig. 7). This angle of attack is called a stall angle of attack and is characterized by a sharp drop of lift and drastic increase of drag. Moreover downstream of the separation point usually consists of a turbulent wake like flow which is very similar to the downstream flow of a bluff body. One can not maintain normal flight with this situation very long with a

conventional airplane, because at this situation the aerodynamic force produced by control surfaces does not respond as designed that a pilot can not control his airplane to his intention.
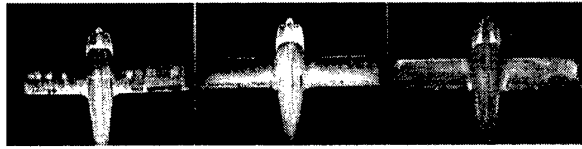
$\alpha = 0°$ $\alpha = 8°$

$\alpha = 16°$

Fig. 7   Flow Pattern at Different Angle of Attack

So many airplanes are equipped with a stall warning device which tells pilots that his airplane is approaching stall angle of attack well before the airplane gets into a dangerous flight envelop.
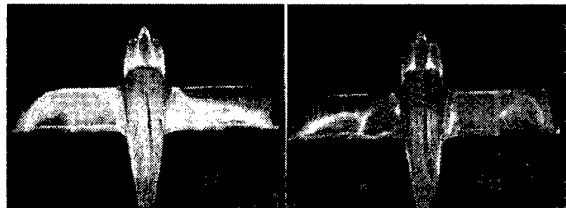
$\alpha = 13°$ $\alpha = 14°$

Fig. 8   Asymmetric Flow Separation

The flow separation phenomena on the wing surface is very sensitive that any small external disturbances can cause a large differences in the shape of separated flow. In fact at a high angle of attack very close to stall, a small differences like propeller wakes or asymmetry of aircraft configuration, or a gust can cause a considerable flow difference between right and left wing surfaces of the airplane(Fig. 8). That means, for example, the right wing still can have considerable attached flow on the wing surface while left wing can completely be stalled. If that happens the lift of the left wing drops sharply and drag increases drastically while right wing still maintain high lift and low drag. The aircraft will respond accordingly. As the left wing lift decreases it will move downward and as drag increases it will be pulled back. This results in a coupled motion of rolling and yawing of an airplane which will

eventually be developed into a full spinning motion along a vertical direction(Ref. 5).

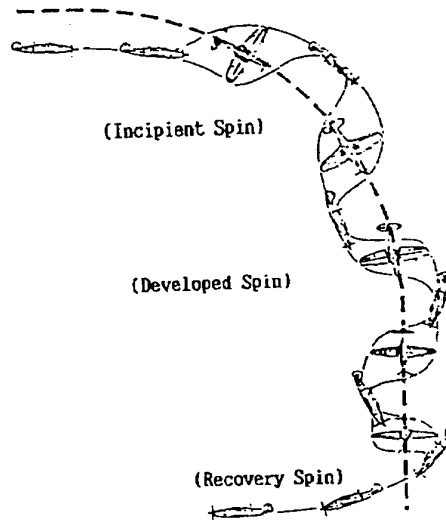
(Incipient Spin)

(Developed Spin)

(Recovery Spin)

Fig. 9   Spin Motion Sequence

The stages of spin is usually divided into three stages which is incipient spin, developed spin and recovery spin(Fig.9)(Ref. 6). Incipient spin stage is initial stage of spinning motion, which usually takes 4 ~ 6 seconds and about 2 rotations. Developed spin stage is a stage when a stable spinning motion is maintained and there exists a equilibrium force relations between aerodynamic moment and moment due to inertial forces. In this stage, the airplane maintains relatively constant angle of attack and revolutionary motion. Recovery stage is a stage when a spinning motion is interrupted by breaking equilibrated force relation between aerodynamic moment and moment of inertia through aerodynamic control input or other methods. The Korean Air Force wanted the KTX-1 to have smooth spin characteristics and simple control input to get in and out of spinning motion. For the training of student the spin characteristics is closely related to the mass distribution, control surface location and wing aerodynamics. The original KTX-1 wing adopted modified NACA 63_2-215 airfoil for higher maximum lift coefficient which has 1.77 at angle of attack 17° compared to the original NACA 63_2-215 airfoil maximum lift coefficient 1.48 at angle of attack 14°(Ref. 7).

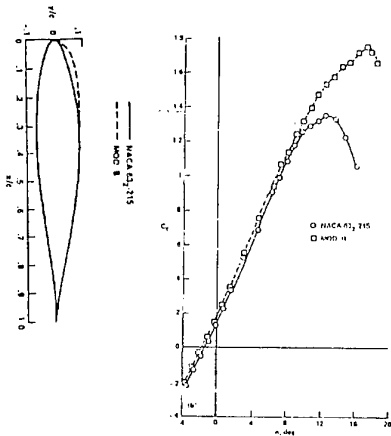The initial Spin Test result showed good entry and recovery

Fig. 10   NACA 63$_2$-215 Configuration & Characteristics

from spin but the measurement and pilot comment revealed it had hesitant, vibrational spin mode. The main contribution of this rough spin mode is thought to be the main wing stall characteristics. During spin, if one wing stalls completely and the other wing does not, the airplane is supposed to have a smooth spinning motion. If the stalled wing's flow separation pattern changes lot during spin, the airplane is going to have a rough spinning motion. It was speculated that the modified airfoil which had higher stall angle of attack is more susceptible to have flow separation pattern changes than the original airfoil. So it was decided to change the airfoil to the original NACA 63$_2$-215 airfoil along with the wing size and the tail configuration.

Prediction of spin recovery characteristics was not an easy task and there was no reliable simple method to use. Four different methods and steps were used to ensure good spin recovery characteristics for the KTX-1.(Fig.11)(Ref. 8). The first one is semi-empirical prediction method which is called URMC(unbalanced rolling moment coefficient)method. This method deals with three(wing, body, rudder)rolling moment and determine whether the sum of this three satisfies the spin recovery criteria(Fig.12). According to the analysis the wing area was increased and horizontal tail moved backward to

ensure unshielded area of the rudder and to increase tail volume. It was predicted that new configuration had better recovery characteristics than the KTX-1 NO.1 airplane.

| Method	Analysis and Result	
URMC(Unbalanced Rolling Moment Power Factor Method)	- Predict Good Recovery Characteristics - Good Agreement with Flight Test Result showing Good Recovery with Control Free Condition	ADD
Vertical wind Tunnel test	- Static Test, Rotary Balance Test, Forced Oscillation Test, etc - Build Aerodynamic Data Base for Predicting Aircraft Flying Performances	TsAGI Russia
Spin Mode Analysis	- Predict Spin Mode including Angle of Attack and Rotation rate, utilizing Vertical Wind Tunnel Test Data - Good Agreement with Flight Test Data	ADD TsAGI
Scaled Model airplane Flight test	- Model Flight Test to Confirm Safety and Recovery Characteristics prior to Real Flight Test - Analysis of Control Surface Effectiveness for Starting and Recovering from Spin	ADD INHA University

Fig. 11   Technical Approach for KTX-1 Spin Study
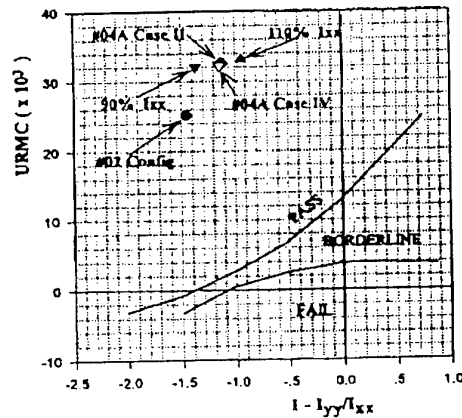
Fig. 12   Unbalanced Rolling Moment Coefficient Method

The second one is vertical wind tunnel test to get aerodynamic data for spin mode analysis(Fig.13). Wind tunnel of TSAGI in Russia was used and static test., rotary balance test and forced oscillation test gave an ample aerodynamic date base. This data was an essential basis for predicting spin mode including angle of attack, rotation rate and etc.

The third one is scaled model flight test. A team of Inha university was involved and made scaled model. Dynamic similarity and power similarity were carefully studied and made a considerable number of flight test.

The final real airplane flight test shows spin characteristics of relaxed motion and with very little oscillations for both left and

right spin. Rotation stop instantly after applying recovery

Test condition Test articles	Test Condition	Test No
Static Test	α = −90 ~ +90 β = −20 ~ +20 V = 25 m/sec R_N = 0.272 × 10^6	58
Rotary Balance Test	α = −90 ~ +90 β = −20 ~ +20 V = 25 m/sec R_N = 0.272 × 10^6	215
Forced Oscillation Test	Small Amp. Pitch/roll/yaw Large Amp. Pitch/yaw	72
	Total	345

Fig. 13   Vertical Wind Tunnel Test

control action. And automatic recovery characteristics were shown when hands off from control for both left and right spin. All these motions were shown to have repeatability and agreed well with spin mode analysis. Loss of altitude during spin is 5000ft for left spin, and 5500ft for right spin. Average loss of altitude per rotation is 500ft for both. For left spin roll rate, P = 80±20 deg/sec, pitch rate, Q = 10±15 deg/sec, yaw rate, R = 90 deg/sec(Fig. 14), and for right spin P = 115±10 deg/sec, Q = 20±5 deg/sec, R = 90 deg/sec(Fig. 15). Right spin looked steeper and showed stronger rolling moment than the left spin. This difference is thought to be due to propeller downs stream, gyroscopic effect of engine and asymmetric configuration of the airplane(Fig. 16).

In summary, through KTX-1 program an airplane which has very good spin characteristics is developed. Its operation is so easy that unexperienced student pilot can handle without much difficulty. At the same time an analysis method was confirmed to give good results with and vertical wind tunnel and model flight test was shown to be a very good method to accumulate data base for spin.

5. Conclusion

KTX-1 was successfully developed and now is in production. Around 80 airplanes will be delivered to the Korean Air Force as a basic trainer KT-1. Follow on program is already issued as XKO-1. which is to modify KTX-1 into Forward Air Controller aircraft. This modification includes

external store for armament and avionics systems. T-50

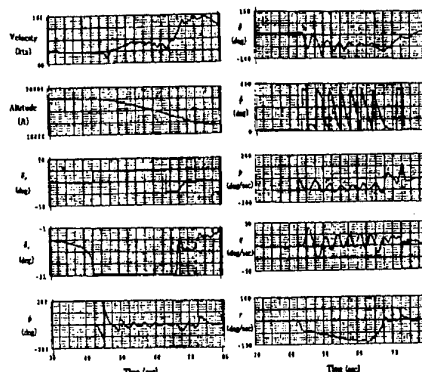● Left Normal Spin (6 Rotation)

Fig. 14   Flight Test Data(1)
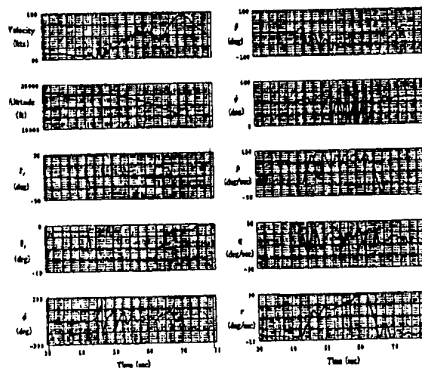
● Right Normal Spin (6 Revolution)

Fig. 15   Flight Test Data(2)

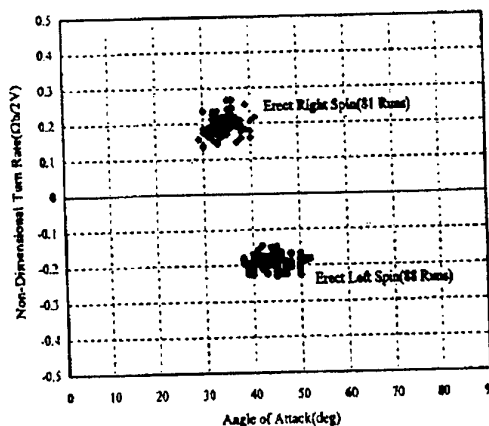● Comparison of Normal Spin Results

Fig. 16   Flight Test Data(3)

program, which was KTX-2, jet trainer is actively progressing

with the help of Lockheed Martin, U.S.A.

Through KTX-1 development program, Korea was able to get various experiences about airplane for the first time in history. During this period they were able to build various testing facilities such as structural test facility, wind tunnel, ground test facility and flight test facility. Though Korean industry is new in aerospace field, they can get further experiences through follow on programs such as T-50. Korea is now trying to absorb advanced aerospace technologies from abroad but I hope someday she can contribute to the world in this field.

References

1. "30 years of Korean Science and Technology ", MOST, 1997

2. "KTX-1 Design Improvement Report" J. LEE. S.Y.LEE. T. Cho. ASDC-501-960349. ADD.

3. "KTX-1 Airplane Flight Manual", K.T.O. 1T-KT1-1 ADD

4. "The Effect of Aspect Ratio on Oil Flow Patterns Observed on a Wing Beyond Stall", Winkelmann & Barlow, TR AE 79-4 University of Maryland, 1979

5. "Flight characteristics for High Angle of Attack (Stall/Spin)", Daeyeol Lee, Bulletin of the Institute for Aviation Management Research, Vol 8, 1991

6. "stall, spin and safety", Samy Mason, Mcraw-Hill series in Aviation

7. "Effects of upper surface modification on the Aerodynamic Characteristics of the NACA 63_2 - 215 Airfoil Section", NACA - TM- 78503. R.Hicks and E.Schairer, NASA   AMES. 1978

8. "A Report on The Spin Flight Test Results of KTX-1" D. Y. LEE and S. J. LEE, T. Cho.

ISL2

SIMULATION OF ROTOR FLOWFIELDS IN HOVER USING UNSTRUCTURED ADAPTIVE MESHES

Oh Joon Kwon [*] and Hee Jung Kang [†]

Korea Advanced Institute of Science and Technology
373-1 Kusong-Dong, Yusong-Gu, Taejon 305-701, Korea

Key Words: Helicopter, Hovering Rotor, Viscous Flow, Computational Fluid Dynamics, Unstructured Adaptive Mesh

ABSTRACT

Three-dimensional viscous flowfields around a helicopter rotor in hover are calculated by using an unstructured mesh methodology. The flow solver utilizes a cell-centered finite-volume scheme that is based on the Roe's flux-difference splitting and an implicit Jacobi/Gauss-Seidel time integration. The effect of turbulence is estimated by the Spalart-Allmaras one-equation model coupled with a wall function boundary condition. A solution-adaptive mesh refinement technique is adopted to capture the tip vortex. Calculations are performed for non-lifting and lifting rotor cases. Comparison of the inviscid and viscous results indicates that inclusion of viscosity significantly affects the surface pressure and the blade airloads for a lifting rotor at transonic tip speed. Good agreement is obtained between the numerical result and the experiment for both the blade loading and the tip vortex behavior.

1. INTRODUCTION

Accurate numerical simulation of the flowfield of helicopter rotors is one of the most complicated and challenging problems in the field of aerodynamics. In order to predict the performance of helicopter rotors, the numerical method must have a capability of accurately capturing the flow not only on the blade but also in the vortical wake generated from the blade tip, which significantly affects the overall rotor performance, vibration, and noise. Even though many researches have been successfully performed for hovering rotors using inviscid methods, the capability of handling viscosity is still a very desirable feature to have for the simulation of realistic flow mechanism such as tip vortex formation. It is particularly true to accurately simulate viscous-inviscid interactions involving shock-induced separation at transonic tip Mach numbers with relatively high collective pitch setting.

Numerical methods contain inherent numerical dissipation which depends on the local grid size and the order of spatial accuracy of the scheme. Accurate capturing of rotor wake requires several grid points inside the vortex core to prevent the tip vortex diffusion and to maintain its strength. An additional difficulty arises from the fact that the trajectory of the tip vortex is usually not known in advance. Within the structured grid topology, high-order spatially-accurate schemes, moving overset grids, and grid redistribution techniques have been adopted to remedy the difficulties.[1-3] In contrast, unstructured mesh methodology has a great flexibility of adding and deleting grid points at the local flow region of interest such as along the tip vortex trajectory. The grid density at far fields away from the blade can still be kept low to minimize the computer resource requirement. The first unstructured

mesh methodology applied to rotor flow computations was carried out by Strawn and Barth[4] using an explicit time integration and a finite-volume scheme. The unstructured mesh was obtained by dividing a regular structured grid into tetrahedra. The mesh was refined along the trace of the tip vortex which was experimentally pre-determined. The tip vortex structure was successfully captured up to 270 degrees of vortex age using more than 1.4 million tetrahedra at the finest adaptation level. Duque et al.[5] used overset structured/unstructured grids with two separate thin-layer Navier-Stokes and Euler flow solvers for each grid topology. Various adaptation indicators were implemented to properly distribute the grid points for the solution-adaptive mesh refinement. Dindar et al.[6] used an FEM method on unstructured meshes to locate the vortex core trajectory by introducing a critical theory based on the eigenvalues of the velocity-gradient tensor for mesh refinement. Kang and Kwon[7] showed that the tip vortex trajectory and its strength can be accurately captured through multi-level wake adaptations. The effect of wake adaptation on the tip vortex behavior and the overall rotor performance were well demonstrated with a modest number of cells on unstructured parallel flow solver.

Even though these unstructured mesh calculations were very successful in accurately predicting the aerodynamic performance and the tip vortex trajectory, calculations were mostly confined within inviscid flows so that viscous phenomena such as flow separation and shock-boundary layer interaction were not properly accounted for. In the present study, an attempt is made to numerically predict the performance of a hovering rotor using an unstructured mesh Navier-Stokes flow solver. The tip vortex trajectory is traced through a series of spatial mesh adaptation starting from a very coarse initial mesh. Formation of the concentrated tip vortex and the shock-induced flow separation on the blade surface are investigated. For the present purpose, a three-dimensional viscous unstructured mesh parallel flow solver is developed based on a cell-centered finite-volume scheme with the Roe's flux-difference splitting. The Spalart-Allmaras one-equation turbulence model is used to simulate the effect of turbulence coupled with a wall function boundary condition. An implicit Jacobi/Gauss-Seidel method is used for the time integration. Calculations are validated by comparing the results with Caradonna and Tung's experimental data.[8]

2. NUMERICAL METHOD

2.1 Governing Equations

The equations governing three-dimensional, viscous, unsteady, compressible flows are the Reynolds-averaged Navier-Stokes equations, which can be recast by using absolute flow variables on a rotational frame of reference in an integral form for a bounded domain V with a boundary

---

[*] Associate Professor, Division of Aerospace Engineering
[†] Doctoral candidate, Division of Aerospace Engineering

∂V:

$$\frac{\partial}{\partial t} \iiint_V \mathbf{Q} \, dV + \iint_{\partial V} \mathbf{F}(\mathbf{Q}) \cdot \vec{n} \, dS =$$
$$\iint_{\partial V} \mathbf{G}(\mathbf{Q}) \cdot \vec{n} \, dS + \iiint_V \mathbf{S}(\mathbf{Q}) \, dV \qquad (1)$$

where $\mathbf{Q} = [\rho, \rho u, \rho v, \rho w, e_o]$ is the solution vector of conservative variables for the mass, momentum and energy equations. The inviscid flux $\mathbf{F}(\mathbf{Q})$ is computed by using the Roe's flux-difference splitting scheme.[9] To achieve higher-order spatial accuracy, estimation of the state at each cell face is calculated by interpolating the solution with a Taylor series expansion in the neighborhood of each cell centroid. The first derivatives of the viscous flux, $\mathbf{G}(\mathbf{Q})$, are evaluated by a linear reconstruction method,[10] which was originally suggested by Mitchell.[11] The source term, $\mathbf{S}(\mathbf{Q}) = [0, \Omega \rho v, -\Omega \rho u, 0, 0]$, is to account for the centrifugal acceleration of the rotating blade about the z-axis. The linear system of equations is advanced in time by using the implicit Jacobi/Gauss-Seidel method. Details of the flux calculation and the time integration can be found in Ref. 7.

The Spalart-Allmaras one-equation turbulence model[12] is used to estimate the eddy viscosity. In the present implementation, the turbulence model equation is solved separately from the mean flow equations by using the same time integration scheme, which results in a loosely coupled system.

2.2 Boundary Condition

In order to predict turbulent boundary layer flows correctly through the laminar, semi-laminar and fully turbulent regions, many grid points are required inside the viscous sublayer with the near wall value of $y^+ \approx 1$. To reduce the memory requirement and the computational cost, a semi-empirical wall function boundary condition is imposed on the surface of the blade for the present turbulent flow calculations. This also accelerates the overall convergence of the solution by removing highly-stretched small cells.

At the far-field boundary, the flux is computed using flow quantities from the adjacent cells and the freestream value determined as suggested by Srinivasan et al.[13] In this method, 1-D momentum theory is used to approximate the inflow/outflow boundary conditions by introducing a 3-D point sink concept to satisfy the conservation of mass. This boundary condition is a function of rotor thrust, which is updated at every iteration as the calculation proceeds.

Due to the periodic nature of the flow for hovering rotors, calculations are performed for a single blade of the rotor and the periodic boundary condition is applied between the blades. Grid periodicity is enforced in the grid generation process, and the cells adjacent to this boundary are treated as interior cells so that interpolation of the flow is not required.

At the far-field boundary, the value of working variable, $\tilde{\nu}$, for the Spalart-Allmaras turbulence equation is extrapolated from the interior for outflow and is specified to be a freestream value for inflow. The freestream value of turbulence is taken to be 10% of the laminar viscosity for the present study.

The initial condition may be set equal to the freestream state everywhere.

2.3 Parallel Implementation

The numerical method previously described is parallelized by partitioning the computational domain into several subdomains. Communication of the data between each processors is achieved by using the MPI(Message Passing Interface) library. For the present cell-centered scheme, the data communication involves flow variables at the nodes, at the face centroids, and at the adjacent cell centroids of the subdomain boundary. The partitioning is performed using the MeTiS library[14] by considering the number of cells assigned to each processor to achieve load balancing.

2.4 Solution-Adaptive Mesh Refinement

Solution-adaptive mesh refinement is applied to better resolve the shock wave on the blade and the tip vortex in the wake. On a coarse initial mesh, tip vortex shows very rapid numerical diffusion and the definite structure of the vortex core can be identified only in the near wake region from the tip of the blade. In order to capture the tip vortex extensively in the far wake and to preserve its strength, local mesh refinement is performed through several adaptation levels along the tip vortex core location.

At first, local maximum of vorticity[15] is searched to determine the vortex core location at every 5 degrees of vortex age starting from the trailing-edge of the blade tip on two-dimensional cutting planes. The search continues until identification of the vortex core fails due to the numerical diffusion for given mesh resolution. Next, the discrete vortex core locations are connected to form a smooth curve using a 3-D parabolic blending. Then, cells on and near the captured tip vortex core trajectory located within six times of the local cell characteristic length are targeted for subdivision. A 1:8 division is made for the targeted cells by inserting new grid points at the centroid of six line elements of each tetrahedron. Buffer cells are required between the targeted cells and the surrounding cells to confirm a valid cell connectivity. These buffer cells are divided as either 1:4 or 1:2. On the solid surface, the coordinates of inserted grid points are determined by using a general 3-D surface curve fitting based on the Hermite polynomial interpolation to guarantee the smoothness.

The refined mesh is re-partitioned for load balancing and the calculation is resumed. This procedure is repeated until a satisfactory result is obtained for the blade loading and the tip vortex.

3. RESULTS AND DISCUSSION

Calculations are made for the experimental hovering rotor of Caradonna and Tung.[8] The experimental model has a two-bladed, untwisted, rigid rotor. The blades are made of a NACA 0012 airfoil section with a rectangular planform of an aspect ratio equal to 6. Two hovering flight conditions are chosen from the experimental data in the present calculations: 1) non-lifting rotor case with tip Mach number $M_{tip} = 0.52$, collective pitch angle $\theta_c = 0^o$, and the Reynolds number based on the blade tip speed and the chord length $Re = 2.22 \times 10^6$; 2) lifting rotor case with $M_{tip} = 0.877$, $\theta_c = 8^o$, and $Re = 3.93 \times 10^6$.

Unstructured tetrahedral meshes used for the present calculations are generated by using an advancing-layers technique[16] for the viscous-dominant flow region around the blade surface and in the near wake and by an advancing-front technique[17] for the rest of the computational domain. The far-field boundary is located at two radii downstream of the rotor, one and half radii upstream of the rotor, and two radii away from the center of rotation in the radial direction. Figure 1 shows the blade surface triangulation and subdomain boundaries partitioned by using the MeTiS library for parallel computing for the non-lifting rotor case.

The viscous mesh is generated not only on the blade surface but also in the near wake vortex sheet region to
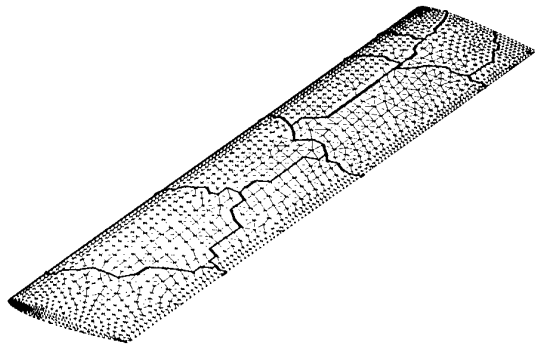
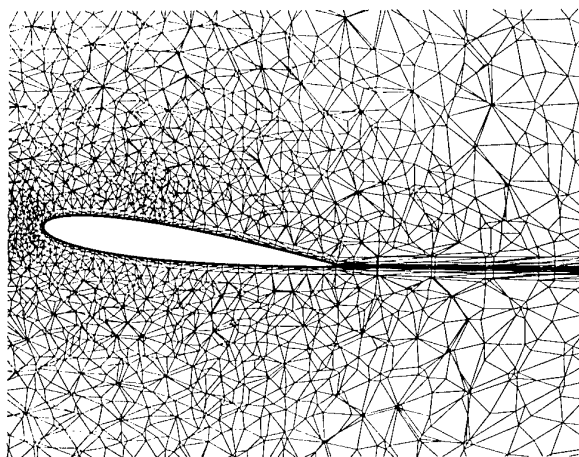Fig. 1   Blade surface triangulation and parallel partitioning.

Fig. 2   Sectional view of the computational mesh at 96% span for the lifting rotor.

properly take into account the wake shear layer effect. This viscous wake mesh is extended up to two and half chord lengths and 30 degrees of vortex age from the blade quarter chord line following the prescribed wake geometry.[18] The grid spacing and the stretching factor for the wake mesh are same to those for the blade surface. A typical sectional view of the mesh at $y/R = 0.96$ is presented in figure 2 showing a transition from the stretched viscous layers to the inviscid mesh around the blade and in the near wake. The normal distance of the first cell center from the blade surface is 0.0003c, which is approximately equivalent to $y^+ \approx 30$. In the case of the non-lifting rotor, the three-dimensional mesh consists of 393,624 tetrahedra and 69,671 nodes, and the surface triangulation on the blade contains 12,124 triangles and 6,817 nodes.

Figure 3 shows the surface pressure distributions at several radial locations of the blade for the non-lifting rotor case. Both inviscid and viscous results show good agreements with the experimental data except at the blade trailing edge where viscous flow simulation represents slightly lower pressure distribution. Due to the symmetry of the airfoil section, both upper and lower surfaces of the blade show the same pressure distribution producing zero net thrust.

Figure 4 represents the pressure and the Mach number contours at 96% span of the blade showing inviscid and vis-
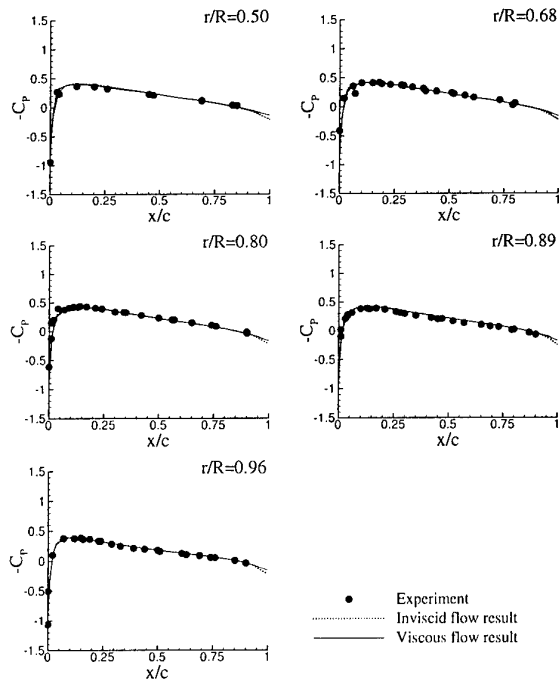

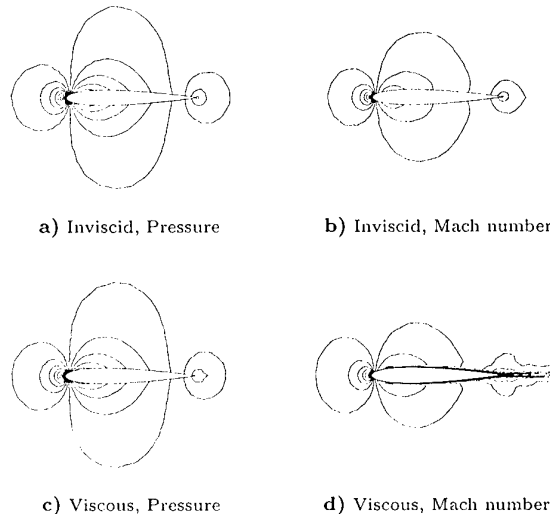Fig. 3   Comparison of pressure coefficient distributions on the blade for the non-lifting rotor.

a) Inviscid, Pressure   b) Inviscid, Mach number

c) Viscous, Pressure   d) Viscous, Mach number

Fig. 4   Pressure and Mach number contours at 96% span for the non-lifting rotor.

cous results of the non-lifting rotor case. As expected from figure 3, almost identical pressure contours are obtained between inviscid and viscous flows showing symmetric distribution on the upper and the lower surfaces of the blade. However, the effect of viscosity is well represented on the Mach number contours showing high velocity gradients on the blade surface and in the near wake.

In order to capture the tip vortex accurately, six levels of mesh adaptation are made in the wake region for the lifting rotor case. The cells located along the tip vortex core are divided until the characteristic length scale of each cell becomes less than 5% of the blade chord length, which is equivalent to the size of the finest wake grid used by Ah-
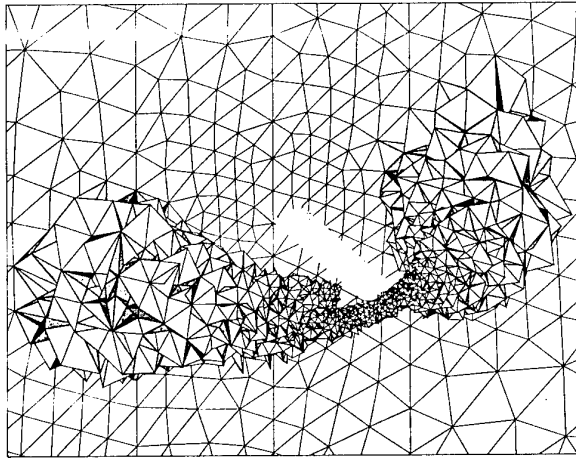
Fig. 5   Adapted cells in the wake of the blade.

a) Tip vortex contraction

mad and Strawn[3] for their viscous flow calculations. At each adaptation level. additional 20 degrees of vortex age are also adapted at the downstream of the last-detected tip vortex core location along the extension of the predicted tip vortex trajectory to enhance the vorticity transportation mechanism. Figure 5 shows cells adapted in the wake of the blade at a typical adaptation level. The initial mesh consists of 558,884 tetrahedra and 98,411 nodes. After six levels of wake adaptation, the final mesh contains 820,610 tetrahedra and 143,636 nodes.

The predicted tip vortex geometry after wake adaptation is compared with the experimental data and previous inviscid predictions[4,7] in figure 6 for the lifting rotor case. The tip vortex is captured up to 420 degrees of vortex age. Almost identical results are obtained between the present viscous simulation and the inviscid simulation based on the same numerical method[7] showing that viscosity may not significantly affect the tip vortex transport mechanism. A similar trend is also found for the numerical result[4] based on an unstructured inviscid simulation even though slight difference is observed depending on the grid resolution and the numerical method. All three predictions show fair agreement of the tip vortex descent with the experiment but much faster contraction.

The predicted surface pressure coefficients are compared with the experiment and the previous inviscid simulation[7] in figure 7 for a transonic tip Mach number of 0.877 at the collective pitch angle of 8° after the wake adaptation is completed. The result shows good agreement with the experiment at all radial stations of the blade. The location and the strength of the shock wave are captured better in the present viscous simulation due to the shock-boundary layer interaction. The growth of the boundary layer tends to weaken the shock strength and moves its position toward the leading-edge of the blade.

Figure 8 shows the sectional thrust distribution along the blade span. Comparison of the present viscous result with the experiment and the inviscid calculation is presented. The predicted value is slightly higher than the experiment especially toward the tip of the blade, which is consistent with the results obtained by previous researchers.[3,4] The viscous simulation predicts slightly less blade loading than the inviscid calculation at the outboard of the blade due to the loss involved with the shock and the locally separated flow.

Formation of the tip vortex is investigated by examining the surface streamtraces and the vorticity field at the tip. Figure 9(a) shows the surface streamtraces for
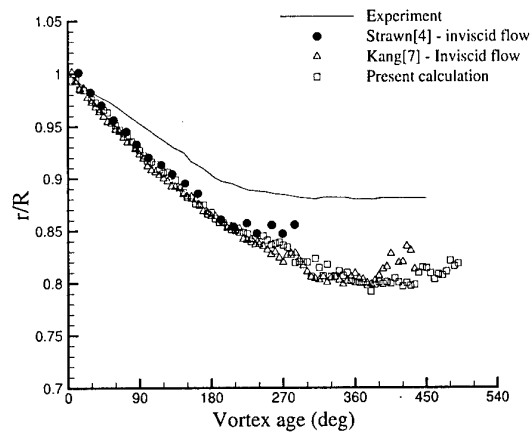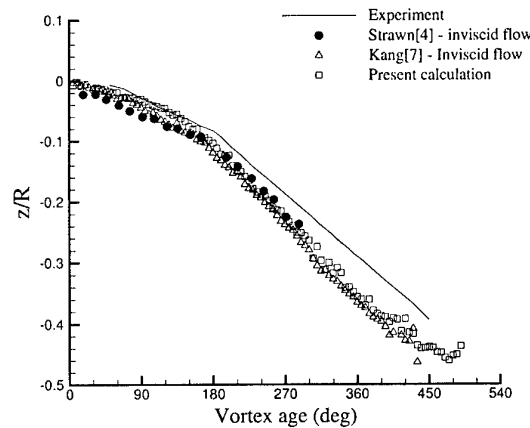
b) Tip vortex descent

Fig. 6   Comparison of predicted tip vortex geometry at $M_{tip} = 0.877$, $\theta_c = 8°$, and $Re = 3.93 \times 10^6$.

$M_{tip} = 0.877$ and $\theta_c = 8°$. Detail of the flow around the square tip is well represented by the flow separation line along the top edge of the blade and the dividing streamlines in the middle of the tip near the leading-edge. The figure also shows the shock-induced boundary layer separation and a pair of counter-rotating vortical flows originating from the inside of the separated flow region. Sectional vorticity contours at several chordwise locations of the blade are shown in figure 9(b). Three distinct vortices, P, V_1, and V_2, are observed in this figure. The primary vortex, P, begins to develop before $x/c = 0.35$ along the top edge of the blade. Two secondary vortices are formed due to the flow separation across the sharp corners and are located on the upper and lower parts of the tip separated by the dividing streamlines as shown in figure 9(a). The secondary vortex, V_2, begins to develop from the leading-edge along the bottom edge of the tip due to the lower surface boundary-layer separation, which merges into the primary vortex forming a strong tip vortex at further downstream near the trailing edge. In addition, a small counter-rotating vortex, V_1, located on the upper part of the tip quickly merges into the upper surface vortex.
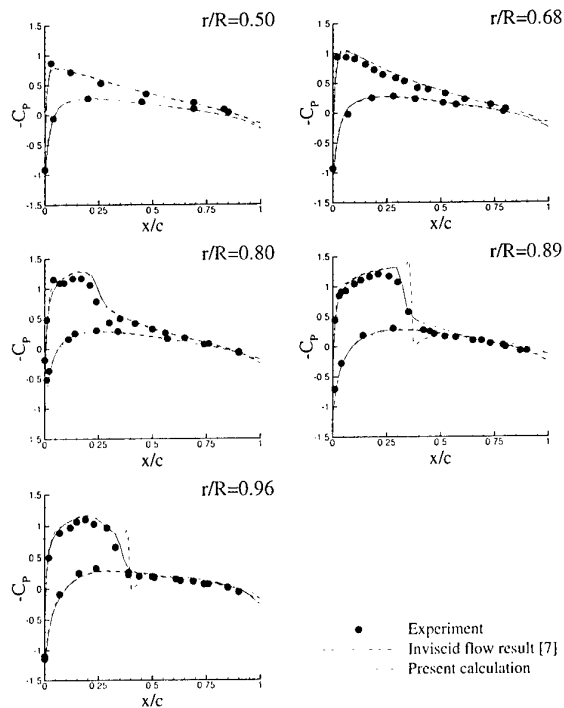
Fig. 7 Comparison of pressure coefficient distributions on the blade at $M_{tip} = 0.877$, $\theta_c = 8^o$, and $Re = 3.93 \times 10^6$.
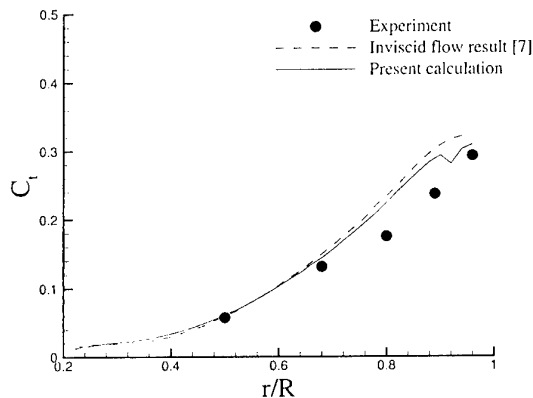

Fig. 8 Spanwise sectional thrust coefficient distributions at $M_{tip} = 0.877$, $\theta_c = 8^o$, and $Re = 3.93 \times 10^6$.

Finally, the convergence history of rotor thrust for $M_{tip} = 0.877$ and $\theta_c = 8^o$ is shown in figure 10. The result is shown for 20,000 iterations where 4th level wake grid adaptation is applied. The result of an inviscid calculation[7] is also compared in the figure. Even though the present calculation is performed for obtaining a steady-state solution, a repeated pattern of oscillatory thrust coefficient is observed after 13,000 iterations with the magnitude variation of 2-3%. This unsteadiness is due to the time-varying flows involving the shock-induced flow separation and the tip vortex formation. The present viscous flow simulation predicts slightly lower thrust than the inviscid flow prediction.
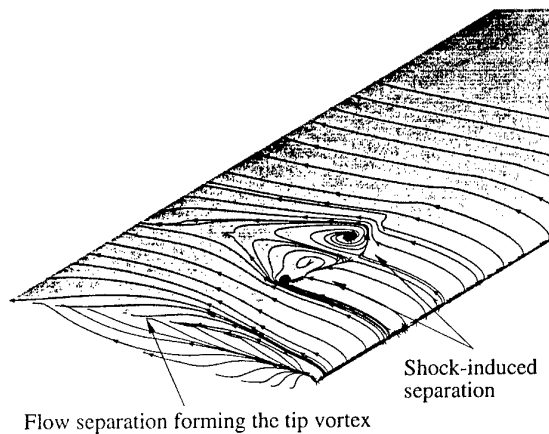
a) Streamtraces on the blade surface
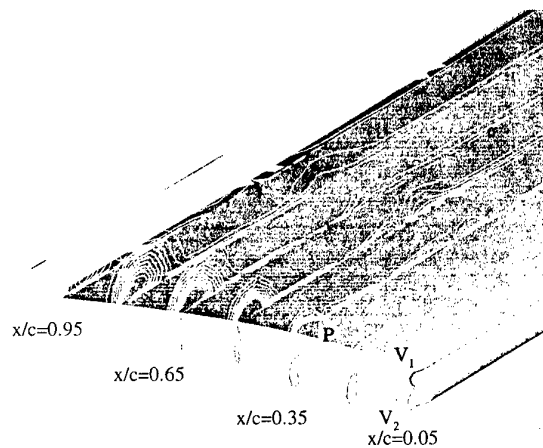
b) Streamwise vorticity contours

Fig. 9 Surface streamtraces on the blade surface and vorticity contours at $M_{tip} = 0.877$, $\theta_c = 8^o$, and $Re = 3.93 \times 10^6$.

4. CONCLUSIONS

A three-dimensional viscous flow solver is developed for predicting the flowfields of a hovering helicopter rotor using a solution-adaptive unstructured mesh refinement technique. Calculations are performed for two experimental rotor operating conditions. The viscous mesh is generated both on the blade surface and in the near wake region to properly take into account the viscous shear layer. Accurate prediction of the blade loading and the tip vortex trajectory is achieved through a series of wake mesh adaptation using less than 830,000 cells. Comparisons of the inviscid and viscous results indicate that inclusion of viscosity significantly affects the surface pressures and the blade airloads for transonic tip Mach number case showing shock-induced separation. The effect of viscosity is not as significant for the tip vortex trajectory. The process of tip vortex formation is qualitatively investigated around the blade tip showing a primary and secondary vortices merging into a single tip vortex coupled with the vortex sheet roll-up. It is demonstrated that the present unstructured mesh methodology is a strong alternative to the previous structured grid methods for the prediction of viscous flow around hovering helicopter rotors at higher numerical effi-
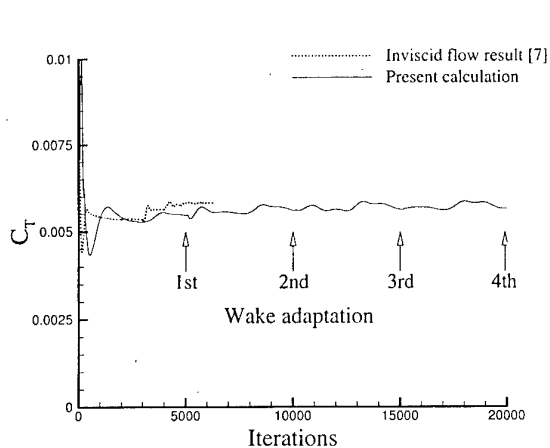
Fig. 10　Convergence history of the rotor thrust coefficient at $M_{tip} = 0.877$, $\theta_c = 8°$, and $Re = 3.93 \times 10^6$.

ciency.

References

[1] Hariharan, N. S. and Sankar, L. N., "First-Principles Based High Order Methodologies for Rotorcraft Flowfield Studies," *Proceedings of 55th Annual forum of the American Helicopter Society*, Montreal, Quebec, Canada, 1999, pp. 1921–1933.

[2] Tang, L. and Baeder, J. D., "Improved Euler Simulation of Hovering Rotor Tip Vortices with Validation," *Proceedings of 55th Annual forum of the American Helicopter Society*, Montreal, Quebec, Canada, 1999, pp. 1934–1948.

[3] Ahmad, J. U. and Strawn, R. C., "Hovering Rotor and Wake Calculations with an Overset-Grid Navier-Stokes Solver," *Proceedings of 55th Annual forum of the American Helicopter Society*, Montreal, Quebec, Canada, 1999, pp. 1949–1959.

[4] Strawn, R. C. and Barth, T. J., "A Finite-Volume Euler Solver for Computing Rotary-Wing Aerodynamics on Unstructured Meshes," *Journal of the American Helicopter Society*, Vol. 38, No. 2, 1993, pp. 61–67.

[5] Duque, E. P. N., Biswas, R., and Strawn, R. C., "A Solution Adaptive Structured/Unstructured Overset Grid Flow Solver with Applications to Helicopter Rotor Flows," AIAA Paper 95–1766, June 1995.

[6] Dindar, M., Lemnios, A., Shephard, M., Jansen, K., and Kenwright, D., "Effect of Tip Vortex Resolution on UH-60A Rotor-Blade Hover Performance Calculations," *Proceeding of the 54th Annual Forum of the American Helicopter Society*, Washington DC, 1998, pp. 45–57.

[7] Kang, H. J. and Kwon, O. J., "Numerical Prediction of Rotor Hover Performances Using Unstructured Adaptive Meshes," AIAA Paper 2000-0258, Jan. 2000.

[8] Caradonna, F. X. and Tung, C., "Experimental and Analytical Studies of a Model Helicopter Rotor in Hover," NASA TM 81232, Sept. 1981.

[9] Roe, P. L., "Approximate Riemann Solvers, Parameter Vectors and Difference Schemes," *Journal of Computational Physics*, Vol. 43, 1981, pp. 357–372.

[10] Frink, N. T. and Pirzadeh, S. Z., "Tetrahedral Finite-Volume Solutions to the Navier-Stokes Equations on Complex Configurations," NASA TM 208961, Dec. 1998.

[11] Mitchell, C. R., "Improved Reconstruction Schemes for the Navier-Stokes Equations on Unstructured Meshes," AIAA Paper 94-0642, Jan. 1994.

[12] Spalart, P. R. and Allmaras, S. R., "A One-Eauation Turbulence Model for Aerodynamic Flows," AIAA Paper 92-0439, Jan. 1992.

[13] Srinivasan, G. R., Raghavan, V., and Duque, E. P. N., "Flowfield Analysis of Modern Helicopter Rotors in Hover by Navier-Stokes Method," *Journal of the American Helicopter Society*, Vol. 38, No. 3, 1993, pp. 3–13.

[14] Karypis, G. and Kumar, V., "Multilevel k-way Partitioning Scheme for Irregular Graphs," *Journal of Parallel and Distributed Computing*, Vol. 48, No. 1, 1998, pp. 96–129.

[15] Strawn, R. C., Kenwright, D. N., and Ahmad, J., "Computer Visualization of Vortex Wake Systems," *AIAA Journal*, Vol. 37, No. 4, 1999, pp. 511–512.

[16] Pirzadeh, S., "Three-Dimensional Unstructured Viscous Grids by the Advancing-Layers Method," *AIAA Journal*, Vol. 34, No. 1, 1996, pp. 43–49.

[17] Löhner, R. and Parikh, P., "Generation of Three-Dimensional Unstructured Grids by the Advancing Front Method," *International Journal of Numerical Methods in Fluids*, Vol. 8, 1988, pp. 1135–1149.

[18] Kocurek, J. D. and Tangler, J. L., "A Prescribed Wake Lifting Surface Hover Performance Analysis," *Journal of the American Helicopter Society*, Vol. 22, No. 1, 1977, pp. 24–35.

Aerodynamic Analysis Concept
of High Speed Flight Demonstration Phase II

Makoto Ueno[*], Yukimitsu Yamamoto[**], Masaaki Yanagihara[†] and Yoshikazu Miyazawa[§] (NAL)

7-44-1, Jindaijihigashi-machi, Chofu, Tokyo, 182-8522, JAPAN
National Aerospace Laboratory of Japan

Key Words: Flight Testing, Aerodynamics, Fluid Dynamics

ABSTRACT

This article explains about the concept of aerodynamic analysis of the High Speed Flight Demonstration Phase II (HSFD Phase II). It is still difficult to acquire the exact aerodynamic characteristics of a re-entry vehicle with a large base plate in ground testing, especially in transonic flight regimes, because there are difficulties both in CFD and wind tunnel testing to predict base flow of such a vehicle. HSFD Phase II is a flight experiment project, which is planned to examine such difficulties. The method hired in this project is highly unique: the experiment vehicle is to be lifted to high altitude by a stratospheric balloon, from which it will be released and accelerate in free fall. Because of the gravity force, it can reach the transonic speed and the measurement of the aerodynamic characteristics will be performed during the quasi-static pitching flight maintaining the Mach number. For comparison, CFD analysis and wind tunnel tests for the same flow conditions will be performed. The first flight is scheduled in August 2002.

1. THE OUTLINE OF THE PROJECT

High Speed Flight Demonstration (HSFD) program is planned as part of NAL/NASDA joint research for the HOPE-X unmanned re-entry vehicle project[1][2]. The program consists of two phases. Phase I is planned to verify landing system for the terminal phase of the return flight from orbit using a jet engine-powered HOPE-X sub-scale vehicle. And, the objective of Phase II is to acquire the aerodynamic characteristics and the base pressure. Additionally, as the experiment vehicles of both phases will fly autonomously, the program will also promote the development of automatic flight control technology.

From the point of view of aerodynamics research, the HSFD Phase II program is planned as an "open-air wind tunnel testing". Both CFD and wind tunnel testing have defects inherently. For CFD analysis, the prediction of separated flow is difficult. Therefore the computation of the flow around a re-entry vehicle with

large base plate such as the HOPE-X re-entry vehicle can have large uncertainties. On the other hand, in a wind tunnel test, the experiment model has to be supported by a sting or a strut. Because it will make interference with the flow around the wind tunnel model, the prediction of the net force exerted on the vehicle in the real flight condition is difficult.

The method hired in the HSFD Phase II is highly unique and the force measurement of the vehicle without any interference stated above will be realized. It is planned that the scaled mock-up vehicle will be pulled up to high altitude by a stratospheric balloon, from which it will be released and accelerate in free fall (Fig. 1). After the acceleration, it can reach to the transonic speed. The Mach number of the flying experiment vehicle will be maintained at aimed one within small deviations, and measurement will be done changing the attack angles of the vehicle quasi-statically. In this program, because the interests are confined only to the longitudinal characteristics, the yaw angles of the vehicle will be fixed to zero during the measurement. The experiment will be conducted at the Esrange test site near Kiruna in Sweden, which is operated by the Swedish Space Corporation (SSC). The flight Mach numbers are set to be M=0.8, 1.05 and 1.2 (Fig. 2). Because before and after passing the sonic speed the aerodynamic characteristics change remarkably, and the flow phenomena around the vehicle are non-linear in transonic speed, the flight Mach numbers are chosen as stated above.

The experiment vehicle is a 25% scaled model of the 11HOPE configuration of the HOPE-X re-entry vehicle project although it has some deviations from the base shape, which are the ADS probe to acquire free stream conditions and antennas for communications (Fig. 3, Fig. 4). The influences of those deviations are confirmed to have negligible effect to aerodynamic characteristics by CFD analysis. In addition, the spread angle of split rudder speed breaks is set at 40 degree and the body flap is set to 10 degrees up for trimming.

The HSFD Phase II flight experiment will be conducted by NAL, NASDA and the Centre National

d'Etudes Spatiales (CNES) of France in collaboration.

2. CFD ANALYSIS

To compare with the results of the flight tests, the computation of the aerodynamic characteristics of the vehicle using multi-block grids made from 3D-CAD data will be performed. Although CFD is becoming a powerful tool for estimating aerodynamic characteristics, the computation of the base flow in CFD with reliable precision is still difficult.

Examples of computations of the base flow of the 11HOPE configuration obtained so far are shown in Fig. 6 and Fig. 7. Though there is no guarantee that the streamlines shown in these figures are fully reliable, the fact that the general flow patterns are similar to those for the real flow is highly suggestive. Both under and over the sonic speed condition, the base flow is dominated by one large vortex, which is larger than the size of the base plate. It means that the base flow may have a large effect to the pressure distribution on the base plate. And, a straight sting, which is inserted to the base plate to support the model in wind tunnel testing can destroy the flow structure behind the large base plate.

To estimate the reliability of the computational results, a parametric study will be held in cooperation with CNES in France and the results will be compared with the results of the wind tunnel tests and the flight tests.

3. WIND TUNNEL TEST

Wind tunnel tests are planned before and after the flight experiment. The tests will be held at the NAL 2m × 2m transonic wind tunnel (NAL-TWT1) and ONERA S2MA which has a test section of 1.770m × 1.750m. Because S2MA can maintain highly pressurized stagnation pressure, it has an ability to achieve the Reynolds number from 10^6, at least, to 10^7. Therefore, Reynolds number effect can be estimated with using it.

The wind tunnel test model was fabricated as an 18% scaled model of the experiment vehicle of the HSFD Phase II, namely, 4.5% of 11HOPE. It was designed to be able to measure six components of forces and pressure distribution. There are pressure ports on the surface of the model as shown in Fig. 9. In Fig. 9, numbered ports are equipped on the model surface, and ports indicated by the small colored circles, are the ports equipped on the experiment vehicle. All pressure ports are drilled at the right half (inclusive of ones on the center line) of the model body, although, in Fig. 9, ports on the lower surface of the right wing are marked on the left wing just for the sake of convenience. Because one of the main objectives of this flight experiment is to acquire the pressure distribution on the base plate, there are many pressure ports on the base plate of both wind tunnel model and experiment vehicle.

In the pre-flight test, the test employing conventional

method will be performed to validate the aerodynamic model used in the design of the control system[3]. The model was designed such that it can be supported with either a straight sting or a dorsal sting.

The basic characteristics of the model will be acquired with the straight sting (Fig. 8(a)). After that, the test of the model supported with the dorsal sting will be performed to acquire the base pressure distribution (Fig. 8(b)). Additionally, the dorsal sting with dummy straight sting will be employed (Fig. 8(c)). It is considered that the measured force data of (c) subtracted from the sum of (a) and (b) will leave the aerodynamic force data without any support.

After the flight experiments, the post-flight wind tunnel test will be held reflecting the real flight conditions acquired in the flight tests because the conditions of elevon angles or Mach numbers can be changed depending on the real-flight regimes.

4. FLIGHT TEST

The outline of the project is stated in Section 1. In this section, the experimental aspect of the project will be explained.

The measurement items concerning aerodynamic characteristics are as follows. The information about the free stream such as total pressure, static pressure, and the flow directions, i.e., angle of attack α and yaw angle β will be measured by ADS (Air Data Sensor) system attached at the nose of the experiment vehicle (Fig. 4). Three forces are measured by the IMU (Inertial Measurement Unit). Deflection angles of the rudders and the elevons are measured by potentiometers and hinge moments are measured by strain gages. The base pressure distribution is measured by electro scanning pressure sensors. Additionally, pressures at some points on the body surface will be measured in accordance with the request from CNES by using flash mounted sensors.

The main interests are concentrated on the longitudinal aerodynamic characteristics and the base pressure distribution in the measurement phase. The reason is that we have not got any good references for base pressure distribution of a re-entry vehicle although the base flow has significant effect on the aerodynamic characteristics of such a kind of vehicles. Additionally, the base flow can have an effect on the trimming of the vehicle.

5. COMPARISON OF DATA

The data acquired in CFD, the wind tunnel tests and the flight tests will be compared with each other. The data acquired in the flight test will be the reference among these three kinds of tests. Generally, the results of the flight tests are considered to have relatively large errors when compared with those of the ground tests. However, the results of the flight tests are not contaminated by any sources, and additionally, the objectives of the ground tests, or the CFD and the wind tunnel tests are to predict the characteristics of

the flight vehicle. This is the reason why we believe that the flight test results must be the reference of this series of tests.

6. DEVELOPMENT PLAN

The development plan of the program including Phase I is shown in Fig. 10. In August 2001, a preliminary test for the Phase II experiment will be conducted at Esrange, during which training for the launch operation will be carried out using a mock-up of the vehicle and actual balloons. Flight test campaigns are planned for August 2002 and May 2003, and six flights in total are planned for these two campaigns.

7. CONCLUSIONS

In this project, comparison among the results of three kinds of analysis, namely, CFD and EFD (wind tunnel tests and flight tests) will be performed. It will make it possible to acquire the data of aerodynamic characteristics and an insight into the base flow of the re-entry vehicle in transonic flight regimes.

It is important to build up a closer connection among the results of those three analysis methods, because we cannot know the true characteristics by only one kind of estimation in reality. This project is composed of these three kinds of analysis and this type of project will become to play an important role in the aerodynamics field.

8. REFERENCES

1) . Sato, N., Akimoto, T., and Miyazawa, Y., "HOPE-X High Speed Flight Demonstration Phase I," AIAA-2001-1806, 2001.

2) . Yanagihara, M., Miyazawa, Y., Akimoto, T., Sagisaka, M., Cretenet, J. C. and Venel, S., "HOPE-X High Speed Flight Demonstration Program Phase II," AIAA-2001-1805, 2001.

3) . J. H. Campbell, II and W. R. Embury, " Aerodynamic Results of a Support System Interference Effects Test Conducted at NASA/LaRC UPWT using an 0.015-scale Model of the Configuration 140A/B SSV Orbiter(0A20B)," NASA-CR-134403, 1974.
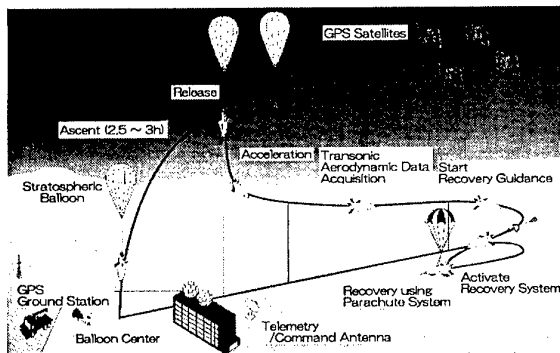
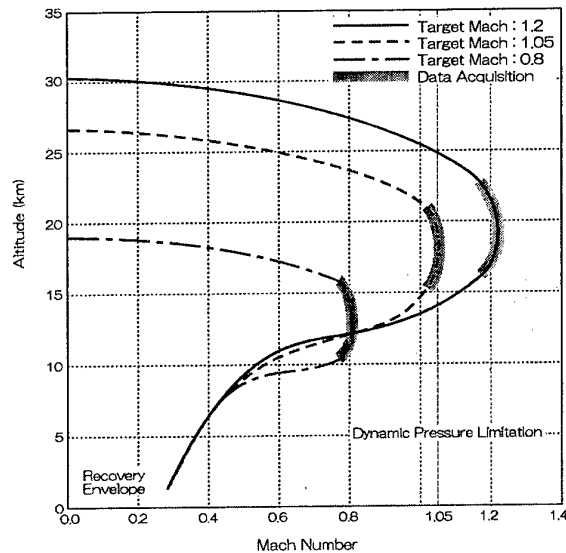Fig. 1: HSFD Phase II Mission Profile.
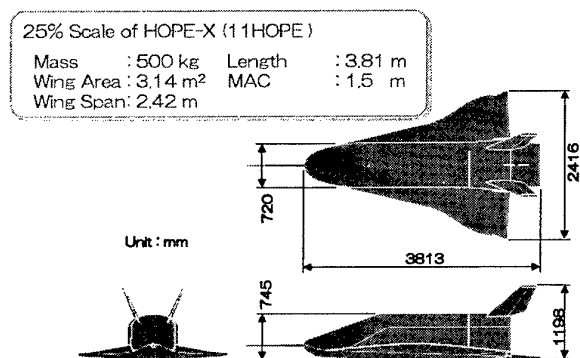

Fig. 2 : Typical Flight Patterns.

25% Scale of HOPE-X (11HOPE)

Mass : 500 kg Length : 3.81 m
Wing Area : 3.14 m² MAC : 1.5 m
Wing Span: 2.42 m

Fig. 3 : Dimentions of Experiment Vehicle.
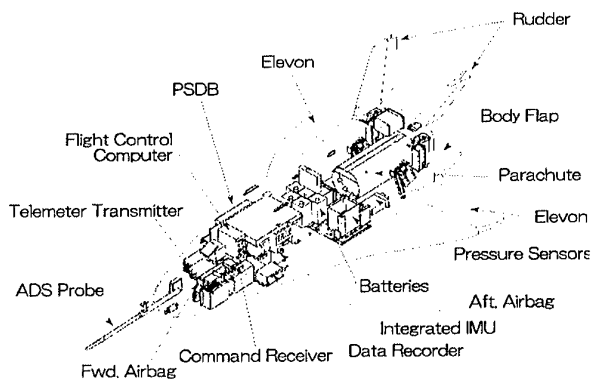
Fig. 4 : Onboard Equipment of Experiment Vehicle
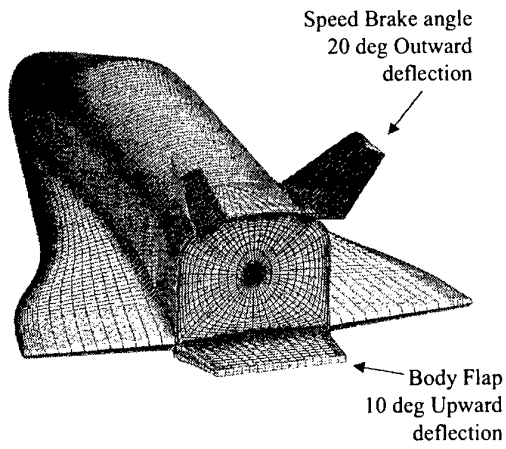
Speed Brake angle
20 deg Outward
deflection

Body Flap
10 deg Upward
deflection

Fig. 5 : Surface Grid of HSFD Phase II.

(a) Straight Sting Support

(b) Dorsal Sting Support

(c) Dorsal Sting Support with Dummy Straint Sting Support
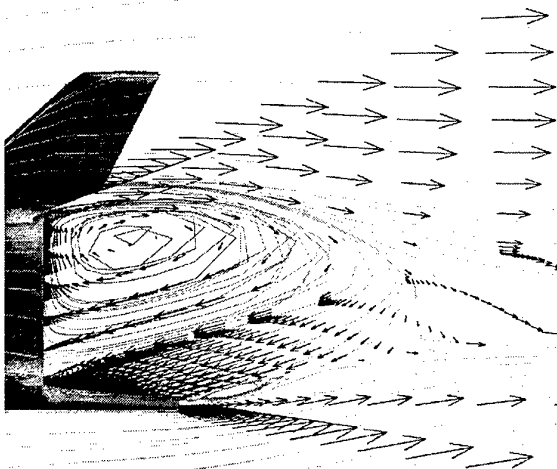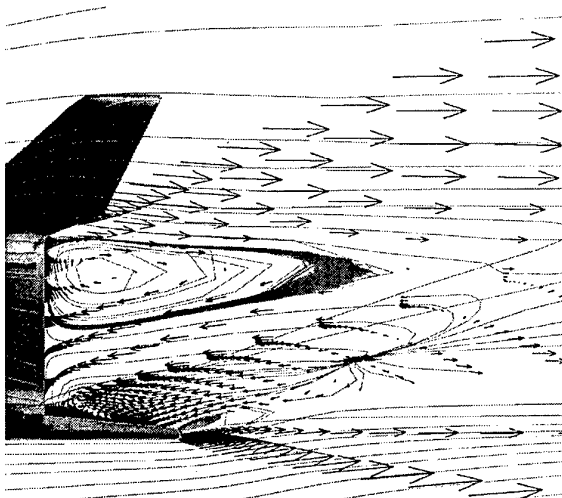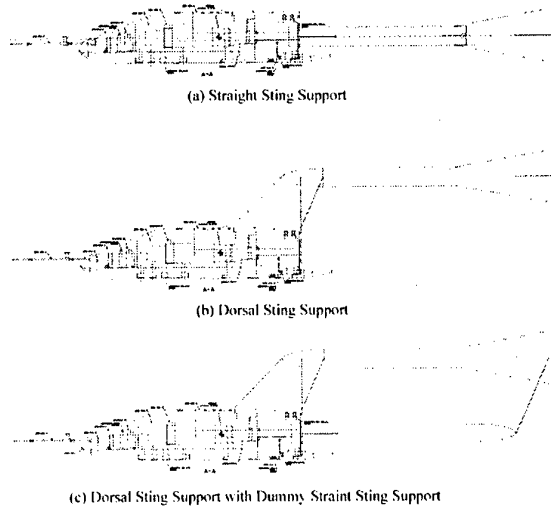
Fig. 8 : Variations of Model Support.

Fig. 6 : Base Flow at α = 15deg. in M = 0.8.
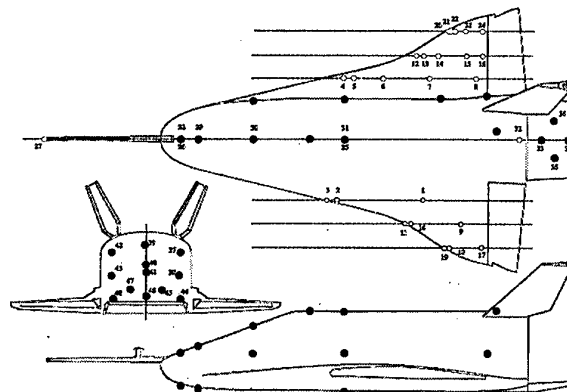
Fig. 9 : Pressure Ports on Wind Tunnel Model and Experiment Vehicle.

Fig. 7 : Base Flow at α = 15deg. in M = 1.05.

JFY 1999	JFY 2000	JFY 2001	JFY 2002	JFY 2003
1999	2000	2001	2002	2003

Preliminary Design
Detail Design
Design Follow-up
Assembly, System Test
(Phase I)
Flight Test
(Phase I)
Preliminary Test
Flight Test 1
Flight Test 2

Fig. 10 : Development Plan.

Development of A Small Canard Aircraft

Seokmin Ahn*, Keunbae Kim**, Jinwon Kim**, and Eungtai Kim***

Aircraft Division
Korea Aerospace Research Institute
Taejon, Yusung P.O.Box 113, Korea

Key Words : Aircraft, Aerodynamic Characteristics

ABSTRACT

A canard type aircraft, which has good wing stall and stall/spin-proof characteristics, is being developed. The first prototype has been built, and the maiden flight in the fall of 2001 will be followed by a series of test flights.

A 1/4-scale model was tested in the wind tunnel to confirm the aerodynamic and stability characteristics. Structural tests and analysis were preformed to substantiate the results. Digital mockup dramatically increased the aircraft detail design and manufacturing efficiency, and then the control system design was verified using an iron-bird. Propulsion, fuel and ignition systems operation were checked using an engine test bed. In addition, composite material curing technology was enhanced through manufacturing and assembling parts of the prototype.

1. INTRODUCTION

A canard is a horizontal stabilizer located at the front of the main wing. Some modern fighters have a canard to improve a low speed performance, while civil aircraft have canards to improve the safety and the flight performance. Among civil aircraft, experimental aircraft have begun to adopt the canard first. When the angle of attack (AOA) of the aircraft is getting higher, a canard which is at front of the center of gravity (CG) stalls before the wing stalls, which generate a nose-down pitching moment. This wing-never-stall characteristic is a very important issue for safety concern. This and a good flying performance are the reasons why a canard type small aircraft is on high demand and is being considered as a next generation's general aviation.

Korea Aerospace Research Institute has conducted research on the core technology for a canard type small aircraft. Computation fluid dynamics, wind tunnel tests, scale model tests, structural analysis, structural static tests and propulsion system tests have been performed. For designing, an infra-structure for digital mockup has been setup. For manufacturing, the process for composite materials has been researched including coupon tests.

The aircraft under development (named Firefly)

has four seats and an engine at the tail of the fuselage (pusher type). The landing gear is a fixed type and there is no flap on the main wing, which is usual as a canard type. Vertical tails are mounted on two booms which is attached to the wing. The CG is 0.52 MAC aft from the leading edge. The canard is not swept and has modified a Roncz 1145MS airfoil. In order to have a higher lift curve slope, the aspect ratio of 10.2 is selected. The airfoil of the main wing is modified a Eppler 1230 with a leading edge droop at the wing tip to improve stall characteristics. The strake is swept back 45 deg. and the main wing is swept 18 deg. The ISO view of the aircraft and its specification are shown (Fig. 1 and Table 1).

Table 1. Performance and specifications of the Firefly

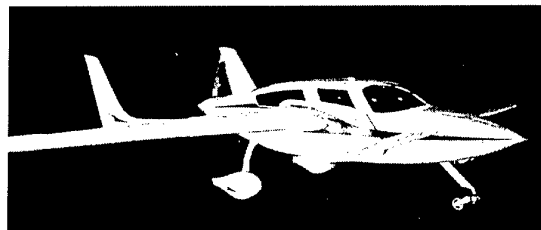| Gross weight	1225 kg	Canard area	1.67 m²
Length	6.64 m	Vert. tail area	1.60 m²
Height	2.38 m	Cruise speed	340 km/h
Wing span	10.2 m	Max. climb rate	6.1 m/s
Wing area	11.15 m²	Take off dist.	430 m
Canard span	4.81 m	Cruise dist.	1850 km

Fig. 1. Canard aircraft developed by KARI

2. THE WIND TUNNEL TESTS

A 1/4 scale model was tested in a wind tunnel which is equipped with 4 m wide test section and a 6 axis external balance (Fig. 2). Most tests were carried out under 50m/sec winds, which is equivalent to Reynold number 1.2×10^6. The model was supported at 3 points with the variation of the angle of attack from –4 deg. to 20 deg. For accurate data, weight tare, strut interference and wall effect were compensated.

* Principal Researcher, Small Aircraft Research Group
** Senior Researcher, Small Aircraft Research Group
***Group Head, Small Aircraft Research Group

Fig. 2. Model installed in the wind tunnel

A total of 260 hours of testing test has been conducted. Effects of the vertical tail and landing gear have been examined. Incidence angle of the canard and deflection angle of control surfaces were varied and tested for the examination of the aerodynamic characteristics and the stability. Vortilons and vortex generators were examined for its effectiveness. Fig. 2 shows a flow visualization test using tuft when vortilons are applied.

Lift coefficient curve with elevator angle variation degrees is shown in Fig. 3. At the low AOA, the more the deflection of the elevator goes down, the higher the lift. But above 6 deg. of AOA, the higher deflection does not generate more lift because the canard stalls. And the more deflection of the elevator makes the lift coefficient lower.

Most small aircraft with canard have an elevator at the canard. For these aircraft, when the elevator is lowered the pitching moment coefficient rises. The wind tunnel test result shows that the increasing ratio of pitching moment coefficient remains small or even decreases when the elevator is lowered more than 10 deg. (Fig. 4.) This proves that the aircraft does not stall even with an elevator fully lowered. It should be noted that the aircraft can be recovered from stall, if it ever stalls, by controlling the elevator up, since the elevator works effectively even at an angle higher than 15 deg.
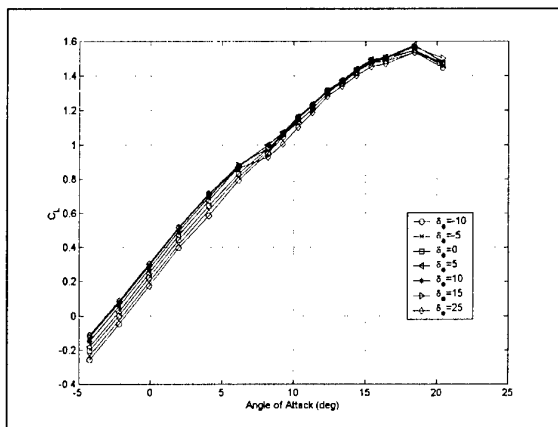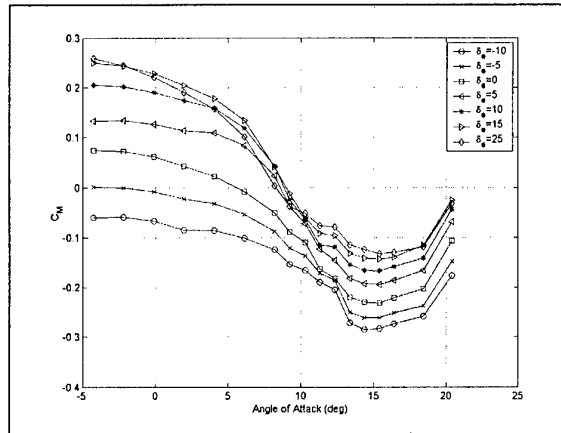

Fig. 4. Pitching moment coefficients for various elevator deflection

3. THE STRUCTURAL ANALYSIS AND TESTS

Most structures of the Firefly are constructed with composite materials. Compared with aluminum, composite material may allow us to build a lighter and cheaper aircraft. In addition, complex shapes can be achieved accurately, which lets the laminar airflow remain on the wing skin as far as aft, which in turn gives higher performance of the aircraft.

However, the uniformity of the product is hard to achieve, since the specification of composite material is not yet standardized, and even worse, the process and the workmanship of each builder can be different. This explains the difference of the Poisson's ratio of coupons made by different workers even with the same material. The structural tests including coupon tests should be followed by the structural analysis for conformity.

Carbon fiber is applied on the center spar cap and the door frame. Glass fiber is used for the rest of the structure. Uni-directional and bi-directional fabric has been accumulated with resin using wet-layup process and cured at a room temperature.

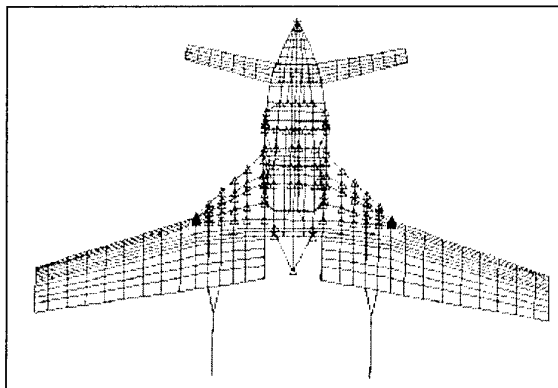Fig. 3. Lift coefficients for various elevator deflections

Fig. 5. The FEM model of the Firefly

The finite element model was obtained using NASTRAN (Fig. 5). With a 6G load applied, the wing tip is deflected 17" (Fig. 6). The strain distribution diagram of the wing (Fig. 7) shows areas where the strake and the wing met are under highest strain. Those areas have been reinforced with carbon fiber. The results of the analysis are followed with a series of structural tests (Fig. 8).

The strains obtained with analysis and tests show the critical area matched (Table 2), where the analysis was done conservatively. The analysis shows the wing can sustain the ultimate load of 8G, which can be higher in the actual wing.
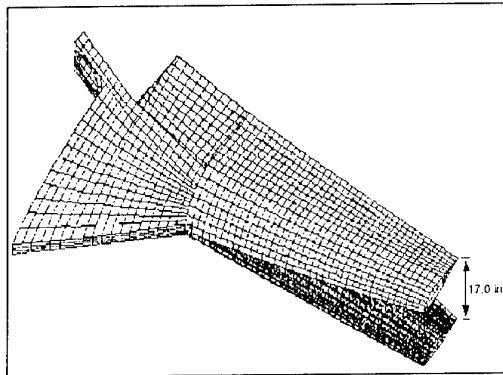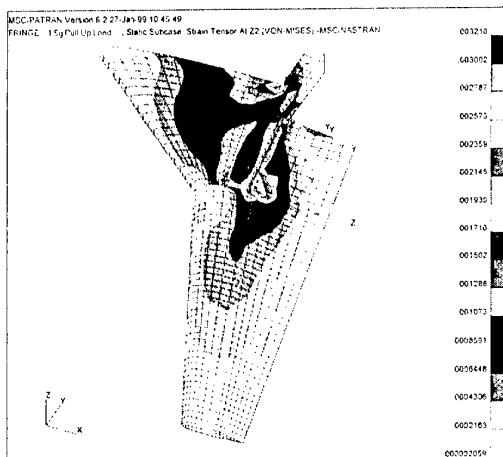

Fig. 6. The deflacted wing under 6G load

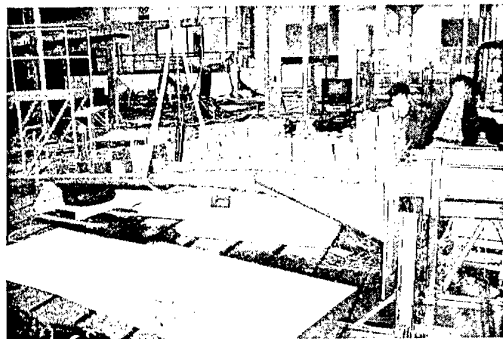Fig. 7. The Von-Mises strain distribution of the wing

Fig. 8. The structural test of the wing

Table 2. Strain comparison between analysis and tests

CH	NASTRAN		TEST	
	ε_L	ε_T	ε_L	ε_T
1	688	-354	603	
2	1428	-347	1609	
3	1740	-920	1325	
4	1534	325	587	-54
7	1351	444	1200	35
10	-4	995	?	1026
11	-33	1547	823	1317
13	-222	104	-771	408
16	-96	43	-201	
18	1510	318	1005	12
22	200	-33	17	67
25	1829	-659	1317	
26	-1690	606	-982	
27	-353	-480	-198	
28	-406	228	-590	
29	-1455	764	-1204	
30	34	-642	?	-715
31	-83	-1361	-1016	-982
33	-1359	-273	-964	250
36	-1314	-350	-972	82
39	-1578	809	-964	
40	-1380	-280	-1210	440

(@3G condition, unit : micro-strain)

4. THE PROPULSION SYSTEM TEST

For the accurate prediction of the aircraft performance it is inevitable to ensure the correct performance of the propulsion system. The manufacturers of the engine and the propeller may supply the data needed to calculate the performance when those are installed in an aircraft. However the characteristics when they are installed together should be confirmed for exactness.

For the installed static performance test of the propulsion system, a ground test rig was built (Fig. 9). The engine is mounted on the firewall. The whole propulsion system can move freely on supporting beams which axes are parallel to the propeller's rotational axis. Load cells are located at the end of supporting beams to measure the static thrust. A rotational type torque meter is installed between the propeller and the engine to measure the torque. Pressure transducers, scanning valve and demodulator are installed for measuring the fuel flow rate and the backpressure of the engine (Fig. 10).

The installed engine is Lycoming's IO-540 (250HP) and the propeller is MT-Propeller's MTV-9-B (70" diameter, variable pitch type). The measured torque shows it is generally proportional to the engine rotational speed. The result also shows that there was not much difference between three cases (case I without an air filter and a muffler, case II with an air filter, case III with an air filter and a muffler). The maximum static torque obtained is about 500 lb-ft, which is quite close to 510 lb-ft calculated (Fig. 11).

The engine static thrust obtained by the test is within 5% of the calculated values (Fig. 12), which are quite satisfactory.
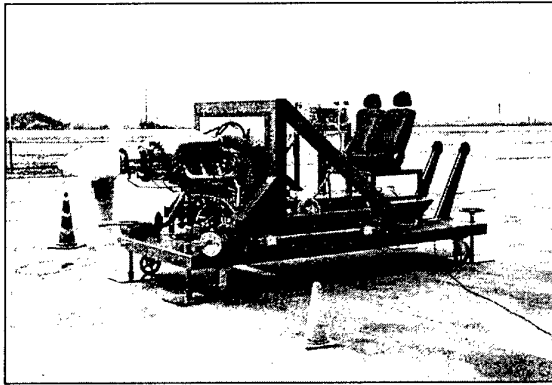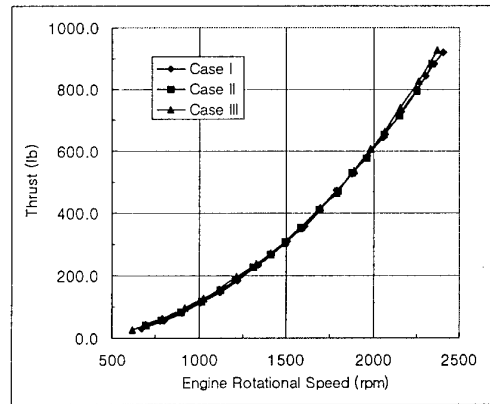
Fig. 9. The engine test bed in operation

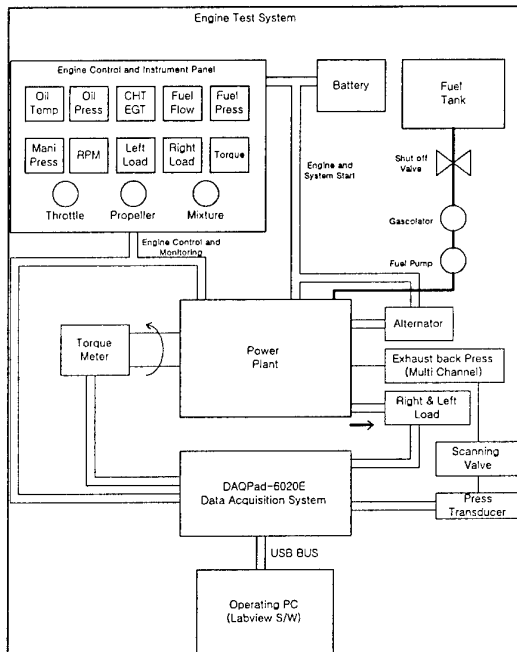Fig. 12. The engine rotational speed vs thrust

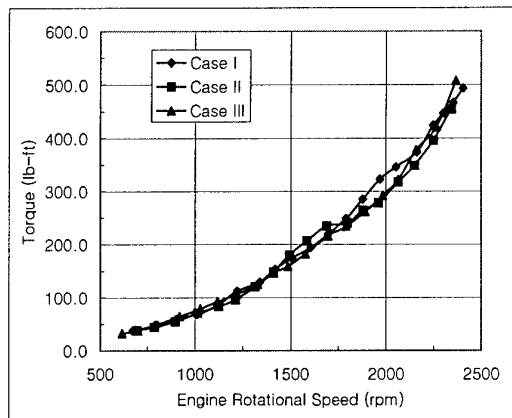Fig. 10. The schematic diagram of the engine test bed

Fig. 11. The engine rotational speed vs torque

5. CONCLUSIONS

A canard type small aircraft is being under development. Research has been conducted to investigate the characteristics and performance of the aircraft using analytical methods and actual tests.

The aircraft has been proved to be safe and to have a good flying performance. Flight tests of a scaled remote controlled aircraft, ground tests and flight tests of the actual aircraft will give more thorough results. The test scheduled will follow soon.

REFERENCES

[1] Roskam, J., "Airplane Design : Part I-VII", Roskam Aviation, Kansas, 1985.
[2] E.T. Kim, K.T. Kim, C. H. Han, J.D Jung, T.H. Cho, "Wind Tunnel Test Results Analysis of a Small Canard Aircraft", Proceedings of the KSAS Fall Annual Meeting '2000, The Korean Society for Aeronautical & Space Sciences, 11. 2000.
[3] D.H. Middleton, Composite Materials in Aircraft Structures, Longman Scientific & Technical, 1990.
[4] J.P. Caffrey and J.M. Lee, MSC/NASTRAN User's Guide - Linear static analysis, Version 68, The MacNeal-Schwendler Corporation, 1994.
[5] J.W. Kim, K.J. Sung and K.T. Kim, "Structural Analysis for the Small Canard Type Aircraft.", Proceedings of the KSAS Fall Annual Meeting '2000, The Korean Society for Aeronautical & Space Sciences, 11. 2000.
[6] K.B. Kim, C.S. Kang, S.M. Ahn "Development of an aircraft Engine Test Stand for Static Performance", Proceedings of the KSAS Fall Annual Meeting '2000, The Korean Society for Aeronautical & Space Sciences, 11. 2000.
[7] Lycoming, "Lycoming Aircraft Engine, Installation Manual", 1963.
[8] Lycoming Spec., "IO-540-C4B5", 1990.
[9] MT-Propeller, MTV-9-B/LD178-102, "Performance Diagram"

2F3   Experimental and Computational Studies on Supersonic Mixing for
Airbreathing Propulsion

Shigeru Aso*, Shingo Kawano** and Kei Inoue**

Kyushu University, Department of Aeronautics and Astronautics,

Fukuoka 812-8581, Japan

Key Words : Fluid Dynamics, Compressible Flows

ABSTRACT

Experimental and computational studies on supersonic mixing by slotted injection have been conducted. In the experiment flat plate model is installed into supersonic free stream of Mach number of 4 and fully developed turbulent boundary layer is established on it. The secondary jet is injected through slot in order to keep the flow in two-dimensional to simulate SCRAM-jet supersonic mixer. Surface pressure distributions and spatial pressure distributions are measured as well as flow visualization by the Schliren picture. The same flow field is simulated by solving Navier-Stokes equations and calculated results are compared with experiments. Quite good agreements are obtained. The results show the newly developed numerical code is quite useful to analyze the supersonic mixing flow physics.

1.INTRODUCTION

SCRAM-jet engine is considered to be one of the useful propulsion system for a super/hypersonic transportation vehicle and various researches were made to develop the engine. However, there are a lot of problems to be solved to develop it and one of them is the problem of the supersonic mixing.

In the SCRAM-jet engine combustor, main air flow is supersonic and residence time of the air is very short (about 1ms). Hence rapid mixing of the air and fuel is necessary but suppression of the mixing shear layer occurs and that makes difficult to mix air and fuel[1]. Also total pressure loss occurs by the shock wave which is made by the interference of the air and fuel. Total pressure loss is not preferable because it leads to the thrust loss and thus development of the injection method where air and fuel is mixed effectively and on the other hand total pressure loss is suppressed is necessary.

In order to understand the detailed flow physics of supersonic mixing both experimental and computational studies had better be conducted at the same time. Also in the practical application two-dimensional slotted injector configuration is one of the promising device to inject much fuel into main air flow. Experimental and computational studies on supersonic

mixing by slotted injection have been conducted. In the experiment flat plate model is installed into supersonic free stream of Mach number of 4 and fully developed turbulent boundary layer is established on it. The secondary sonic jet of nitrogen is injected through slot in order to keep the flow in two-dimensional to simulate SCRAM-jet supersonic mixer.Surface pressure distributions and spacial distributions are measured as well as flow visualization by the Schliren picture. The same flow field is simulated by solving Navier-Stokes equations and calculated results are compared with experiments. Quite good agreements are obtained. The results show the newly developed numerical code is quite useful to analyze the supersonic mixing flow physics.

2. EXPERIMENTAL STUDY ON SUPERSONIC MIXING BY SLOTTED INJECTION

Experiments were conducted in a supersonic wind tunnel, whose nominal Mach number is 4 and total pressure is 1.2 MPa. The total temperature is atmospheric temperature. Test section size is 150mm high and 150mm wide. Flat plate model was set in the test section. The schematic diagram of the flat plate model is shown in Fig.1. Distance between the upper surface of the model and the upper wall of the wind tunnel is 75mm. Aerodynamic fences were set at both ends of the slit in order to eliminate 3-dimentionality of the flow and realize highly 2-dimentional flow experimantally.
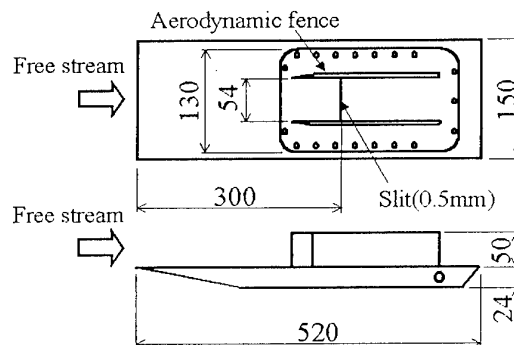

Fig.1 Schematic of the flat plate model

---

*   Proffessor, Department of Aeronautics and Astronautics.
**   Graduate student, Department of Aeronautics and Astronautics.

Sonic nitrogen was injected from the slit. Average experimental condition for various runs is shown in table.1.
In the experiments surface pressure distributions and spatial distributions are measured as well as flow visualization by the Schliren picture. Those results will be discussed with calculated results.

Free Stream	Gas	Air
	Mach Number	3.76
	Total Pressure	1.12MPa
	Total Temperature	284.7K
Secondary Gas	Gas	Nitrogen
	Mach Number	1.0
	Total Pressure	0.20MPa
	Total Temperature	284.7K

Table.1 Experimental conditions

3.COMPUTATIONAL STUDY ON SUPERSONIC MIXING BY SLOTTED INJECTION

The same flow fields are simulated numerically by solving 2-dimentional full Navier-Stokes equation using AUSM-DV scheme[2] with MUSCL interpolation for convective terms and full implicit LU-ADI factorization method[3] for time integration. Central difference is used for viscous terms and Baldwin-Lomax turbulence model[4] is also employed. Equation solved in the code is shown below.

$$\frac{\partial Q}{\partial t} + \frac{\partial (E\text{-}Ev)}{\partial x} + \frac{\partial (F\text{-}Fv)}{\partial y} = O$$

$$Q = \begin{pmatrix} \rho \\ \rho u \\ \rho v \\ e \\ \rho f_s \end{pmatrix}, \quad E = \begin{pmatrix} \rho u \\ \rho u^2 + p \\ \rho u v \\ (e + p)u \\ \rho u f_s \end{pmatrix}, \quad F = \begin{pmatrix} \rho v \\ \rho u v \\ \rho v^2 + p \\ (e + p)v \\ \rho v f_s \end{pmatrix}$$

$$Ev = \begin{pmatrix} 0 \\ \tau_{xx} \\ \tau_{xy} \\ u\tau_{xx} + v\tau_{xy} + \kappa T_x + \rho \sum h_s D_s \frac{\partial f_s}{\partial x} \\ \rho D_s \frac{\partial f_s}{\partial y} \end{pmatrix}$$

$$Fv = \begin{pmatrix} 0 \\ \tau_{yx} \\ \tau_{yy} \\ u\tau_{yx} + v\tau_{yy} + \kappa T_y + \rho \sum h_s D_s \frac{\partial f_s}{\partial y} \\ \rho D_s \frac{\partial f_s}{\partial y} \end{pmatrix}$$

$$\tau_{xx} = \frac{2}{3}\mu(2u_x - v_y), \quad \tau_{yy} = \frac{2}{3}\mu(2v_y - u_x)$$

$$\tau_{xy} = \tau_{yx} = \mu(u_y + v_x)$$

2-dimentional flow field with sonic gaseous nitrogen injected from the slit was solved involving inner nozzle flow of the slit. Grid number is 238 × 100 in x-direction and y-direction

respectively for the main flow above the flat plate and 20×53 for the flow inside the nozzle of the slit. Grid employed in the calculation is shown in Fig.2. Calculation region is from 80mm upstream from the slit center to 120mm downstream from the slit center. Calculation grid height is 160mm and effect of the reflection shock from the upper wall of the wind tunnel is not considered in the calculation. As an inflow boundary for the main flow, values obtained from the rather simple calculation with grid number 168×100 solving merely the flow above the flat plate were imposed on i=1 and i=2 plane. As an inflow boundary for the inner flow of the slit, conditions below were imposed and total temperature and total pressure were set identical to that of the experiments assuming the isentropic flow at the inlet plane.

$$u_{j=1,nozzle} = u_{j=2,nozzle} \quad , \quad v_{j=1,nozzle} = v_{j=2,nozzle}$$

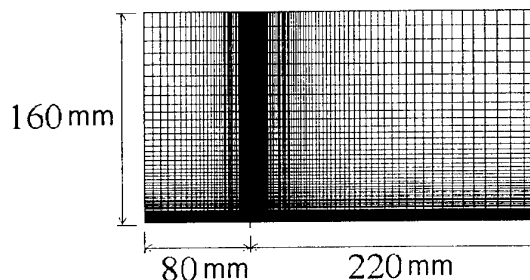4 grids overlap at the exit of the slit in order to maintain the 2-order accuracy.

Fig.2 Calculation grid

4.EXPERIMENTAL AND COMPUTATIONAL RESULTS AND DISCUSSIONS

Experimental and computational Wall pressure distribution are shown in Fig.3. Both are normalized by static pressure of the main flow (p_{ref}). Experimental pressure distribution shows sharp increase due to flow separation before injection point at first and shows plateau pressure until injection point. After the injection point pressure shows minimum pressure followed by local maximum pressure due to flow recompression. The numerical simulation predicts separation point and pressure plateau precisely in front of the injection point. The calculated pressure distribution shows lower pressure recovery. This is due to underestimate of the recompression shock wave strength.
Pitot total pressure distributions were also measured along x=0,5,10 and 20mm plane. Comparisons between experiment and calculation are shown in Fig.4, 5, 6 and 7. Pitot pressure is non-dimentionalized by the total pressure of the main stream (p_o). In the calculation, pitot total pressure was calculated using Rayleigh pitot-tube formula(Eq.1). Although using this fomula in the calculation, computational result and experimental result show quite good agreement.

$$\frac{p_{pitot}}{p} = \left\{ \frac{(\gamma - 1)M^2}{2} \right\}^{\frac{\gamma}{\gamma-1}} \left\{ \frac{\gamma + 1}{2\gamma M^2 - (\gamma - 1)} \right\}^{\frac{1}{\gamma-1}} \qquad (1)$$

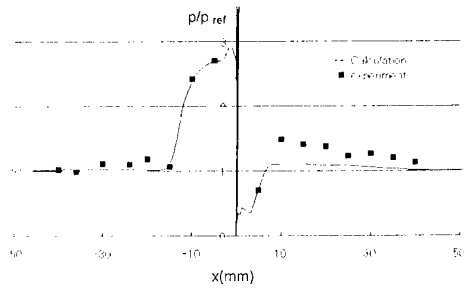Mach contour obtained by the calculation is shown in Fig.8.
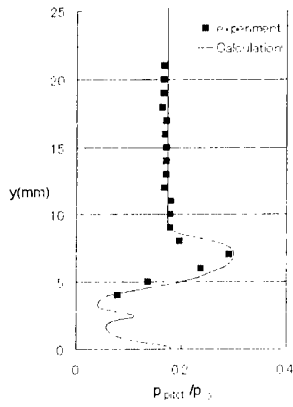

Fig.3 Static wall pressure distribution

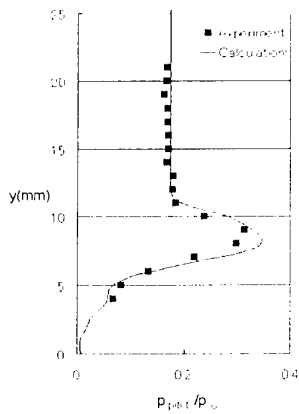Fig.6 Pitot total pressure distribution(x=10mm)

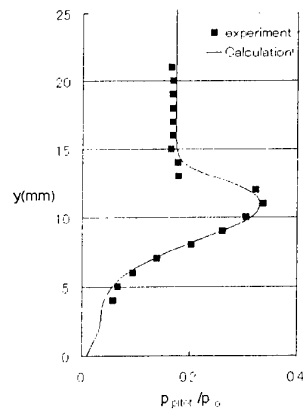Fig.4 Pitot total pressure distribution(x=0mm)

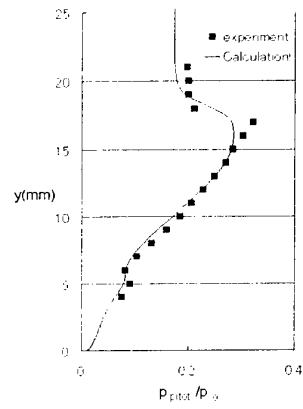Fig.7 Pitot total pressure distribution(x=20mm)

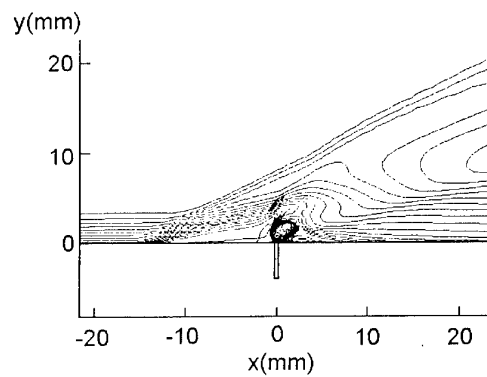Fig.5 Pitot total pressure distribution(x=5mm)

Fig.8 Mach contour

5.CONCLUSIONS

Experimental and computational studies on supersonic mixing by slotted injection have been conducted in order to understand the flow physics of supersonic mixing with two-dimensional configurations. Surface pressure distributions and spatial distributions are measured as well as flow visualization by the Schliren picture. The same flow field is simulated by solving Navier-Stokes equations and calculated results are compared with experiments. Quite good agreements are obtained. The results show the newly developed numerical code is quite useful to analyze the supersonic mixing flow physics.

REFERENCE

1. Bogdanoff, D.W., "Compressibility Effects in Turbulent Shear Layer," AIAA journal Vol.21, No.6, pp.926-927, 1983.
2. Wada, Y. and Liou, M.S., "A Flux Splitting Scheme with High-Resolution and Robustness for Discontinuities," AIAA paper 94-0083, Reno, Nevada, Jan. 1994
3. Obayashi, S., Matsushima, K., Fujii, K. and Kuwahara, K., "Improvements in Efficiency and Reliability for Navier-Stokes Computations Using the LU-ADI Factorization Algorithm," AIAA paper 86-0338, Reno, Nevada, Jan, 1986
4. Baldwin, B.S. and Lomax, H., "Thin Layer Approximations and Algebraic Model for Separated Turbulent Flows," AIAA paper 78-257, Huntsville, Alabama, Jan, 1978

EXPERIMENTAL INVESTIGATION OF AXISYMMETRIC NOZZLE – VANES – PLUG TVC ARRANGEMENT

A. A. Hashem[*]
Cairo University, Cairo, Egypt
AND
W. A. Aissa[**]
High Institute of Energy, Aswan, Egypt

Key Words: TVC, Externally mounted vanes, Plug

ABSTRACT

Thrust Vector control (TVC) is the only option for many situations in which aerodynamic control fails namely, STOL, post stall maneuverability, and maneuverability at transonic and supersonic speeds. The development of an efficient and practical TVC arrangement which can vertify the requirements of thrust vector and magnitude control of aircrafts in both cruise and transient flight is reported. The arrangement of interest utilizes two vanes installed on the nozzle sidewalls and deflected in and out the flow to provide thrust vectoring. Floating conical plug is mounted at axisymmetric convergent nozzle centerline and moved relative to its exit to control thrust magnitude. The purpose of the present work is to investigate the performance parameters of this combination when statically tested for various NPR, vane deflection angle and location of floating conical plug relative to nozzle exit.

1. INTRODUCTION

TVC allows supermaneuverability of aircrafts by deflecting nozzle exhaust jet away from axial direction[1]. Experimental work[2-5] was conducted for the analysis of pitch and yaw thrust vectoring by utilizing externally mounted vanes post the nozzle . The performance when mounting a plug and moving it axially relative to axisymmetric convergent nozzle equipped with externally mounted vanes[6] was invistigated. Dimensional analysis was utilized[7] to prove that transient test results can be treated as as quasi-steady flow. Moreover, genealized force and moment coefficients were formulated and used to analyze thrust vectoring performance of axisymmetric convergent nozzle equipped with externally mounted post exit vanes.
This paper represents one of the first efforts to successfully integrate floating conical plug into an efficient axisymmetric convergent nozzle/externally thrust vectoring vanes arrangement and to analyze its performance parameters.

2. EXPERIMENTAL SETUP

Pressurized clean dry air is allowed to flow from a suitable tank volume to venturi-meter, to measure its mass flow rate
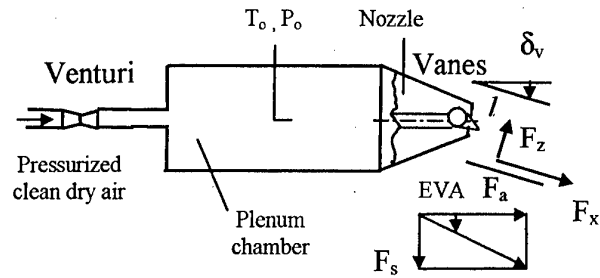

Fig. 1 Experimental setup

; Fig. 1, and settles in plenum chamber where its stagnation temperature and pressure T_o , P_o are measured. Test is conducted in transient mode as tank pressure decreases. Two vanes are mounted post the nozzle exit and deflected in and out the flow to control the engine thrust vector. Vane pivots about point p. Its internal flow passage is a segment of a cone of a half cone angle; $\delta = 2.9°$,and its length; l is 50.8 mm. The upper vane internal pressure is measured using sixteen pressure taps.
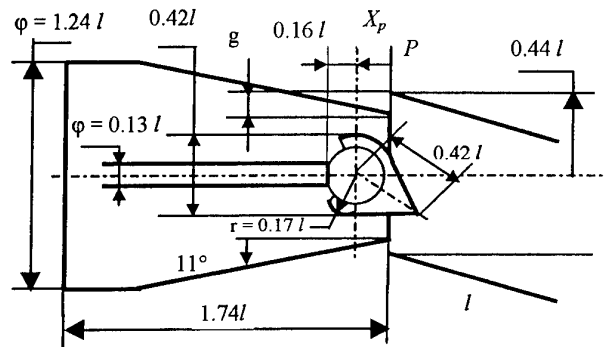
Location	a	b	c
Configuration	Ca	Cb	Cc
X_p/l	0.423	0.213	0

Fig. 2 Schematic drawing of
Nozzle/plug/vanes configurations

[*]Associate Professor, Aerospace Department
[**] Assistant Professor, Mechanical Power Department

The tested plug nozzle; Fig. 2, is a baseline convergent nozzle which throat area is varied by moving the plug axially relative to the nozzle exit area, where plug location a (designated by Ca) refers to maximum throat area, while location c (designated by Cc) refers to minimum throat area, and location b (designated by Cb) refers to intermediate throat area. The nozzle exit diameter is $0.69l$.

Data Acquisition system is used to store measured data (line pressure, vane inner surface static pressures, venturi meter upstream and throat sections static pressures, plenum chamber stagnation pressure and temperature).

3. EXPERIMENTAL DATA ANALYSIS

Vane pressure distribution is obtained using fifth order polynomial function to fit the vane sixteen static pressure measured points. Three-dimensional plots are used to present the pressure coefficient distributions over the vane surface area as defined by,

$$C_P(x,s) = (P - P_a)/P_a \qquad (1)$$

Where s is the circumferential distance measured from the vane highest point at the axial distance x.

The pressure at a point on the vane surface (x,s), as evaluated by the interpolation scheme is used to calculate the incremental forces and moments. The incremental force components ($\delta F_x, \delta F_y, \delta F_z$) and moment components ($\delta M_x, \delta M_y, \delta M_z$) referred to vane fixed coordinates are evaluated. The incremental hinge moment is then estimated. Integrating, the resultant components of force and moment are obtained for both the inside and outside vanes. The resultant force is resolved into axial (Fa) and side force (Fs) components.

The aerodynamic performance of the vane is rationalized[7]. the side force, axial force, and hinge moment coefficients were defined as:

$$F_s = q_{ref} \, n \, A_{vp} \, C_{Fs}, F_a = q_{ref} \, n \, A_{vp} \, C_{Fa} \qquad (2)$$

$$M_h = q_{ref} \, n \, A_{vp} \, lC_{mh} \qquad (3)$$

Where n is the number of vanes and q_{ref} is a reference dynamic head[7], given by

$$q_{ref} = P_0 \, (1 - (1/NPR)^{(\gamma-1)/\gamma}) \, f(\gamma) \qquad (4)$$

Where, $f(\gamma) = \dfrac{\gamma}{(\gamma-1)} (\dfrac{2}{\gamma+1})^{\frac{1}{\gamma-1}}$ \qquad (5)

, nozzle pressure ratio (NPR) is defined as

$$NPR = P_0/P_{atm} \qquad (6)$$

These force and moment coefficients help in systemizing the experimental work and generalizing its results. The coefficients depend on the non-dimensional vane/nozzle geometry: length to radius ratio (l/d_{th}), vane width to length ratio (w/l) , plug non-dimensional axial location (x_p/l), and radial gap ratio (g/d_{th}), besides the vane angle.

An effective vane angle representing the vane resultant force direction is defined as

$$EVA = \tan^{-1}(F_s/F_a) \qquad (7)$$

Nozzle discharge coefficient is given by

$$C_d = \dot{m}_a / \dot{m}_i \qquad (8)$$

4. RESULTS AND DISCUSSION

Fig. 3 presents samples of the inward moving vane pressure distribution, at NPR equal 6.0, for convergent nozzle with plug at locations a, b and c. The effect of varying NPR and vane deflection ange was previously desribed in reference 7, which also gave an insight view of effect of flow pattern downstream the nozzle exit.

a) Ca, 30°   b) Ca, 10°

c) Cb, 30°   d) Cc, 30°

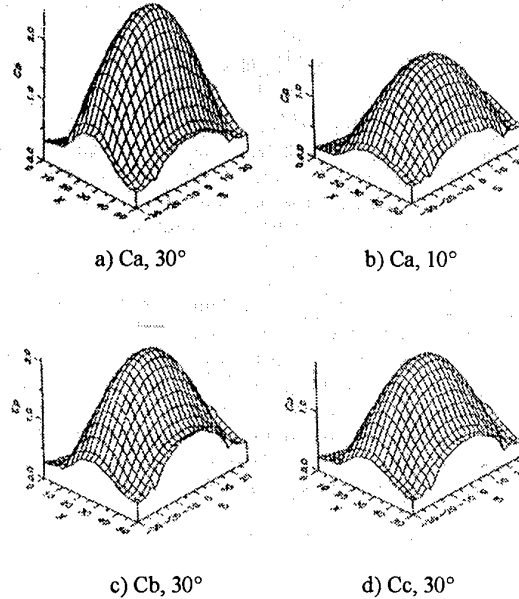Fig. 3 Vane pressure distribution for upper vane
(convergent nozzle with floating concal plug, NPR = 6.0)

Comparing Figs. 3-a and 3-b, It could be remarked that upper vane has bigger pressure distribution and more forward point of maximum pressure for 30 degrees delection angle compared to that for 10 degrees deflection angle, this is as the waves emanating from the nozzle throat impinges the vane surface at a point which is closer to the vane leading edge. Figs. 3-a, 3-c and 3-d show that pressure distribution in the case of location a is bigger than that of location b which in turn is bigger than that of location c due to higher jet momentum.

The performance of convergent nozzle with plug at locations a,b and c for different nozzle pressure ratios and vane deflection angles is illustrated in Figs. 4 to 8.

Nozzle internal performance is represented by nozzle discharge coefficient (Cd) and and axial force coefficient (CFa).

Fig. 4 shows nozzle discharge coefficient variation, it could be remarked that location a has bigger discharge coefficient compared to location b which in turn is bigger than that of location c. It could be remarked also that discharge coefficient decreases with the increase of vane deflection angle for both locations a and c for all measured deflection angle range. However, for location b, it decreases with the increase of vane deflection angle for vane deflection angles less than 20° , and is constant for vane deflection angles bigger than 20°. This may be due to for plug nozzle (locations a and c) and the whole measured vane deflection angle range and plug nozzle location b and deflection angles less than 20° , plug nozzle forms convergent flow passage, while it forms convergent divergent flow passage for plug nozzle location b and deflection angles greater than 20°.
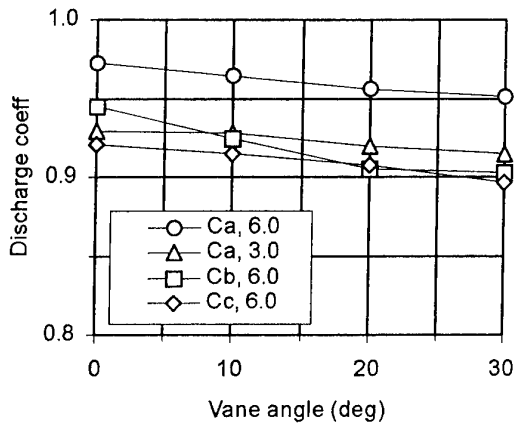
Fig. 4 Nozzle discharge coefficient

While axial force increases with NPR increase, it decreases with inceasing vane deflection angle ; Fig. 5, due to deflecting thrust vector away from axial direction. Axial force for location a is greater than that of location b which in turn is greater than that of location c due to incease of vane pressure distribution.
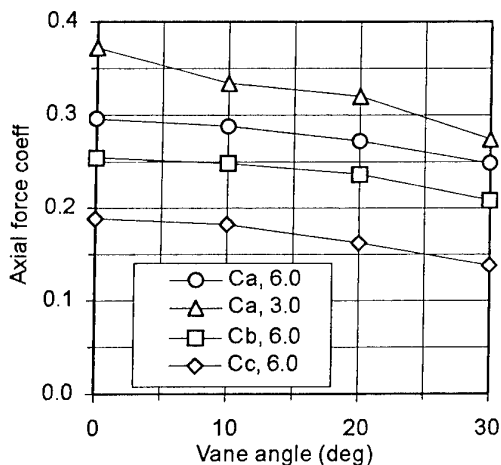

Fig. 5 Axial force for floating conical plug

As pressure distribution for the inflow and outflow vanes are identical in the case of zero vane deflection angle, hence the plug rotates such that its centerline coincides with that of the nozzle, and the net side force is zero as shown in Fig. 6.

However, in the case of vane deflection, the inflow vane pressure is remarkably bigger than that of the out of flow vane as out of flow vane rarely catches the flow as discussed in Ref. 6, and the plug rotates to vertify an equilibrium position; as shown in Fig. 2. Thus, side force increases with the increase of NPR and vane deflection angle.

Hinge moment increases with the increase of NPR due to higher jet momentum and with vane deflection angle due to bigger side force; Fig. 7. However, as it could be remarked in equations (2) and (3), the force and moment coefficients can represent variations in the corresponding forces and moments. However, although force (axial or side) and moment increase with the increase of NPR; as mentioned in Ref. 6, force and moment cofficients; Figs. 5-7, decrease with the increase of
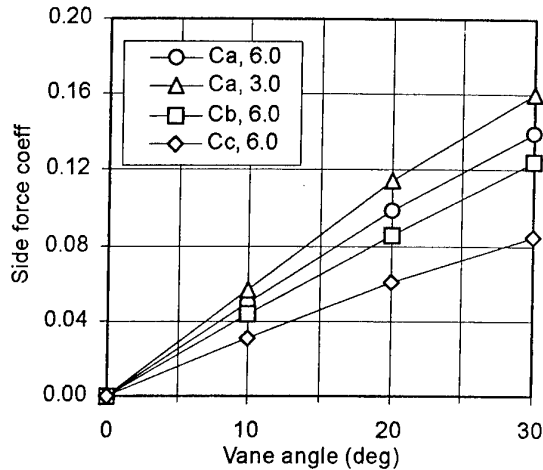
NPR as the increase of dynamic head due to NPR increase is bigger than the corresponding increase in force and moment.

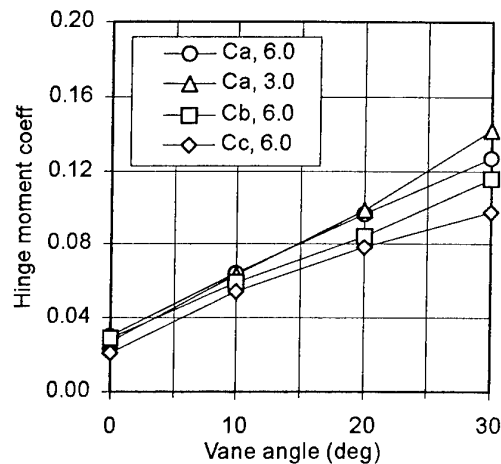
Fig. 6 Side force for floating conical plug

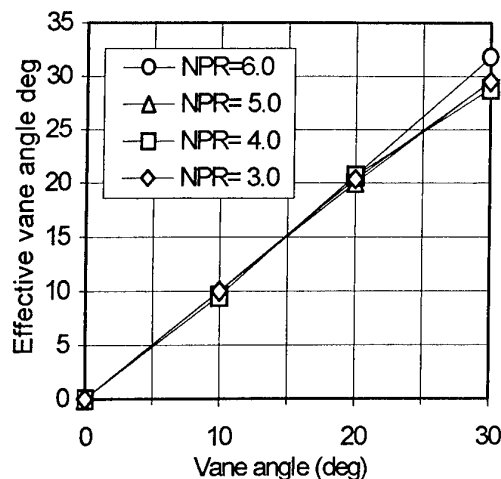Fig. 7 Hinge moment coefficient variation

Fig. 8 Effective vane angle for floating conical plug-location b

Fig. 8 reveales that the difference between effective vane angle and geometric vane angle increases with the increase of vane deflection angle, this may be due to flow separation at high vane deflection angles. It could be concluded that EVA is not greatly senstive to NPR variation.

5. CONCLUSIONS

A static test for evaluating the performance of thrust control arrangement has been discussed. Data for an axisymmetric convergent nozzle in which two vanes are mounted post the nozzle exit and a central floating plug of conical profile have been presented. Results have been obtained for different nozzle pressure ratios, vane deflection angles, and plug location relative to the nozzle exit. Results indicate that performance is in general sensitive to the above mentioned testing variables. However, some parameters are not greatly affected by NPR variation. Axial force, side force, and hinge moment are rationalized. Although axial force, side force, and hinge moment increase with NPR increase, the corresponding force and moment coefficients decrease for NPR increase. For plug locations close to the nozzle exit, the nozzle plug combination forms a convergent divergent flow passage.

REFERENCE

1. Gal-OR, B., "Fundamental Concepts of Vectored Propulsion," J. Propulsion, Vol. 6, No. 6, Nov. - Dec. 1990.
2. Tamrat, B. F., and Antani, D. L., "Static Test Results of an Externally Mounted Thrust Vectoring Vane Concept," AIAA paper AIAA-88-3221, AIAA
3. Bare, E. A., and Reubush, D. E., "Static Internal Performance of a Two - Dimensional Convergent-Divergent Nozzle with Thrust Vectoring," NASA TP-2721, July 1987.
4. Berrier, B. L., and Mason, M. L., "Static Performance of an Axisymmetric Nozzle with Post-Exit Vanes for Multiaxis Thrust Vectoring," NASA TP - 2800, May 1988.
5. Mason, M. L., and Berrier, B.L., "Static Performance of Non axisymmetric Nozzles with Yaw Thrust-Vectoring," NASA TP-2813, May 1988.
6. Aissa, W. A., "Thrust Control Using Combined Vanes and Plug Arrangements," Ph. D Thesis, Cairo University, May 1999.
7. Aissa, W. A., and Hashem, A. A.. "Experimental Analysis of Thrust Control Using External Vanes,", To be published.

A STUDY OF 2-D TURBINE BLADE PROFILE TO MINIMIZE THE PRESSURE LOSS

Soo-Yong Cho* Eui-Soo Yoon** and Bum-Seog Choi***

* Gyeongsang National University and Chinju, KOREA, 660-701
, * Korea Institute of Machinery and Materials and Daejeon, Jang-dong 171, KOREA, 305-343

Key Words: Viscous Flows, Compressible Flows, Turbulent Flows

ABSTRACT

A two-dimensional axial-type turbine blade is optimized. Shape parameters are used to design a blade profile, and these shape parameters are employed as design variables for optimization. These consist of polynomial function for suction and pressure side, ellipse for leading edge and circle for trailing edge. As an objective function, the pitchwise averaged total pressure is selected at the 30% downstream of axial chord length from the trailing edge, which is the inlet location of next stage turbine blade. Aerodynamic, mechanical and geometry constraints are imposed to ensure that the optimized profile meets all engineering restrict conditions. Two-dimensional compressible flow analysis codes are applied and validated with the experimental results on the VKI turbine blade. A turbine blade profile for optimization is selected at the mean radius of turbine rotor using a heavy-duty gas turbine. 11 design variables are chosen for blade design. On the optimized turbine rotor, the total pressure reduction is 6%, which is same to the 0.6% total-to-total efficiency increase.

NOMENCLATURE

A	blade sectional area
Cl	blade loading coefficient
Cp	pressure coefficient
Cx, Ct	axial and tangential chord
d_{te}	straight section of trailing edge
h	enthalpy
o	throat
P	pressure
Px, Py	peak point of pressure surface
$P_t{}^*$	total pressure
Re	Reynolds number
r_{le}, r_{te}	leading and trailing edge radius
Sx, Sy	peak point of suction surface
v	absolute velocity
w	relative velocity
Y	total pressure loss coefficient
β_{in}, β_{out}	inlet and exit blade angle
$\varepsilon_{up}, \varepsilon_{up}$	inlet upper and lower wedge angle
η_{ux}, η_{uy}	half of major and minor axis of upper ellipse
η_{lx}, η_{ly}	half of major and minor axis of lower ellipse
φ	turning angle on pressure surface
κ, λ	leading and trailing edge turning angle
ρ	Density
ξ	enthalpy loss coefficient
ζ	unguided turning angle

Subscripts

0	initial value
t	stagnation
∞	value at reference location
1,2,3	nozzle inlet, nozzle exit, rotor exit

1. INTRODUCTION

The turbine efficiency is the most important factor on the performance of heavy duty gas turbines for power plants, air turbines, or turbo expanders etc.,. Losses in the turbine consist of mechanical losses due to rotating parts or bearings, tip clearance losses due to the tip gap, secondary flow losses due to curved passages, and profile losses due to the blade shape. More than 60% of total loss on one stage of turbine is generated by two latter loss mechanism. These losses could be reduced how to design a turbine blade profile. So, it needs to develop a new design technology for optimum turbine blade profile.

Blade profiles have been designed according to the inlet and exit conditions with considering the aerodynamic characteristics such as incidence or deviation angle as well as the structural characteristics. Many methods to design a blade profile have been developed such as a method using multi-polynomial [1], method using shape parameters [2], and inverse method [3] etc.,. Even blades have been designed according to the design point by any one among several methods, it is not known the relationship between the blade profile and its efficiency.

3-D turbine blade profile is usually designed by stacking 2-D blade profiles which are designed according to the flow conditions at several radial locations, therefore; the optimization of 2-D blade profile gives lots of effect to the efficiency of 3-D turbine blade. It was tried by using Bezier curves [4]. In this study, shape parameters, which can modify the blade profile directly, are applied to optimize a 2-D blade profile. This method has advantages such as it can be figured out the relationship between a blade profile and its efficiency directly because the blade profile is controlled by shape parameters.

It is selected the pitchwise area averaged total pressure at 30% axial chord downstream from the trailing edge as an objective function. It is maximized without losing blade loading and blade sectional area. This is same to minimize the total pressure loss in the passage.

2. SELECTION OF DESIGN VARIABLES

* Assistant Professor, Department of Aerospace and Mechanical Engineering
** Principal Researcher, Department of Environmental and Thermal-Fluid Engineering
*** Senior Researcher, Department of Environmental and Thermal-Fluid Engineering

Shape parameters which are able to design general axial-type turbine blades are induced from a seriously twisted turbine blade. Fig. 1 show these parameters, which was good enough to design general axial type turbine blades [5].

Using many shape parameters could express the blade profile well and has a flexibility to control the profile locally, but it requires much computational time for optimization and makes the method of blade design complex. 11 shape parameters are chosen without reducing the accuracy of blade design basis on the shape parameters which have strong effect [6]. Shape functions for optimization do not need because the chosen design variables can change the shape of blade profile directly.
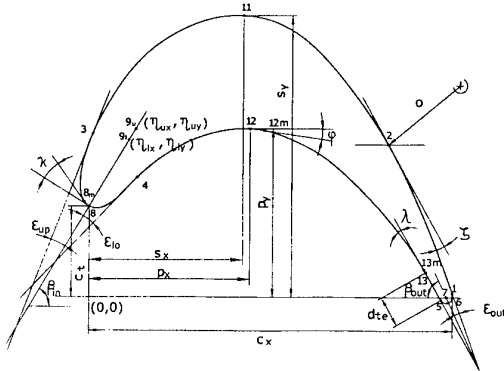

Fig. 1 Shape parameters for designing general axial-type turbine blades

Table 1 Shape parameters and design variables for blade optimization

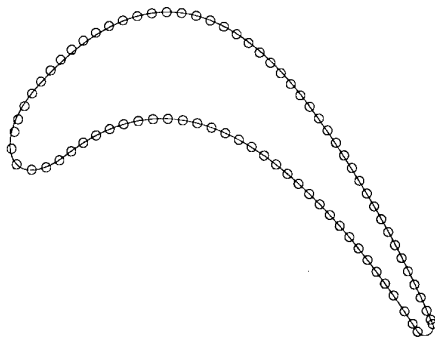| Shape parameters	Design variables
ζ	θ_2, θ_1
ε_{up}	θ_3, pt3 (x_3, y_3)
ε_{lo}	θ_4, pt4 (x_4, y_4)
ε_{out}	θ_5, θ_1
η_{ux}, η_{uy}	θ_3, pt3 (x_3, y_3)
η_{lx}, η_{ly}	θ_4, pt4 (x_4, y_4)
o	θ_2, pt2 (y_2)
c_t	pt8 (y_8)

Fig. 2 Comparison of redesigned blade profiles using design variables

To make a blade profile by using 11 design variables listed in table 1, ellipse from the leading edge(pt8) to pt3 on the suction surface, 3rd order polynomial from pt3 to the throat(pt2), and circle from the throat to the trailing edge(pt1) are employed. On the pressure surface, ellipse from the leading edge to pt4, 3rd order polynomial from pt4 to pt5, and circle at the trailing edge(pt5-pt1) are employed.

Fig. 2 shows redesigned blade profiles using design variables by the solid line. It shows some deviations between the original and redesigned blade profile at the fore part of suction surface. Standard deviation(σ) between the original and redesigned blade profile is calculated. σ is 0.45% on the suction surface and 0.17% on the pressure surface, so totally less than 0.33%. It is enough to start optimization because its shape is changed in the optimization process

3. OPTIMIZATION AND FLOW ANALYSIS ALGORITHM

3.1 Objective Function and Constraints

We can choose the blade loading as an objective function on the turbine blade, but the increment of blade loading should accompany with the increment of blade area due to larger torsional stress. In this study, total pressure loss instead of blade loading is chosen as an objective function. Minimizing the total pressure loss is equivalent to maximize the pitchwise area averaged total pressure at 30% axial chord, which is approximately axial gap between blade to blade, downstream from the trailing edge. Constant total pressure is maintained at the inlet during optimization.

$$\text{Maximize ; obj} = P_t(X) \text{ at } x = 1.3Cx \qquad (1)$$
$$A \geq A_0$$
$$Cl \geq Cl_0$$

Constraints are applied to the initial blade sectional area and blade loading, and these values should not decrease than initial values in the optimization process. Another constraint comes from geometry conditions. Ellipse is applied to the shape of leading edge, and its shape depends on the inlet wedge angle. To use an ellipse as a blade profile, maximum and minimum wedge angles should be restricted not to generate a wiggled profile.

The initial blade sectional area and blade loading coefficient are 0.2133 and 1.467, respectively. The initial total pressure coefficient, which is the pitchwise area averaged at 30% axial chord downstream from the trailing edge and normalized by $\rho_\infty U_\infty^2$, is 2.9037.

3.2 Optimization Algorithm

Optimization is a procedure to find design variables(X), which make the objective function to be optimized (maximization, minimization, or target), without violating given constraints. In this study, VisualDOC[7], which is developed as a commercial code by Vanderplaats, is used for blade optimization. MMFD(Modified Method of Feasible Direction) among many methods is applied with constraints.

3.3 Flow Analysis Scheme

Continuity equation, momentum equations, equation of state, and energy equation are used for compressible viscous flow analysis. For turbulent flow analysis, two-equation extended k-ε turbulence model [8] is applied with standard wall function. The difference between the two-equation standard k-ε turbulence model and extended k-ε turbulence model occurs on the dissipation rate equation. The extended k-ε turbulent model includes two time scales to allow the dissipation rate to respond to

the mean strain more effectively than that of the standard k-ε turbulent model [9]. Computed results with the extended k-ε turbulent model were better than those with the standard k-ε turbulent model for complex turbulent flow problems [8,9].

The governing equations are transformed to the generalized coordinates and differentiated within the finite control volume. A 2nd order central differencing scheme is applied to the convective terms with adaptive 2nd and 4th order dissipation terms. The viscous and source terms of the governing equations are discretized by 2nd order central differencing scheme. A 2nd order upwind scheme is employed for all scalar transport equations including turbulence modeling equations. A pressure based predictor/multi-corrector solution procedure is employed to ensure divergence free flowfield solutions at the end of each time marching step. A time centered Crank-Nicholson scheme is used for the temporal discretization. To solve the system of linear algebraic equations, an iterative ADI method is employed.

In the computational region, exit is selected at the far downstream not to be affected by the disturbance of passage flow and velocities at the exit are compensated to be constant mass flow rate. Computational blocks are inserted to avoid grid skewness and distortion at the leading and trailing edge. Inserted computational blocks improve the smoothness and orthogonality of grids. Fig. 3 shows the grids developed with multi-blocks on the turbine blade.
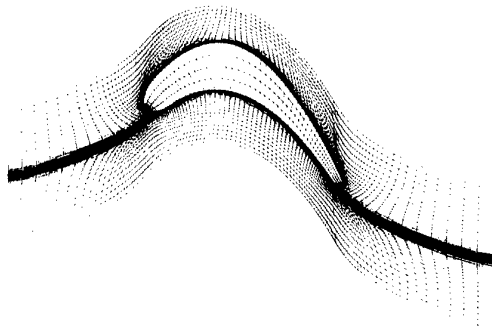

Fig. 3 Computational grids generated with multi-blocks within a turbine passage

4. RESULTS AND DISCUSSIONS
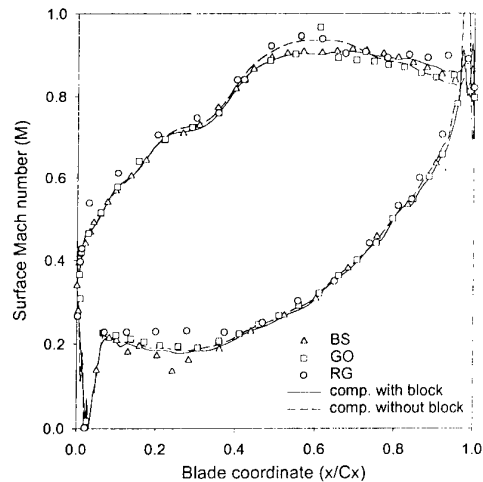
4.1 VKI Turbine Blade

Flow structures on the VKI turbine blade [10] are calculated in order to validate the flow analysis code. Flow conditions set equally to the experimental conditions, and inlet Mach number is 0.265. As a first case, the transonic flow is calculated. The exit Mach number is 0.97. Reynolds number and temperature at the inlet are 8.6×10^5 and 293K, respectively. 85x24 grids are employed. In a transonic flow condition, shock wave occurs at the throat and expansion wave occurs at the trailing edge. The computed results also show the shock and expansion wave as shown in experimental results from the density contours clearly.

Fig. 4 shows the surface Mach number, which is obtained from the relationship between the surface static pressure and total pressure. In the figures, computed results show that employing multi-blocks gives more stable and accurate computed results due to improve the orthogonality and smoothness of grids. Fig. 4(b) shows the surface Mach number compared with those tested in pure subsonic flow conditions. Reynolds number and exit Mach number are 7.8×10^5 and 0.78, which are same to the experiment conditions. The computed results agree well with the experimental

results. As shown in Fig. 4(a), the results computed with multi-blocks are better than those with single computational block. From these results, the multi-blocks are employed in the computational region for the following turbine blade optimization.
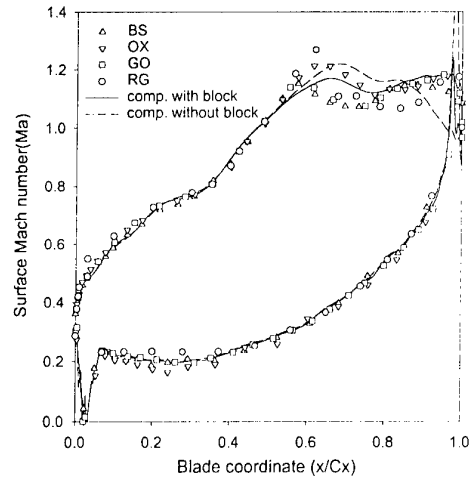
(a) Transonic flow, $Ma_{ex}=0.97$ and $Re=8.6 \times 10^5$

(b) Subsonic flow, $Ma_{ex}=0.78$ and $Re=7.8 \times 10^5$

Fig. 4 Comparison of surface Mach numbers computed with multi-block and single block grid on the VKI turbine blade with the transonic or subsonic flow condition

4.2 Blade on a Heavy Duty Gas Turbine

A turbine rotor using on a heavy-duty gas turbine is selected and 2-D blade profile at the mean radius of turbine rotor is chosen for optimization. In the optimization process, boundary conditions at the inlet and exit set to operating conditions on the design point [11] which is shown in Table 2. Inlet Mach number is 0.5462 and Reynolds number is 1.74×10^6. In order to decide the number of grids without grid dependence, it is checked whether the surface pressure coefficient is converged or not according to the various grid number. The surface pressure coefficient is not changed even grids are increased more than 81x41. 101x51 grids are employed for sufficient grid independence. It is necessary 3800 iterations to obtain to 0.5×10^{-5} residual which is selected as the convergence condition. In this condition, the variation of objective function is

less than 0.1×10^{-3} even reducing the residual by more iteration.

Table 2 Operating and flow condition at the inlet and outlet to optimize

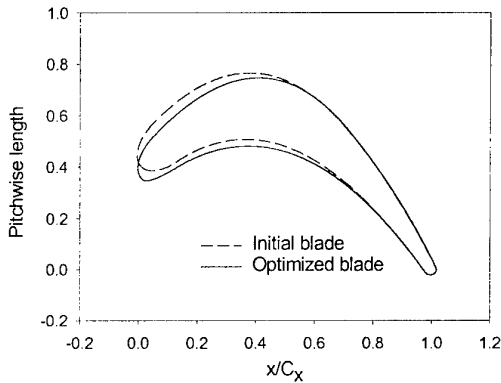| Contents	Inlet	Outlet
Pitch (Pitch/Cx)	0.75	0.75
Velocity (m/sec)	$U_\infty = 393.66$	
Static temperature (K)	$T_\infty = 1392.01$	$T_{out} = 1366.33$
Static pressure (Pa)	$P_\infty = 741918$	$P_{out} = 626509$
Flow angle (degree)	$\beta_{in} = 61.28$	$\beta_{out} = 61.84$
Density (kg/m³)	$\rho_\infty = 1.86$	

Fig. 5 Comparison of initial blade profile with optimized blade profiles

Axial chord of turbine blade is fixed in the optimization process. If the axial chord is not fixed, an objective function can not be decided as well as gas turbine has to modify seriously due to axial length change. So, it is allowed only the tangential chord length (Ct), which is shown in Fig. 1. It needs 45 iterations to reach the minimized total pressure loss in the passage without violating the given constraints. The blade sectional area and blade loading has no gain. Total pressure loss as an objective function is decreased to 6%.

Fig. 5 shows the difference between the initial blade and optimized blade. The difference in the rear part of blade is negligible, but the fore part moves downward circum-ferentially. From the optimization, the tangential chord length at the leading edge is decreased and the size of fore part on the blade is a little reduced. The reduced size of fore part on the blade prevents strong static pressure drop generated by fast turning flow around the leading edge, and makes the static pressure drop smoothly along the passage.
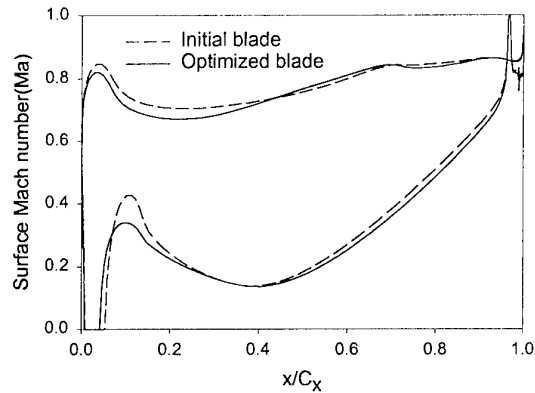
Fig. 6(a) shows the surface pressure coefficient, and the phenomena mentioned previous paragraph are shown clearly. The small static pressure drop on the fore part of the blade makes the change of surface Mach number weak. Fig. 6(b) shows that the surface Mach number is reversely changed to the static pressure change shown in Fig. 6(a). However, the surface pressure and Mach number are related with the flow area change along the passage directly.

Area of turbine passage is calculated by the size of circle between the pressure and suction surface. Fig. 7 shows the radius of circle within the optimized blade. This figure shows that the area within the passage is expanded to the maximum area, and then reduced to the throat after passing to the peak point of suction surface smoothly. The area on the rear part of the blade is

not changed. However, the changing rate of area on the optimized blade is small. This causes the reduction of total pressure loss.
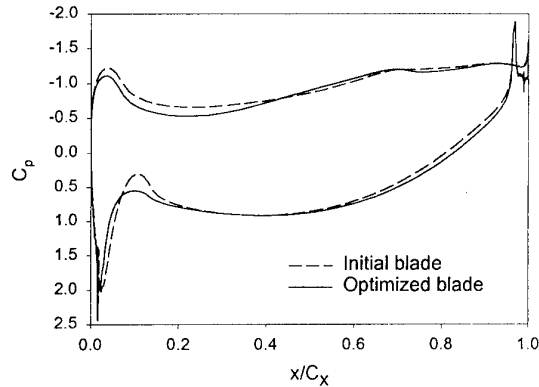
(a) Surface pressure coefficient

(b) Surface Mach number

Fig. 6 Surface pressure coefficient and surface Mach number on the initial and optimized blade
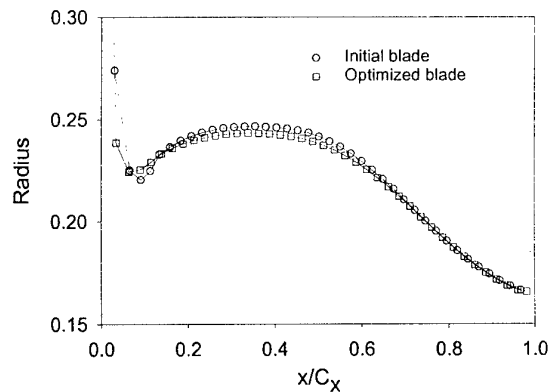

Fig. 7 Radius of circles between the pressure and suction surface within a passage to compare with the blade passage area

The reduction of total pressure loss at the exit is directly related with the efficiency increase. However, the efficiency is calculated from the enthalpy change. It needs the relationship between enthalpy loss coefficient and total pressure loss coefficient. In the incompressible flow, the total pressure loss coefficient could be simplified to $Y_N \cong \xi_N$. The relationship between Y_R and ξ_R is obtained by the same method as done on

the nozzle. Total-to-total efficiency is calculated using enthalpy loss coefficient from equation(2) defined by Horlock [12] as follows:

$$\eta_{t-t} = \cfrac{1}{1 + (\xi_R w_3^2 + \xi_N v_2^2)(1 + \cfrac{\gamma - 1}{2} Ma_3^2)/2(h_{t1} - h_{t3})} \quad (2)$$

P_t^* is defined as $P_t/(\rho_\infty U_\infty^2)$, and it is related with Y_N as follows;

$$Y_N = \cfrac{P_{t1} - P_{t2}}{\cfrac{1}{2}\rho_\infty U_\infty^2} = 2(P_{t1}^* - P_{t2}^*) \quad (3)$$

In the computation, Y_N is simplified to ξ_N because Mach number is less than 1 even the flow is compressible. Before optimization, ξ_N is 0.346, but ξ_N is changed to 0.326 after optimization with constraints. That is 6% reduction of total pressure loss. In order to apply these values to the equation(2), the equation part of denominator assumes to the O(0.1) with assumption of general turbine efficiency. 6% reduction of total pressure loss is same to the 0.6% total-to total efficiency increase with considering the enthalpy change due to the decrease of total pressure loss. This is obtained on only one stage of turbine. That effect is increased with the number of turbine stages.

Fig. 8 shows the curvature of blade surface. The quick change of blade curvature causes the flow separation and pressure loss [13]. It is important to design blade profile smooth. Constant curvature is generated on the rear part of suction surface because the circle is applied to that area. The changing rate of curvature on the optimized blade is smooth. Even the changing rate of curvature on the optimized blade is increased on the suction surface compared with the initial one, it is not steep but smoothly changed in a whole region.
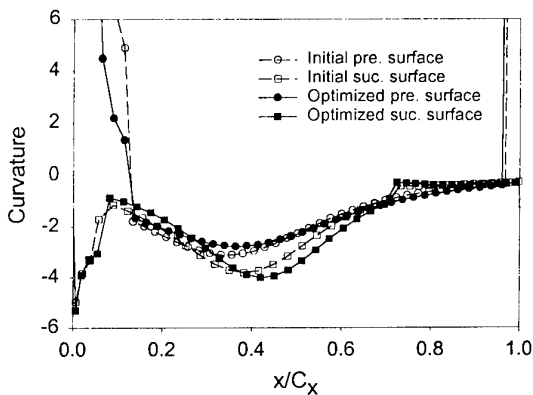

Fig. 8 Curvatures on the pressure and suction surface of blades

5. CONCLUSIONS

Blade is designed using shape parameters, and optimized. The axial chord of blade is fixed, and 11 design variables are employed for optimization. It is selected as an objective function the pitchwise area averaged total pressure at the 30% axial chord downstream from trailing edge, which is the inlet location of next turbine blade. Without reducing initial blade sectional area and blade loading, 6% of total pressure loss in the passage is reduced. This is same to 0.6% increase of total-to-total efficiency on the

one stage of turbine. The efficiency is increased with the number of turbine stage.

The size of fore part on the optimized turbine blade is a little reduced and the circumferential length of the leading edge is decreased. The optimized blade shape is not changed from the initial one in the rear part of blade i.e., from the throat to the trailing edge. The changing rate of blade passage area on the optimized blade is small compared with that on the initial one. This causes the reduction of profile loss and total pressure loss.

In the actual application, The optimization of 3-D blade is necessary. The method using shape parameters will expand to 3-D blade.

REFERENCES

1. Engeli, M., Zollinger, H. J. and Allemann, J. C. A Computer program for the design of Turbomachinery Blades. ASME 78-GT-36, 1978.
2. Cho, S. Y., Oh, K. S. and Choi, B. S. A Study of Design Parameters for Designing an Axial Turbine Blade Geometry. In *Proceedings of the 8th International Symposium on Transport Phenomena and Dynamics of Rotating Machinery*, Hawaii, Jan, pp. 222-228, 2000.
3. Demeulenare, A. and Braembussche, R. Three-Dimensional Inverse Method for Turbomachinery Blading Design. *J. of Turbomachinery*, 120, 247-254, 1998.
4. Goel, S., Cofer IV, J. I. and Singh, H. Turbine Airfoil Design Optimization. 96-GT-158, 1996.
5. Cho, S. Y., Oh, K. S. and Choi, B. S. Study of Reverse Design for an Axial Turbine Blade Profile and Design Parameters for Design Blade Geometry. *J. of Fluid Machinery*, 3(2), 7-14, 2000.
6. Cho, S. Y., Oh, K. S., Yoon, E. S. and Choi, B. S. Study on the Minimization of Shape Parameters for Reverse Designing Axial Turbine Blade Geometry. In *The International Symposium on Energy, Environment, and Cold Region*. Kitami, June No.109, 2000.
7. VisualDOC Reference Manual Version 1.0. Vanderplaats R&D Inc. 1998.
8. Chen, Y. S. Compressible and Incompressible Flow Computations with a Pressure Based Method. AIAA-89-0286, 27th Aerospace Science Meeting, 1989.
9. Chen, Y. S. and Kim, S. W. Computation of Turbulence Flows using a Extended k-ε Turbulence Closure Model. NASA CR-179204, 1987.
10. Kiock, R., Lehthaus, F., Baines, N. C. and Sieverding, C. H. The Transonic Flow Through a Plane Turbine Cascade as Measured in Four European Wind Tunnels. *J. of Eng. for Gas Turbines and Power*, 108, 277-284, 1986.
11. Oh, K. S., Kim, S. Y. and Cho, S. Y. Design of a Heavy Duty Gas Turbine Engine for Power Generation. UCN2000-613.M., 1998.
12. Horlock, J. H. Axial Flow Turbine, Robert Krieger Publishing Co., pp. 60-66, 1973.
13. Korakianitis, T. Hierarchical Development of Three Direct-Design Methods for Two-Dimensional Axial-Turbomachinery. Cascades, *J. of Turbomachinery*, 115, pp. 314-324, 1993.

2F6
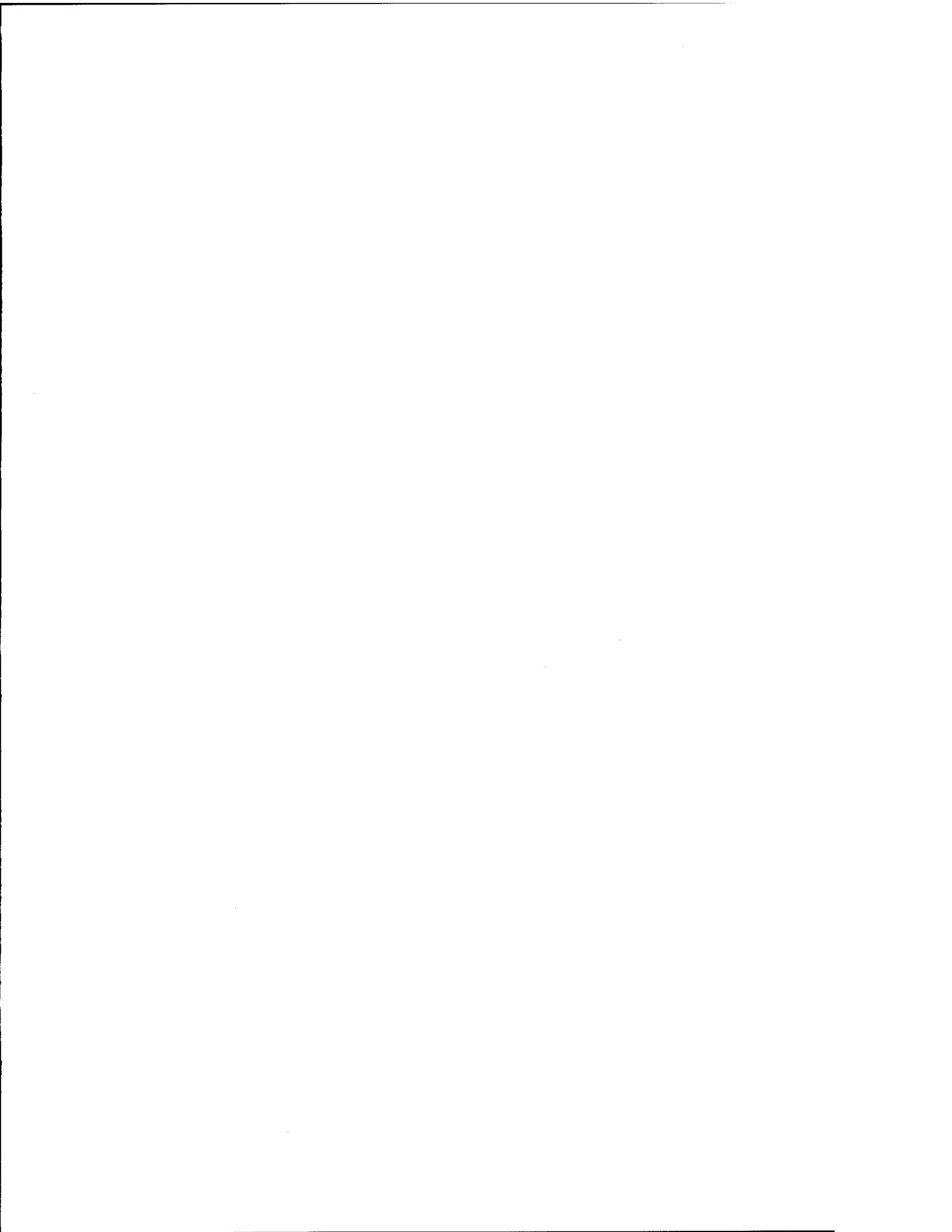
Flow behavior around square section model due to a drag reduction using stepped front corners

Anang Cakrawala* and Akira Umemura**

Department of Aerospace Engineering, Nagoya University, Nagoya 464-8603, Japan

E-Mail: anang@prop.nuae.nagoya-u.ac.jp

Key Words: Drag Reduction, Numerical Simulation, Rectangular, Stepping Notch

Abstract

For many decades, the flow around rectangular or square obstacle has been the subject of intense research. One of drag reduction treatments for these obstacles is cutting a small rectangular region at both front corners to form step. From numerical simulation conducted in the present study, it is found that the drag coefficient of the notched obstacle is mainly determined by the negative pressure coefficient on the back surface. The boundary layer flow developed on both sides of the obstacles changes in the presence of the stepping notches, which reduces drag and suppresses lift oscillation due to Karman vortex shedding.

1. Introduction

It is known that drag force arises from body placed against a stream of air. Square or rectangular shapes are often used in many areas, like transportation, building construction, etc. The drag forces are mainly determined by the negative pressure on the back surfaces. In this paper, we will describe drag reduction mechanism due to modification in forebody shape.

Many researchers attempt to reduce the drag of square and rectangular obstacles. The following methods are available for drag reduction; (1) Rounding out of the forebody shape. In this method, the forebody shape is made streamlined. However, the negative pressure acting on the back surface remains at high value. (2) Notching a rectangular region out of either fore body corner. In this method, the flow becomes unstable in the notched region because inverse pressure gradient appears where the flow turns into the notched region. However, by virtue of vortex generation there, this method is effective to reduce drag. We are focusing on the second method.

The objective of this study is to clarify the drag reduction mechanism relevant to the notched rectangular obstacle by means of numerical simulation.

2. Theoretical Consideration

In the present numerical calculation, the ratio of step height to the width of a square or rectangular obstacle is fixed and the ratio of step length to height, SR, is varied. Obviously, the variation of step height itself may affect the aerodynamic characteristics of stepping notches significantly. The following consideration would provide a hint for step geometry most effective to drag reduction.

We consider a two-dimensional potential flow around a semi-infinitely long body placed parallel to a uniform stream of an unbounded fluid.

---

* PhD. Student Department of Aerospace

** Professor Department of Aerospace

It can be proved that any semi-infinitely long body experiences no drag force so far as the fluid flows in the uniform flow direction along the two parallel boundaries of the body at infinity far downstream. This conclusion is important because it holds irrespective of the shape of forebody. Especially it holds even when the flow partially separates in the forebody part. Let us consider an angular forebody with stepping notches at both corners. The flow, which satisfies this downstream condition, is the case when the flow separates at either edge of the front surface and reattaches to the edges of the body sides tangentially to the side surface. In this case, the region enclosed by the step surface and the free streamline should be a dead flow region. The relevant, complex potential is derived as follows.

$$f(w) = \phi + i\Psi = A\left[\frac{1}{w-q} + \frac{1}{\frac{1}{w}-q} - \frac{1}{w+q} + \frac{1}{\frac{1}{w}+q}\right] \quad \text{Eq. 1}$$

where

$$A = \cfrac{1}{2\left[\cfrac{1-q^2}{q(1+q^2)} + \cfrac{1}{q^2}tan^{-1}\cfrac{1}{q} - tan^{-1}q\right]}$$

$$w = \frac{df}{dz} = \frac{df}{dw}\frac{dw}{dz}$$

$$z = A\pi\left[\left(1-\frac{1}{q^2}\right)i + \frac{2w}{q(w^2-q^2)} + \frac{1}{q^2}ln\frac{w-q}{w+q} \frac{w}{q\left(w^2-\frac{1}{q^2}\right)} - ln\frac{w-\frac{1}{q}}{w+\frac{1}{q}}\right] \quad \text{Eq. 2}$$

The coordinate z=x+iy and velocity w=u-iv are non-dimensionalized by using the body half-width and the uniform velocity, respectively. The length a and height b are expressed as functions of free stream speed q as

$$a = \frac{\pi A}{q^2} - 1 \quad\quad\quad \text{Eq. 3}$$

$$b = A\left[\frac{2(1+q^2)}{q(1-q^2)} + \frac{1-q^2}{q^2}ln\frac{1-q}{1+q}\right] \quad \text{Eq. 4}$$

Figure 1 shows the allowable step geometry in terms of step length and step ratio as function of step height. Correspondingly, the value of pressure in the dead space varies. The forces acting on the front surface and step walls cancel out. The force acting on the step walls can be calculated from

$$C_{D,step} = \left(1 - \frac{1}{q^2}\right)\frac{a}{1+a} \quad\quad \text{Eq. 6}$$

The net force acting on the step walls takes small

value at small step height even though the pressure drop increases as the step height decrease to zero. On the other hand, as the length of front surface decreases to zero, the solution approaches the well-known plate solution in which the pressure of the dead flow region is equal to the uniform value. As a result, the dimensionless thrust force acting on the step walls takes the maximum value 0.533 at the step height 0.09 or step ratio 1.52 as shown in Fig.1. This condition is consistent with the condition that the minimum drag coefficient was obtained in Watanabe's experiment conducted for a circular cylinder with stepping notch. Figure 2 is his experimental result and shows the variation of drag coefficient with step height. The total drag coefficient decreases with increasing step height. It should be noted that the reduction rate of drag coefficient is very large at small step height, implying the efficiency of small step. When the step height is increased to 0.1, the drag coefficient decreases from unity to 0.2.

Figure 2 Step model experimental result

3. Numerical Simulation

Figure 3 Computational domain

Figure 3 defines the shape of obstacle model and computational domain. In the present calculation, the height of step is fixed at a=0.1 and the length b is varied. The inflow boundary and side boundaries of the computational domain are located at a distance of five times the model width from the front and side surfaces of the model, respectively, while the distance from the model back surface to the outflow boundary is ten times the model width.

Fractional step method with time splitting was used to solve 2-D incompressible Navier Stokes equations. The mesh employed in the calculations has non-uniform grid resolution. The grid becomes gradually finer close to the model surface. The total number of mesh is about 50 000 to 60 000, where the minimum size of mesh is 0.015, small enough to resolve the boundary layer structure. Reynolds number (Re) based on the uniform flow velocity U and the model width (d) is 10000. The time step was taken to be $\Delta T = 5.0 \times 10^{-4}$. The pressure convergence criterion ranged from 1.0×10^{-6} to 1.0×10^{-7}.
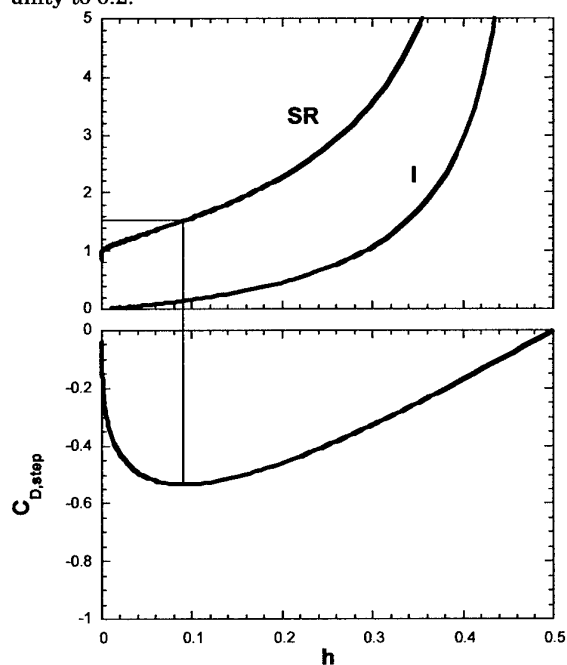

Figure 1 Step length and step ratio as function of step height

The detail of vortex flow is represented by the dead flow and the free streamline enclosing the vortices structure formed on the step is not taken into account in this dead flow theory. Instead, the vortices flow is represented by dead flow and the free streamline enclosing the vortex structure. This approximation will be valid when there is a main vortex on the step, but fail when there appear a number of vortices. This is the case at large step height, although the dead flow theory predicts small drag coefficient. In fact, it is easily imagined that, since the flow separated from the front surface edges reattaches the step flow by the appearance of turbulence, the attached flow impinges on the step wall to increase the drag coefficient beyond a certain value of step height.
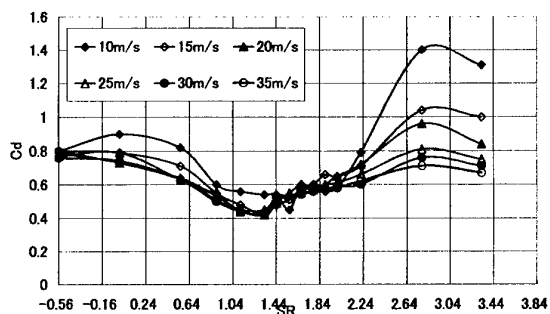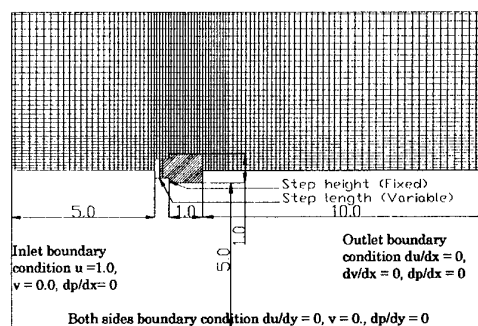
4. Result and Discussion

Numerical simulation shows that the flow becomes quasi-steady after the elapse of dimensionless time of O(10). The following flow characterization is made for such quasi-steady state.

4.1 A square in an unbounded, uniform stream

There are a number of literatures regarding the numerical calculation of uniform stream past a square

model. We conducted a similar calculation for reference and for validation of our numerical calculation scheme (Table 1.) The square placed in a uniform stream of unbounded fluid brings about the separation of flow at both edges of the front surface, yielding the time-averaged drag coefficient Cd = 2.16 and Strouhal number St = 0.15 in our calculation, consistent with other researchers' calculations.

Table 1 Comparison of mean drag force coeff.

Authors	Reynolds number	Mean Cd
A. Cakrawala et al. SR = 2.0	1.0×10^4	1.47
A. Cakrawala et al. (Square)	1.0×10^4	2.16
Ian Taylor DVM [7]	2.0×10^4	2.38
Naudascher (exp.)	1.06×10^5	2.00
Koutmos et al.	1.4285×10^4	2.37
N. Kondo et al.	1.0×10^4	2.5
Tamura et al.	1.0×10^4	2.4

4.2 Step notch effect

In this paper, the drag coefficient is determined from the integration of the pressure coefficient (Cp) on the vertical walls of the model. In figure 4, the drag coefficient is plotted against the step ratio. The drag coefficient of a rectangle obstacle with width h and length l is also drawn for reference. It is confirmed that the notching the front edges of rectangular obstacle reduces the drag coefficient. The drag coefficient of rectangular obstacle decreases as the length of the obstacle increases. However, the drag coefficient of step model slightly increases when the step ratio increases from 1.33 to 2.0. As a result, the degree of drag reduction due to notching the front edges of rectangular obstacle decreases for this change of step ratio.
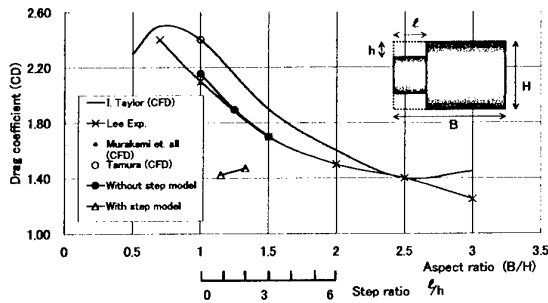

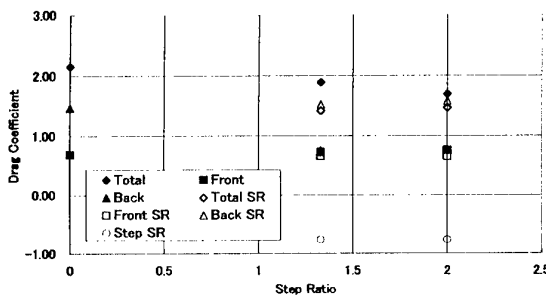Figure 4 Variation of drag coefficient with step ratio

Figure 5 Constitution of drag coefficient

It is concluded that flow separation reattaches just at corner causes high velocity flow of the sidewall of the model. This result to high negative pressure on back surface of the model then makes the Von Karman

Vortices of stepped model higher than square model.

Figure 5 shows the constitution of the drag coefficient, from which we can know the contribution of front and back surfaces of the step model. In the case of rectangular obstacle, the contribution of front surface is almost independent of the obstacle length whereas the contribution of back surface decreases with increasing obstacle length. Thus, it is found that the drag coefficient of a longer rectangular obstacle becomes smaller because the pressure recovers downstream on the obstacle sides. The thrust force acting on the step walls is greater than the drag force acting on the front surface. Therefore, the step model experiences a net thrust force in the forebody part. This partially cancels the drag force acting on the back surface. It is interesting to note that the back surface of step model experiences greater drag force than that of rectangular obstacle and is almost invariant with step ratio. Since the length of main body of the step model is fixed in the present calculation, the boundary layer flow developed on the side surfaces does not change significantly with step ratio so far as the flow separated from the front surface edges reattaches at the leading edges of side surfaces. This implies that the step model that satisfies the above-mentioned flow condition approximately has the same negative pressure on the back surface.

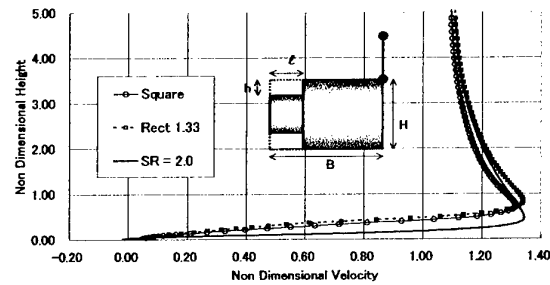## 4.3 Pressure distribution on body surface

Figure 6 Velocity distribution at model side wall

The distribution of time-averaged pressure coefficient along the body surface is shown in Fig. 7 for the three-step ratio in comparison with the corresponding rectangular obstacle case. The values are plotted against distance measured along the body's perimeter from the center of the front surface and moving clockwise around the body.

It should be noted that the magnitude of the negative pressure acting on the step walls is very large. This implies that the step notching at the front corners is very effective to reduce the drag force acting on the forebody. For comparison, let us consider the pressure distribution on the surface of a round nose. As the fluid flows along the round nose surface, the pressure decrease to the same value as the negative pressure on the step walls. However, the axial force component acting on the round nose surface reduces its magnitude near the part where the surface becomes parallel to the uniform stream direction. As result, the negative pressure due to flow acceleration cannot effectively contribute to create thrust force on the round nose. Therefore, it can be said that the step notching is an excellent device, which utilizes the pressure drop to produce thrust force.

There is a certain step size, which has a significant drag reduction effect, as demonstrated in Watanabe's experiments. Consider two limiting cases; First, when the step length is too short, the accelerating flow which separates at the leading edge of the step base attacks and pushes the step wall. Therefore, the net drag force acting on the body rather has a grater value than the square case. This includes the case when the step length is too long that the separated flow reattaches the base of step. Second, when the step height is too small, the step is totally immersed in the separated flow region so that the step has no significant effect on the drag reduction.

In the calculation of step ratio 1.33, as seen in Fig. 7, the pressure coefficient becomes minimum at midway point on each of the step bases and walls. This indicates that a strong vortex is trapped inside the step region and the flow reseparates at the leading edges of the side surfaces. In the case of SR = 2.0, the vortex is also trapped at the step location. However, the flow separated at the leading edges of the step bases reattaches at the leading edges of the side surfaces. Then, the fluid goes downstream without separation. In either case, there are no significant temporal changes in the pressure distribution on the forebody surface, while the instantaneous pressure, acting on the back surface strongly depends on the configuration of Von
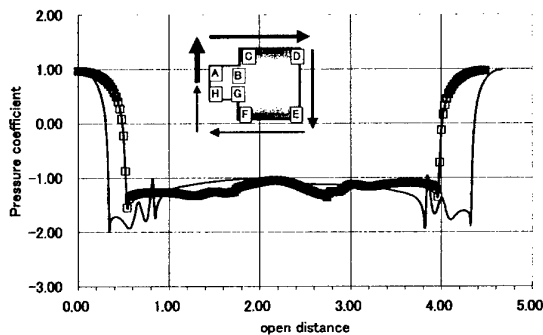

Figure 7 Time-averaged surface pressure coefficient distribution in comparison with rectangular model in case of step ratio 1.33
Karman Vortices.

4.4 Strouhal Number
In order to determine the frequency of vortex shedding, a fast Furrier transform (fft) is performed of the pressure fluctuation at a point near the corner on the back surface of the model. The spectrum for the square in an unbounded uniform stream shows good agreement with other researches, identifying a predominant frequency, which corresponds to Strouhal number 0.12. It has multi-modal distribution over a rather wide frequency range because the flow separates from the front corners of the model and various scales of vortices are generated. For the step model, the width of the wake flow region becomes narrower so that Strouhal number of vortex shedding increases. At the same time, it is found that the spectrum is concentrated on a certain frequency. These changes indicate that the both step corners prohibits the flow from separating from the model except at the back corner and that the vortex shedding frequency is

determined by the neutrally stable arrangement of Karman vortices. In fact, equating the distance of separation between the counter-rotating vortex series to the obstacle width d, the stable condition leads to the value of Strouhal number St = 0.2. The step not only reduces the drag force acting on the forebody but also suppress the flow separation from the front surface edges. Interestingly, these effects are caused by the flow acceleration due to the fluid exclusion by presence of the body itself. The flow impinging on the body must turn around its edges. The step provides a mechanism that result in the pressure drop of the turning fluids, which become a suction force to the forebody.

5. Conclusion
The flow impinging on the body must turn around its edges. The step notching provides a mechanism that utilizes the pressure drop of the turning fluid to gain a suction force to the forebody. The degree of drag reduction depends on the stepping ratio. It is found that the most significant drag reduction for stepping model is when the stepping ratio is equal to 1.33.

References
1. N. Kondo, S. Yamada, Computational Method App. Mechanical Engineering 127, P87-97, 1995
2. Hoerner, Fluid-Dynamic Drag, 3-1, 3-28, (1975)
3. I. Taylor, M. Vezza, Journal of Wind Engineering and Industrial Aerodynamics, Vol. 82, P271 – 291, 1999
4. T. Tamura, T. Miyagi, Journal of Wind Engineering and Industrial Aerodynamics, Vol. 83, P135-145, 1999
5. A. Sohankar, C. Norberg, L. Davidson, Journal of Wind Engineering and Industrial Aerodynamics, Vol. 69-71, P189-201, 1997
6. Kyoji Watanabe, Doctoral Thesis, 1997 (In Japanesse)

CONTROL OF FLOW SEPARATION ON BLUFF BODIES AT TRANSONIC SPEED

Thombi Layukallo[*] and Yoshiaki Nakamura[**]

Nagoya University, Furo-cho, Chikusa-ku, Nagoya 464-8603, Japan

Key Words: Aerodynamics, Compressible flows, Unsteady flows

ABSTRACT

A method to suppress drag and flow oscillations on bluff bodies at transonic speed has been considered. The method incorporates the use of small tabs inside the separated region that is dominated by reverse flow. The method is applied to a circular cylinder at M=0.6 and 0.73, and a square cylinder at M=0.56 and 0.71. In the circular cylinder case, drag reduction of 32% is achieved at M=0.6, whereas in the square cylinder case, an estimated 40% reduction is achieved at M=0.56. Pressure fluctuations around the cylinders were also greatly reduced. This is probably due to favorable changes in the wake profile that are associated with drag reduction.

1. INTRODUCTION

Reduction of aerodynamic drag on bluff bodies is important for many engineering applications. In many cases it is also of interest to reduce flow instabilities that are commonly developed around such bodies. Most researches in this subject have been oriented toward the low speed flow regime. This paper deals with the issue in the transonic flow regime, where drag is high and flow unsteadiness is severe.

The investigation looks at the effectiveness of installing small tabs inside the otherwise fully separated regions to reduce drag and flow unsteadiness. This approach is based on the premise that the reverse flow inside the separated region plays a significant role in the flow separation mechanism, such that when reverse flow action is suppressed the severity of separation can be lessened. Therefore, the tabs are expected to suppress the reversed flow inside the separated region, hence reducing the severity of flow separation. Any reduction in drag will be accompanied by favorable changes in the wake profile of the bodies. Since from instability theory the wake profile is associated with instability growth inside the wake, it is expected that drag reduction on the bodies will be followed by reduction in flow unsteadiness around the bodies as well.

2. EXPERIMENT

The bluff bodies considered in this investigation are circular and square cylinders. The circular cylinder has a diameter of 30mm and the square cylinder has a side length of 25mm. The schematic of the models is shown in Fig. 1. The experiment was conducted in the Nagoya University Transonic Wind Tunnel, which has a slotted-wall test section with dimensions of 0.3m x 0.4m. The test Mach numbers are 0.6 and 0.73 in the circular cylinder case, and 0.56 and 0.71 in the square cylinder case. The models were equipped with pressure taps, which were connected to pressure transducers for steady and unsteady pressure measurements. All tests were conducted with atmospheric stagnation conditions.
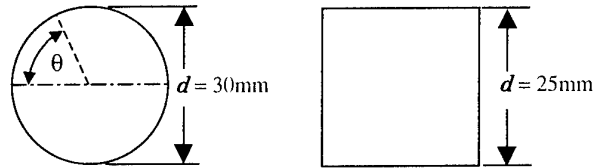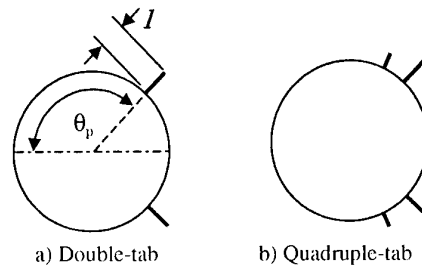

Fig.1   Schematic of cylinder models.

a) Double-tab   b) Quadruple-tab

Fig.2 Schematic of tabbed circular cylinder

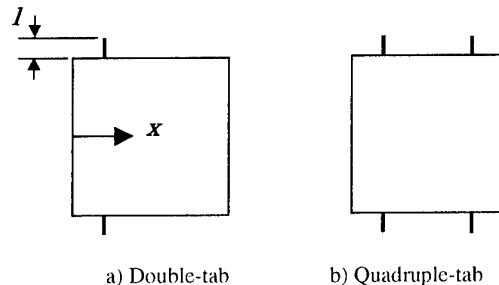a) Double-tab   b) Quadruple-tab

Fig. 3 Schematic of tabbed square cylinder

In the tabbed circular cylinder are shown in Fig. 2, two different tab length ratios were used: l/d = 0.1 and 0.2. These tabs were installed perpendicularly on the rear surface of the cylinder ($115° < |\theta_p| < 180°$), where flow is already separated otherwise. A quadruple-tab configuration was also tested with the shorter tabs installed at $\theta_p = \pm 120°$ and the longer ones at $\theta_p = \pm 140°$.

Schematic of the tabbed square cylinder configurations is shown in Fig. 3. The tabs had an $l/d=0.12$ and were installed on the side surfaces where flow is also separated. In the double-tab case, where one tab is installed on each side surface, two tab locations were considered: $x/d=0.2$ and 0.8. These positions are also used in the quadruple-tab configuration, where two tabs are installed on each surface.

[*]   Graduate student, School of Engineering

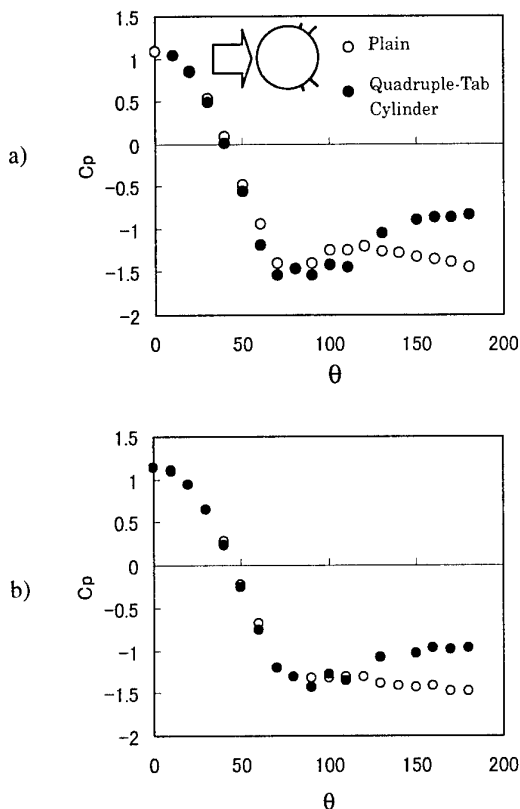[**]   Professor, Department of Aerospace Engineering

Fig. 4 Pressure distribution on circular cylinder;
a) M=0.60, b) M=0.73

clearly distinguished, the presence of the tabs increases the vortex formation length. In addition, the wake of the quadruple-tab cylinder is noticeably narrower than that of the plain cylinder. At M=0.73, the presence of the tabs lead to the formation of double shock waves that are aligned parallel to each other, as seen in Fig. 8. There has been no evidence thus far to link this phenomenon to flow three-dimensionality along the span of the cylinder. This phenomenon should be subject to further investigation.
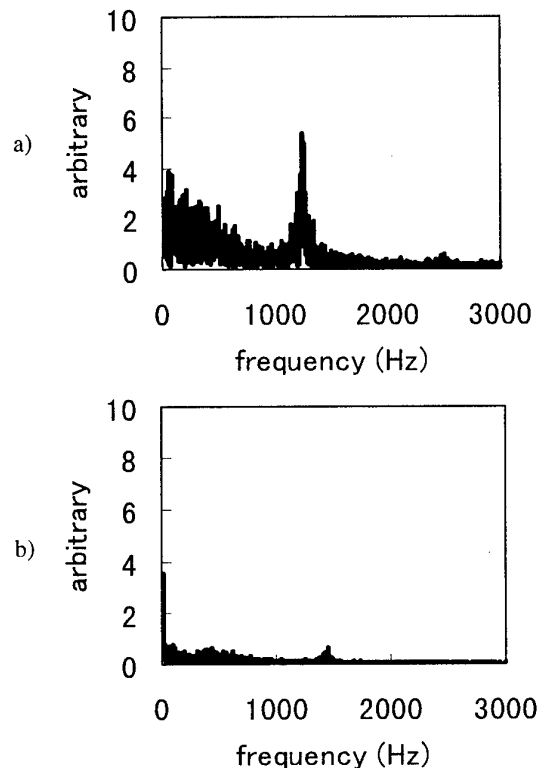

Fig. 5 Frequency spectra of pressure fluctuation at $\theta_p=90^0$ on circular cylinder at M=0.6; a) plain, b) quadruple-tab

The installation of the tabs also results in much steadier flows around the cylinder, as evidenced in Fig. 5. These figures show the frequency spectra of pressure fluctuations measured at $\theta=90^0$. At M=0.60, the pressure peak that is associated with the Karman vortex shedding is greatly reduced. In addition, the Strouhal number that is associated with the vortex shedding frequency is increased from about 0.18 to about 0.21. At M=0.73, when tabs are installed, no fluctuation peaks could be detected at all measurement locations on the cylinder surface. Therefore, the change in Strouhal number at this Mach number is not known. It is presently understood that reduction in the wake deficit that is associated with drag reduction may be responsible for the reduced instability in the near wake and around the cylinder.

3. RESULTS

In the circular cylinder case, the best results were achieved by the quadruple-tab configuration. In this case the shorter tabs were located at $\theta_p=\pm120^0$ and the longer tabs at $\theta_p=\pm140^0$. The pressure distributions on the cylinder surface are shown in Fig. 4 for both Mach numbers. As depicted in the figures, a large increase in base pressure is obtained when the tabs are installed. In addition, pressure increases are created across the tabs, resulting in forces on the tabs whose axial components are directed upstream, hence against drag. As a result, drag is lower by as much as 32% at M=0.60 and 18% at M=0.73

Schlieren pictures of Fig. 7 show the flows around the cylinder at M=0.60 with and without the quadruple tabs. As
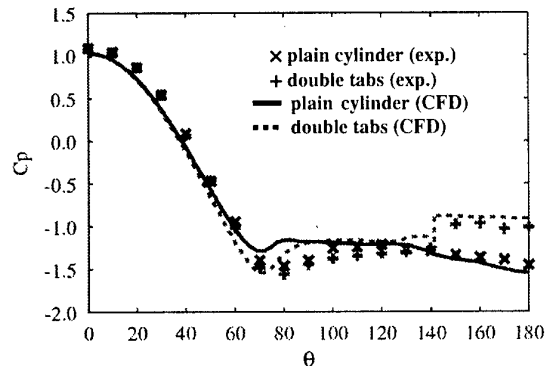

Fig. 6. Comparison between experimental and numerical pressure distributions at M=0.6.

Schlieren pictures of Fig. 7 show the flows around the cylinder at M=0.60 with and without the quadruple tabs. As

— 100 —

clearly distinguished, the presence of the tabs increases the vortex formation length. In addition, the wake of the quadruple-tab cylinder is noticeably narrower than that of the plain cylinder. At M=0.73, the presence of the tabs lead to the formation of double shock waves that are aligned parallel to each other, as seen in Fig. 8. There has been no evidence thus far to link this phenomenon to flow three-dimensionality along the span of the cylinder. This phenomenon should be subject to further investigation .
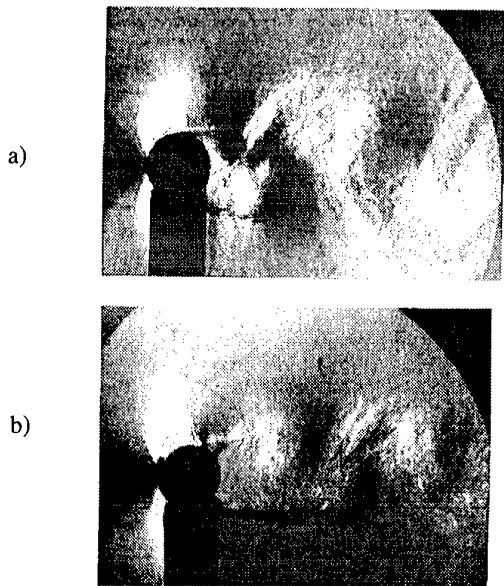

a)

b)

Fig. 6. Schlieren pictures of circular cylinder at M=0.60;
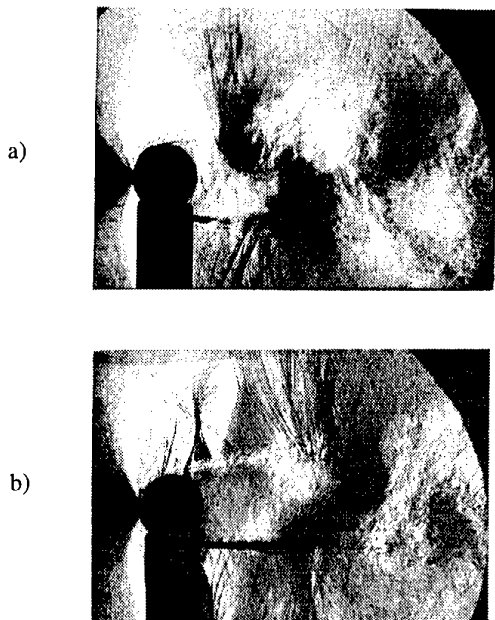a) plain, b) quadruple-tab

a)

b)

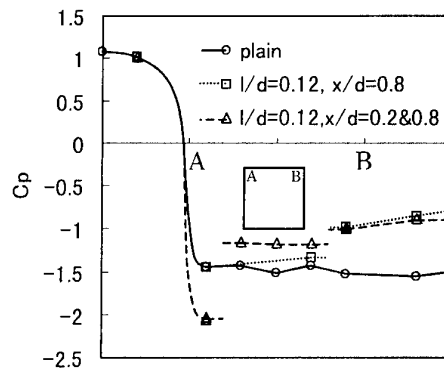Fig. 8. Schlieren pictures of circular cylinder at M=0.73;
a) plain, b) quadruple-tab

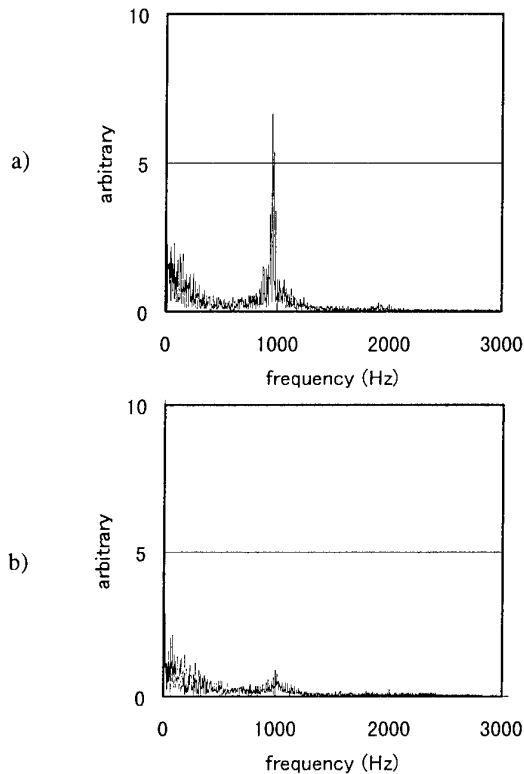Fig. 9 Pressure distribution on square cylinder at M=0.56

a)

b)

Fig. 10 Frequency spectra of pressure fluctuation at x/d=0.5 on square cylinder at M=0.56; a) plain, b) quadruple-tab

In the square cylinder case, larger effects were obtained when the tabs were installed at x/d=0.8 rather than 0.2. Even larger effects were achieved by the quadruple-tab configuration. The pressure distributions on the cylinder surface at M=0.56 are shown in Fig. 9. As in the circular cylinder case, higher pressures are achieved at the cylinder base, and pressure increases are also created across the tabs, both of which result in significant drag reduction. At M=0.56 the resulting drag reduction amounts to about 33% for the double-tab case and 40% for the quadruple-tab case. At M=0.71 drag reduction is somewhat smaller.

Figure10 shows the pressure fluctuations measured at x/d=0.5 on the cylinder surface where flow is at M=0.56. As in

the case of the circular cylinder, the peak that corresponds to the Karman vortex shedding is also suppressed in this case. The vortex shedding frequency also shows a tendency to increase, although the increase is not very significant.

4. CONCLUSIONS

A method to suppress drag and flow oscillations around bluff bodies at transonic speeds by using simple tabs inside the otherwise fully separated region has been investigated. The tabs supposedly suppress the reverse flow action, hence relaxing the severity of the separation.

Implementation of this method on a circular and a square cylinder led to large pressure increases at the base of the cylinders. In addition, pressure was increased across the tabs, such that the axial components of the forces acting on the tabs are directed against drag. As a result, a drag reduction of as much as 32% was achieved for the circular cylinder at M=0.6, and 40% for the square cylinder at M=0.56. These were accompanied by increases in vortex formation length and reductions in the wake width. At higher Mach numbers the effects are somewhat smaller.

The tabs have also been observed to suppress flow oscillations around the cylinders. It is understood that the favorable changes in the wake profile associated with drag reduction may be responsible for the reduced flow instability. In addition, Strouhal number shows an increasing tendency.

These observations suggest that reverse flow plays a significant role in the mechanism of flow separation, such that its suppression may result in significant favorable changes in the flows around aerodynamic bodies.

REFERENCE

1. Roshko, A., "On the Wake and Drag of Bluff Bodies," J. Aero. Sci. 22, pp. 124-132, 1955.

2. Sakamoto, H., Tan, K. and Haniu, H., "An Optimum Suppression of Fluid Forces by Controlling a Shear Layer Separated From a Square Prism," J. Fluids Eng. 113, pp. 183-189, 1991.

3. Delaunay, Y. and Kaiktsis, L., "Active Control of Cylinder Wakes: Use of Base Suction and Blowing," Proceedings of Third International Workshop on Vortex Flows and Related Numerical Methods, Vol. 7, pp. 104-119, 1999.

4. Gowen, F. E. and Perkins, E. W., "Drag of Circular Cylinders for a Wide Range of Reynolds Numbers and Mach Numbers," NACA TN 2960 (1953).

5. Nakagawa, T., "Vortex Shedding Behind a Square Cylinder in Transonic Flows," J. Fluid Mech. 178, pp. 303-323, 1987.

6. Lyn, D. A. and Rodi, W., "The Flapping Shear Layer Formed by Flow Separation from the Forward Corner of a Square Cylinder," J. Fluid Mech. 267, pp. 353-376, 1994.

2F8

SUPPRESSION OF EDGE-TONES IN HIGH-SPEED FLOWS

Mohammed K. IBRAHIM*, Tsukasa SOUMA* and Yoshiaki NAKAMURA**

Department of Aerospace Engineering, Nagoya University, Nagoya, 464-8603, Japan

Key Words: Aerodynamics, Aeroacoustics, Noise Suppression, Edge tone

ABSTRACT

Experimental investigation has been carried out on edge tone generated by a sonic jet issuing from a square convergent nozzle and impinging on a wedge shaped edge. Acoustic measurements showed that there is a minimum breadth required for a tone to be generated. At a wedge distance beyond the minimum breadth, the narrow-band spectrum of near field pressure signals indicates the simultaneous existence of several discrete frequencies, and amplitude dominant frequencies show different stages. A semi-empirical frequency formula of the edge tone has been proposed for the present jet-wedge system.

1. INTRODUCTION

The edge tone is a tone of discrete sound produced when a jet of gas issuing from a nozzle impinges on a wedge-shaped edge placed at a short distance from the nozzle exit[1]. Powell[2] has proposed the mechanism by which this tone is generated as a feedback-driven hydrodynamic jet instability. As described by Rockwell and Naudascher[3], highly organized oscillations of the impinging jet flow are sustained through a series of interacting events: feedback, or upstream propagation, of disturbances from the impingement region to the sensitive area of the jet free shear layer; inducement of localized vorticity fluctuation in this region by the perturbation; amplification of these vorticity fluctuations in the shear layer up to impingement; production of organized disturbances at impingement. The first event, that is the disturbance feedback, is an essential feature of this sequence. It provides direct communication between processes near the impingement surface and the receptivity region, thereby ensuring that the shear-layer oscillation is a globally organized phenomenon. Therefore, a comprehensive theory of edge tone should include the stability characteristics of the jet, the details of the outside flow, and the details of the coupling between the outside flow and the oscillating jet.

Generally the edge tone has been examined for rectangular jet with a relatively large width to height ratio. In the present paper, experimental investigation for square jet, has been carried out. The results have been compared with other researchers' results of a rectangular jet having a large width to height ratio. A semi-empirical frequency formula has been proposed for the present jet-wedge system.

2. EXPERIMENTAL FACILITY

The experiment was conducted in the open jet facility at the Department of Aerospace Engineering, Nagoya University. A square convergent (sonic) nozzle having a side

length of 8.88 mm was used to produce the primary jet flow. The nozzle is attached to a cylindrical plenum chamber that has a diameter of 220 mm and a length of 400 mm. High-pressure air is supplied from a tank with a volume of 12 m^3 stored at a pressure of 12 kgf/cm^2 which is connected to the plenum chamber. A high precision pressure regulator and a solenoid valve were used in order to control the pressure of the plenum chamber within a 0.25% accuracy.

Two microphones have been employed for acoustic measurements. One is a RION UC-29 1/4" condenser microphone that has a maximum frequency of 100kHz and a maximum SPL of 160 dB. This is used as a reference microphone. The other microphone is an ONO-SOKKI LA-5110 that has a maximum frequency of 100kHz and a maximum SPL of 130 dB. The sound spectra have been obtained and analyzed by using a two-channel ONO-SOKKI multi-purpose FFT analyzer CF-5210 that can analyze a maximum frequency of 100kHz.

The outside surfaces of the plenum chamber and other bodies placed in the near field were covered with two layers of acoustically absorbent, 6 mm thick polyurethane foam to reduce strong reflections from the plenum chamber. In the present measurements, the background noise was 37.5 dB in A weighted SPL.
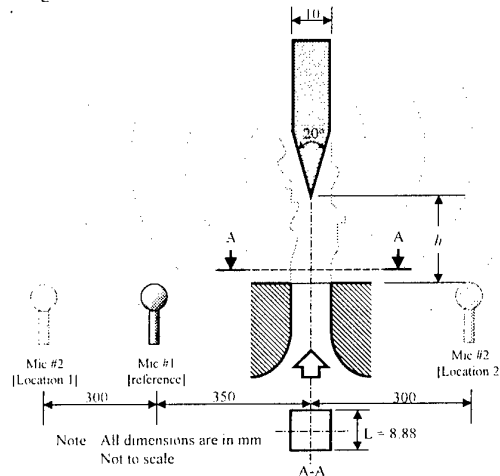

Fig. 1 Experimental setup

The main parameters governing the problem are 1) Mach number M and Reynolds number Re of the jet near the exit, 2) the flow state at the nozzle exit, 3) the geometry and disposition of the wedge with respect to the nozzle exit, and

4) the condition of the ambient medium into which the jet is issuing.

In the present investigation the exit Mach number is 1.0, i.e., sonic jet, which corresponds to a Reynolds number of 1.5 × 10⁵. A 20-deg two-dimensional wedge has been selected. Figure 1 shows the experimental setup.

3. RESULTS AND DISCUSSION

One of the main features for edge tone is the "minimum breadth," which is the minimum distance h_o required for the tone to be first generated. Figure 2 shows the variation of h_o with two exit Mach numbers for the present square jet, as well as the results of Krothapalli et al.[4] for a rectangular jet having a width to height ratio of 16.7.
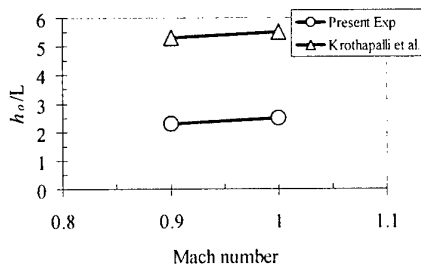
Fig. 2 Variation of the minimum breadth with Mach number

L in Fig. 2 represents the width of the rectangular nozzle or the minimum dimension of the nozzle. As seen from this figure, as Mach number increases, the minimum breadth increases. The rectangular jet or two-dimension jet has a higher minimum breadth than the square jet for a given Mach number and wedge geometry.

Narrow band spectral analysis of the sound signals has been made. The spectral analysis showed that, for a given nozzle exit Mach number, the frequency of the edge tone decreases gradually as the edge distance is increased over the minimum breadth. This frequency continues to decrease until a certain edge distance is reached where the edge tone will suddenly jump to a new, higher frequency. This new mode of operation is known as stage II, while the first mode is stage I. As the edge distance is further increased, the frequency of stage II again decreases with distance until another jump in frequency takes place, where the edge tone is said to operate in stage III. The appearance of the higher stages depends on experimental conditions. At large edge distances, the edge tone will be lost due to irregular or turbulent flow. Two consecutive stages could exist together, as shown in fig. 3. In this figure, sound spectra at two-wedge locations are shown. Stages II and III overlap at h/L = 4.73, while Stage II only exists at h/L = 4.62.

Figure 4a shows the edge tone frequencies for the present jet-wedge system. Six stages exist in the present experiments for the edge distance of up to h/L = 7. The overlap between stages is clearly shown in this figure. The amplitude of the corresponding frequencies are shown in Fig. 4b. The amplitude distribution during each stage shows first a sharp rise, then a constant amplitude region, and finally a drop at

the end of the stage. The peak amplitude during the third stage of operation is the highest as compared to other stages.
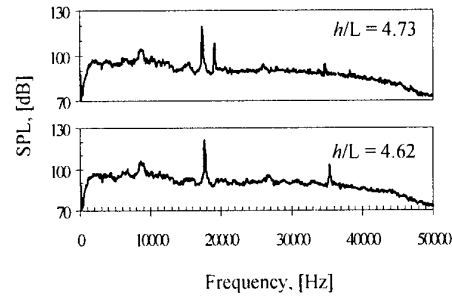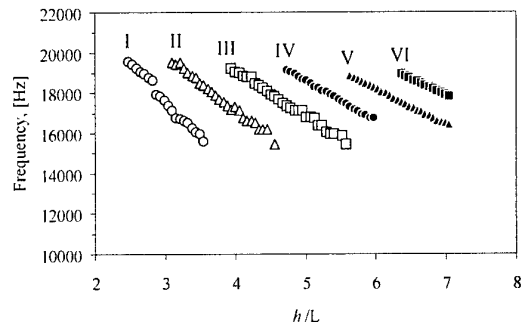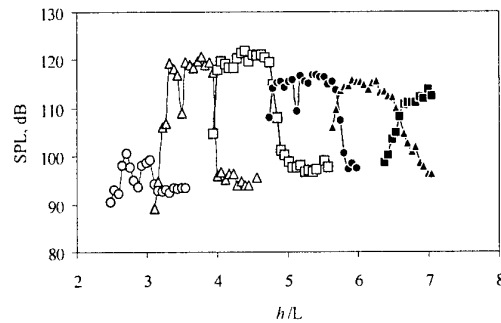
Fig.3 Sound spectra at two different wedge locations

a) Frequency

b) Amplitude

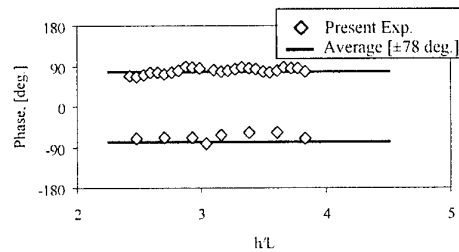**Fig. 4** Frequency and amplitude variations with the edge distance.

Fig. 5 Variations of phase difference between a reference microphone and another with the edge distance.

The phase difference of the edge tone frequency was measured between a reference microphone. MIC #1. and the other microphone. MIC #2, at location 2. as shown in Fig. 1. The results are shown in Fig. 5 at different edge distances. The two signals were out of phase by a constant value of about ± 78 deg.

4. FREQUENCY FORMULA

If, in the jet, a disturbance with frequency f and wavelength λ is propagating with a uniform convection velocity u_c, the frequency is given by:

$$f = \frac{u_c}{\lambda} \qquad (1)$$

Once u_c and λ are determined in terms of the parameters of the problem, a formula for the frequency is obtained. For the sake of simplicity, in the present investigation the convection velocity is set constant and equal to the sound propagation velocity. The sound propagation velocity was obtained by applying the cross correlation technique to the signals of the two microphones (MIC #1 for reference. and MIC #2 at location 1) as shown in Fig. 1. The results are shown in Fig. 6 for the edge location at $h/L = 2.65$. From this figure, the time delay between the two microphones for the same incident sound wave could be determined. Since the separation distance between the two microphones is known. the sound propagation velocity could be calculated easily. Figure 7 shows the sound propagation velocity at different edge distances. It is clear from this result that the sound propagation is constant and equal to 350 m/sec.
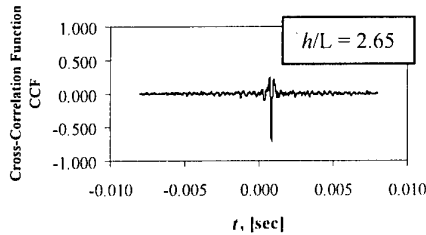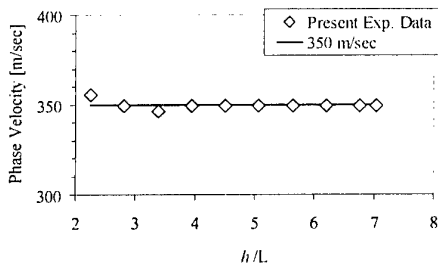
Fig. 6 Cross-Correlation function.

Fig. 7 Sound propagation velocity variation with the edge distance.

From the frequency results shown in Fig.4a and Eqn. (1), the wavelength, λ, can be calculated easily. Figure 8 shows the wavelength variation with edge distance.
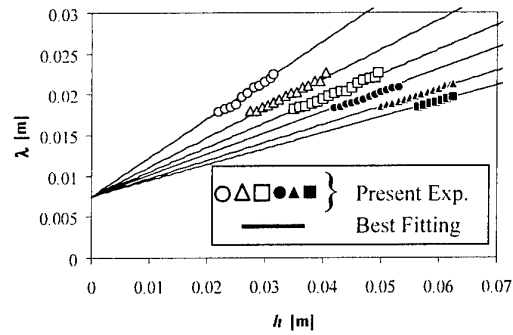
Fig. 8 Wavelength variation with edge distance.

The wavelength is linearly proportional to edge location. h, as shown in Fig. 8. This linear relation could be written as follow:

$$\lambda = C_1 + C_2 h \qquad (2)$$

where

$$C_1 = 0.0075 \qquad (3)$$

and

$$C_2 = C_2(n) = 0.16 \ln\left(\frac{1}{n}\right) + 0.475 \qquad (4)$$

Where n is an integer denoting the stage of the edge tone operation. It is clearly shown that the wavelength is a function of edge distance h and operations mode n. This is agrees with the measurements by Brown[5] the wavelength in the disturbed two-dimensional jet of an edge-tone system. Brown measured the wavelength from smoke pictures of the disturbed jet and found that the edge distance is connected to the wavelength by the relation

$$\lambda = \frac{h}{\left(n + \frac{1}{4}\right)} = \overline{C_2} \, h \qquad (5)$$

Figure 9 shows results of slope, C_2, the present experiments Eqn. (2), the best fitting represented by Eqn.(4), and the Brown's measurements for two-dimensional jets by Eqn (5).
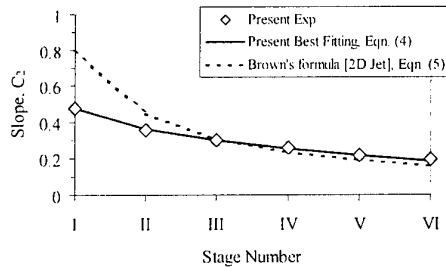
Fig. 9. Slope variation with stage number

This similarity in the slope variation with the stage number suggests that mechanism of edge tone generation for the present jet-wedge system is the same as the two-dimensional jet-wedge system[2]. Frequency formula for the present jet-wedge system could be obtained by substituting Eqn. (2) into Eqn. (1). Figure 10 shows a comparison between the present experimental data and predications based on Eqn. (1) as well as a two-dimensional jet-wedge model.
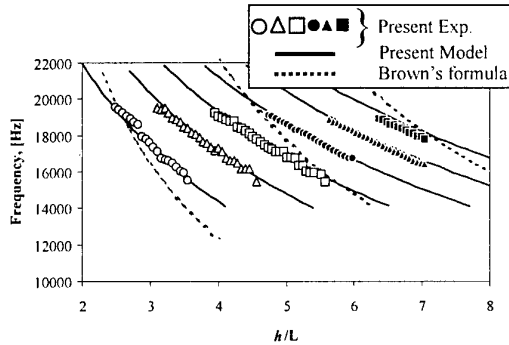

Fig. 10 Edge tone Frequency predication

5. EDGE - TONE SUPPRESSION

During the course of the experimental investigation, it was found that the edge tone could be suppressed by placing two plates normal to the centerline of the undisturbed jet in the outside flow region, as shown in Fig. 11. Consequently, experiments were made to determine for any given location of the edge the plate location at which the edge tone is suppressed. Such measurements were made for stage III, where the peak amplitude of the edge tone exists, with a fixed edge distance h/L equal to 4.45.
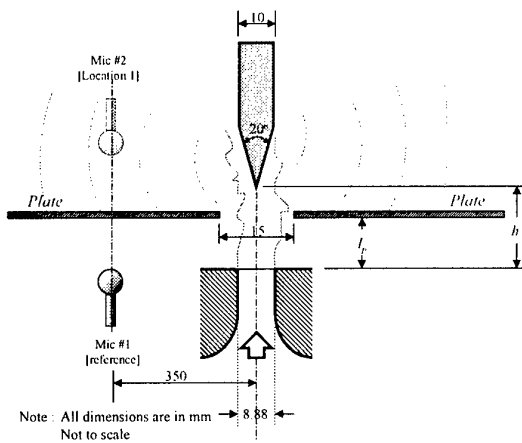

Fig. 11 the setup of Edge-tone suppression experiment.

The sound spectra for both the baseline jet-wedge system and the system with plates are shown in Fig. 12. In this figure, the plate distance l_p was equal to 1.13, where the edge-tone has a minimum amplitude for the present configuration. It is clearly shown that the edge tone was suppressed by about 19 dB. The high frequency spectra have also been reduced. This

suggests that the plate makes the upstream propagation of disturbances weaker, consequently inducing of localized vorticity fluctuations.
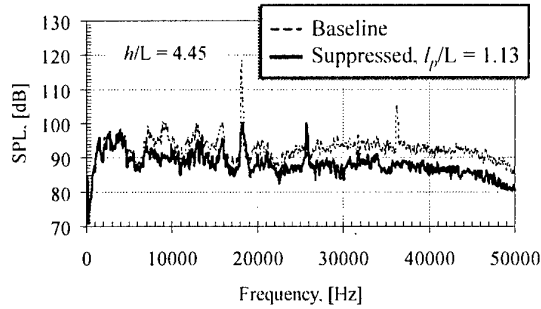

Fig. 12 Sound spectra of edge tone suppression experiments

6. CONCLUSION

Experimental investigation has been carried out on edge tone generated by a sonic jet issuing from a square convergent nozzle and impinging on a body with a wedge shaped edge. Acoustic measurements showed that there is a minimum breadth required for a tone to be generated. The square jet has a lower minimum breadth than the rectangular jets having a high width to height ratio for a given Mach number and wedge geometry. A semi-empirical frequency formula has been proposed for the present jet-wedge system. Preliminarily results also showed that the edge tone could be suppressed by placing two plates normal to the centerline of the undisturbed jet in the outside flow region.

7. REFERENCES

1. Karamcheti, K., Bauer, A., Sahield, W.L., Stegen, G., and Woolley, P.J., "Some Features of an Edge Tone Flow Field," NASA SP-207, 1969, pp. 275-304.
2. Powell, A., "On the Edgetone," Journal of the Acoustical Society of America. Vol. 33,No. 4, 1961, pp. 395-409.
3. Rockwell, D. and Naudascher, E., "Self-Sustained Oscillations of impinging Free Shear Layers," Ann. Rev. Fluid Mech. Vol. 11, 1979, pp. 67-94.
4. Krothapalli, A., Karamcheti K., Hsia, Y., and Baganoff D., "Edge Tones in High-Speed Flows and Their Application to Multiple-Jet Mixing," AIAA Journal. Vol. 21, No. 7, 1983, pp.937-938.
5. Brown, G. B., "The Vortex Motion Causing Edge Tones," Proc. Phys Soc. (London), Vol. 49, 1937a, pp. 493.

2F9   Numerical Study of Hypersonic Blunt Body with Ablation Jets

Taizo MATSU-URA*, Kenzo KAGA † and Toshi FUJIWARA‡

Department of Aerospace Engineering, Nagoya University, Nagoya 464-8603, Japan
Key Words: High-Enthalpy Flow, Shock Wave

ABSTRACT

This paper treats numerical simulation of an experimentally-observed phenomenon that we have called "artificial ablation", where Helium gas jets are injected from the stagnation region of blunt body to exaggerate real ablation phenomena. The two-temperature model of Park and the Yos formula for transport coefficients are used. Since the flow is assumed laminar, the Navier-Stokes equations are used as fundamental ones. In addition, both freestream and injected gases are assumed to consist of only nitrogen, for simplicity, where the effects of radiation emission/absorption are neglected. A hybrid (structured and unstructured) mesh technique is used to take advantage of both mesh characters. A finite- volume method is used to solve the governing equations. As typical numerical results, the distributions of various physical properties are visualized, which clearly give the effects of gas injection.

1. INTRODUCTION

The MUSES-C is a sample return mission to an asteroid, planned at ISAS, Japan. The launch of MUSES-C spacecraft is scheduled in July 2002 using an M-V rocket. The target asteroid will be (10302) 1989ML. MUSES-C is scheduled to arrive at the asteroid October 2003, departing April 2003 and returning back to earth June 2006. There are various difficulties foreseen during all relevant stages.

The velocity of sample-return capsule during reentry into Earth atmosphere is estimated as 12km/sec, which is an experimentally un-reproducible hypersonic speed. Therefore, the capsule is exposed to a high-temperature gas behind a strong bow shock wave. In order to protect the capsule from such critical thermal conditions, the ablation of surface material is used in MUSES-C mission as the only effective technique for thermal protection. However, it is important to know the location of transition from laminar to turbulence, because the transition increases the convective heat transfer causing higher rates of ablation. In view of this, one important problem is whether the interaction between ablated gas and hypersonic incoming flow would trigger earlier transition to turbulence.

Using a Stalker tube of our laboratory, the experimental studies of transition phenomenon, using an ablation model, have been conducted recently. After initial attempts using real ablation models, we came to realize that the running time 150 μ sec of our Stalker tube was not enough; it needed several times longer time for the surface material to vaporize. Thus, we have decided to resort to "artificial" ablation. In this numerical study, a hypersonic blunt body injecting nitrogen gas jets from stagnation region is simulated.

2. NUMERICAL ANALYSIS

In the present analysis, the convective heat transfer rate is calculated for the experimental models with and without gas injection. The freestream gas is nitrogen both in experiment and numerical analysis. Although the injected gas is Helium in experiment, nitrogen is used in the analysis, for simplicity. The effects of molecular/atomic radiation emission/ absorption are not taken into account.

2.1 Chemical Model

Since the freestream is hypersonic, the flow

---

*Graduate Student
†Graduate Student
‡Professor of Physical Gasdynamics

induced by the extremely high temperatures behind bow shock wave is in both thermally and chemically non-equilibrium, necessitating, for example, the two-temperature model of Park [2] as a physical model; (1) the transnational-rotational and (2) the vibrational-electron-electronic-excitation temperatures. The Yos formula [3] are used for transport coefficients. A thermally and chemically non-equilibrium 5-species (N_2, N, N_2^+, N^+ and e^-) gas is considered.

2.2 Governing Equations

Since the flow is assumed laminar, the fundamental equations are Navier-Stokes ones. The two-dimensional axisymmetric cylindrical coordinate system is adopted in the present problem. The spatial distribution of chemical species number densities and temperatures can be visualized, by solving Navier-Stokes equations coupled with the vibrational-electron-electronic-excitation energy conservation equation, as given below:

$$\frac{\partial U}{\partial t} + \frac{\partial F}{\partial x} + \frac{\partial G}{\partial y} = \frac{\partial F_v}{\partial x} + \frac{\partial G_v}{\partial y} + S_c + S_v + \frac{H}{y},$$

where x is the axial coordinate, y the radial coordinate, t the time, U the vector of conserved variables, F and G the convective flux vectors, F_v and G_v the dissipation flux vectors, S_c the source term vector of chemical reactions, S_v the relaxation term vector of energy, and H the cylindrical coordinate transformation term vector. More detailed information on these vectors is given in Reference 5.

2.3 Numerical Scheme and Grid System

A finite-volume method is used to the governing equations converted into integral equations. Since a very strong stiffness occurs in the source terms representing chemical reactions and vibrational conservation, a semi-implicit method is used.

A hybrid (structured and unstructured) mesh technique is introduced here to take advantage of both mesh characters. Advantages of structured mesh can be described as follows:

(1) Fine grids can be formed near a body surface with minimum waste.

(2) Nodal points along the direction of layer around a body surface can be arranged easily. On the other hand, advantages of unstructured mesh can be expressed as follows:

(1) Flexibility of grid is high.

(2) Grid can be formed in far-body space with minimal waste.

2.4 Experimental System

The specifications of Stalker Tube used in the present experiment are given as:

- Running time: 150 μ sec.
- Mach number at nozzle exit: 12.85.
- Pressure: 543Pa at nozzle exit.
- Temperature: 146K at nozzle exit.
- Density: 4.77×10^{-3}kg/m^3 at nozzle exit.

These data are provided from the measured values and the numerical calculation that assumes the flow to be isentropic. Freestream properties are from these data.

2.5 Artificial Ablation Model

The experimental model for simulation is shown in Fig.1. Nitrogen gas jets are injected from the sintered metal at stagnation region to simulate ablation phenomena. More detailed information on this model is given in Reference 1.

Fig.1 Artificial ablation model

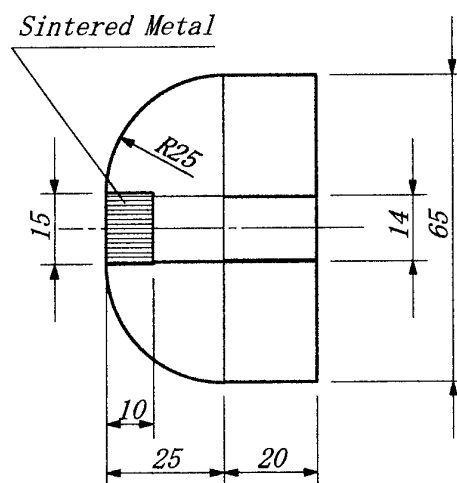## 2.6 Wall Conditions

The physico-chemical conditions on blunt body wall are assumed as non-slip, isothermal, non-catalytic and solid, where the wall temperature is set to 1200K which is probably higher than the one in actual case. The temperature value, however, is selected for computational convenience. Properties of injected gas are given as: the density 0.32771kg/m^3, the velocity

150m/s and the temperature 1200K.

2.7 Calculation Technique

Calculation is carried out in the following manner:

(1) Generate an initial grid system and give initial conditions.

(2) Solve the flow using Navier-Stokes equations.

(3) Adapt the grid and go back to Step (2).

(4) Solution continues until convergence.

The solution procedure starts from a coarse grid, which consists of a structured grid near body surface and an unstructured grid in the remaining region. After having acquired the grid data, including cell geometric properties, the flowfield is calculated up to a certain degree of convergence. This first-step result is used to improve the grid quality in the next step.

In the first step, the number of grid points is 1,176 and the number of structured layers is set to 1 in both cases (with/without jets). In the final step, the number of total grid points has become 4,693 for a no-jet case, while 4,997 for a with-jet case (Fig.2), where the number of structured layers is set to 20 in both cases. The minimum grid size normal to surface is set to 1μ m which is enough to resolve boundary layer.
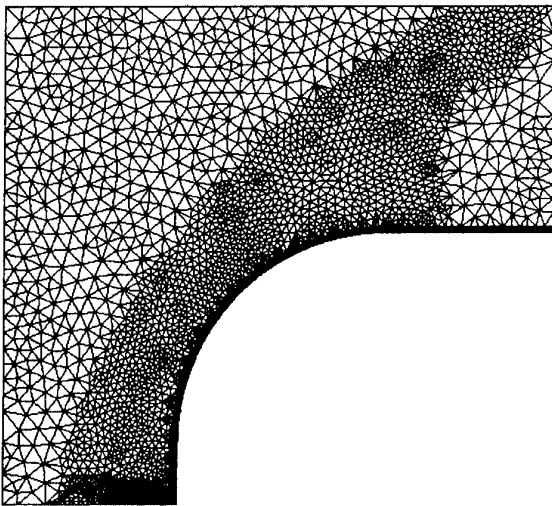
Fig.2 Final grid for a with-jet case

3. COMPUTATIONAL RESULTS

The pressure distribution for both cases is shown in Fig.3. In the upper, the gas jet increases the shock layer by pushing the bow shock ahead, as shown in the experimental results. The injected flow direction is reversed and compressed again in the body shoulder part. The heat flux distribution along with-jet wall, shown in Fig.4, shows a rapid increase of heat flux over non-ablating location. However, the heat flux value is still much lower than the without-jet case (Fig.5). The effect of artificial ablation is shown conspicuously.

5.0E+002   1.2E+005

Fig.3 Pressure distribution [Pa]

Fig.4 Convective heating for a with-jet case

Fig.5 Convective heating with/without jet

Fig.6 Temperature distribution
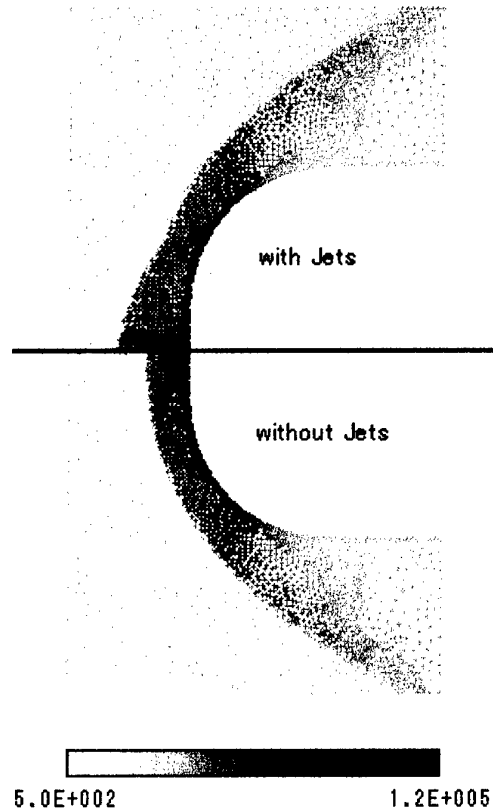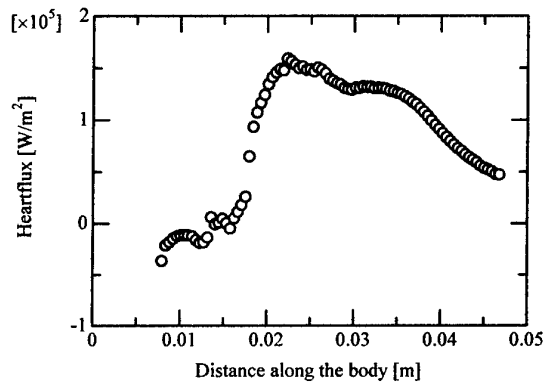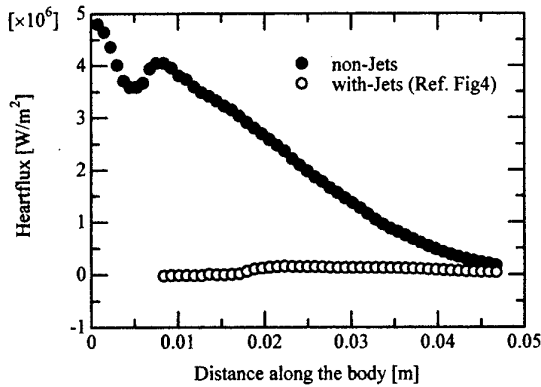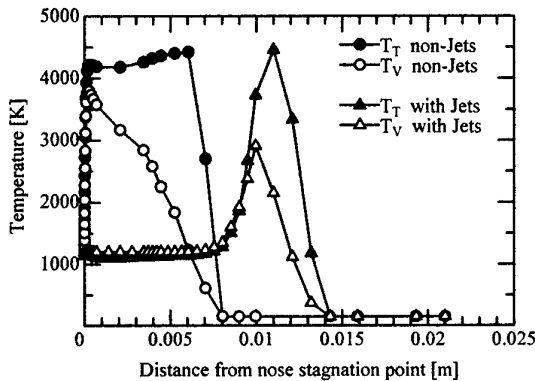**on stagnation streamline**

The temperature distribution on stagnation streamline is shown in Fig.6, where the subscripts T and V on temperatures signify the transnational-rotational and vibrational-electron-electronic excitations. Since the dissociation of N_2 begins only at T>4,000K, the chemical components of flow behind bow shock wave would be nearly entirely N_2 in both with-jet/without-jet cases. If the energy is proportional to the temperature, the vibrational temperature can be written as

$$T_V = T_V^E\left[1 - \exp\left(-\frac{t}{\tau_V}\right)\right]$$

where T_V^E is the vibrational temperature at equilibrium, τ_V the vibrational energy relaxation time, which is a given value behind bow shock wave, and t the time. In a without-jet case, t is calculated as L/V=2.20×10^{-5} sec from the distance L between the bow shock position and the position where the

vibrational temperature becomes maximum and the flow velocity V. If T_V^E is equal to 4,416K, the translational temperature behind bow shock, the vibrational temperature T_V is evaluated as 3,807K, which is confirmed by the present numerical simulation.

4. CONCLUDING REMARKS

A numerical code simulating our experiments has been developed. The distribution of various physical properties is visualized, clearly giving the effects of gas injection. It has turned out to be necessary, however, to utilize the injected gas conditions identical to experiments, because distinct differences are seen regarding the pressure distribution and aerodynamic heating.

REFERENCES

[1] T. FUJIWARA, K. MURAKAMI, K. KAGA and T. MATSU-URA: Numerical and Experimental Study of Heat Transfer to Hypersonic Reentry Body, 1st Korea-Japan Symposium on Aircraft Parts Technology (2000), pp.91-98.

[2] C. Park: Assessment of Two-Temperature Kinetic Model for Ionizing Air, J. Thermophysics and Heat Transfer 3 (1989), pp.233-244.

[3] J. M. Yos: Transport Properties of Nitrogen, Hydrogen, Oxygen and Air to 30,000K, Tech. Memo. RAD-TM-63-7 (Contract AF33 (616) 7578), AVCO Corp (1963).

[4] S. Kano and K. Nakahashi: Flow Computations around Delta Wings Using Unstructured Hybrid Grids, Journal of Aircraft, Vol.36, No.2, March-April 1999.

[5] P. A. Gnoffo, R. N. Gupta and J. L. Shinn: Conservation Equations and Physical Models for Hypersonic Air Flows in Thermal and Chemical Nonequilibrium, NASA Technical Paper 2867, 1989.

[6] J. D. Anderson Jr.: Hypersonic and High Temperature Gas Dynamics, McGraw-Hill.

NUMERICAL SIMULATIONS OF LEADING-EDGE SEPARATION VORTICES

Toshiyuki Horie*1, Kozo Fujii*2, Hattori Naozo*3

*1, *3 Science University of Tokyo, 2641 Yamasaki, Noda-shi, Chiba 278-8510
*2 The Institute of Space and Astronautical Science, 3-1-1 Yoshinodai, Sagamihara-shi, Kanagawa 229-8510

Key Word: Numerical Simulation, Leading-Edge Separation Vortex, Delta Wing, Double-Delta Wing

ABSTRACT

Vortical flows over delta wings and double-delta wings are numerically simulated. The reliability of the simulations for both types of wings is investigated. The results obtained with different grid resolutions and different entropy fixes show that characteristics of the secondary vortex, which in turn influences the strength and the position of the primary vortex, strongly depend on these parameters. Although the computed primary vortex on the delta wing disagrees with the experiments on both strength and location, these discrepancies compensate each other and the compensation leads to good agreement with the experiments on the aerodynamic characteristics. On the other hand, the interactions of the two primary vortices on the double-delta wings are influenced by the strength and the location of the vortices. More research is necessary for an accurate simulation of the leading-edge separation vortices especially over a double-delta wing.

1. INTRODUCTION

Delta wings and double-delta wings are often used as main wings for supersonic transports (SST) and space planes. For these wings at moderate to large angle of attack in taking off and landing, the flow separates from the leading-edge and forms a pair of spiral-shaped vortices above the upper surface of the wing. These vortices become the predominant factors of the resulting aerodynamic characteristics of the wing.

Figure 1 shows the computed total pressure contour plots over a double-delta wing as an example. The total number of grid points is about 120,000 and the angle of attack is 12 degrees. The result shown in Fig. 1 (a) indicates the existence of two vortices over the upper surface: one emanating from the strake leading-edge and the other from the main-wing leading-edge. The two vortices merge in the main-wing region due to the mutual interaction. Figure 1 (b) shows the result obtained with the slightly increased entropy fix[1],[2] (numerical viscosity which only influences the region where eigen value is zero). The contour plots change dramatically, and the flow structure as shown in Fig. 1 (a) can not be observed.

A large number of numerical studies have been reported for delta wings, and they showed accurate simulation results[3],[4]. For double-delta wings, the flow fields are greatly influenced by small factors as mentioned above. Therefore flow simulations for the wings like double-delta wings must be carried out more carefully compared to delta wings as most of the practical wings used in the next generation are similar to double-delta wings.

*1 Graduate Student, Department of Mechanical Engineering
*2 Professor, Research Division for Space Transportation
*3 Professor, Department of Mechanical Engineering

In this study, vortical flows over a delta wing and a double-delta wing are numerically simulated. By changing entropy fixes and grid resolutions, the reliability of the simulations for a delta wing is reconfirmed, and the influences to the flow fields for both types of wings are investigated.
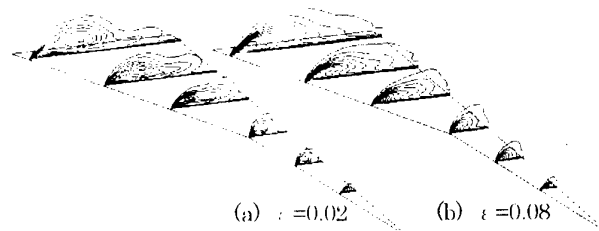

Fig. 1 Total pressure contour plots over a double-delta wing.
(a) ε =0.02   (b) ε =0.08

2. NUMERICAL METHOD

The governing equations are three-dimensional thin-layer Navier-Stokes equations. The convective terms are evaluated by the Roe scheme[5]. High-order space accuracy is obtained using the MUSCL[6], the primitive variable interpolation. The viscous terms are evaluated by the central differencing and the boundary layers are assumed to be laminar. Only the steady-state solutions are considered, and the FF-SGS[7] factorization time integration algorithm is used.

A coarse grid distribution which consists of about 110,000 grid points and a fine grid distribution which consists of about 810,000 are used for the investigation of grid resolution effect for both types of wings. The influences of entropy fixes are further investigated by changing the parameter ε which determines the entropy fix (ε =0.02 and 0.08).

The body geometries of delta wing and double-delta wing are the same as those used in the experiments by Hummel[8] and by Brennenstuhl and Hummel[9], respectively. The delta wing has a leading-edge sweep angle of 76°, and the double-delta wing has a leading-edge sweep angle of 80° at the strake and 60° at the wing. The leading-edge geometries of both types of wings are different: the delta wing has a sharp leading-edge and the double-delta wing has a rounded one.

Table 1 shows the flow conditions used in the present computations. The angles of attack are the same as those used in the experiments[8],[9]. The Mach number of 0.3 is used so that comparison can be made with the low-speed experiments[8],[9].

Table 1 Flow conditions.

	Mach	Re (root chord)	α
Delta wing	0.3	0.9 × 10⁶	20.5°
Double-delta wing	0.3	1.3 × 10⁶	12°

3. COMPUTED RESULTS

3.1 Delta Wing

Figure 2 shows an example of the computed total pressure contour plots over a delta wing. The result shows the existence of a separation vortex emanating from the leading edge. The secondary separation vortex can be also observed near the leading-edge due to the flow separation over the upper surface.
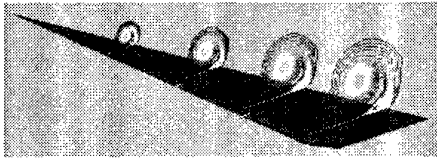

Fig. 2 Total pressure contour plots (Fine grid, ε =0.02).

Aerodynamic Characteristics

Figure 3 shows the computed C_p distributions in three chordwise sections on the upper surface of the wing. The results obtained with the fine grid and the coarse grid are shown together with the experimental data. The results for fine grid show one suction pressure peak near 60% spanwise location. This peak occurs due to the leading-edge separation vortex. The results also show the other suction pressure peak near 90% spanwise location. This peak occurs due to the secondary separation vortex. The computed result with the fine grid shows good agreement with the experiment at all the chordwise section. The computed result with the coarse grid shows that agreement with the experiment is still acceptable although the pressure peak due to the secondary separation vortex is weak and, as a result, the pressure peak due to the main leading-edge separation vortex is located slightly near the leading edge.

The computations were carried out for two sizes of entropy fix (ε =0.02 and 0.08). There was almost no difference between the results for the two conditions, except that the suction pressure peak by the primary vortex is located slightly toward the leading-edge when the entropy fix is strengthened (ε =0.08). The result is not presented here.

Figure 4 shows the numerical and experimental results of lift coefficient as a function of angle of attack α, and Fig. 5 shows those of pitching moment coefficient. Both computed coefficients are in good agreement with the experiments although the computations were carried out only for one angle of attack.
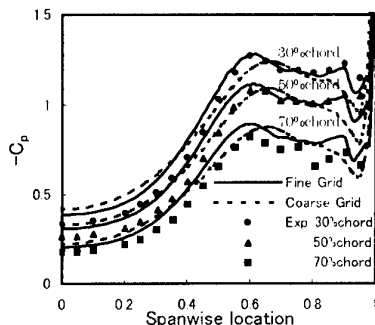

Fig. 3 Pressure coefficient distributions (ε =0.02).
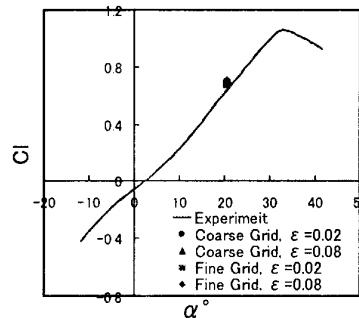

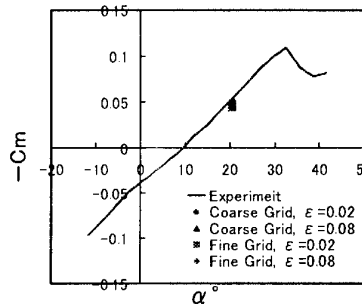Fig. 4 Lift coefficient versus angle of attack.

Fig. 5 Pitching moment coefficient versus angle of attack.

The computed aerodynamic characteristics for a delta wing show good agreement with the experiments regardless of grid resolutions and entropy fixes. However, in fact the flow structure is influenced by these numerical factors. The discussion is given below.

Influences to Flow Fields

The influences of grid resolutions to the flow fields are investigated in this section. Figure 6 shows the computed total pressure contour plots at 70% chordwise section. Figures 6 (a) and (b) show the results obtained with the fine grid and the coarse grid respectively. These figures show that the characteristics of the secondary separation vortex strongly depend on the grid resolutions. The secondary vortex for the fine grid simulation separates more intensively than that of coarse grid, and that in turn influence the strength and the position of the primary vortex.

Figure 7 shows the static pressure of the vortex core in three chordwise sections, and Fig. 8 shows the height of the vortex core from the upper surface of the wing. The suction pressure of vortex core for the coarse grid simulation is weaker and the height is lower than that for the fine grid at all the chordwise section.

Regardless of such discrepancies of the strength and the position of the primary vortex, the computed pressure coefficient distributions for both fine and coarse grid show good agreement with the experiments as discussed in Fig. 3. The center of the vortex is stronger but farther when the fine grid was used, and is weaker but closer to the wing surface when the coarse grid was used. As a result, the induced negative pressure peaks over the upper surface of the wing become similar. This is the reason for the pressure distributions and

forces to agree with the experiments either with the fine grid or with the coarse grid.

The similar phenomena were observed to entropy fixes (not shown here). A series of computations for a delta wing presented here indicates that good agreement with the experiments on aerodynamic characteristics does not necessarily indicate that the flow fields are accurately simulated.
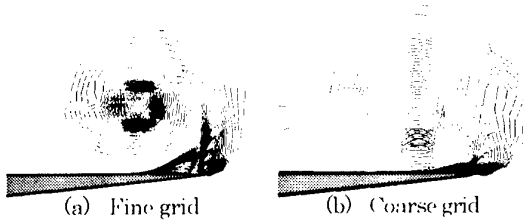

(a) Fine grid   (b) Coarse grid

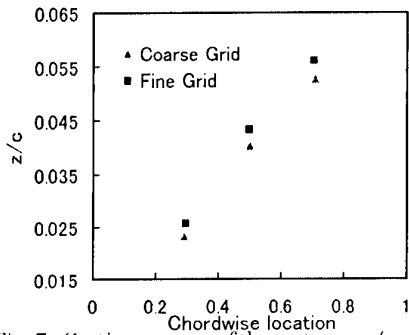Fig. 6 Total pressure contour plots in 70% chordwise section.

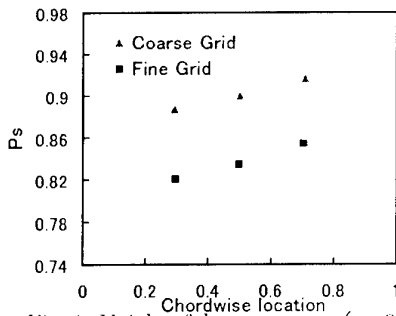Fig. 7 Static pressure of the vortex core (t =0.02).

Fig. 8 Height of the vortex core (t =0.02).

3.2 Double-Delta Wing

Figure 9 shows an example of the computed total pressure contour plots over a double-delta wing. Two vortices, one from the strake and the other from the wing leading-edge, are clearly observed. These two vortices interact each other in the main wing region and merge together at the downstream station.
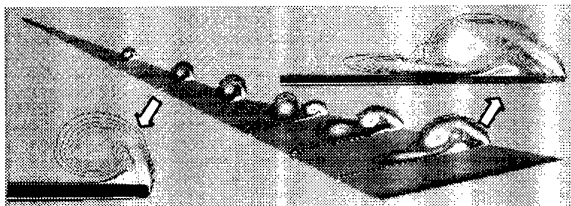

Fig. 9 Total pressure contour plots (Fine grid, t =0.02).

Aerodynamic Characteristics

The computed C_p distributions on the upper surface of the double-delta wing are shown in Fig. 10, together with the experimental data. The results shown in Figs. 10 (a) and (b) are obtained at 62.5% and 75% chordwise sections, respectively. The experimental data in both chordwise sections show the existence of two suction pressure peaks. One suction pressure peak observed near 50% spanwise location is induced by the vortex emanating from the strake leading edge. The other suction pressure peak observed near 80% spanwise location is induced by the vortex emanating from the main-wing leading edge.

The computed result for the coarse grid (about 140,000 grid points) shows much weaker suction peaks at 62.5% chordwise section than those of the experiments (Fig. 10 (a)), and only one peak is observed at 75% chordwise section (Fig. 10 (b)).

From Figs. 10 (a) and (b), results for fine grid (about 810,000 grid points) show two obvious pressure peaks at both chordwise sections. The peak of the strake vortex at 62.5% chordwise section especially shows good agreement with the experiments. However, the peak of the wing vortex disagrees with the experiment at both chordwise sections.

In any case, the solutions are obviously improved by increased number of grid point. Therefore, the computation using still finer grid (about 1,000,000 grid points) is carried out. The pressure peak of the "strake" vortex in Figs. 10 (a) and (b) show further improvement. However, the peak of the "wing" vortex still disagrees with the experiment at both chordwise sections.

As mentioned above, the computed C_p distributions for a double-delta wing disagree with the experiment even when either the same or still finer grid distributions as those used in the computations for a delta wing are used.

Figures 11 and 12 show the lift and pitching moment coefficients, respectively. The computed lift coefficient shows good agreement with the experiment. On the other hand, the computed pitching moment coefficient shows about 60% less value than that of the experiment. The main reason for this discrepancy comes from inaccurate pressure distributions in the main-wing region.

Generally speaking, aerodynamic characteristics of a delta wing can be predicted accurately, but aerodynamic characteristics of a double-delta wing are difficult.
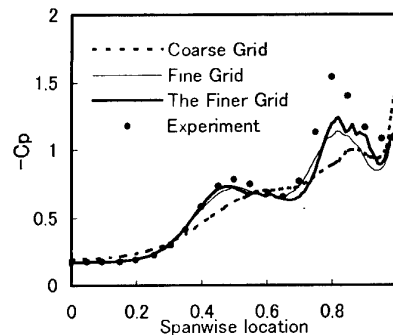
(a) 62.5% chordwise location.

(b) 75% chordwise location.

Fig. 10　Pressure coefficient distributions (ε =0.02).

Fig. 11　Lift coefficient versus angle of attack.

Fig. 12　Pitching moment coefficient versus angle of attack.

Influences to Flow Fields

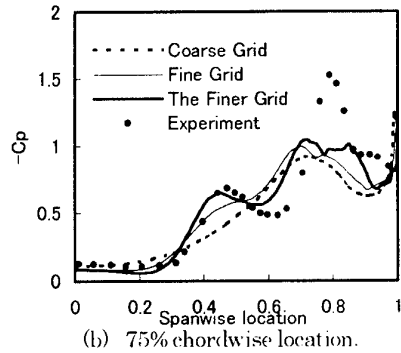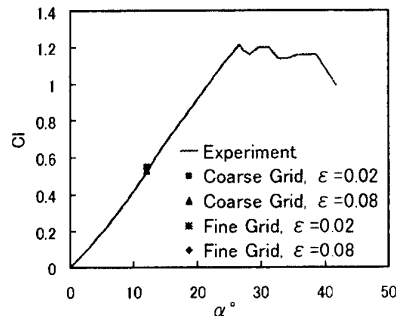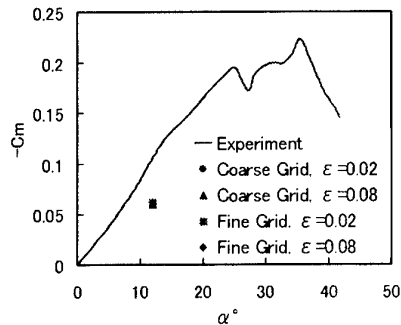The contour plots shown in Fig. 9 show the existence of the secondary separation vortices emanating near the leading edge in both strake and main-wing region. Grid resolutions and entropy fixes influence the characteristics of the secondary vortices, which in turn change the strength and the position of the two primary vortices from the strake and the main-wing leading edge.

The computed off-surface particle traces are shown in Fig. 13. The results shown in Figs. 13 (a) and (b) are obtained with the coarse and the fine grid, respectively. The computed results for two entropy fixes are shown for each grid resolution. The location of the vortex merging tends to occur in the aft region of the wing when the fine grid is used. Different entropy fixes also change the location of the merging even when the same grid resolution is used. The main reason for the discrepancy of the interaction and the merging of vortices comes from inaccurate predictions of the strength and the position of the primary vortices, which leads to difficulty in predicting the

aerodynamic characteristics of the double-delta wing.
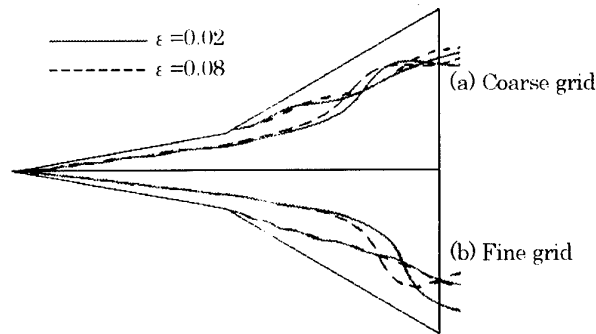
Fig. 13　Off-surface particle trace.

4.　CONCLUSIONS

Computations of vortical flows over a delta wing and a double-delta wing have been carried out. The reliability of the simulations for both types of the wing was investigated. Aerodynamic lift force and moment as well as the pressure distributions showed good agreement with the experiments for the delta-wing simulation with either the coarse or fine grid. However, the details of analysis of the flow field showed that the location and the strength of the separation vortex showed dependency on the grid resolution.

For the double-delta wing simulation, difficulty exists for the prediction of the pressure distributions, and as a result of the pitching moment even when the still finer grid is used. Accurate simulation of the flow field over a double-delta wing still requires more research effort.

REFERENCES
(1)　A. Harten, "On a Class of High Resolution Total-Variation-Stable Finite-Difference Schemes", SIAM J. Num. Anal. , Vol. 21, pp. 1-23, 1984.

(2)　Yee, H. "Upwind and Symmetric Shock-Capturing Schemes", NASA TM 89464, May, 1987.

(3)　J. L. Thomas, S. L. Taylor, and W. K. Anderson, "Navier-Stokes Computations of Vortical Flows over Low Aspect Ratio Wings", AIAA Paper 87-0207, 1987.

(4)　J. A. Ekaterinaris and Lewis B. Schiff, "Numerical Prediction of Vortical Flow over Slender Delta Wings", Journal of Aircraft, Vol.30, No.6, Nov.-Dec. 1993.

(5)　Roe, P.L., "Approximate Riemann Solvers, Parameter Vectors, and Difference Schemes", Journal of Computational Physics, 43, 357-372, 1981.

(6)　Van Leer, B. "Toward the Ultimate Conservative Difference Scheme, 5, A Second-Order Sequel to Godunov's Method", Journal of Computational Physics, 32, 101-136, 1979.

(7)　Fujii, K., "Efficiency Improvements of Unified Implicit Relaxation/Time Integration Algorithms and Their Applications", AIAA Paper 97-2105, 1997.

(8)　Hummel, D., "On the Vortex Formation over a Slender Wing at Large Angles of Incidence", High Angle of Attack Aerodynamics, AGARD-CP-247, Paper No.15, 1997.

(9)　Brennenstuhl, U. and Hummel, D., "Vortex Formation Over Double-Delta Wing", ICAS Paper82-6.6.3, 1982.

NONLINEAR FLIGHT CONTROL BASED ON MODEL INVERSION
USING NUERAL NEWTORKS

Hyunjae Lee* and ChangHo Hong**
Chungnam National University, Daejeon Korea

Hyochoong Bang ***
Korea Advanced Institute of Science & Technology, Daejeon Korea

Key Words: Inversion control, Neural Networks, Coordinated-turn

Abstract
In this paper a model inversion nonlinear control strategy for unknown nonlinear systems is presented. The whole strategy is to make a linear system from a nonlinear system by input-output feedback linearization and design a linear controller. The Neural Networks are applied to implement the unknown nonlinear systems. This control strategy is applied to the aircraft flight control for a specific flight profile. Numerical simulation for aircraft coordinated-turn control by the model inversion-based control technique using neural networks for unknown flight dynamics is performed, which demonstrate the practical potential of the theoretical results.

I. Introduction
Flight control design based upon classical control theory has been applied over a broad class of applications. Due to the recent upgrade in aircraft performance, new control system requirements such as robustness and nonlinearity have emerged as new challenging issues. Also diverse aircraft configurations such as tailless aircraft and tilted rotor type require high maneuverability and high angle of attack.

As a nonlinear controller design technique, the feedback linearization is based upon exact dynamic modeling of a system. But modeling of generic flight dynamics, in particular, reliable aerodynamic modeling poses significant difficulty. There has been considerable effort in nonlinear control system design last decades, and the input-output feedback linearization has received noticeable attention.

The principal idea of the feedback linearization is to derive input-output relationship over the plant to be controlled, and derive the control input signal satisfying the prescribed input-output relationship. This method is essentially inverse transform for the input-output, and called inversion control. In general the input and output are represented in the first-order form. If control input does not appear explicitly in the output equation, successive differentiation operation is taken until the control input appears in the expression. The control input is then obtained in terms of state variables in such a way that the output equation is satisfied. The underlying assumption for feedback linearization is that all state variables are available. Such assumption may be a constraint in practical applications. Many efficient algorithms to overcome the limitation are under study.

Neural networks are employed in an effort to resolve the observability issue of state variables. In other words, the neural networks take advantage of approximating systems with unknown states and uncertainties. Stability of the system with the neural networks is proved by using Lyapunov stability theory.

The feedback stabilization in conjunction with neural networks mentioned above is applied to coordinated-turn maneuver of aircraft in this study. The coordinated-turn is a frequently used maneuver for guidance and navigation purpose. As the aircraft tends to perform coordinated-turn unwanted sideslip angle may be induced due to the typical roll/yaw coupling effect.

The principal idea of this study is to maintain the coordinated-turn by minimizing induced sideslip angle. The control surface needed in such maneuver is rudder, and multi-input, multi-output control scheme is applied.

This paper consists of the following steps. First, feedback linearization with input-out relationship is briefly introduced. Then the neural networks are combined to approximate aircraft dynamics under uncertainties. Stability analysis is followed for the neural networks. Finally controller design for coordinated-turn maneuver is presented. Simulation results are presented to verify the proposed method.

II. Inversion Controller Design
For a nonlinear system represented in the form

$$\dot{x} = f(x, u, t)$$
$$y = h(x, u, t) \tag{1}$$

If the input-output relationship is defined as

$$y(t) = h(x(t)) + g(x(t))u(t) \tag{2}$$

then the control input becomes

$$u(t) = \frac{y(t) - h(x(t))}{g(x(t))} \tag{3}$$

If the output and input variables are not related in the above relationship, but ρ th order derivates of the output satisfy the following equation

$$y(t)^{(\rho)} = h(x(t)) + g(x(t))u(t) \tag{4}$$

Let us assume that $g(x(t)) \neq 0$ and $y(t)^{(\rho)} = v(t)$. Then the new control law is given in the form

$$u(t) = \frac{y(t)^{(\rho)} - h(x(t))}{g(x(t))} = \frac{v(t) - h(x(t))}{g(x(t))} \tag{5}$$

If a reference trajectory $r(t)$ is given, the feedback control law can be shown to render the output($y(t)$) follow the reference input. In this case the error equation satisfies

$$e^{(\rho)}(t) + \alpha_{(\rho-1)}e^{(\rho-1)}(t) + \cdots + \alpha_1 e^{(1)}(t) + \alpha_0 e(t) = 0 \tag{6}$$

where $e = y(t) - r(t), e^{(1)} = y^{(1)}(t) - r^{(1)}(t) \cdots$ and $\alpha_{(i)}$ are appropriate design parameters. The command input can be written as

$$v(t) = r^{(\rho)}(t) - \{\alpha_0 e(t) + \cdots + \alpha_{(\rho-1)}e^{\rho-1}(t)\}$$

*Research Assistant, Dept. of Aerospace Engineering,
**Professor, Dept. of Aerospace Engineering,
*** Assistant Professor, Dept. of Aerospace Engineering

which, upon substitution into Eq. (5), yields

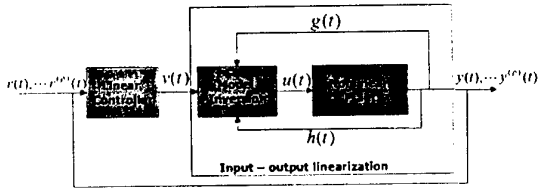Let us define $E = \Lambda e$ as the filtered error signal. Also, it should be noted.

Fig. 1 Block diagram for model inversion controller

$$u(t) = \frac{r^{(\rho)}(t) - \{\alpha_0 e(t) + \cdots + \alpha_{(\rho-1)} e^{\rho-1}(t)\} - h(x(t))}{g(x(t))} \quad (7)$$

$$Y_d = -r^{(\rho)}(t) + \{\alpha_0 e(t) + \cdots + \alpha_{(\rho-1)} e^{\rho-1}(t)\}$$

As a model inversion controller, a PID type linear controller is introduced. Then the following error equation is obtained by the control law in Eq. (7).

$$\dot{E} = h(x(t)) + g(x(t))u(t) + Y_d + K_v E \quad (8)$$

Now the exact control law by model inversion is represented in the form

$$u(t)_{exact} = \frac{Y_d - h(x(t))}{g(x(t))} \quad (9)$$

However, in general, exact modeling for such control command is not feasible, and the following modified control law is proposed.

$$u(t)_c = \frac{-Y_d - \hat{h}(x(t))}{g(x(t))} \quad (10)$$

where $\hat{h}(x(t))$ is an approximation of $h(x(t))$. The closed-loop dynamics with the approximation is given by

$$\dot{E} \cong h(x(t)) + g(x(t))u_c(t) + Y_d - K_v E$$
$$= h(x(t)) - \hat{h}(x(t)) - K_v E = \tilde{h}(x(t)) - K_v E \quad (11)$$

where $\tilde{h}(x(t)) = h(x(t)) - \hat{h}(x(t))$

III. Neutral Networks for Approximation

The control law designed so far needs fundamental assumption that exact system dynamics should be modeled. Stability as well as performance of the controlled system therefore depend on how accurate the system modeling is. In particular, for the nonlinear systems such as aircraft with high maneuverability, the accurate knowledge on system dynamics is not easy to acquire. In this study, neural networks are used to partially resolve such modeling issues. A multi-layer neural networks architecture is used for the specific application.
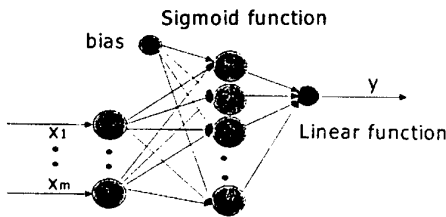

Fig. 2 Neural networks architecture

Let v be weighting parameters between input and hidden layer. In addition, W denotes weighting parameters between

hidden and output layers. The output of the network can be represented in terms of the input as

$$y = W\sigma(Vx)$$

where $\sigma(\cdot)$ is a sigmoid function commonly adopted in neural networks. The function $h(x(t))$ in the model inversion controller may be replaced by the neural networks to avoid potential modeling errors.

The output of neural networks with respect to the ideal weighting parameters can be written as

$$h(x(t)) = W\sigma(Vx) + \varepsilon \quad (12)$$

where the modeling error(ε) is within a bound

$$\|\varepsilon\| < \varepsilon_N$$

The new weighting parameters estimated by learning process are used to produce the corresponding output function

$$\hat{h}(x(t)) = \hat{W}\sigma(\hat{V}x)$$

By Taylor series expansion, the above expression may be approximated as

$$\tilde{h}(x(t)) = \tilde{W}(\hat{\sigma} - \hat{\sigma}'\hat{V}x) + \hat{W}\hat{\sigma}'\tilde{V}x + w \quad (13)$$

where w denotes high order terms in series, and following notations are introduced.

$$\tilde{W} = W - \hat{W}, \quad \tilde{V} = V - \hat{V}$$

$$\tilde{\sigma} = \sigma - \hat{\sigma} = \sigma(Vx) - \sigma(\hat{V}x),$$

$$\sigma'(\hat{z}) = \left[\frac{d\sigma(z)}{dz}\right]_{z=\hat{z}} .$$

Therefore, one of the functions in the original inversion controller is replaced by the output of the neural networks. Thus substitution of Eq. (13) into Eq. (11) yields

$$\dot{E} \cong -K_v E + \tilde{h}(x(t))$$
$$= -K_v E + \tilde{W}(\hat{\sigma} - \hat{\sigma}'\hat{V}x) + \hat{W}\hat{\sigma}'\tilde{V}x + w \quad (14)$$

Weighting parameters for the neural networks are updated as

$$\dot{\hat{W}} = M(\hat{\sigma} - \hat{\sigma}'\hat{V}x)E - \kappa|E|M\hat{W}$$
$$\dot{\hat{V}} = NEx\hat{W}\hat{\sigma}' - \kappa|E|N\hat{V} \quad (15)$$

where M, N are positive definite matrices, and κ is a positive learning rate. With the introduction of new function by neural networks, the stability of the whole system need to be examined. For stability proof, a Lyapunov function is introduced as

$$L = \frac{1}{2}E^2 + \frac{1}{2}tr\{\tilde{W}^T M^{-1}\tilde{W}\} + \frac{1}{2}tr\{\tilde{V}^T N^{-1}\tilde{V}\} \quad (16)$$

Time derivative of the Lyapunov function yields

$$\dot{L} = -K_v E^2 + E(\tilde{W}(\hat{\sigma} - \hat{\sigma}'\hat{V}x) + \hat{W}\hat{\sigma}'\tilde{V}x + w)$$
$$+ tr\{\tilde{W}^T M^{-1}\dot{\tilde{W}}\} + tr\{\tilde{V}^T N^{-1}\dot{\tilde{V}}\}$$

From the following relationships,

$$\dot{\tilde{W}} = \dot{W} - \dot{\hat{W}} = -\dot{\hat{W}}, \dot{\tilde{V}} = \dot{V} - \dot{\hat{V}} = -\dot{\hat{V}}$$

stability of the system in the Lyapunov sense is proved.

$$\dot{L} = -K_v E^2 + E(\tilde{W}(\hat{\sigma} - \hat{\sigma}'\hat{V}x) + \hat{W}\hat{\sigma}'\tilde{V}x + w)$$
$$+ tr\{\tilde{W}^T M^{-1}(M(\hat{\sigma} - \hat{\sigma}'\hat{V}x)E - \kappa|E|M\hat{W})\}$$
$$+ tr\{\tilde{V}^T N^{-1}(NEx\hat{W}\hat{\sigma}' - \kappa|E|N\hat{V})\} \quad (17)$$
$$= -K_v E^2 + Ew$$

In other words, if $K_v E > w$, Lyapunov stability is guaranteed.

IV. Coordinated-Turn Control

The feedback linearization or model inversion controller discussed in the previous sections is applied to the control of aircraft coordinated-turn maneuver. In general, when aircraft tries to make a turn by bank angle, unwanted sideslip may be created. Sideslip angle thus degrades the performance of

coordinated-turn. Thus the control objective of here in is to maintain bank angle at a desired level while controlling sideslip angle to minimum.
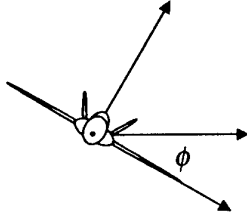

Fig. 3 Coordinated-Turn flight

The output variables are defined as $y_d = [V \ \phi]^T$

where V is the sideslip velocity and ϕ is the bank angle. The output equation is used to design model inversion controller. First, the nonlinear governing equations of motion for aircraft are given by

$$\dot{U} = RV - QW - g_0 \sin\theta + F_x / m$$
$$\dot{V} = -RU + PW + g_0 \sin\phi \cos\theta + F_y / m \quad (18)$$
$$\dot{W} = QU - PV + g_0 \cos\theta \cos\phi + F_x / m$$
$$\dot{P} = (c_1 R + c_2 P)Q + c_3 L + c_4 N$$
$$\dot{Q} = c_5 PR - c_6 (P^2 - R^2) + c_7 M$$
$$\dot{R} = (c_8 P - c_2 R) + c_4 L + c_9 N$$

where each parameter is given as

$$\Gamma = I_x I_z - I_{zx}^2, \Gamma c_1 = (I_x - I_z)I_z - I_{xz}^2$$
$$\Gamma c_2 = (I_x - I_y + I_z)I_{xz}, \Gamma c_3 = I_z$$
$$\Gamma c_4 = I_{xz}, c_5 = \frac{I_z - I_x}{I_y}, c_6 = \frac{I_{xz}}{I_y}$$
$$c_7 = 1/I_y, \Gamma c_8 = I_x(I_x - I_y) + I_{xz}^2, \Gamma c_9 = I_x$$
$$g_0 = g/m$$

The side velocity equation is used to find inversion controller

$$y_d = V$$

and

$$\dot{y}_d = \dot{V} = -RU + PW + g_0 \sin\phi \cos\theta + Fx/m \quad (19)$$

From Eq. (19) we can see that the side force equation is in effect to build control input. The control input (Fx/m) is generated by a rudder, but the magnitude is relatively small to directly affect the side acceleration. The aerodynamic control surfaces are primarily engaged in developing control moment. Thus one more differentiation of Eq. (19) is taken to yield

$$\ddot{V} = -\dot{R}U - R\dot{U} + \dot{P}W + P\dot{W} \\ + g_0 \cos\phi\dot{\phi}\cos\theta + g_0 \sin\phi \sin\theta\dot{\theta} + \dot{F}x/m \quad (20)$$

From Eq. (20) each angular acceleration term is produced by aerodynamic moments such as L, M, N . The aerodynamic moment can be represented as

$$L = L_0(x) + L_u \delta u$$
$$M = M_0(x) + N_u \delta u$$
$$N = N_0(x) + N_u \delta u$$
$$F_x = F_{x0}(x) + F_{x_u} \delta u \quad (21)$$
$$F_y = F_{y_0}(x) + F_{y_u} \delta u$$
$$F_z = F_{z_0}(x) + F_{z_u} \delta u$$

where x represents the aircraft state vector and the control input δu consists of both aileron and rudder. Eq. (21) is used

to rewrite Eq. (20) as

$$\ddot{y}_d = \ddot{V} = -\dot{R}U - R\dot{U} + \dot{P}W + P\dot{W} \\ + g_0 \cos\phi\dot{\phi}\cos\theta + g_0 \sin\phi \sin\theta\dot{\theta} + \dot{F}z / m$$

or

$$\ddot{y}_d = -((c_8 P - c_2 R)Q + c4L + c_9 N)U \\ - R(RV - QW - g_0 \sin\theta + Fx/m) \\ + ((c_1 R + c_2 P)Q + c_3 L + c_4 N)W \quad (22) \\ + P(QU - PV + + g_0 \cos\phi \cos\theta + Fz/m) \\ + g_0 \cos\phi\dot{\phi}\cos\theta + g_0 \sin\phi \sin\theta\dot{\theta} + \dot{F}z / m$$

The above equation is re-arranged into a function

$$h_1(x(t)) = -((c_8 P - c_2 R)Q + c4L_0(x) + c_9 N_0(x))U \\ - R(RV - QW - g_0\sin\theta + F_{x0}(x)/m) \\ + ((c_1 R + c_2 P)Q + c_3 L_0(x) + c_4 N_0(x))W \quad (23) \\ + P(QU - PV + + g_0 \cos\phi\cos\theta + F_{z0}(x)/m) \\ + g_0\cos\phi\dot{\phi}\cos\theta + g_0\sin\phi\sin\theta\dot{\theta} + \dot{F}_{z0}(x)/m$$

and

$$g_1(x(t)) = Uc_4 L_u \delta u - RFx_u \delta u / m + W(c_3 L_u \delta u \\ + c_4 N_u \delta u) + PFz_u \delta u / m) + \dot{F}z_u \delta u(x) / m \quad (24)$$

Next the inversion control for the bank angle equation is attempted.

$$y_d = \phi$$

Thus time derivative of the bank angle yields

$$\dot{y}_d = \dot{\phi} = P + \tan\theta(Q \sin\phi + R \cos\phi) \quad (25)$$

Furthermore

$$\ddot{y}_d = \ddot{\phi} = (c_1 R + c_2 P)Q + c_3 L + c_4 N + \sec^2\theta\dot{\theta}(Q\sin\phi + R\cos\phi) \\ + \tan\theta((c_5 PR - c_6(P^2 - R^2) + c_7 M)\sin\phi + Q\sin\phi \quad (26) \\ + ((c_8 P - c_2 R)Q + c_4 L + c_9 N)\cos\phi - R\sin\phi)$$

The above equations are re-arranged resulting in

$$h_2(x(t)) = (c_1 R + c_2 P)Q + c_3 L_0(x) + c_4 N_0(x) \\ + \sec^2\theta\dot{\theta}(Q\sin\phi + R\cos\phi) \\ + \tan\theta((c_5 PR - c_6(P^2 - R^2) + c_7 M_0(x))\sin\phi + Q\sin\phi \quad (27) \\ + ((c_8 P - c_2 R)Q + c_4 L_0(x) + c_9 N_0(x))\cos\phi - R\sin\phi)$$

$$g_2(x(t)) = c_3 L_u\delta u + c_4 N_u\delta u + c_7 \sin\phi\tan\theta M_u\delta u \\ + \tan\theta \cos\phi(c_4 L_u\delta u + c_9 N_u\delta u) \quad (28)$$

Next from the definition of $y(t)^{(\rho)} = v(t)$, the following approximations are resulted.

$$\ddot{V} \approx v_1(t), \quad \ddot{\phi} \approx v_2(t) \quad (29)$$

Equation (29) is used to build linear control laws as

$$v_1(t) = \ddot{V}_c + k_{11}\dot{e}_1 + k_{10}e_1 \\ v_2(t) = \ddot{\phi}_c + k_{11}\dot{e}_2 + k_{10}e_2 \quad (30)$$

where $e_1 = V - V_c$ and $e_2 = \phi - \phi_c$ are error signals for each variable.

V. Simulation Study

A control law by feedback linearization technique has been applied to a coordinated-turn maneuver of aircraft. First bank angle control by an open-loop command and inversion control command are presented. In the model inversion control case, the sideslip angle was set to equal to zero during maneuver. Control gains are set to

$$v_1(t) = \ddot{V}_c + 5.4\dot{e}_1 + 10.1e_1 \\ v_2(t) = \ddot{\phi}_c + 3.1\dot{e}_2 + 8.2e_2$$

Simulation results are presented in Figs. 4 to 6 for bank angle, sideslip angle as well as yaw angle responses.
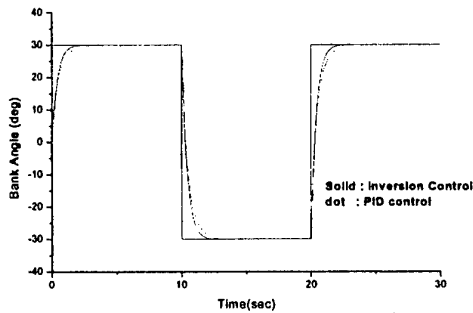
Fig. 4 Bank angle response by inversion control

As it can be shown from the simulation results, some sideslip component is induced during pure bank angle control. This is rather general phenomenon for general banked turn maneuvers. Model inversion controller is shown to be handling such unwanted sideslip angles within satisfactory accuracy.
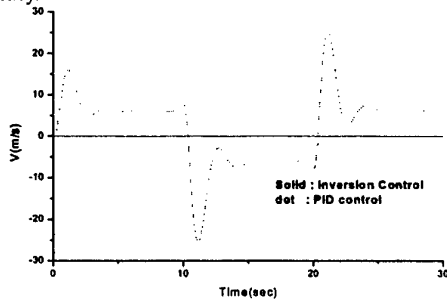
Fig. 5 Side velocity response
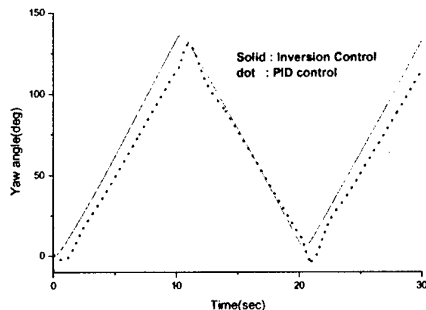
Fig. 6 Yaw angle responses

Next modeling errors are accounted by incorporating neural networks into the control loop. Simulation results are presented in Figs. 7,8 and 9.
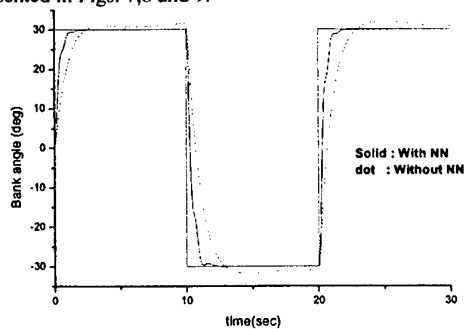
Fig. 7 Bank angle response by neural network control
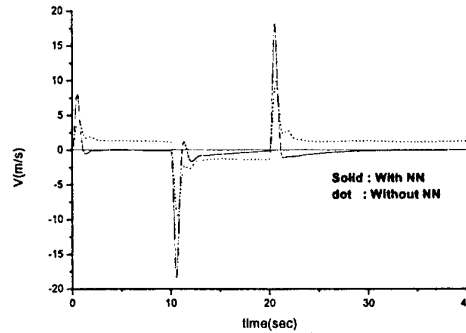
Fig. 8 Sideslip response by neural network control

From the simulation results, the inversion controller obviously is subject to performance degradation under modeling errors. Neural networks can partially overcome such modeling errors. Thus, Neural network-based controller may be applied to the case where modeling error exist to a significant extent.
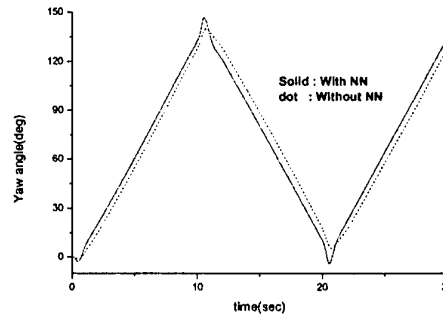
Fig. 9 Yaw response by neural network control

VI. Concluding Remarks

Feedback linearization controller is applied to the coordinated-turn maneuver of aircraft. The inherent roll/yaw coupling effect has been successfully handled with the proposed approach. The modeling errors existing in the original plant dynamics can be partially handled by neural networks which replace functions with uncertainties. The proposed approach may potentially applied to other nonlinear maneuvers of aircraft. Simulation results were used to verify the proposed control strategies.

References

[1] H.K. Khalil, "Adaptive Output Feedback Control for Nonlinear Systems Represented by Input-output Feedback", *IEEE Transactions on Automatic control*, Vol. 41 No. 2, pp.177-188,1996.

[2] Li W, Slotin J-J E, "Neural Network Control of Unknown Nonlinear Controller" *Proceedings of 1989 American Control Conference*, Pittsburgh, PA Vol. 2 pp. 1136-1141.4.

[3] F.L.Lewis, S. Jagannathan and A. Yesildirek " Neural Network Control of Robot Manipulators and Nonlinear Systems" *Taylor & Francis Inc.* 1999

[4] B.L Stevens and F.L Lewis "Aircraft Control and Simulation" *John Wiley & Sons Inc*

[5] F.C Chen and C.C Liu, "Adaptively Controlling Nonlinear Continuous Time Systems using Multi-layer Neural Networks" *IEEE Trans, on Automatic Control*, Vol..39, No.6 pp. 1306-1310 , 1994.

Development of a Medium Size 3-Axis Rate Table

Choonbae Park[*], Keeyoung Choi[†], Jongjin Kim[‡]

Department of Aerospace Engineering, Inha University, Inchon, 402-751, Korea

Key Words: Hardware in the Loop Simulation (HILS), Rate Table, UAV

Abstract

Flight dynamics and control laboratory at Inha University (FDCLI) is developing a 3-axis rate table of medium size and moderate price. FDCLI has developed a single axis rate table successfully, and is expanding the work to a 3-axis system. The maximum speed will be 2 rev/sec for roll axis and 1 rev/sec for yaw axis. The maximum angular accelerations will be 26 rad/sec^2 for roll axis and 4.5 rad/sec^2 for yaw axis. To achieve these dynamic performance specs, two DC motors of 0.25 N-m torque rating is used for the yaw axis and two motors of 0.017 N-m for the roll axis, all with proper gear reduction. The limits on the rotation angles are removed by using slip contact. The position accuracy is 30 arc minutes for the all three axis. The overall system is about 76 cm tall and 48 cm wide. This paper presents the detailed performance specifications of the rate table along with descriptions of the components.

1. Introduction

For the current commercial aircraft, avionic system shares about 1/3 of the total cost, about equally with the propulsion and structural systems. However, different from the other two systems which show steady and slow improvement, the avionic systems develop dramatically to meet the ever increasing demand. In these days improving the flying quality is most directly achieved through the usage of sophisticated control systems. Pilot workload is also reduced with improved pilot aiding systems such as well-organized glass cockpit and autopilot systems. These remarkable improvements are made possible with rapid developments in computer engineering and electronic components such as micro controllers and sensors. The prices of these parts are dropping rapidly while the functionalities are improving. Along with the rapid development of micro controllers and sensors, demands on the avionic systems are also increasing, and as a result, the avionic systems become more complex.

As the system becomes more complex, it is naturally more prone to malfunction due to component failure and design fault. Thus, to assure the reliability, it is crucial to test the avionic systems thoroughly before they are used. The simplest test of the avionic systems is to use simulations of software only, which can validate part of the logics and codes. As the functionality becomes more complex, checking all the logics in realistic situation using an off-line simulation is becoming tougher; using a pilot-in-the-loop-simulation (PILS) is a better choice, since the pilot can drive the simulation to realistic situationg and test all the implemented functionalities. To test the actual hardware system, the simulation is modified in such a way that the part of simulation program that simulates avionic equipments is replaced with actual hardware. In this way, the simulation software simulates aircraft dynamics only, and interfaces with the actual hardware. Combining this hardware-in-the-loop-simulation (HILS) with the PILS, the avionic system can be thoroughly checked from the early stage of development process. This should reduce the development cost significantly while shortening the development time.

One of the most basic usages of the HILS system is testing inertial sensors, especially gyroscopes. Inertial sensors such as rate gyroscopes are tested on top of rate tables which are driven to match the aircraft attitude as computed by the simulation program. For this kind of HILS test, the rate tables play the key role. Three-axis rate tables have complex mechanism, and making them to operate with high accuracy is a challenging problem. Due to this difficulty, high precision rate tables are usually expensive. And also, the three-axis rate tables are usually developed for full-scale aircraft or missile development, and thus are bulky. Because of the high price and bulky size, the availability of the rate tables has been limited to large research facilities or industries. On the other hand, compact and efficient inertial sensors such as MEMS accelerometers and vibrating gyros are newly developed with the aid of micro machining techniques. These components are mass-produced and the prices are significantly lower than those of conventional mechanical sensors. Even though the accuracies of these components still do not match with those of the more expensive high-end equipments, they are improving rapidly. Because of the low price and easy availability, their application fields are ever widening.

Low cost UAV can directly benefit from these equipments. Dependency on the airborne electronics of UAV is bigger than manned aircraft, in a sense. Because of low purchasing price and operation cost, UAV are considered to be an efficient system that can replace manned aircraft for certain missions, which is not necessary true. Due to the lack of the flexibility and adaptability of experienced human pilots, the mission profiles of UAV are significantly limited compared to manned aircraft. Since UAV should perform the missions autonomously, it should be more flexible and reliable than the manned aircraft. The flexibility can be partially acquired by using sophisticated software that utilizes many different types of sensors, and the reliability can be improved by using the concept of redundancy. With the availability of the efficient (in terms of size and cost) sensors, UAV avionics are rapidly developing. Testing these equipments needs different paradigm than the full-scale aircraft; rate tables of low cost, small size are the keys.

Flight dynamics and control laboratory at Inha University (FDCLI) is developing a medium size 3-axis rate table with the purpose of easy availability to university researchers with moderate budget. This paper describes the features and construction of rate table that Inha University is developing.

*Professor
† Assistant Professor
‡ Graduate Student

2. Single Axis Rate Table

As a pilot program, a single axis rate table is developed.[1] The final assembled system is shown in Figure 1. This section describes the components of this system in detail, since some parts and concepts are used in the three-axis system too.
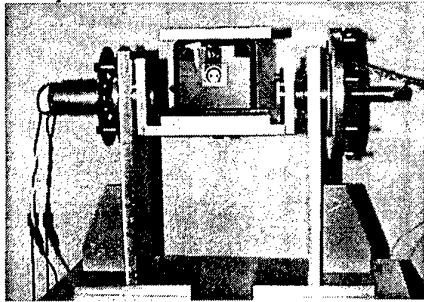

Fig. 1 Single Axis Rate Table

A. Performance Specification

The system is designed to operate with a payload of 3 kg. The maximum size of the payload is set to 100 x 50 x 50 mm^3. The clearance margins are set to 50 % in each direction. The maximum rate is set to 1 rev/sec, which is typical maximum rate for aircraft roll motion. As shown in the figure, the position can assume any value in the range of 360 degrees with the resolution of 1 degree without any mechanical limit.

B. Motor and Driving Mechanism

To produce the maximum torque required using small motors, multiple motors and gear reduction may be used. The number of motors and gear ratio must satisfy the following condition:

(Gear ratio) x (Number of motor) > (Max Torque Req.)   (1)

With the performance specs, the maximum torque required is computed as 0.7471 N-m. Considering the size of the overall system and the torque required, a DC motor of SM-3657 is selected. The rated torque of SM-3657 is 0.15 N-m. To achieve this requirement with margin, two SM-3657 motors and gear ratio of 7 is used.

The motors are driven with PWM signal. They should run in both directions. An H-bridge circuit that use 24V input is used for this purpose. PC817 components are used between IO board and motor circuit to electrically insulate them while supplying the necessary power.
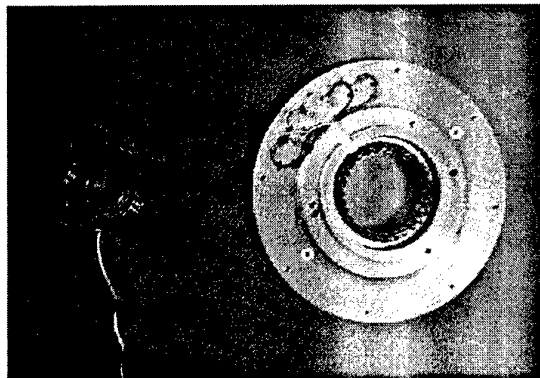
Fig. 2 Kearfott Two Piece Resolver (left: rotator, right: stator)

C. Sensor

The position is measured with a resolver. A resolver consists of a stator and a rotator which is fixed to the shaft. As the shaft rotates, the rotator rotates with respect to the stator, which induces current. By measuring this induced current, it is possible to measure the position of the shaft. Commercial chips are used to interpret the induced current, and compute the rotation angle. An AD2S90 resolver-to-digital-converter chip from Analog Devices is used here.[2]

D. Interface

Since the rotating part with payload rotates with respect to the fixed base without angular limit, wires cannot be used for data connection. A slip ring connection is used as the electrical connections between the rotating and the fixed parts. A slip ring of 30 is developed. (Fig. 3)
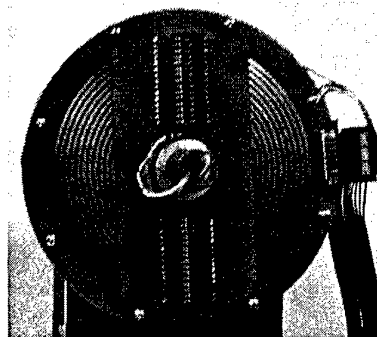
Fig. 3 Slip Ring
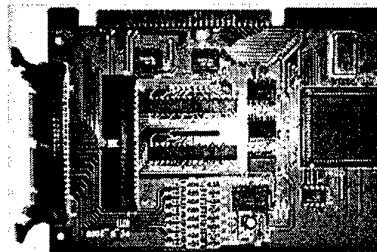
Fig. 4 IO Interface Board

For data traffic, a general purpose IO interface board is developed. (Fig. 4) The specifications of the interface IO board are as follows:
- Digital Input: 16 bit, decoupled by using photo coupler
- Digital Output:8 bit
- PWM Output: 4 channel, 8 bit
- Analog Input: 8 channels (12 bit AD conversion)
- Variable Frequency Pulse Output
- Memory: 1K bit flash ram(93c46)
- Serial Input: 3 channels

E. Control

The system is tested for position command. A proportional feedback controller is used as an initial test. For 30 and 50

degree step inputs, the system entered the 2% settling zone within 0.34 sec and 0.58 sec respectively. The same configuration is also tested for sinusoidal inputs. The slip ring followed the command input within the tolerance of 1 degree, but with non-uniform phase delay. Since this delay is inversely proportional to the amplitude, it is believed to be caused by the friction from slip ring.

3. Three-Axis Rate Table

With the successful completion of the single-axis system, a three-axis system is designed and being assembled. The overall design shape is shown in Fig. 5. As shown in the figure, the axes are arranged to rotate in accordance with the conventional Euler angle definition. Same as the single axis system, the gimbals can rotate in any direction without limits on the angular positions.
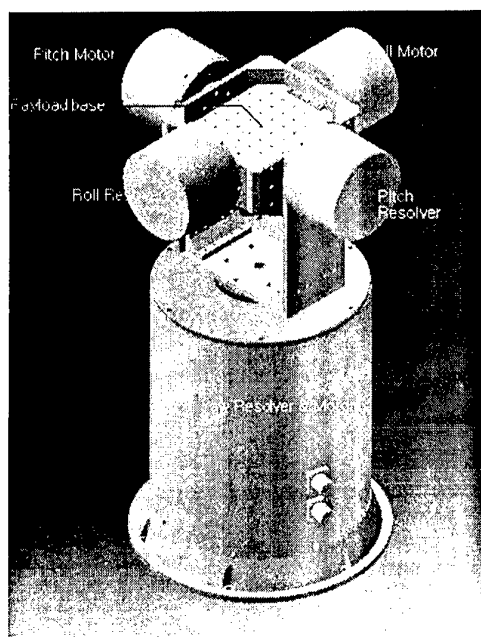
Fig. 5 Three Axis Rate Table

A. Performance Specification
Performance of one of the typical full-scale rate tables is listed as follows (Cargo Electronics S-470):
- Max. Roll Rate: 999 deg/sec
- Max Yaw Rate: 350 deg/sec
- Max. Roll Acceleration: 6.1 deg/sec^2
- Height: 1.4 m
- Weight: 2000 kg

As shown here, typical full-scale rate tables are oversized and overpowered for small UAV equipments. With the purpose of UAV equipment testing, the size is determined as shown in Table 1. Maximum speed is set to 2 rev/sec for the roll axis and 1 rev/sec for the yaw axis. The target accuracy is 0.1 degree. By comparing existing rate tables, maximum angular accelerations are set as shown in Table 2. These specs are used to compute the maximum torque required.

Table 1 Physical Configurations

Materials	Duralumin/Steel
Payload Capacity	5 kg
Payload Base Dimension	210mm(W)x170mm(D)x10mm(H)
Overall System Dimension	480mm(W)x472mm(D)x761mm(H)
Weight	120 kg
Controller Type	PID controller
Power Requirements	220 V AC

B. Motor and Driving Mechanism
Since all three gimbals move independently, the moments of inertial of the outer two axes vary continuously. To find the proper motor size, the moments of inertia are computed for various configurations. Among the various configuration data, the maximum numbers are shown in Table 2.

Table 2 Axes Properties (Moment of inertia and Target Performance)

Axis	Moment of inertia	Angular rate	Angular acceleration	Torque
Roll	0.0036	12.25 rad/s	26 rad/s^ 2	0.0936
Pitch	0.1386	7.9 rad/s	6 rad/s^ 2	0.8316
Yaw	0.2994	6.28 rad/s	4.5 rad/s^ 2	1.3473

With this data, motors and gear reduction ratio are determined. As explained for the single axis system, these two parameters along with the rated torque of the motor determine the maximum torque level. Table 3 shows the designed gear ratio, motor type, and number of motors.

Table 3 Driving Motors

Axis	Motor Model No.	Motor Torque (Nm)	Motor number	Gear ratio
Roll	SM-3657	0.0167	2	10
Pitch	SM-3657	0.0167	5	10
Yaw	9ISO-24AA	0.2543	2	6

C. Sensor
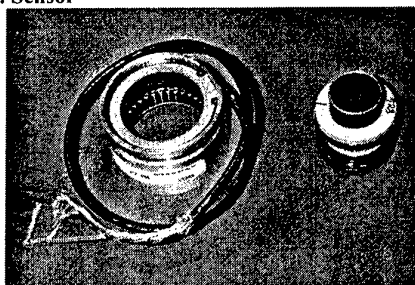
Fig. 6 Brushless Resolver (Harowe 21BRCX-610)

Same as the single axis system, a resolver is used to measure the angular position of the shaft. For better resolution and cleaner configuration, a frameless brushless system, shown in Fig. 6, is used. Compared with the one used for the single

axis system (Fig. 2), there is no lead wire attached to the rotator, which makes the system configuration simpler. The standard accuracy is 7 arc minutes.

D. Interface

The same type of interface boards as the one used for the single axis system are used.

E. Control
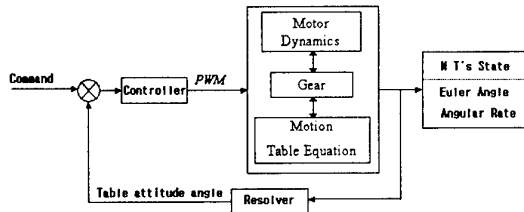
Fig. 7 Control Schematics

To test the control system, a nonlinear motion simulation is set up.[3]   This simulation features fully couple 3-axis nonlinear equations of motion of the gimbals and gears, and motor dynamics. Fig. 7 shows the control and simulation schematics.   A PD controller is tested with the simulation program to test the feasibility of position control.   For step command, the PD controller satisfied prescribed accuracy requirement.   However, as the command motion becomes more complicated, the system performance degraded.   It is concluded that rate feedback is necessary.   As the configuration changes, the system characteristics change.   Due to this fact, the performance of the control system should be evaluated for the off-nominal conditions.   Eventually, controller should be design with the concepts of robust stability and robust performance in mind.

Conclusions

Inha University developed a single axis rate table successfully, and is expanding the work to a three-axis system. The system is designed to be used effectively for small and moderate size equipments such as UAV systems.   According to the design data, this system will provide great usability for the development process of low cost equipments, with the low system price and comparable dynamic range and accuracy.

Acknowledgement

References

1. Kim, R., *Design Study on a Single DOF Gimbal Table for HILS*, Master Thesis, Inha University, Korea, Feb. 2001, (in Korean)
2. http://www.analogdevices.com
3. Song, S., *A Development of Simulation Tool for a design of Three Axis Motion table*, Master Thesis, Inha University, Korea, Feb. 2001, (in Korean)

3F3   Quantitative Models on Corrosion Fatigue Crack Growth Rates in Metals

Sangshik KIM*, Youngik SEO** and Sugeun LIM***

Gyeongsang National University, ReCAPT, 900 Gazwa-dong, Chinju Gyeongnam, 660-701, Korea.

Key Words : corrosion fatigue crack growth, environmental effect.

Abstract

Approaches to predict da/dN- Δ K for environmental situations; including empirical interpolative equations, linear superposition of mechanical fatigue and time-based environmental cracking, and mechanism-based models; are presented. For several material-environment systems, these models were incorporated in fracture mechanics life prediction methods, and successes have been reported in evaluating the corrosion fatigue contribution. Considerable uncertainties are, however, associated with these models. The linear superposition analysis is emphasized; material-environment systems that are severely environment-sensitive should be adequately described by this method. Direct and indirect methods exist to define time-based crack growth rates for use in linear superposition predictions of da/dN.

The linear superposition approach is effective, but only for those cases where K_{ISCC} is high relative to typical flawed component stress intensity levels. Empirical curve-fit models require an extensive environmental crack growth rate data base, which are costly to develop, and are effective for interpolations but not predictions of fatigue crack growth data. Mechanism-based models for broad predictions of cycle-time dependent da/dN versus Δ K, and other variables such as frequency or hold time, are in an infant state.

1. Introduction

Traditional fatigue life prediction methodologies are typically based on smooth specimen yielding and fatigue data in moist air environment where the time-dependent chemical action of aggressive environments has been often ignored [1-3]. To implement the corrosion fatigue contribution into the existing damage tolerant life prediction is an immense challenge due to the extreme complexities associated with environment-affected fatigue behavior [4-7].

First challenge is invoked from the fact that environmental damage generally increases with prolonged exposure time; that is, da/dN increases with decreasing loading frequency at fixed Δ K. The long term corrosion fatigue behavior of alloys in components is, therefore, difficult to predict based on short term laboratory data. For example, it is important to predict the 40 year life of marine structures. With the loading frequency of interest, 0.2 Hz, 300 days of loading are required to characterize the endurance limit at 5×10^6 cycles for smooth specimens. While Paris regime crack growth rates are easily measured for loading frequencies as low as 10^{-4} Hz, a fracture mechanics characterization of near threshold response requires extremely long time for loading frequencies on the order of 1 Hz [8]. Total fatigue life is often dominated by low growth rate crack propagation.

---

*, *** : Associate Professor, Div. of Materials Science and Eng. ReCAPT

**   : Div. of Materials Science and Eng. ReCAPT

Since fracture mechanics methods characterize the kinetics of fatigue crack propagation, models can in principle be developed to predict the effect of frequency, thus providing a means of relating short term laboratory data to long term component performance for a variety of pre-existing defects.

As a second challenge, a wide range of variables can affect environmental fatigue crack propagation for metallic materials [4,5,7,9,10]. Interactions of these variables are widespread. Generally a given material will be sensitive to corrosion fatigue crack propagation for specific conditions of alloy composition, microstructure and chemical environment. Compared to moist air, identification of the pertinent environmental fatigue crack growth rate law for use in life prediction is greatly complicated. The need in this regard is to develop predictive models based on the fundamental embrittling mechanism, which is hydrogen embrittlement for many structural alloys in gases and electrolytes.

There are several approaches to incorporate the environmental effects into fatigue life prediction [11-16]. The simplest approach for life prediction is to measure the crack growth rate for those materials, environment, loading and frequency conditions which are exactly selected to reproduce a specific application. The work of Vosikovsky and Cooke provides an example of this approach for environmental fatigue crack propagation in a welded carbon steel pipeline carrying H_2S contaminated oil [17].

A second approach involves a detailed literature search to define the upper bound on environment sensitive crack propagation behavior for a specific material/environment system from a broad data base and for those chemical, frequency and material conditions which represent a worst case scenario. Hudak, Burnside and Chan employed this approach for welded carbon steel tubular components of oil and gas production platforms which operate in aggressive marine environments [15].

Ford, Wei, Nicholas and coworkers advocate the development of crack growth models which enable prediction of the effects of important variables, particularly ΔK, environment chemistry and frequency [5,12,18-22]. These models are based on: (1) empirical curve fitting, (2) linear superposition of mechanical fatigue and monotonic load environmental cracking data, or (3) mechanistic models of the plastic deformation-chemical reaction production of damage at the crack tip. Andresen et al. describe the application of this approach, particularly employing mechanism-based models, to monotonic load and fatigue crack propagation in ferritic and austenitic steels exposed to pure water environments at elevated temperatures, typical of commercial nuclear reactor systems [14,21]. Van Stone et al. applied this approach, specifically employing linear superposition, to elevated temperature crack growth in nickel based superalloy for jet engine turbine disks [22].

The state of the art in corrosion fatigue crack growth rate models is summarized and assessed in this paper. Here, three types of model are considered: (1) linear superposition model for time-dependent fatigue crack growth, (2) empirical curve fitting, and (3) mechanism based model of cycle-time-dependent crack growth. Factors complicating corrosion fatigue life prediction are also discussed.

2. Linear superposition

An early approach to predict corrosion fatigue crack growth rate versus stress intensity range relationships involving a linear superposition concept was first proposed by Wei, Landes, Gallagher and Bucci [12,13,23]. Linear superposition predicts environment enhanced crack growth rate, da/dN_e by combining inert environment fatigue crack growth rate, da/dN_m, with time-dependent, monotonic load environmental crack growth rate, da/dN_{SCC}:

$$da/dN_e = da/dN_m + da/dN_{scc} \qquad (1)$$

Da/dN_{SCC} is computed by integrating the sustained-load crack

growth data and the applied time-dependent stress intensity factor in a single fatigue load cycle K(t). Mathematically, da/dN_{SCC} is given by:

$$da/dN_{scc} = \int_0^{\frac{1}{f}} [da/dt(K)][K(t)]dt \qquad (2)$$

Fig. 1 schematically illustrates the concepts involved in the linear superposition approach, and the elements of Equation 1 [12].
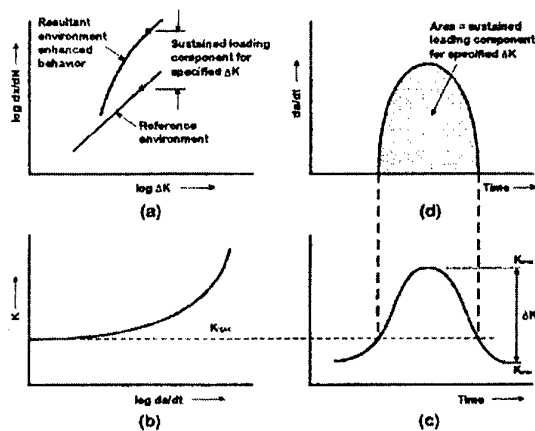
Fig. 1. Schematic diagram illustrating a linear superposition hypothesis; (a) integrated effects on environment and ΔK on fatigue crack growth rate, (b) rate of crack growth under sustained load in an aggressive environment, (c) environmental contribution to crack growth in fatigue, and (d) stress intensity spectrum in fatigue [12].

K(t) for the fatigue cycle is stated as a function of time, employing the loading parameters ΔK and R (or K_{min} and K_{max}). An example of a sinusoidal load cycle, with frequency f, is:

$$K(t) = K_{min} + \frac{\Delta K}{2 - \cos(2\pi f t)} \qquad (3)$$

The linear superposition model reasonably predicts environmental FCP rates as a function of ΔK, R, f and waveform; if two conditions are met. K_{max} during the fatigue cycle must be above K_{ISCC} and the increment of crack advance for a single load cycle and from da/dt must be substantial compared to that from purely mechanical fatigue. da/dN_m.

Wei, Landes and Gallagher demonstrated the accuracy of linear superposition by predicting the frequency and stress ratio dependencies of corrosion fatigue crack growth in several high strength steels exposed to water vapor, H_2 and NaCl [12,13]. A specific example is given in Fig. 2 for AISI 4340 steel fatigued in distilled water [23].
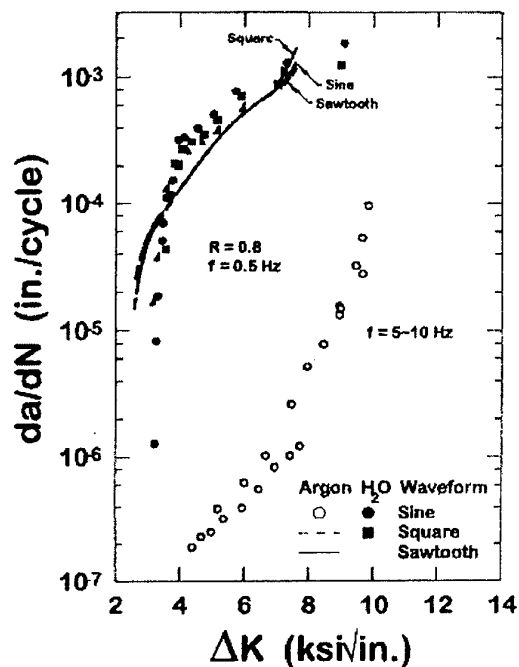
Fig. 2. Time-dependent corrosion fatigue above K_{ISCC} for high-strength type 4340 (UNS G43400) steel in water vapor, modeled by linear superposition; after Wei, et al. [12].

Apparently, this early superposition model ignores the cycle-time-dependent environmental contribution below K_{ISCC}. This cyclic dependent term, da/dN_c, was later

introduced into the original formula by [24,25]:

$$da/dN_e = da/dN_m + da/dN_c + da/dN_{scc} \quad (4)$$

As being recognized that plasticity-driven pure mechanical fatigue and corrosion fatigue can proceed by different micromechanisms and occur concurrently or in parallel, the superposition model was further modified by the following [26],

$$da/dN_c = da/dN_m(\theta) + da/dN_c(\Phi) \quad (5)$$

where θ is the fraction of the crack surface formed by mechanical fatigue, and Φ is the fraction formed by "pure" corrosion fatigue. The stress corrosion cracking term which is considered as a sequential contribution is not included in this equation for simplicity. θ and Φ are measured by fractographic analysis. For two parallel processes when $\theta = (1 - \Phi)$, the equation may be rewritten into the following form:

$$da/dN_e - da/dN_m = (da/dN_c - da/dN_m)(\Phi)$$
$$= da/dN_{cf} \quad (6)$$

This equation indicates that the phenomenological difference between inert and aggressive environment fatigue rates from the da/dN- ΔK relationship (da/dN$_{cf}$) is equivalent to the difference between the rates of chemical-mechanical (da/dN$_c$) and mechanical (da/dN$_m$) fatigue times the fractional occurrence of the former. The rigorous derivation of da/dN$_c$ is discussed in the ensuing section.

Several specific cases of Eq. 2 are important. Materials that are sensitive to SCC (e. g., high strength steels or nickel based superalloys in H_2, water vapor or electrolytes) are likely to exhibit crack growth above a sharply defined K_{ISCC} and at a constant or plateau velocity, da/dt$_p$ [27]. Eq. 2 is then reduced to:

$$da/dN_{scc} = (da/dt_p)\Delta t \quad (7)$$

where Δt is the time during fatigue loading where stress intensities are above K_{ISCC}. If K_{ISCC} is small compared to K_{max}, or if the load cycle is a square wave, then Δt is approximately by (1/f) and:

$$(da/dN_e - da/dN_m) = (da/dt_p)(1/f) \quad (8)$$

Eq. 8 describes purely time-dependent behavior; the logarithm of da/dN$_c$ linearly depends on the logarithm of f, with a slope of -1, as demonstrated by the data contained in Fig. 3.
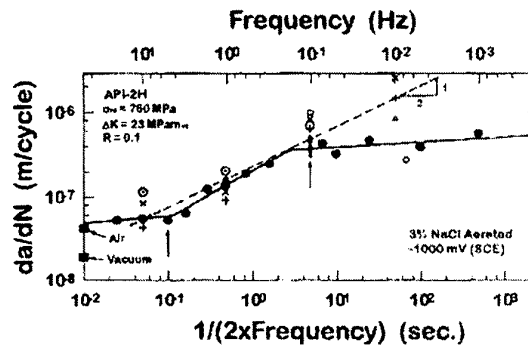
Fig. 3. Effect of frequency on corrosion fatigue crackpropagation in the plateau regime on ΔK for API-2H steel in 3% NaCl with cathodic polarization; after Gangloff [74].

Eq. 8 indicates that, by measuring both da/dN$_m$ (frequency independent) and da/dN$_c$ as a function of frequency at one or more constant ΔK levels, da/dt$_p$ can be calculated for the corresponding K_{max} level(s). The resulting da/dt$_p$ can be employed with Eqs. 7 and 8 to predict da/dN$_c$ for a wider range of frequency, hold time, stress ratio and load waveform conditions.For nickel-based superalloys in moist air at elevated temperatures, time-dependent crack growth rate depends on applied K according to:

$$da/dt = CK^n \qquad (9)$$

where C and n are material constants. This equation can then be combined with Eq. 2 to yield:

$$da/dN_c = da/dN_m + C(\Delta K)^n_{t\,eff} \qquad (10)$$

where t_{eff} equals 1/f for a square wave hold-time cycle and can be expressed as:

$$t_{eff} = \{(1-R)^{n+1}/(n+1)\}(1/f) \qquad (11)$$

for a symmetric and linearly increasing/decreasing stress intensity versus time cycle.

Data indicate that monotonic load environmental cracking may only contribute to da/dN$_c$ during the loading portion of the fatigue cycle, introducing the term (1/2f) in Eqs. 10 and 11 [28,29]. (1/2f is only strictly applicable for a symmetric load cycle.)

Eqs. 10 and 11 were employed to predict time dependent crack growth in high-strength nickel-based superalloys at elevated temperature, as illustrated in Fig. 4 [30,31].
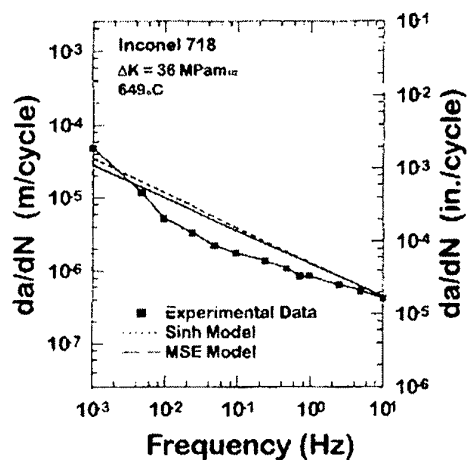
Fig. 4. Effect of loading frequency on fatigue crack propagation

in IN718 exposed to moist air at elevated temperature and constant ΔK; after Nicholas, et al. [30].

Nicholas and coworkers demonstrated that this approach is reasonably successful in predicting sustained-load crack growth for Inconel 718 at 649°C at low stress ratios [30,31]. At high stress ratios and high frequencies, however, the linear superposition model was proven to have a limited predictive capability.

Austen and Walker argued that corrosion and mechanical fatigue processes are competitive, rather than superposable [32]. They assume that environmental fatigue crack growth rates are controlled by the dominant of two processes, be it mechanical fatigue or cycle-time-dependent corrosion fatigue, and can be expressed as:

$$da/dN_e = C(\Delta K + d\Delta K)^n \qquad (12)$$

where dΔK is an adjustable parameter representative of the corrosion fatigue contribution, and C and n are materials constants that bear same significance as in Paris law description of FCP. This competition model is a spacial case of Eq. 6, in that Φ = 1 and da/dN$_m$ << da/dN$_c$. This model is weak when environmental crack growth involves a significant amount of mechanical fatigue at relatively high rates. Studies indicate that this model overestimates environmental crack growth rates at K levels below K_{ISCC} for high-strength aluminum alloys in electrolytes and for steel in gaseous hydrogen.

Linear superposition is an effective approach for predicting the kinetics of environmental FCP, but only for those material-environment systems where the sustained load crack growth kinetics make substantial contribution to da/dN$_c$. Additionally, da/dt must be known as a function of applied stress intensity. Apart from high strength steels in hydrogen producing environments and nickel-based superalloys in

elevated temperature moist air, such data are neither commonly available nor easily determined. For many materials, K_{ISCC} is high relative to typical flawed component stress intensity levels and environmental FCP is substantial below K_{ISCC}. For these cases, more sophisticated models must be developed to predict da/dN_c as a function of ΔK and the other pertinent variables.

3. Summary

The fatigue crack growth in corrosive environments are largely governed by the delicate, synergistic interaction of the plethora of variables, including stress ratio, frequency, environmental activity, loading waveform, yield strength and microstructure. The quantitative corrosion fatigue model must be able to predict the effects of these variables. In this paper, several quantitative models developed for evaluating corrosion fatigue contribution based on linear superposition, empirical curve fitting, and chemical damage mechanism-based through similitude concept have been reviewed. While there have been some successes reported for each model in specific alloy-environment systems, comprehensive corrosion fatigue crack growth models are lacking. The ability of fracture mechanics-based life prediction is more complicated by the presence of crack closure and small crack mechanics. The corrosion fatigue models need to compromise such extrinsic mechanistic factors.

4. References

1. *Methods and Models for Predicting Fatigue Crack Growth Under Random Loading, ASTM STP 748*, J.B. Chang and C.M. Hudson, eds., ASTM, Philadelphia, PA (1981).
2. *NASCRAC-NASA Crack Analysis Code User's Manual*, Failure Analysis Associates, Inc., Palo Alto, CA (1989).
3. *Mechanics and Physics of Crack Growth: Application to Life Prediction*, R.B. Thompson, R.O. Ritchie, J.B. bassani and R.H. Jones, eds., Elsevier, London (1988).
4. R.P. Gangloff, R.S. Piascik, D.L. Dicus and J.C. Newman, "Fatigue Crack Propagation in Aerospace Aluminum Alloys", *Journal of Aircraft* (1992).
5. R.P. Wei and R.P. Gangloff, in *Fracture Mechanics: Perspectives and Directions, ASTM STP 1020*, R.P. Wei and R.P. Gangloff, eds., ASTM, Philadelphia, PA, pp. 233-264 (1989).
6. *Environment Induced Cracking of Metals*, R.P. Gangloff and M.B. Ives, eds., NACE, Houston, TX (1990).
7. *Corrosion Fatigue Technology, ASTM STP 642*, H.L. Craig, Jr., T.W. Crooker and D.W. Hoeppner, eds., ASTM, Philadelphia, PA (1978).
8. D. Taylor, *Fatigue Thresholds*, EMAS, Warley, U.K., (1981).
9. *Corrosion Fatigue: Mechanics, Metallurgy, Electrochemistry and Engineering, ASTM STP 801*, T.W. Crooker and B.N. Leis, eds., ASTM, Philadelphia, PA (1984).
10. *Fatigue: Environment and Temperature Effects*, J.J. Burke and V. Weiss, eds., U.S. Army Materials Technology Laboratory, Watertown, MA (1984).
11. *Proceedings, Conference on the Influence of Environment on Fatigue*, Inst. Mech. Engr., London (1978).
12. R.P. Wei and J.D. Landes, in *Matls. Res. Stds.*, Vol. 9, pp. 25-28 (1969).
13. R.J. Bucci, *PhD Dissertation*, Lehigh University, Bethlehem, PA (1970).
14. P.L. Andresen, R.P. Gangloff, L.F. Coffin and F.P. Ford, in *Fatigue 87*, R.O. Ritchie and E.A. Starke, Jr., eds., EMAS, West Midlands, England, pp. 1723-1751 (1987).
15. S.J. Hudak, O.H. Burnside and K.S. Chan, in *J. Energy Resources Tech., ASME Trans.*, Vol. 107., pp. 212-219 (1985).
16. P.M. Scott, T.W. Thorpe and D.R.V. Silvester, in *Corrosion Science*, Vol. 23, pp. 559-575 (1983).
17. O. Vosikovsky and R.J. Cooke, in *Int. J. Pres. Ves. & Piping*, Vol. 6, pp. 113-129 (1978).
18. R.P. Gangloff and D.J. Duquette, in *Chemistry and Physics*

of Fracture, R.M. Latanision and R.H. Jones, eds., Martinus Nijhoff Publishers BV, Netherlands, PP. 612-645 (1987).

19. P.L. Andresen and F.P. Ford, in *Matls. Sci. Engr.*, Vol. A103, pp. 167-184 (1988).

20. R.P. Wei, in *Fatigue 87*, R.O. Ritchie and E.A. Starke, Jr., eds., EMAS, West Midlands, UK, pp. 1541-1560 (1987).

21. F.P. Ford, D.F. Taylor, P.L. Andresen and R.G. Ballinger, "Environmentally Controlled Cracking of Stainless and Low-Alloy Steels in Light Water Reactor Environments", *EPRI Report* No. NP-5064M, EPRI, Palo Alto, CA (1987).

22. R.H. Van Stone, in *Matls. Sci. and Engr.*, Vol. A103, pp. 49-61 (1988).

23. J.P. Gallagher and R.P. Wei, in *Corrosion Fatigue, Chemistry, Mechanics and Microstructure*, O. Devereux, A.J. McEvily and R.W. Staehle, eds., NACE, Houston, TX, pp. 409-423 (1972).

24. R.P. Wei, in *Fatigue Mechanisms*, ASTM STP 675, J.T. Fong, ed., ASTM, Philadelphia, PA, pp. 816-840 (1979).

25. T.W. Weir, G.W. Simmons, R.G. Hart and R.P. Wei, in *Scripta Metall.*, Vol. 14, pp. 357-364 (1980).

26. R.P. Wei and M. Gao, in *Scripta Met.*, Vol. 17, pp. 959-962 (1983).

27. R.P. Gangloff, in *Corrosion Prevention and Control*, Proc. Sagamore Army Materials Research Conference, Vol. 33, M. Levy and S. Isserow, eds., U.S. Army Materials Technology Laboratory, Watertown, MA, pp. 64-111 (1987).

28. M.O. Spiedel, in *Stress Corrosion Cracking and Hydrogen Embrittlement of Iron Based Alloys*, J. Hochmann, J. Slater, R.D. McCright and R.W. Staehle, eds., NACE, Houston, TX, pp. 1071-1094 (1977).

29. M.O. Speidel, in *High Temperature Materials in Gas Turbines*, P.R. Sahm and M.O. Speidel, eds., Elsevier, Amsterdam, Netherlands, pp. 207-251 (1974).

30. T. Nicholas, T. Weerasooriya and N.E. Ashbaugh, in *Fracture Mechanics, ASTM STP 905*, J.H. Underwood, et al., eds., ASTM, Philadelphia, PA, pp. 167-180 (1986).

31. T. Nicholas, T. Weerasooriya, in *Fracture Mechanics, ASTM STP 905*, J.H. Underwood, et al., eds., ASTM, Philadelphia, PA, pp. 155-168 (1986).

32. I.M. Austin and E.F. Walker, in *Proc. Intl. Conf. Influence of Environment on Fatigue*, I. Mech. Engr., London, UK, pp. 1-16 (1977).

DEVELOPMENT OF HEAT TREATMENT TECHNIQUES FOR DEFORMATION CONTROL OF LANDING GEARS

Sung-Ki LYU*, Tae-Hyeon NAM** and Su-Gun LIM***

Gyeongsang National. University, ReCAPT , 900 Gazwa-dong, Jinju Gyeongnam, 660-701, KOREA.

ABSTRACT

This study deals with the characteristic of refrigerant for heat-treatment deformation control of SM45C steel. The control of heat-treatment deformation must need the progress of production parts for a landing gear. Most of the deformation is occurred on inconsistent cooling. The inconsistent cooling is occurred by a property of quenching refrigeration. When a heated metal is deposited in the refrigeration, the cooling speed is so slow in early period of cooling because of occurring a steam-curtain. After more cooling, the steam-curtain is destroyed. In this progress, the cooling speed is very fast.

The object of this study is to control the deformation of heat-treatment for landing gear by improving the conditions of quenching. The cooling curves and cooling rates of water, oil and polymer solution are obtained and illustrated. From the characteristics of the quenching refrigerant, the effects of heat-treatments on thermal deformation and fatigue strength are also investigated.

1. INTRODUCTION

The landing gear for the aircraft is a highly valued product as well as one of the most important mechanical parts. Most crucial in the manufacture of landing gears are heat-treatment and surface treatment processes. Lisic[1] devised an apparatus that can systematically assess quenching solution, and Beck[2] drew the cooling curves of silver and steel test piece in order to examine cooling capacities of various hardening oils. Ueyma[3] & Kim[4] elucidated heat deformation based finite element method, but they failed in identifying the causes of deformation by heat-treatment.

Presently, deformation due to heat-treatment accounts for faulty mechanical parts. In this regards, intensive studies should be made to suggest better ways of controlling heat deformation in mechanical part manufacturing industries.

Aircraft landing gears are largely made of 4240 steel and 300M steel[5,6]. These are among the representative high tension steels, which gain high strength through the formation of martensite and tempering. Thus oil quenching is usually applied to the steel with far higher hardening capacity due to the addition of alloy elements. In the case of large parts such as aircraft landing gears, however, heat-treatment deformation tends to occur owing to their large sizes and inconsistent cooling. Because mechanical correction of heat-treatment deformation is not allowed in the manufacture of landing gears, the occurrence of heat deformation at the last process of heat-treatment process means faulty and useless products. Therefore exact control of heat-treatment deformation is indispensable in the manufacture of landing gears.

Most of the heat deformation is attributed to inconsistent cooling of the mechanical parts. While some cases of inconsistent cooling may be due to the shapes of the parts, a more fundamental factor should be found in the characteristics of quenching cooling solution. At the early cooling stage, heated metals, which are drowned in quenching solution, cool down very slowly due to the steam-curtain formed on the surface. At later cooling stages, the steam-curtain is destroyed and cooling rate increases greatly as the metals are cooled down by evaporation heat of the cooling material. When water and oil are used together as a cooling solution the destruction of steam-curtain occurs locally, which results in inconsistent cooling rate and subsequent deformation. Therefore, in order to control heat-treatment deformation due to inconsistent cooling, it is essential to employ a cooling solution that can ensure uniform destruction of steam-curtain on the whole surfaces of the mechanical parts. Drowning the parts in polymer solution may be recommended as an alternative to make possible the uniform destruction of steam-curtain on the whole surfaces, thereby effectively controlling heat-treatment deformation due to inconsistent cooling.

2. MANUFACTURE PRIOR TO THE EXPERIMENT

2.1 Specifications of Experimental test pieces

This study employed SM45C as experimental test pieces whose chemical composition is presented in Table 1. For the convenience of the experiment, standard test pieces(No.10) were manufactured, because the complicated shape of the landing gear makes it cumbersome for the experiment. The shape of the standard test pieces is shown in Fig. 1.

Table 1 Chemical composition of SM45C

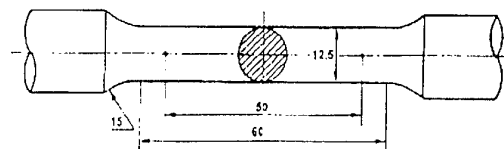| SM45S	C	Si	Mn	P	S	Ni	Cr	Cu
Range	0.42 ~ 0.48	0.15 ~ 0.35	0.60 ~ 0.90	≤ 0.03	≤ 0.035	≤ 0.25	≤ 0.25	≤ 0.20
Measured	0.44	0.28	0.73	0.026	0.019	0.12	0.20	0.16

Fig. 1 Shape of standard test piece

2.2 Processing Procedures and Heat-treatment Techniques for the test Pieces

A SM45C cylinder (18 mm in diameter) was cut down into small pieces, and a center hole was made on each piece to process it into a test piece on a programmed CNC lathe. Cylindrical grinder to obtain zero circularity and straightness grounded each test piece.

PAG (polyalkylene glycols) was adopted as the cooling solution for the experiment, while employing water and oil as a comparative cooling solution. Quenchotest(manufactured IVF) was used to measure cooling rate; the diagram of cooling rate measurement apparatus is presented in Fig. 2. The principle of measuring cooling rate on this apparatus is that when the probe is quenched in the bath after being heated to 845°C in the furnace, a thermocouple in the probe detects temperature and sends the signal to recorder, which transmit the data to a computer connected to it.

To measure variations in cooling rates of the cooling solution, fixed agitation speed of 2.36 m/s was applied to the polymer solution while varying concentration to 15% and 20% and temperature to 20°C, 40°C, and 60°C. Since water has no variations in concentration, fixed agitation speed was 2.36 m/s employed to water, with temperature varied to 20°C, 40°C, and 60°C. In the case of oil, temperature was varied to 20°C, 40°C, 60°C and 80°C.

The optimal heat-treatment conditions obtained in the above experiment was adopted in heat treating the SM45C steel test pieces in order to heat deformation in each test piece; after the heat-treatment, the test pieces were fastened and evolved on the cylindrical grinder to measure their circularity with a dial indicator, and the table of the grinder was conveyed to measure straightness.

The heat-treatment process is presented in Fig. 3. The test pieces underwent one hour of austenizing, then quenching, and one hour of tempering treatment in 425°C. All the heating treatment procedures were carried out under ambient Argon gas to prevent oxidation.
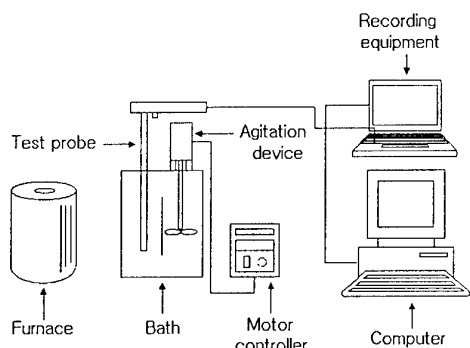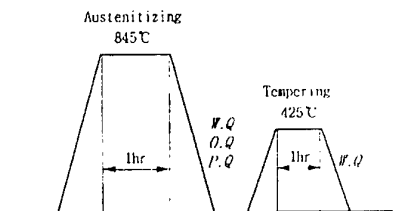

Fig. 2 Apparatus for measuring cooling rate

Fig. 3 Schematic diagrams of heat-treatment

2.3 Characteristics of the Cooling materials
2.3.1 Water

Fig. 4(a) and (b) present temperature-time cooling curve and differential cooling rate curve, obtained when the Ni base super alloy heated to 845°C was quenched in the cooling solution fixed at 2.36 m/s. Almost no steam-curtain was observed when the cooling solution was at 20°C, but with the temperature increasing from 40°C to 60°C, the steam-curtain increased.
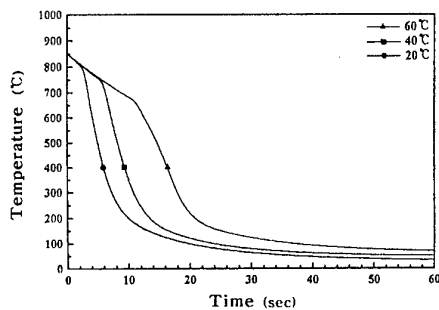
2.3.2 Polymer Solution

Generally speaking, two major factors having the greatest effect on the heat-treatment deformation in manufacturing materials are temperature and concentration. The temperature of the polymer solution was varied to observe temperature effect.

Fig. 5(a) and (b) show the temperature-time cooling curve and cooling rate curve respectively. Temperature increase from 20°C to 40°C showed a slight increase in steam coating stage, but significantly greater increase was observed at 60°C. It may be because heating polymer solution over 60°C may lead to its separation from water, resulting in lowered cooling capacity. Thus this study set the optimal temperature of the cooling materials as 20°C. The temperature of the cooling solution was fixed at 20°C and the concentration was varied so as to investigate its effect on cooling rate, which is shown in Fig. 6(a) and (b). Also included in the Figures were the curves obtained when water was selected as cooling solution.

As shown in Fig. 6(a), steam-curtain stage showed significantly great increase when the concentration of polymer solution was at 20%. Fig. 6(b) indicates that at the concentration of 15% maximum cooling rate was greater than at 20% but lower than when water was used. Cooling rate was found to be lowered at 400°C, around the temperature at which Martensite transformation of steel materials starts to occur. In order to maximize hardening effect and to minimize heat-treatment deformation, steam-curtain stage should be shortened and cooling solution with slower cooling rate at air stage should be selected.

In this regard, this study decided on 15%, 20°C polymer solution as the optimal concentration.

(a) Temperature-time cooling curve
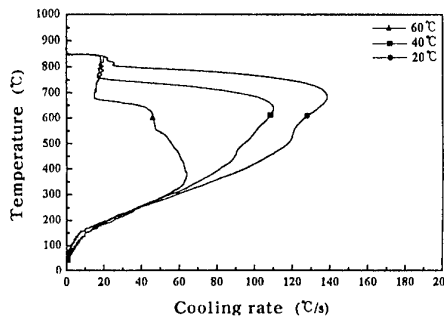
(b) Differential cooling rate curve

Fig. 5 The quenching characteristics of polymer solution (Concentration = 15%)

(a) Temperature-time cooling curve
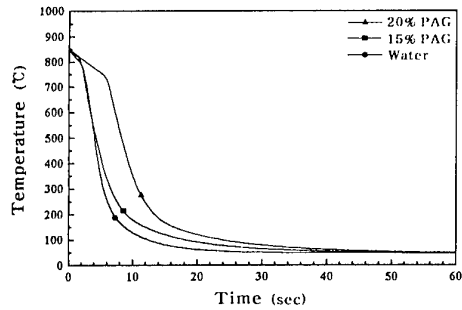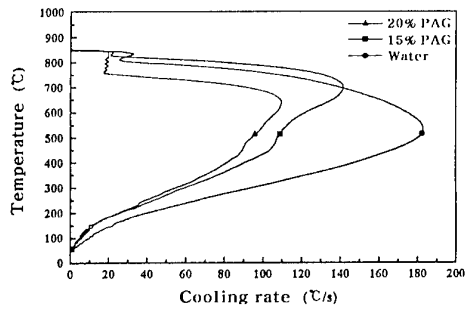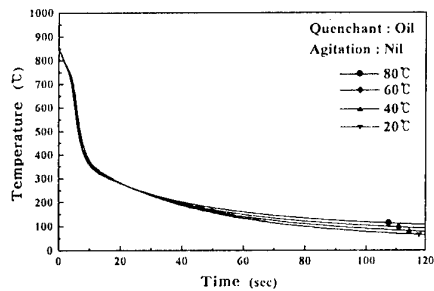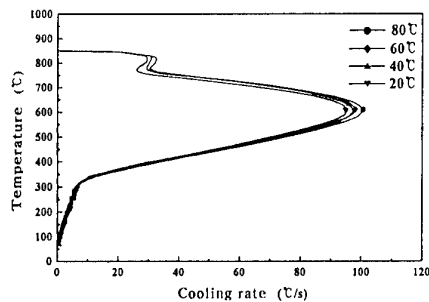

(b) Differential cooling rate curve

Fig. 6 The quenching characteristics of polymer solution
(Temp. = 20°C)

(a) Temperature-time cooling curve

(b) Differential cooling rate curve

Fig. 7 The quenching characteristic of oil

2.3.3 Oil

Fig. 7(a) shows measurements of temperature changes in heat-treatment oil with time. The figure indicates that at the initial stage, oil showed similar cooling characteristics at all the temperatures, but 80°C oil led to a slightly better cooling performance.

This may be because at this temperature the oil has better fluidity at temperatures higher than normal temperature and thus tends to enhance cooling rate. In particular, 80°C oil cools down more slowly than other cooling solution at temperatures less than 300°C. Fig. 7(b) suggests that 80°C oil may be the optimal condition because at this temperature oil shows the highest cooling rate.

It was found that water showed the highest cooling rate, while that of oil was the lowest. Water and polymer solution cooling rates were the highest at 680°C and 590°C respectively. Polymer solution eliminated steam-curtain all at once and thus could remove the steam-curtain occurring in water-cooling, and it also took less time in reaching the maximum cooling rate than water cooling.
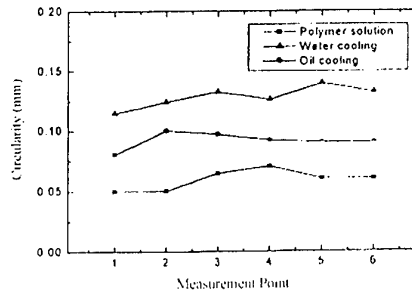
Fig. 8 Circularity of standard test piece
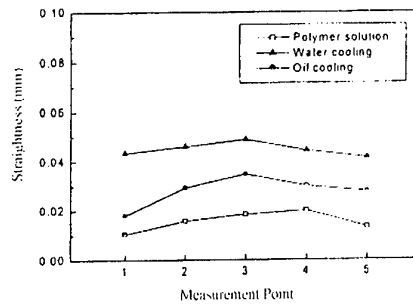
Fig. 9 Straightness of standard test piece

3. HEAT DEFORMATION AND SURFACE CHARACTER

3.1 Measurements of Heat Deformation and Discussion

Prior to heat-treatment, test pieces were ground so that their circularity and straightness[7] equaled zero. After heat-treatment, test pieces were fastened on the cylindrical grinder to measure circularity with the dial indicator; their straightness was measured by grinding the table. Test pieces were heat treated in 15%, 20°C polymer solution, 80°C oil, and 20°C water at agitation speed of 2.36 m/s before measuring circularity and straightness, which are shown in Fig. 8 and 9. When water was employed as cooling solution, it caused the greatest heat deformation because steam-curtain surrounding the test pieces broke away, which led to inconsistent cooling, and because cooling rate is high even at 400°C, around temperature of Martensite transformation. As shown in Fig. 8 and 9, circularity and straightness were great in the order of polymer solution, oil and water, and 15%, 20°C polymer solution produced the lowest circularity and straightness.

4. FATIGUE TEST

4.1 Rotation Bending Fatigue Test Apparatus

Fatigue Strength was obtained by the rotational bending fatigue tester(4 point bending fatigue of Ono's method). The bending moment M applied to the test piece is obtained by:

$$M=(P/2)a \qquad (1)$$

Where P refers to balancing weight and a refers to the distance between half side of knife edges, and when this bending moment is applied all over the test piece, bending stress σ is obtained by:

$$\sigma = 32M/\pi d^3 \qquad (2)$$

Where d refers to the diameter of test part. Evolution speed can be in the range of 1, 500 to 6,000 per minute, but 3,000 per minute is usually adopted.

Ono's method rotational bending fatigue tester was employed to performed fatigue tests on test pieces with no heat-treatment and on test pieces heat treated in water, oil, and polymer solution, and the S-N curve based on the obtained results was presented in Fig. 10.

The fatigue strength of each test piece was calculated by the formulation $\sigma_u=S_0+\Delta d$ of staircase method. Where S_0 refers to stress level value at the starting point of the test, and d refers to the interval of stress level values. Coefficient Δ is calculated as the ratio of stress level value interval(d), fatigue strength, and standard deviation(σ).

The fatigue strength of each test piece was calculated as the mean value of five repeated tests. It was found that fatigue strengths were; 271 MPa for the test piece with no heat-treatment, 324 MPa for oil solution, 356 MPa for water, and 377 MPa for polymer solution.

Heat-treatment effect obtained in the test was found to be between 26% and 39%, and polymer solution led to greater fatigue strength than any other cooling solution.
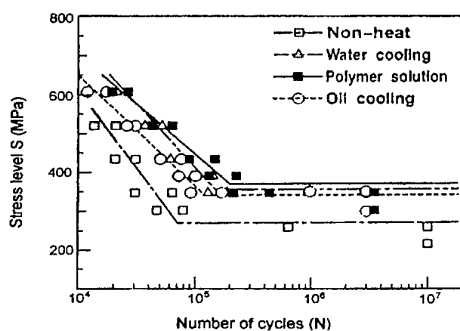
Fig. 10 S-N curves of test pieces

5. CONCLUSION

The purpose of this study was to develop a better method of controlling heat-treatment deformation in aircraft landing gears by improving quenching conditions. The cooling curves, cooling rates, and quenching characteristics of the three cooling solutions (water, oil and polymer solution) were examined with tests in order to investigate the effect of these heat-treatments on heat deformation and fatigue strength.

The results of this study are as follows:

1. The optimal quenching conditions of cooling solution were; 20°C for water, 15% concentration and 20°C for polymer solution, and 80°C for oil.

2. Circularity and straightness was great in the order of polymer solution, oil and water, and 15%, 20°C polymer solution produced the lowest heat deformation in the test pieces.

3. Hardness measurements indicated that test piece hardness was high in the order of oil, polymer solution, and water.

4. Fatigue test result suggested that heat-treatment improved fatigue strength by 26-39%, with polymer solution producing 6-10% higher fatigue strength than other cooling solutions.

REFERENCES

1. Lisic, B., "Assessing the Absolute Quenching Capacity During Hardening from the Surface Temperature Gradient", Haterei-Techn, Mitt., 33-4, pp. 197-191, 1978.
2. Beck, G., DUMONT. C., MOREAUX, F., and SIMON, A., "Guiding Principles in Choosing and Selection a Hardening Oil", Haterei-Techn, Mitt., 30-6, pp. 346-358, 1975.
3. T. Ueyama etc., "Improved Computer simulation Method for Shadow Mask Thermal Deformation", Japan Display 89, pp. 558-561, 1989.
4. H. Kim and S. Im, "Analysis of Beam Landing Shifts due to Thermal Deformation of Shadow Mask", IEEE Transaction on Consumer Electronics, 40-1, pp. 44-54, 1993.
5. S. Lee, New Metal Heat-Treatment, Wonchang, pp. 299-306, 1993.
6. J. Song and T. Chung, The Application of Geometric Tolerancing Techniques(using customary inch system), Sunandang, pp. 39-40, 1999.
7. J. Song and T. Chung, The Application of Geometric Tolerancing Techniques(using customary inch system), Sunandang, pp. 46-48, 1999.

IL2 Progress and Challenges in Sonic Boom Research

By

Christine M. Darden

NASA Langley Research Center

Hampton, Virginia, USA

ABSTRACT

A review is given of the three-pronged approach to sonic boom research in the recent NASA High Speed Research Program: acceptability studies, configuration design and operation, and atmospheric propagation studies. Progress made in design, prediction, propagation and acceptability is discussed. Challenges which remain are also discussed.

INTRODUCTION

Predicted growth in aircraft traffic in the Pacific rim has led to renewed interest in the development of a second generation, long range supersonic transport. Such a transport cruising at Mach 2.4 could reduce the current 13 hours for a 6500 nautical mile trip to less than 6 hours. Because of the sonic boom, laws that prohibit overland commercial supersonic flight currently exist in many countries. The economic viability of a supersonic transport would be improved considerably if the accompanying sonic boom could be eliminated or reduced to a level that is acceptable for overland flight.

Sonic-boom research during the NASA High Speed Research (HSR) Program that ended in 1999 was directed at answering three basic questions: "What is an acceptable level of the sonic boom? Can a practical airplane be designed to produce that level? What effect will atmospheric turbulence have on that 'acceptable' waveform shape?" Other concerns directly related to these basic questions include the validity of prediction methods for both steady state and focused booms and minimization methods. This paper will review the sonic boom phenomena and progress that resulted from research during the HSR Program.

The Sonic Boom Phenomenon

What is the sonic boom? As an airplane moves through the air, it produces pressure disturbances that propagate spherically through the air at the speed of sound. Because the airplane itself is moving faster than the disturbances when it is flying supersonically, all of the disturbances are enclosed within a Mach cone which extends backwards from the aircraft's nose as shown in Fig. 1. Ambient, free stream pressures are ahead of the cone, and the higher pressures caused by the airplane are within the cone. As the Mach cone intersects the ground, the abrupt change in pressure as indicated by the signature on Fig. 1 is heard as the "boom" by the observer. At cruise conditions, all existing supersonic airplanes, including the Concorde, produce an "N-wave" signature at the ground. Due to the level of annoyance created by these signatures, restrictive laws have been mandated.

A view of the sonic boom signature as it propagates to the ground is shown in Fig. 2. Note that near the airplane the signature is very complex with shocks, which are identifiable with various aircraft components such as the wing or engines. As the signature propagates through the atmosphere to the mid-field, the intermediate shocks coalesce, and there is less correspondence between the aircraft components and shocks. Generally, by the time the signature intersects the ground, only the bow shock and tail shock remain---thus the name "N-wave."
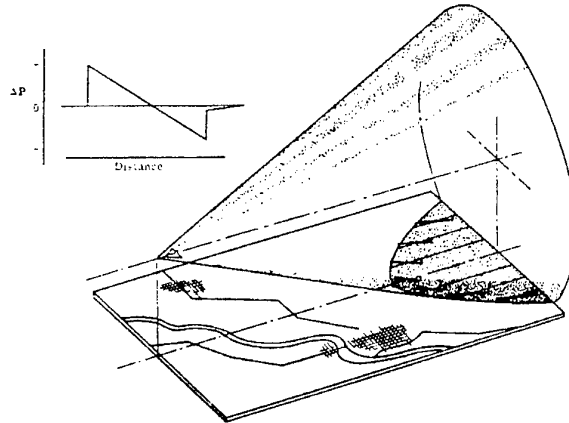
Figure 1. The sonic boom pressure

Most currently sonic boom predictions methods are based on theories developed by Whitham[1] for supersonic projectiles and by Walkden,[2] who extended the analysis to include lifting bodies. These theories combined with the supersonic area rule theory developed by Hayes[3] led to the generally accepted prediction methods described in some detail in Ref. 4. Originally, it was felt that all sonic boom pressure signatures would have attained the
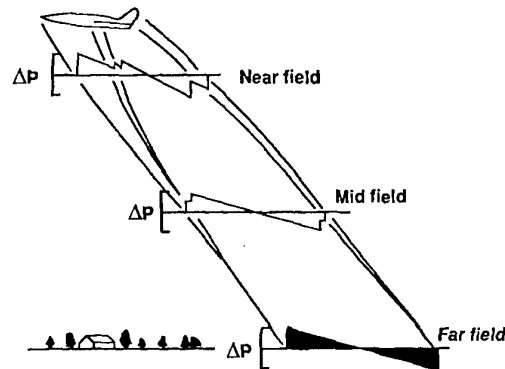
Figure 2. Signature propagation.
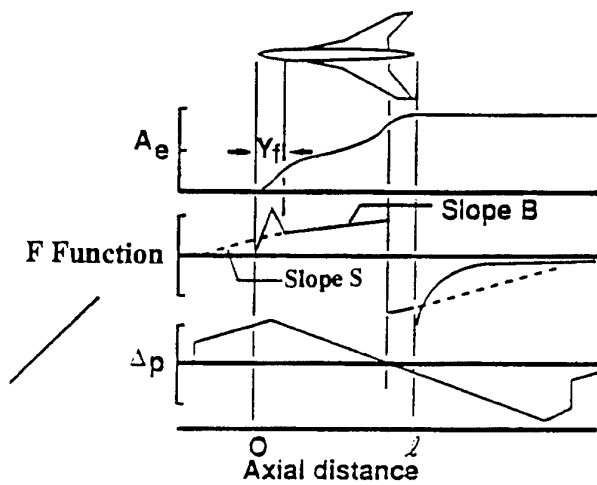
(a) Minimizing F-Function
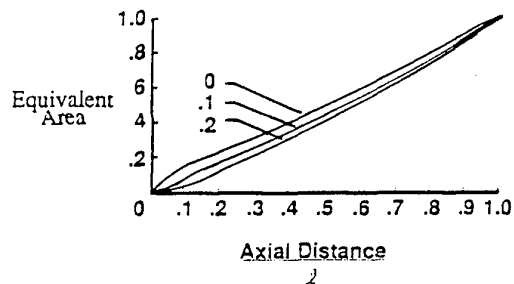
(b) Effect of varying noselength on equivalent area.
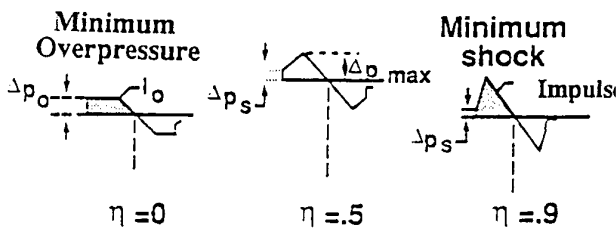
© Resulting types of pressure signatures.

Figure 3. Minimization concepts and parameters which may be varied.

standard N-wave shape when they intersected the ground. Work by McLean[5] indicated that this was not so for airplanes with extensive lifting surfaces. The "freezing" effects of the real atmosphere pointed out by Hayes[6] reinforced the idea that the signature may still retain mid-field characteristics when it intersects the ground. A mid-field signature retains effects of the airplane shape and, thus, offers shaping as a possible avenue of minimizing annoyance associated with the sonic boom.

Using as a basis the sonic boom prediction method, the idea of propagating the mid-field signature to the ground and work by Jones[7] on the far-field minimum, Seebass and George developed a procedure[8] which predicted a minimizing equivalent area distribution for given flight conditions. Extensions to this procedure for the real atmosphere and nose bluntness relaxation effects are given in Ref. 9. Working with a defined level or shape of sonic boom, an airplane can be developed to match that constrained area distribution. This process was used to design three flat-wing configurations which were experimentally tested for sonic boom levels.[10] Conclusions from that study indicated that the approach is valid but that the boundary layer and wake effects should be considered in the design process. Two feasibility studies[11,12] in which systems, passenger loads, safety, and airplane efficiency considerations were included, indicated that a low-boom aircraft was within the realm of possibility but that further in-depth, trade-offs studies were needed. Certain characteristic features of low-boom aircraft seem to evolve from the studies. These features included a large wing area, long wing chord, positive dihedral, and canards.

Review of Minimum Boom Concepts

The basic concepts of the Seebass and George minimization scheme are outlined in the upper portions of Fig. 3. Sonic boom minimization is based on an assumed form of the Whitham F function − a source distribution which at some distance from the aircraft gives the same disturbance as the aircraft. In traditional sonic boom prediction methods, the F function is defined mathematically from the equivalent area distribution of the aircraft. In minimization theories, one begins with the F function which relates directly to the resulting pressure signature. Through an inverted integral equation the F function also relates to the equivalent area distribution, A_e, of the aircraft. It has been shown[8] that the minimizing form of the F function has a Dirac Delta Function at the axial location of 0. Two types of pressure signatures result with this approach to minimization: a flat top, in which overpressure is minimized or a minimum shock, in which the initial shock is minimized. As a convenience, the slope of the F function behind the initial Delta Function shall be defined by η, the ratio of the slope B behind the spike, to the slope S, the dashed line ahead of the spike. For the flat-top signature, B=0, thus $\eta = 0$. For a minimum shock signature, the slope B ranges from 0 to slope S, and η ranges from 0 to 1.0. The effect of varying this slope on the resulting pressure signature shape is shown in the lower right section of Fig. 3. Variation of η also gives flexibility to the designer in the location of area growth associated with the wing.

Depending on the design objective, each of these signatures offers advantages. Given identical conditions of Mach number, length, weight and altitude, the minimum overpressure signature results in a larger bow shock but lower total impulse, I (the integral of the positive portion of the pressure signature). As η increases, slope B increases, the rise time of the segment with slope B decreases, the level of the bow shock decreases, and the impulse of the signature increases. The rise time of the segment with slope B is defined as the time it takes to go from minimum pressure to maximum pressure of that segment. In the limit, at an η of 1.0, theoretically, the bow shock becomes 0, but the rise time also becomes zero and in reality, an n-wave with a very large bow shock results. When designing with this option, generally a value of η between 0.4 and 0.6 is used. The option on η is included in the minimization algorithm to allow flexibility in the design and to

provide information on a wide range of signatures since the sonic boom metric which should be minimized has not yet been defined.

As noted previously, the minimizing form of the F function includes a Dirac Delta Function at the axial location of zero. This Delta Function corresponds to an infinite gradient at the nose of the equivalent area distribution. Aircraft designed to match these area distributions generally have extremely blunt nose shapes which result in increased drag. This result, though seemingly paradoxical, can be explained by the shock-attenuation pattern in which the shock strengths and, therefore, the drag are greatest near the aircraft. Because of shaping and area growth, secondary shocks from the other aircraft components do not overtake and enhance the bow shock during the propagation of the wave front. The net result of this process is weaker shocks at larger distances because of attenuation, but an overall increase in drag. To allow for some flexibility in nose bluntness, the minimization algorithm was modified to incorporate a spike with a finite-distance based called the nose length.
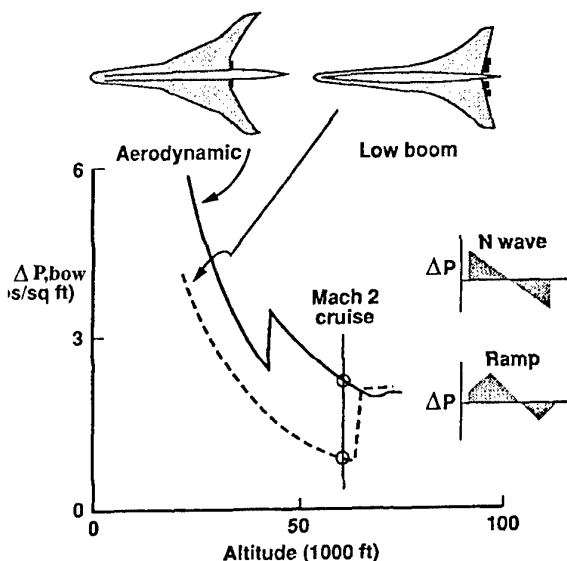

Figure 4. Comparisons of overpressures predicted for an aerodynamic and a low boom configuration. Mach 2, weight 600,000 lbs.

The effect of minimizing with nose lengths, y_f, other than 0 is seen in Fig. 3(b). The upper equivalent area distribution results when the Dirac Delta Function is used. For a ratio of nose length to overall length of 0.1, the middle area distribution results. Note that a cusped region is defined in the forward part of the area distribution and that the entire curve is affected. Generally, the larger nose lengths require a longer thin region at the nose of the aircraft. The bow shock resulting from the middle equivalent area distribution is somewhat higher than that resulting when the Delta Function is used, but the use of the nose length parameter does allow flexibility to trade between sonic boom levels and drag levels in design studies.

When using this minimization approach to achieve a given level of bow shock, use of the minimum shock signature allows

one to achieve the given level with a shorter length aircraft. Conversely, use of a minimum shock signature to achieve a given bow shock allows a heavier aircraft for a given length. Other factors such as sensitivity to atmosphere and human response must also be considered.

Configuration Design Studies

Using these minimization theories, two low boom concepts were designed[13]: a Mach 2 concept designed to produce a flat-top signature with a bow shock level of 1.0 psf; and a Mach 3 concept designed to produce a minimum shock signature with a bow shock of 1.0 psf. Unlike the flat-wing concepts discussed in Ref. 10, these concepts featured a cambered and twisted wing, cambered fuselage, dihedral, fin and nacelles. The major emphasis in these designs was constrained-boom-theory validation for compete configurations with only secondary consideration given to aerodynamic performance.

Shown in Fig. 4 is a comparison of bow shock overpressures from a baseline, Mach 2 configuration, and the low-boom Mach 2 concept[14]. The baseline configuration has been designed for optimum aerodynamic performance with little consideration given to the sonic boom. These calculations were performed for configurations cruising at Mach 2 and weighing 600,000 lbs. The discontinuity in the overpressure curves on Fig. 4 occurs when the intermediate shocks in the mid-field signature coalesce into the bow shock to form an N-wave. Note that the low-boom configuration produces a lower bow shock for the entire altitude range shown, with the major benefit being at the altitudes of 40,000 to 58,000 ft. where the low boom sonic boom signature maintains its mid-field features and the aerodynamic configuration has transitioned to an N-wave. Design cruise altitude is 55,000 ft. for the configurations.

Test set-up is shown in Fig. 5 where the twelve-inch model of the Mach 3 low boom concept is mounted in the NASA Langley Unitary Tunnel in its test configuration. During tests the model is translated longitudinally and the pressures are read by probes mounted on the wall. A differential pressure gage measures the pressure differences between the two probes.
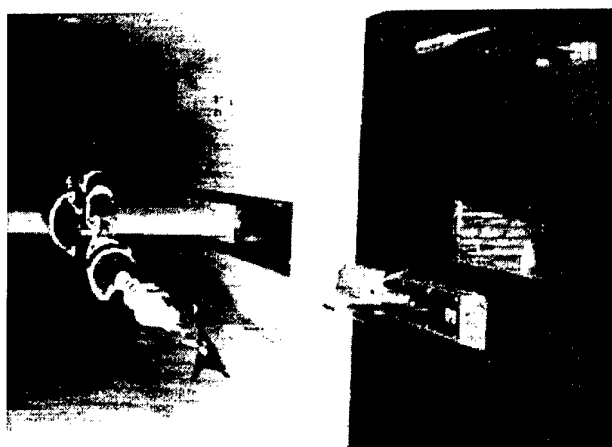

Figure 5. Sonic-boom test set-up.

A comparison of extrapolated Mach 2 wind tunnel test data, the predicted results, and the target signature are shown in Fig. 6. The agreement between the theory and the extrapolated

experimental data, especially in the forward portions, essentially validates the minimization methodology at Mach 2 for this twisted and cambered configuration. During the test, difficulties arose with shocks from the nacelle region of the configuration and the results shown in Fig. 6 are for the configuration without nacelles.
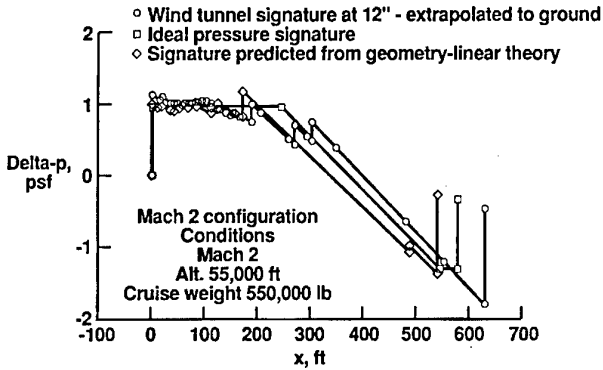

Figure 6. Comparison of predicted and extrapolated pressure signatures.

An analysis of the difficulties encountered with the nacelles is discussed in Ref. 15, and the addition of F-functions for this discontinuous surface was recommended.

The use of high speed computers also began to be employed both in the analysis of sonic boom models and in the design of the models. Ref. 16 discusses the application of full potential methods, marching Euler methods, relaxation methods, and thin-layer Navier-Stokes methods for sonic-boom predictions. One difficulty encountered in the application of CFD methods for sonic-boom prediction, has been that of generating an accurate flow-field some distance from the body. At Mach 2.0, to generate the signature at one body-length away from the body, calculations must be made approximately two body-lengths downstream. This is almost impossible for many relaxation methods because of the grid density and time required. For marching methods, the fidelity of the shocks is lost because of the grid spreading which has occurred at this distance. A topology change was introduced into the grid for making sonic boom calculations. The grid is retained only between two Mach angles which capture the region of flow disturbance. Thus, the spreading of the grid is reduced, and flow fidelity is retained to a larger distance in a radial direction..

Shown in Fig. 7 is an example of one of the models designed using computational fluid dynamics (CFD) methodology[17] to generate multi-shock signatures on the ground rather than flat-top or ramp signatures. Also shown is a signature measured in the NASA Ames 9- by 7-Foot Supersonic Wind Tunnel at a normal force coefficient of 0.068 amd at am j/l of 1.16. the figure inset at the lower right of Fig. 7 shows wind tunnel measurements which have been extrapolated to the ground. Measurements which were extrapolated were at CN's of 0.068, 0.094, and 0.114. CN(Design), based on the projected weight of the model, was 0.08.

From these results, one might conclude that at a CN – 0.08, a multi-shock signature would be successfully generated at ground level with this concept. There is discussion within the sonic-boom community that multi-shock signatures such as these may be more stable than the ramp-type when propagating through a real atmosphere. Calculated loudness of these signatures and their simulation within the NASA Langley Sonic-Boom Simulator

demonstrate that these multi-shock signatures present a viable alternative to strictly shaped flat-top or ramp signatures.
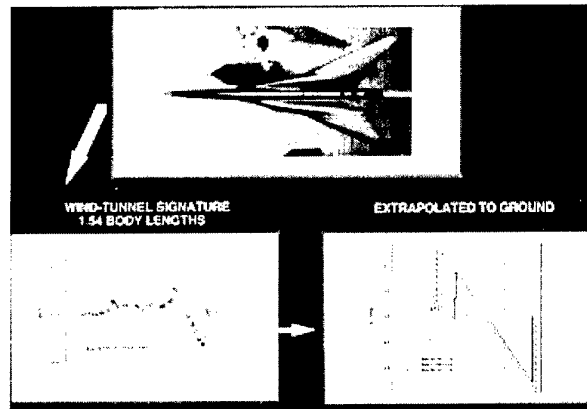
Figure 7. CFD-Designed Model with experimental results.

Nearfield pressure signatures shown from a second low-boom model designed using the equivalent area for a minimized shock signature are shown in Fig. 8. The design of the model generating these signatures also incorporated the new method for incorporating the nacelles. Analysis of the completed model also indicated that the fully defined mission could be met with less than a 5 percent weight penalty over the mission baseline.
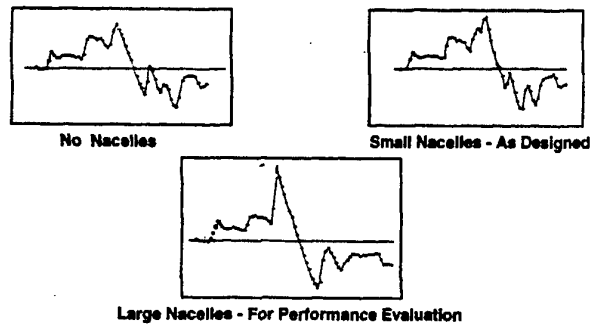
Figure 8. Pressure Signatures for LB16 design: M=1.6, h=20 inches, CL = C$_{Lcruise}$.

Configuration Operation

The sonic boom of a supersonic configuration must be within acceptable limits not only during the cruise portion of the flight but also during the supersonic climb-to-cruise. Shown in Fig. 9 is an analysis of ground sonic boom signatures during the entire supersonic mission of the Mach 2 low-boom concept[19]. The inset signatures are all plotted to the same scale with the signature shown at the start of cruise having a 1.0 psf bow shock. These sonic boom levels were calculated based on steady-state calculations. Including the effects of converging rays and focused booms should typically result in even higher levels. In Fig. 9(a), where the optimum performance flight profile is shown, it is seen that all of the ground signatures generated during the supersonic climb-to-cruise exceed the arbitrarily imposed 1.0 psf cruise limit. Figure 9(b) shows that

in order to stay within the 1.0 psf limit with this configuration, supersonic speeds should not be reached until the configuration has achieved an altitude of approximately 43,000 ft. The penalty in range for flying the boom constrained flight profile would be approximately 9 percent. Also, proper account must be taken of converging, diverging and intersecting rays which occur during accelerating and turning flight.

(a) Optimum performance path.

(b) Boom-constrained path; delta P (max) = 1.0 psf.

Figure 9. Ground signatures predicted for complete mission: Mach 2 configuration, take-off gross weight, 590,000 lbs.

Higher Order Prediction Methods

The design of low-boom configurations which produce mid-field signatures and which have acceptable performance has increased the need for accurate flow-field information within one to two body lengths so that proper component integration and design fine tuning can be achieved. Traditionally employed sonic boom prediction and minimization methods are based on linearized theory. Though these methods have proved invaluable to the level of understanding in sonic boom, they are only valid in those regions where nonlinear effects are second order. This is not the case less than one or two body lengths away from the configuration, and may not be true at high Mach numbers or following propagation through thousands of feet of atmosphere, where the accumulation of nonlinear terms may become first order.

During recent years, improved capabilities in CFD has increased the feasibility of its application to sonic boom prediction. CFD methods can potentially become a very effective partner to wind tunnels in assessing particular features of an aircraft's design which may need tailoring so that the proper

signature   is   attained.   CFD   also
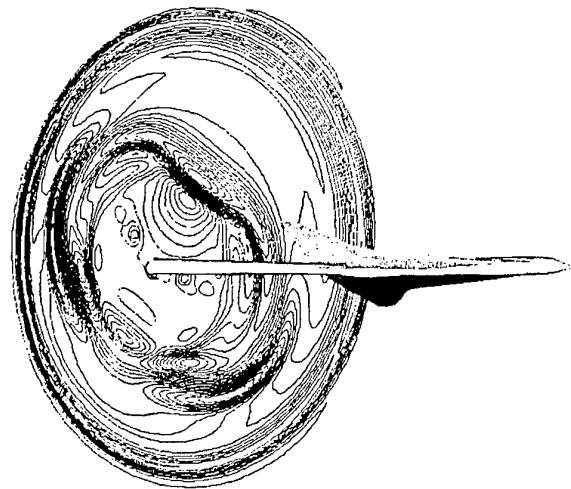
Figure 10. Pressure contours at one body length behind low boom concept.

has the potential for sideline measurements and predictions out to several body lengths of very complex configurations. As low-boom models become larger to capture more configuration features, measurements at several body lengths in many supersonic tunnels becomes impossible because of tunnel size. Because CFD has traditionally been used to predict surface pressures, modifications may be necessary before they can reliably be applied to predict pressures at several body lengths away.

Fig. 10 shows a CFD-generated pressure field results obtained using a Marching Euler Code[16]. The contour lines indicate that the strongest shocks of concern seem to be the shocks from the wing. This qualitative view of the flow-field is quite helpful to the designer and indicates that in sonic-boom minimization the non-zero azimuthal planes cannot be ignored.
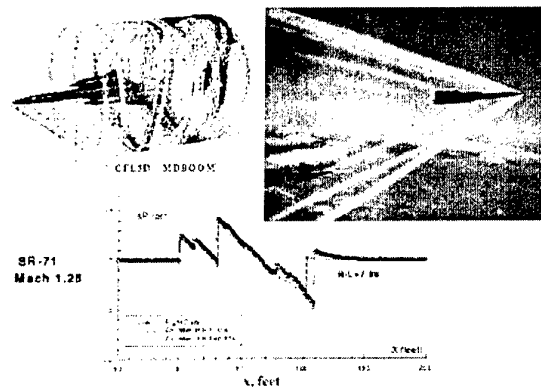
Figure 11. Measured and predicted sonic boom pressure field of an SR71.

To validate the CFD prediction of a sonic boom signature, an F16 was configured to measure the pressure field of an SR-71 flying at Mach 1.6. The SR71 in flight includes the exhaust which may not

be properly accounted for in wind tunnel or theoretical models. Shown in Fig. 11 is an enhanced photograph of the two aircraft along with the measured and predicted signatures of the SR71. Overall, the agreement between the measured and predicted signatures is excellent.

Atmospheric Propagation Effects

Another area of concern in the sonic boom research effort is the effect of the atmosphere on the signature as it propagates for thousands of feet. Current sonic boom prediction methods account for horizontal stratification of atmospheric temperatures, densities, and pressures and have some allowance for winds. However, real atmospheric effects of turbulence and vertical variations are beyond the level of current theoretical capabilities. Flight tests in the 1960's when all signatures were N-waves yielded the signature variation in overpressure shown in Fig. 12.[4] The predicted signature occurred the largest percentage of the time, but rounded (longer rise time) and peaked signatures also occurred in significant numbers. Theoretical research is now being done to model atmospheric molecular relaxation (absorption) and turbulence so that their effects on shaped signatures can be assessed. Shown by the solid line in Fig. 12 is a theoretical prediction for rise time as a function of shock overpressure based on the current absorption models[21]. Rise times from measured data are indicated by the cross-marks. Immediately obvious from this figure is the fact that rise time has an inverse relationship to overpressure. Thus, lower bow shocks of shaped signatures will also promote greater rise times. Assuming turbulence to be the only other atmospheric effect on the data, then Fig. 12 shows that turbulence must increase the rise time of the signature shock.

Shock Overpressure, Pa
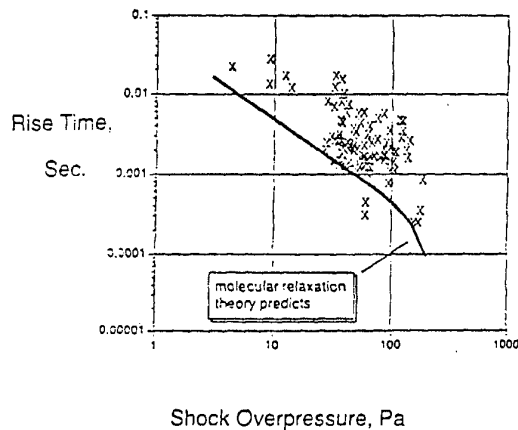
Figure 13. Sonic boom rise times based on absorption model.

Sonic Boom Acceptability

The determination of an acceptable level of sonic boom exposure requires, as a first step, a noise metric that is suitable for the assessment of individual sonic booms, regardless of their shape. This would enable the quantitative comparison of sonic boom signatures predicted for candidate High Speed Civil Transport (HSCT) aircraft. To

Figure 14. Sonic Boom Simulator.

address this need, a loudness prediction model[22] was developed, the validity of which is being assessed by means of the sonic boom simulator shown in Fig. 14. The simulator consists of an array of loudspeakers mounted in the door of a concrete enclosure lined with sound-absorbing foam. Simulated sonic boom pressure signatures are computer-generated in order to attain precise control of the amplitude and phase of the signal and to overcome some of the inadequacies of the sound reproduction system. Results from a study conducted using the simulator are also shown in Fig. 15. Test subjects judged the loudness of sonic booms representing different combinations of duration, rise time,

Delta p (Meas) / Delta P (calc)

Figure 12. Sonic boom variability caused by the atmosphere.

overpressure and shape. The plot of the average subjective loudness response as a

Figure 15. Subjective response studies at Langley Research Center.

function of peak overpressure of the signatures indicated that this measure alone provides a poor indication of people's reaction to sonic booms. In the case of N-waves, the rise time is an additional important characteristic of the signature. For the shaped boom, the characteristics of the initial pressure jump (i.e., rise time and amplitude) have a strong influence on the subjective response. The predicted loudness
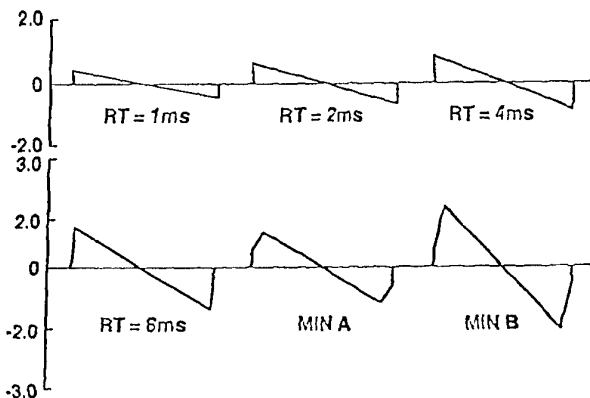
Figure 16. Signatures judged equally loud based on simulation booth studies.

(Perceived Level, dB) utilizes the entire waveform of the sonic boom and, as shown in the figure, provides a reasonably precise prediction of the mean subjective response. Thus, the loudness calculation procedure represents a valid method for the comparative assessment of HSCT sonic boom signatures.
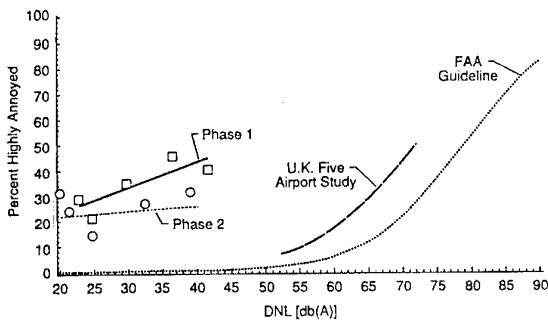
Figure 17. Percent of subjects highly annoyed by sonic booms at Nellis Air Force Base.

Based on the simulator studies, all of the signatures shown in Fig. 16 were judged equally loud by the subjects.

The determination of a level of sonic boom exposure that would be acceptable to the general population requires that subjective response be examined under real-life conditions. Another phase of the human acceptability studies consisted of surveys of persons who had routinely been subjected to sonic booms over a period of years because of their proximity to military operational areas. Initial results of the Nellis survey are reported in Ref. 23 and shown in Fig. 17. In this figure, loudness is plotted in DNL, a metric which incorporates the effects of repeated sonic booms and the effects of sonic booms occurring at times other than during the daylight hours. Included on the chart for reference are the percentages of persons predicted to be highly annoyed based on studies done by CHABA (Committee on Hearing and Bioacoustics of NRC) and airport noise studies. The Nellis survey studies (completed in two phases) indicate that people are much more annoyed by the sonic booms than was predicted by either of the other studies. These results coupled with performance penalties resulted in the entire sonic boom effort of the HSR Program being directed more toward corridor flight rather than unrestricted overland flight.

CONCLUDING REMARKS

A review of HSR sonic boom research in human acceptability, configuration design, and atmospheric propagation has been given. Based on this review, the following summarizing statements are given:

1) Low-boom design theories have been validated for configurations without nacelles at Mach numbers up to 2.0.
2) Nonlinear effects such as high Mach number flight, discontinuous changes in shape as with nacelles or wing junctures or extrapolation over great distances may not be properly accounted for in the currently used linear methods.
3) Rise times introduced by the atmosphere will increase as shock strengths become lower with current low boom concepts.
4) For outdoor listening conditions, loudness in PLdB has been validated by experiment to be an appropriate measure of sonic boom disturbance.
5) For an equivalent loudness in PLdB, shaped signatures with low bow shocks allow greater overpressure levels and thus larger aircraft weights than the traditional N-wave.

Though much progress has been made in understanding the sonic boom pressure signature and its propagation characteristics, much work remains to be done in determining acceptable levels and in designing a low boom configuration that will be aerodynamically competitive.

REFERENCES
[1]Whitham, G.B., "The Flow Pattern of a Supersonic Projectile," *Commun.Pure & Appl. Math.*, Vol. V, No. 3, Aug. 1952, pp. 301-348.
[2]Walkden, F., "The Shock Pattern of a Wing-Body Combination Far From the Flight Path." *Aeronaut.Q.*, Vol.IX, Pt. 2, May 1958, pp. 164-194.
[3]Hayes, Wallace D., "Linearized Supersonic Flow," Rep. No. AL-222, North American Aviation, Inc., June 18, 1947.

[4]Carlson, Harry W. and Maglieri, Domenic J., "Review of Sonic-Boom Generation Theory and Prediction Methods," *J. Acoust. Soc. America*, Vol. 51, No. 2, Pt. 3,Feb.1972, pp. 675-685.

[5]McLean, F. Edward, "Some Nonasymptotic Effects on the Sonic Boom of Large Airplanes," NASA TN D-2877, 1965.

[6]Hayes, Wallace D., "Brief Review of Basic Theory. Sonic Boom Research," A.R. Seebass, ed., NASA SP-147, 1967, pp.3-7.

[7]Jones, L.B., "Lower Bounds for Sonic Bangs in the Far Field." *Aeronaut. Q.*, Vol. XVIII Pt. 1, Feb.1967, pp. 1-21.

[8]Seebass,R. and George, A.R., "Sonic-Boom Minimization," *J. Acoust. Soc. America*,Vol. 51,No.2, Pt 3, Feb.1972, pp.686-694.

[9]Darden, Christine M., "Sonic Boom Minimization with Nose Bluntness Relaxation," NASA TP-1348, 1979.

[10]Mack, R.J. and Darden, C.M., "Some Effects of Applying Sonic Boom Minimization to Supersonic Cruise Aircraft Design," *J.Aircr.*, Vol 17, No. 3, Mar. 1980, pp. 182-186.

[11]Carlson, Harry W., Barger, Raymond L., and Mack, Robert J., "Application of Sonic-Boom Minimization Concepts in Supersonic Transport Design," NASA TN D-7218, 1973.

[12]Sigalla, A., Runyan, L.J. and Kane, E.J., "The Overland Supersonic Transport with Low Sonic Boom---A Feasibility Study,"*Acta Aeronaut.*,Vol 4,No.1 1/2, Jan./Feb. 1977,pp.163-179.

[13]Mack, Robert J., and Needleman, Kathy E., "A Methodology for Designing Aircraft to Low Sonic Boom constraints," NASA TM-4246, 1991.

[14]Needleman, Kathy E., "A Study of Sonic Boom Overpressure Trends with Respect to Weight Altitude Mach Number and Vehicle Shaping," AIAA Paper 90-0367, 1990.

[15] Mack, Robert J.: Some Considerations on the Integration of Engine Nacelles into Low-Boom Aircraft Concepts. NASA CP-3173, Oct 1992, pp. 221-236.

[16]Siclari, M.J. and Darden, C.M., "CFD Predictions of the Near Field Sonic Boom Environment for Two Low Boom HSCT Configurations," AIAA Paper 91-1631, 1991.

[17]Cliff, Susan E., Computational / Experimental Analysis of Three Low Sonic boom Configurations with Design Modifications. NASA CP-3173, Oct 1992, pp. 89-117.

[18]Baize, Daniel G.; McElroy, Marcus O.; Fenbert, James W.; Coen, Peter G.; Ozoroski, Lori P.; Needleman, Kathy E.; Domack, Chris S.; and Geiselhart, Karl A.: A Performance Assessment of Eight Low-Boom High-Speed Civil Transport Concepts. NASA HSR Sonic-Boom Workshop, NASA CP-1999-209699, 1999.

[19]Coen, Peter G: "Development of a Computer Technique for Prediction of Transport Aircraft Flight Profile Sonic Boom Signatures." Master's Thesis, George Washington University, May 1991.

[20]Haering, Edward A., Jr.; Whitmore, Stephen;, and Ehernberger, L.J.: Measurement of a Basic SR71 Airplane Near-Field Signature." NASA HSR Sonic Boom Workshop, NASA CP-1999-209699.

[21]Pierce Allan D., and Sparrow, Victor W.: "Relaxation and Turbulence Effects on Sonic Boom Signatures." First Annual High Speed Research Workshop, Williamsburg, VA, May 14-16, 1991.

[22]Shepherd, K.P., and Sullivan, B.M., "A Loudness Calculation Procedure Applied to Shaped Sonic Booms," NASA TP-3134, 1991.

[23]Fields, James; Moulton, Carey; Baumgartner, Robert M.; and Imm-Thomas, Jeff: Resident's Reactions to Long-Term Sonic-Boom Exposure: Preliminary Results, NASA HSR Sonic-Boom Workshop. NASA CP-3279, 1994.

SL3   THE EXTRAORDINARY MISSION OF MARS GLOBAL SURVEYOR

Arden Albee

Division of Geological and Planetary Sciences, California Institute of Technology,Pasadena CA 91125 USA

ABSTRACT

The Mars Global Surveyor (MGS) spacecraft entered an elliptical orbit at Mars on September 11, 1997.   Until March 1999 it acquired scientific data from decreasing-size orbits as it alternated between aerobraking and nadir-pointing modes.   This time period provided tremendous advances in our knowledge of the shape and topography, the gravity field, the magnetic field, and the atmospheric structure and dynamics of Mars.   From April 1999 to January 2001 MGS carried out its planned two years of mapping in the nadir mode. In this mode the high-gain antenna tracks Earth so that the instruments can take data continuously and so that the camera system can return high-resolution data in real-time. IR spectral and temperature data, as well as high-resolution images are providing additional insight into the geologic evolution of Mars.   All data is being archived at about six month centers so that it is available in electronic format to the international community. Currently MGS continues to acquire data and is preparing to support Odyssey aerobraking in 2001 and the landing of the Mars Exploration Rovers in 2004.

1. MARS GLOBAL SURVEYOR MISSION

Mars Global Surveyor (MGS) is the initial mission in the NASA Mars Surveyor Program, an integrated series of missions to explore Mars. This Program was initiated after the loss of Mars Observer (MO), a mission that was to make systematic orbital observations for a Mars year, following up on the results of the Viking mission. Over the next decade the Program will launch orbiters or landers every 25 months, using advanced technology to develop a comprehensive portrait of Mars. The Program focuses on understanding present and past climatic conditions on Mars, determining whether Mars developed prebiotic compounds and life and identifying resources that might be of use during human expeditions to the surface. Determining the locations and states of water reservoirs now and in the past are key objectives.

The objectives of Mars Global Surveyor, like that of MO, is to obtain a number of data sets that provide global coverage over a complete Mars year, studying the atmosphere, the surface and the interior. Studies prior to MO had shown that this could be done economically by a spacecraft in a nearly polar orbit, carrying a suite of complementary instruments that would operate concurrently and continuously.   In order to reduce launch mass the mission plan for MGS replaced the propulsive maneuvers of MO by about four months of aerobraking. This process utilizes repeated dips into the upper atmosphere to slow the spacecraft down from its initial 45-hour elliptical orbit to the final two-hour near-circular mapping orbit. Large solar array panels extend from each side of the spacecraft and provide the aerobraking drag. The planned mapping orbit is near circular, near polar, and sun-synchronous and has a 117-minute period with a 7-day near-repeat cycle. As a result the planet is repeatedly mapped in 26-day cycles with a constant sun angle (2 a.m., 2 p.m.), permitting differentiation between those characteristics that vary daily from those that are due to seasonal changes. No movable scan platform is provided as in most past missions. During the mapping configuration at Mars the spacecraft --and its instruments-- is continuously nadir-pointed, rotating at the orbital rate, as the antenna tracks Earth and the solar arrays track the Sun. Measurements are made continuously from the mapping orbit over the 687-day Martian year, permitting repetitive observations of the surface and gravity field and seasonal variations of the atmosphere and magnetic field.

2. MGS SPACECRAFT

MGS used spare components and science instruments from MO in a configuration only about half the size of MO, and it was launched on a smaller launch vehicle. Consequently, the two heaviest instruments from MO had to be accomodated on later missions in the program. The experiments include: Mars Orbiter Camera (MOC), a system of three line-scan cameras; TES, a Thermal Emission Spectrometer; Mars Orbiter Laser Altimeter (MOLA), a laser altimeter; Radio Science (RS), using the spacecraft X-band radio system as controlled by an ultrastable oscillator; MAG-ER, dual MAGnetometers complemented with an Electron Reflectometer; and Mars Relay (MR), a radio communication system to relay data to Earth from landers on the surface of Mars.   The spacecraft accelerometer and the horizon sensor were utilized as additional atmospheric sensors during the aerobraking period.

Mass was saved by constructing the spacecraft from panels of composite surface sheets on Al honeycomb which are edge clamped without a frame. Using spare MO electronic assemblies, which in turn permitted the reuse of much of the flight software, saved costs. The area of the solar array "wings" was chosen to provide the necessary area for aerodynamic drag within the heating constraint, hence it was populated with a combination of GaAs and Si cells to provide the necessary power at the least cost. Solid state recorders replaced the MO tape recorders. A series of sun sensors, a celestial sensor, an inertial reference unit, a Mars horizon sensor, and four reaction wheels provide three-axis attitude control. A single 596 N bi-propellant engine provided the thrust for Mars orbit insertion and twelve 4.45 N monopropellant

thrusters provide for momentum unloading, thrust vector control, and all other maneuvers. Telecommunications are provided by a 25 watt X-band system with the high-gain antenna deployed on a short boom with two axis gimbals in order to view Earth during orbital operations.

3. CRUISE AND AEROBRAKING PHASE
The MGS spacecraft was launched on November 7, 1996. However, deployment of the solar panels in early cruise resulted in damage to one panel such that it would not properly latch for orbit insertion. Analyses suggested

Ground tests and analysis of spacecraft data suggested that aerobraking could continue, but only at atmospheric pressures of about one-third that previously planned. Entry into the circular mapping orbit was delayed for an entire Martian year, requiring more than 900 lower-pressure aerobraking dips into the atmosphere. The delay, accomplished by a pause in aerobraking, put the spacecraft into the 2:00 a.m. (relative to the sun) position rather than in the originally planned 2:00 p.m. position; this timing made it possible to operate the spacecraft and its instruments in the geometric relationships for which they had been designed.
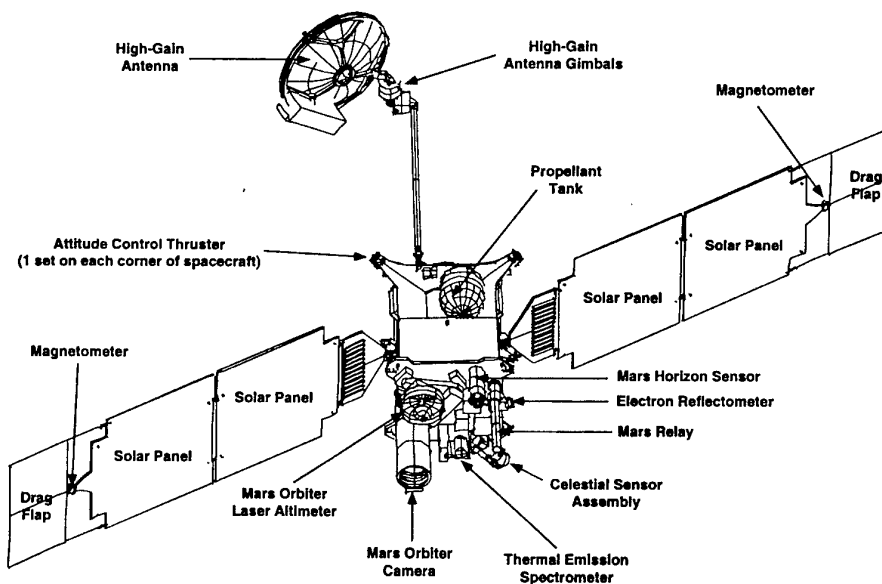
that reversing that panel during entry, putting the cells into the flow, might force the panel into its latched position. After successful insertion into a 45-hour elliptical orbit at Mars on September 11, 1997 MGS entered a period of aerobraking, utilizing utilized repeated dips into the upper atmosphere to slow it so as to attain the low altitude (378 km) circular-mapping orbit. According to plan it would have reached this orbit early in spring of 1998. However, the weakening of the damaged solar panel became abruptly clear about a month into aerobraking. Immediately the orbit periapsis was raised higher in the atmosphere to lower the pressure on the panel. The science instruments were operated in their design nadir orientation in the near-periapsis portion of each 35.4-hour elliptical orbit for a month during assessment of the problem. In these 16 orbits the periapsis altitude was only 174 km and the spacecraft passed in and out of the ionosphere on each orbit. Excellent, although unanticipated, science data was acquired during this period as alternative plans were considered (*Science*, special issue, 1998, 279:1671-97).

Scientific observations were obtained during most of this delay. Low-altitude (high-resolution) data, especially important for the magnetometer and gravity investigations, were obtained over most of the planet. Such coverage was possible because during this period of time the periapsis position of the continuously-decreasing elliptical orbit migrated from 45 degrees north over the north pole and then down and over the south pole. Science data was collected from 372 elliptical orbits, 175 km by 17,850 km, from March 27, 1998 to September 23, 1998. During the periapsis portion of each 11.6-hour orbit the spacecraft was turned to the nadir-pointing position so that the instruments pointed to Mars for about 22 minutes. The altimeter, thermal emission spectrometer, and camera obtained data in near-normal mode during the nadir portion of these orbits and acquired lower-resolution global image and thermal data during the rollout from the nadir position to the earth-point position. The magnetometer-electron reflectometer obtained data throughout the entire orbit during most of this period, but radio tracking was limited.

Science data was also obtained during the aerobraking orbits. The atmospheric density of Mars at the aerobraking altitude demonstrated great variation over time as well as large orbit-to-orbit differences. So that the spacecraft could adjust its orbit, the density had to be predicted for each orbit to determine the appropriate and safe depth within the atmosphere for the aerobraking passage. Although science data acquisition during the aerobraking phase was not in the original mission plan, MOC, TES, the accelerometer, the electron reflectometer, and the horizon sensor all acquired data to support prediction of the atmospheric density. MGS returned 2140 MOC images, 11 million TES spectra, 206 MOLA profiles with 2.6 million points, 465 radio-occultation profiles and 1000 MAG low altitude passes during this unexpected bonus prior to the primary mission. Moreover, atmospheric data were obtained over a range of daily times, other than the fixed 2:00 p.m./a.m. position of the mapping mission.

4. PRIMARY MAPPING PHASE

After a period of orbit adjustment, instrument calibration, gravity measurements, and acquisition of a seven-day data set from all instruments the high-gain antenna (HGA) was deployed on its boom from the fixed position attached to the body of the spacecraft. This deployment permitted initiation of the planned mapping mission, which requires the HGA to track earth and return data simultaneously with data taking by the instruments. During mapping the spacecraft operates in a low-altitude, near-circular, near-polar, Sun-synchronous orbit with a short repeat cycle. Specific orbital parameters include a "frozen" orbit with a period of 117.65 minutes and an 88 revolution near-repeat cycle of about seven sols (Martian days). The index altitude of 378 km is a measure of the difference between the semi-major axis length from the center of mass and the equatorial radius of Mars (3397.2 km). The height of the spacecraft above the actual surface of Mars ranges between 368 km and 438 km. This "frozen" orbit essentially balances the secular motion of periapsis due to J2 by the variation due to the J3 component of the gravity field, thereby providing more stable spacecraft operation over an extended period. The 88 revolution near-repeat pattern results in orbits spaced 242 km apart at the end of 7 days and four patterns produce a planned cycle of 60 km ground track spacing. Each successive cycle fills in this spacing further and, under ideal conditions, would result in 26 global cycles and a spacing of about 3 km at the equator at the end of the two-year mapping mission.

The sun-synchronicity was chosen as 2 p.m./2 a.m., relative to the mean sun position, to balance the requirements of the various instruments. The MOC prefers late afternoon for long shadows whereas TES prefers an orbit closer to 1:00 PM where higher ground temperature would result in a higher signal to noise ratio. However, the true Sun position actually varies during the course of the mission from nearly an hour

ahead to nearly an hour behind the mean Sun position. During mapping the spacecraft is continuously nadir-pointed, rotating at the orbital rate, as the antenna tracks Earth and the solar arrays track the sun. The instruments are mounted on the nadir platform, permitting the use of simple, fixed, line-scan instruments, each with its own computer. This configuration, along with adequate data storage, downlink rate, and power margins, make it possible for all instruments, including radio science, to be operated simultaneously and continuously with a single 10 hour pass per day on a 34 m Deep Space Station (DSN) ground station. The downlink process consists of a daily playback of the spacecraft solid state recorders plus a real-time data return about every third day. Three different data rates are used during the mission to accommodate the variation in Earth-Mars distance. The science data are placed in the project database in packets as formatted by the individual instruments. Averaged over the mission, the raw data rate is more than 120 Mbits/day. An unexpected limitation in the movement of the High Gain Antenna (HGA) gimbal has shortened the playback time during periods of certain orbit-earth-sun geometry.

5. SCIENCE EXPERIMENTS

MOC is currently photographing portions of Mars at unprecedented resolution looking at the surface effects of wind, water, ice, volcanic eruption, earthquake faulting, slope failures, and other geological processes. The narrow-angle camera can capture small areas at its highest resolution of 1.4 m per pixel, but because of the high data volume required only small "samples"— postage stamps-- can be imaged at this resolution. Features as small as 3-4 m across, such as boulders, craters, and dunes, are recognizable and evidence of the action of surface processes are visible in every high resolution image. MOC also scans the entire planet daily with the red and blue wide-angle cameras in order to build up synoptic coverage of the surface and atmosphere, much like earth-orbiting weather satellites. These cameras also image targeted strips at a medium resolution and will produce color stereoimagery of the entire surface over the course of the mission.

TES uses a Michelson interferometer that measures the emitted infrared spectrum, at high spectral resolution to determine the mineral composition and thermal properties of Martian rocks and soils and the composition of ices, atmospheric dust, and clouds. TES continuously measures temperature and pressure, providing 12 profiles per day of the atmosphere from pole to pole. These provide a basis for understanding the atmospheric dynamics and the energy balance between the Martian surface and atmosphere. In addition, as the radio transmission from the spacecraft passes through the Mars atmosphere it is diffracted by the atmospheric electrons and provides high vertical resolution profiles of the temperature and pressure in the atmosphere. Preliminary analyses of the TES spectra, after removal

of the atmospheric and dust components, are providing insight into the surface thermal properties (grain size) and the mineral composition of the surface materials (predominantly "basaltic").

MOLA uses the flight time of a laser pulse from the spacecraft to the surface and return in conjunction with knowledge of the spacecraft position to map the shape and topography of Mars with precision of about five meters. The laser fires ten pulses per second illuminating ~160-m circle on the surface. MOLA has now provided a precise map of the shape and topography of Mars, now known better than the Earth's continents in an overall sense. The most striking feature remains the ~5 km difference in elevations and the difference in roughness between the smooth northern plains and the southern cratered highlands. On June 30, 2001 MOLA ceased to work due to a chip failure; its laser had fired 671 million times in space.

The RS team use data provided by the spacecraft's radio system and an onboard ultrastable oscillator to map spatial variation in the gravity field of Mars by measuring instantaneous velocity changes of the spacecraft in its orbit. Removal of the gravitational signal of the topography makes it possible to gain some understanding of the internal density anomalies that are associated with thermal or compositional differences in the interior of the planet. The rough, elevated southern hemisphere has a relatively smooth gravitational signature indicating a state of near-isostatic compensation, while the low, flat northern plains display a wider range of uncompensated gravity anomalies that indicates a thinner but stronger crust than in the south.

The MAG investigation measures the magnetic field on Mars. The presence of a magnetic field provides direct evidence for the existence of active motions in a fluid core, either at the present or at some time in the past. The electron reflectometer measures electronic properties as the spacecraft passes through the upper atmosphere and can infer the presence of weak remnant crustal magnetization. Almost immediately upon arrival at Mars the magnetometer experiment showed that Mars lacks a global magnetic field at the present time. This resolved a long-standing controversy and places an important constraint on the present nature of the Martian core. More importantly, however, during the low portions of the elliptical orbit the magnetometer has mapped crustal magnetic anomalies of surprisingly high strength in the older rocks of the southern hemisphere and these anomalies are interpreted as evidence of a vigorously convecting dynamo in the early core.

6. END OF PRIMARY MISSION
At 4:18 p.m. (PST) of January 31, 2001 at the end of its 8505th orbit the Mars Global Surveyor spacecraft completed its planned 687 day Mars year of mapping, meeting the last of its primary objectives. In addition, the year of aerobraking and science phasing orbit observations had contributed an unexpected data set from an additional 1855 elliptical orbits. Science measurement acquisition has continued since then in an extended mission with emphasis on the support of future missions.

7. EXTENDED MISSION
Landing site selection for the Mars Exploration Rovers (MER) in 2004 is being supported by normal nadir data collection as well as an off-nadir mode involving a spacecraft roll, that has been developed to provide additional landing site observations. The relay capability on MGS has been tested and will be used during the landing and operations of the MER landers. In addition MGS will provide continuous global coverage of Mars to monitor the presence of dust storms, that would lead to density increases that could risk the Odyssey mission due to thermal damage during aerobraking beginning in October 2001. Science measurements will continue during this long period, an extension made possible by putting MGS into a 16-degree pitch position that minimizes use of the reaction wheels and fuel. One reaction wheel has been lost and replaced by use of the skew wheel.

8. CONCLUSION
Currently data are still being returned at a very high rate and continue to be archived for electronic public access by the Planetary Data System(HYPERLINK http://www.pds.jpl.nasa.gov). Published collections of early results from Mars Global Surveyor are: *Science* 1998 279:1597-1816, *Geophys.Res.Ltrs.* 1998 25:4393-4420, *Science* 1999 284:1495-1502, *Nature* 1999 397:584-594, *Jour. Geophys. Res., Planets* 2001, in press.

HOME SITES FOR MGS AND THE INSTRUMENTS:
MGS   http://mars.jpl.nasa.gov/mgs/index.html
MAG/ER   http://mgs-mager.gsfc.nasa.gov/
MOC   http://www.msss.com/
MOLA   http://ltpwww.gsfc.nasa.gov/tharsis/mola.html
RS   http://nova.stanford.edu/projects/mgs/dmwr.html
TES   http://emma.la.asu.edu/

To date, the MGS spacecraft has transmitted almost twice as many images as returned by the two spacecraft Viking Orbiter mission, and more data from Mars is now in hand from this Mission than all previous Mars missions combined. Following is a list of ten significant achievements of MGS during its first mapping year - ordered from the interior of the planet outward.

TABLE 1. SOME SIGNIFICANT ACHIEVEMENTS OF MGS AT MARS

1)   **MAGNETIC FIELD--SIGNIFICANT REMNANT MAGNETIZATION OF THE MARTIAN CRUST IS EVIDENCE OF AN EARLY MOLTEN INTERIOR**

WITH A VIGOROUS CORE DYNAMO. NO CURRENT GLOBAL FIELD (MAG).

2) **GRAVITY AND FIGURE**--THE ELLIPSOIDAL SHAPE OF MARS IS FLATTENED BY ~20 KM DUE TO ROTATION AND THE CENTER OF FIGURE IS OFFSET BY NEARLY 3 KM, INDICATING THAT THE NORTH POLE IS ABOUT 6 KM LOWER THAN THE SOUTH POLE. RELIABLE GLOBAL MODELS OF THE STRUCTURE OF THE CRUST AND LITHOSPHERE SHOW NEAR ISOSTATIC COMPENSATION IN THE ROUGHER SOUTH AND A RANGE OF UNCOMPENSATED GRAVITY ANOMALIES IN THE SMOOTHER NORTH (RS & MOLA).

3) **TOPOGRAPHY**--THE BEST GLOBAL TOPOGRAPHIC MODEL PRODUCED FOR ANY PLANET, INCLUDING EARTH, SHOWS A 30-KM RANGE OF TOPOGRAPHY, A POLE-TO-POLE SLOPE THAT CONTROLLED THE TRANSPORT OF WATER IN EARLY MARTIAN HISTORY, AND A FLAT NORTHERN DEPRESSION THAT MAY REPRESENT THE LOCATION OF A LARGE ANCIENT OCEAN. HIGH RESOLUTION TOPOGRAPHY PERMITS DETAILED TRACING OF CHANNEL NETWORKS AND EPHERMERAL LAKES THAT DRAIN INTO A CLOSED EQUIPOTENTIAL CONTOUR IN THE NORTHERN PLAINS (MOLA).

4) **VOLCANISM**--THICK LAYERED SEQUENCES OF STRATA IN VALLES MARINERIS SUGGEST THE POSSIBILITY OF EXTENSIVE VOLCANISM DURING EARLY TO MID-MARTIAN HISTORY (MOC).

5) **BASALT AND WEATHERING**--THERMAL EMISSION SPECTRA SHOW WIDE OCCURENCE OF BASALTIC ROCKS IN THE SOUTH AND ANDESITIC ROCKS IN THE NORTH. WIDESPREAD OCCURRENCE OF PLAGIOCLASE AND PYROXENE AND THE LACK OF WEATHERED HYDRATED MINERAL ATTEST TO THE ABSENCE OF PERVASIVE WEATHERING. HIGH-ALBEDO AREAS HAVE A NON-DIAGNOSTIC SPECTRUM, MUCH LIKE THE ATMOSPHERIC DUST (TES).

6) **HYDROTHERMAL DEPOSITS**--DETECTION OF SEVERAL COARSE-GRAINED HEMATITE DEPOSITS, POSSIBLE INDICATIVE OF DEPOSITION IN A SURFACE HYDROTHERMAL ENVIRONMENT. NO AREAS OF CARBONATE, SULFATE, OR QUARTZ HAVE BEEN DETECTED (TES).

7) **AEOLIAN PROCESSES**—CURRENT AEOLIAN PROCESSES ARE EVIDENCED BY DUST DEVILS, DUST STORMS, STREAKS, DUNES, AND SAND SHEETS. STRATIGRAPHIC EVIDENCE FOR A COMPLEX DEPOSITIONAL AND EROSIONAL HISTORY ELUCIDATES THE IMPORTANCE OF AEOLIAN TRANSPORT ON THE GLOBAL AND LOCAL SCALE (MOC). THE EVOLUTION OF A MAJOR DUST STORM HAS BEEN FOLLOWED IN DETAIL (MOC & TES).

8) **POLAR CAPS**--A RELIABLE ESTIMATE OF WATER VOLUME IN THE PRESENT POLAR CAPS AND EVIDENCE FOR DISTINCTIVE EVOLUTION OF THE NORTH AND SOUTH POLAR CAPS (MOLA & MOC).

9) **CHANNELS AND SAPPING**--CLEAR EVIDENCE OF A SAPPING ORIGIN OF MANY CHANNELS FROM PROBABLE MELTING OF GROUND ICE AND POSSIBLE EVIDENCE FOR RECENT LIQUID WATER IN NUMEROUS SPATIALLY-ISOLATED REGIONS (MOC).

10) **ATMOSPHERIC DYNAMICS.**-- SIGNIFICANTLY IMPROVED UNDERSTANDING OF ATMOSPHERIC DYNAMICS FROM CONTINUED MONITORING OF TEMPERATURE, PRESSURE, AND OPACITY, AND MEASUREMENT OF CLOUD HEIGHTS (TES, RS, MOLA, ACC, MOC). VALUE OF DATA IS GREATLY ENHANCED THROUGH COMPUTER SIMULATIONS USING GENERAL CIRCULATION MODELS (GCMs).

MECHANISM OF FLOW TYPE CHANGES
WITH LENGTH-TO-DEPTH RATIO IN CAVITY FLOW

J. Zhang[*], E. Morishita[**], T. Okunuki[***], and H. Itoh[***]
Department of Aeronautics and Astronautics,
University of Tokyo, Tokyo, Japan,113-8656

Key Words: Aerodynamics, Compressible flow, Turbulent flow

ABSTRACT

Compressible flows over cavities with a series value of length-to-depth ratio (L/D) were investigated experimentally and computationally, with the objective to elucidate the physics of the transition of types of cavity flows as their L/D increases or decreases. The freedom of backflow inside the cavity is found to be crucial in smoothing out adverse pressure gradient. The spreading of the shear layer and its gradual approaching towards the cavity floor as L/D increases tend to suppress the freedom of backflow, causing the cavity flow to change from the open-type to the transitional-type. In the transition from closed- to open-type cavity flow, the effect of the upstream separation wake on the downstream recompression wakes was found to be non-negligible basing on pressure coefficient distribution from experiment and friction coefficient distribution from numerical simulation.

1. INTRODUCTION

Compressible flows over cavity-like geometries occur widely in aerospace and aeronautical vehicles. Past researches have established that the defining parameter for such flows is their length-to-depth ratio (L/D). Closed flows occur for cavities with L/D greater than 13. Open flows occur for cavities with L/D less than 10. For L/D between 10-13, transitional cavity flow occurs. However, little effort has been directed towards the understanding of the changes of cavity flow with L/D. Understanding of such mechanism is not only of profound academic interest, but also helpful in suggesting new ideas for the control of cavity flows. To the author's limited knowledge, no theory or explanation for the closing of cavity is available in open literature. The mechanism for the opening of a closed cavity as the value of its L/D decreasing was proposed by Charwat et al[1]. They suggested that the cavity opens when the vertices of the upstream recompression wake and downstream separation wake merge and backflow occurs inside the cavity. However, Stalling and Wilcox[2] found that Charwat's formula under-predicted the measured critical values throughout their test Mach number range. No explanation was given in Stalling and Wilcox's report.

The present work set out to investigate the compressible cavity flows with a series value of L/D both experimentally and numerically, with the objective to elucidate the physics of the transition of cavity flow types as their L/D increases or decreases.

2. WIND TUNNEL, MODEL, AND TEST CONDITIONS

*Ph.D. student, Department of Aeronautics and Astronautics
**Professor, Department of Aeronautics and Astronautics
***Technical Staff

The tests were conducted in the supersonic wind tunnel of Department of Aeronautics and Astronautics, University of Tokyo. The test section has a rectangular cross section of 80mm by 140 mm. A nozzle with Mach number 1.94 was used in the current work. The boundary layer just upstream of the position where cavities are to be installed was measured and judged to be of turbulent, its thickness estimated to be about 8mm. Reynolds number per unit meter is 4.2×10^7. Pressure coefficients at cavity walls are calculated as follows:

$$C_p = \frac{2}{\gamma M_\infty^2}(\frac{p}{p_\infty}-1)$$

Schlieren visualization was taken during all of the test run. Oil flow visualizations using oil (500CS) mixed with TiO_2 were conducted for some of the test cases. The schematic for the pressure orifice locations is shown in figure 1.

3. RESULTS AND DISCUSSIONS

Effects of length-to-depth ratio and $(L/D)_{cr}$

Surface flow pattern as shown in figure 2, drawn from videos of oilflow visualization, indicated relatively weak 3D flows in open- and transitional-type cavities and much stronger one in the closed-type cavity. The video of a closed-type cavity flow shows a pair of big vortices behind the exiting shock wave beside the two side walls, with the vortex axis somewhat perpendicular to the cavity floor. It reveals that the boundary layers over the wind tunnel sidewalls first thicken, then separate under the severe adverse pressure gradient associated with the impinging and exiting shock waves over the cavity. The $(L/D)_{cr}$ for the present model configuration is judged to be $14^{[4]}$.

Mechanism for the opening of closed type cavity flow

The author believes there are two fundamental weaknesses in Charwat's formula for the prediction of $(L/D)_{cr}$. Firstly, the lengths of the separation wake for rearward-facing step flow and recompression wake for forward-facing step flow may not be rigorously defined. Secondly, even if some kind of lengths can be defined, it is not a constant in the cavity flow as L/D changes. The two wakes are not independent from each other and the interaction begins well before the possible meeting of the vertices of the two separate wakes, as the two wake vertices are covered by the compression fans at the foot of the impingement and exit shock waves. The strong interaction tends to extend the recompression wake upstream as L/D decreases from a large value.

Plotting the pressure distributions with the same reference

length and different alignment clearly reveals the different response of the two wakes to the interaction. Figure 3 compares the pressure coefficient distributions for closed-type cavity flows and the rearward-facing step flow, with the longitudinal distance aligned with the front face and normalized with the depth. It is readily visible that the front portion of all the curves of closed-type cavity flows collapse on that of rearward-facing step. It indicates that separation wake is essentially not influenced by the approaching of the cavity rear face. This is to be expected as the attached flow over the mid-region of the floor is essentially supersonic, and, in a supersonic flow, disturbances can not propagate upstream. In contrast, the recompression wake is clearly affected by the approaching of cavity front face, as shown in figure 4, where the curves are aligned with the rear face. As L/D decreases, the pressure in the region ahead of the rear face decreases, suggesting a decrease in the strength of the exit shock wave. The location at which the pressure starts to rise abruptly moves slightly forward. The above observations are supported by the results of Stallings and Wilcox, with more evident upstream extension of the recompression wake[2].

Basing on the pressure distribution, schlieren and oil flow visualizations obtained in the present test, the process of the opening of closed cavity flow can be described as follows (See figure 5):

● When the L/D of a cavity is sufficiently large, the separation wake and the recompression wake are well separated apart, with a reattaching boundary layer and main flow in between. Impingement and exit shock waves are generated due to the deflection of the main flow. The gradual change of the direction of the shear layer produces compression fans at the foot of the two shock waves. The pressure distribution along the floor features a flat region between two regions of dramatic rise.

● As the value of L/D decreases, especially when the innermost edges of the two compression fans approach each other, the interaction between the two wakes begins. When the attached boundary layer is fully covered by the two compression fans, it will thicken considerably for being subjected to much increased pressure gradient. The thickened boundary layer will further deflects the main flow, causing the compression fan at the foot of the exit shock waves to move upstream and the separation region behind it to extend.

● At a critical value of L/D, the length of the reattached boundary layer reduces to zero; the shear layer impinges on the floor and separates again immediately. The impingement and exit shocks merge into a single shock. The flat region in the pressure distribution disappears accordingly, marking the change of flow from the closed to the transitional-closed type.

A new model for the prediction of the critical length-to-depth ratio might be obtained by investigating the behavior of a shear layer under the influence of the wave system over the cavity in a closed-type cavity flow.

Mechanism for the closing of open type cavity flow

For open-type cavity flows, it was found that the pressure near the cavity front corner is directly linked with the backflow inside the cavity[4]. A plate was installed laterally near the mid-portion of the cavity floor. The cavity had a

L/D equal to 5. Two tests were taken, with the height of the plate being 2mm and 4mm respectively. It was found that the more the backflow is blocked, the lower the pressure at the front part and the higher the pressure at the rear part of the cavity floor. The approaching of the developing shear layer over the cavity toward the cavity floor acts like a plate in hindering the backflow inside the cavity.

Extensive schlieren and oil flow visualizations in the present investigation, supplemented with the flow fields generated from numerical simulation, helped to lead to the following understanding of the physics of the closing of cavity flows as L/D increases from a value corresponding to open cavity flows (See figure 6):

● When the L/D of a cavity is small, the separating shear layer strikes at the trailing edge of the cavity, increasing the pressure near the rear wall. The backflow occurs freely inside the cavity, since the shear layer has yet to be sufficiently developed and the space between it and the floor is ample. A weak shock wave emanating from the leading edge is generated to adapt the freestream to the high pressure over the cavity.

● At an increased value of L/D, the shear layer gets developed for a longer distance. The momentum with which it strikes the trailing edge increases, resulting in even higher pressure near the rear face of the cavity. As the shear layer grows thicker, it approaches the floor gradually. The presence of the floor hinders the free development of the lower part of the shear layer, and pushes it upwards. The main flow over the cavity gets deflected, producing a compression fan. On the other hand, the space between the shear layer and the floor diminishes, and the momentum of the fluid flowing downstream in the shear layer increases, making it more and more difficult for the high pressure fluid at the rear part of the cavity to travel upstream. In fact, the streamlines inside cavity, as predicted from numerical simulation, reveal that the backflow is squeezed at the mid-portion by the shear layer and the floor into a dumb-bell like shape. In the meantime, the air at the front part of the cavity is continuously scavenged by the shear layer above it, the balance of mass flow causing the pressure at there decreases. The shock wave at the leading edge weakens. The size of the recirculation near the front corner shrinks.

● Further increasing the value of L/D, the shear layer approaches so close to the floor that the backflow is essentially separated into two parts. Two new recirculations, embedded in the backflow and linked with only a thin layer of fluid with upstream velocity just over the floor, are formed. Due to reduced air supplement, the pressure near the front corner decreases below that of the freestream. An expansion fan replaces the weak shock wave at the leading edge, and the external flow begins to deflect into the cavity, initiating the transitional-open type cavity flow. The compression fan over the cavity gets strengthened.

● At a critical value of L/D, the shear layer suddenly impinges onto the floor, dividing the backflow into two separate recirculations. The deprivation of air supplement through backflow from the rear part of the cavity causes the pressure near the front part

drops to a minimum. A strong expansion fan is formed at the leading edge. The deflection of the main flow at the floor produces a single shock wave that marks the transitional-closed type cavity flow.

Computational Results

The governing equations are the 2D Favre-averaged Navier-Stokes equations with Spalart-Allmaras[3] one-equation turbulence models. A new way, both efficient and adequately accurate, of systematically specifying the inflow profiles of all of the needed variables was proposed in the pricipal author's doctoral thesis[4].
The simulated effects of length-to-depth ratios on cavity centerline pressure distribution are shown in figure 7. The general trend as observed from experiment is reproduced. The friction coefficient distributions along floor of closed-type, with front wall and rear wall alignment respectively, are compared in figure 8. It confirms the experimental observations that the recompression wake extends upstream as L/D decreases for closed cavity flows.

4. CONCLUSION

Experimental and computational investigation of compressible flows over cavities with a series value of

length-to-depth ratio (L/D) found that the freedom of backflow inside the cavity is crucial in smoothing out adverse pressure gradient. The spreading of the shear layer and its gradual approaching towards the cavity floor as L/D increases tend to suppress the freedom of backflow, causing the cavity flow to change from the open-type to the transitional-type. In the transition from closed- to open-type cavity flow, the effect of the upstream separation wake on the downstream recompression wakes was found to be non-negligible basing on pressure coefficient distribution from experiment and friction coefficient distribution from numerical simulation.

REFERENCES

1. Charwat, A. F.; Roos, J. N.; Dewey, F. C., Jr.; and Hitz, J.A: J. Aerosp. Sci., vol. 28,no.6, June 1961, pp. 457—470.

2. Stallings, Robert L., Jr., and Wilcox, Floyd J., Jr.: NASA TP- 2683, 1987.

3. Spalart, P. R., Allmaras, S. R., AIAA 92-0439, 1992.

4. Zhang J. B., Experimental and Computational Investigation of Supersonic Cavity Flows, Ph. D. thesis, University of Tokyo, Japan, Sept., 2000.

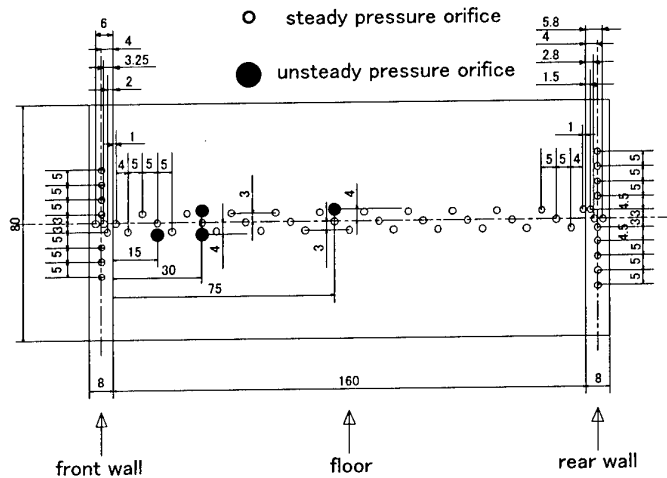Fig. 1 Pressure orifice locations (linear dimensions are in millimeter)

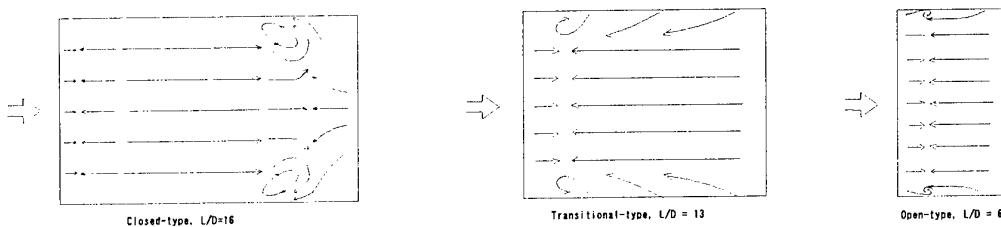Fig. 2 Surface flow patterns for three-types of cavity flows

Fig. 3 Pressure distributions of closed cavity
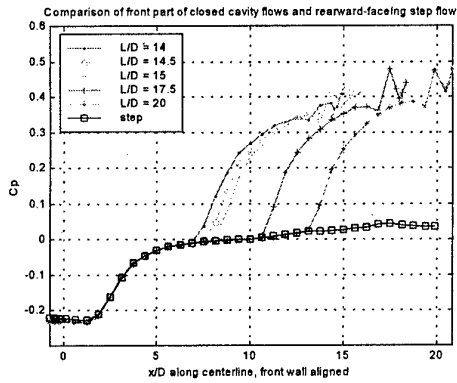flows and step flow (front corner aligned)

Comparison of front part of closed cavity flows and rearward-faceing step flow

L/D ≒ 14
L/D = 14.5
L/D = 15
L/D = 17.5
L/D = 20
step

Cp

x/D along centerline, front wall aligned

Fig. 4 Pressure distributions of closed
cavity flows (rear corner aligned)

Comparison of rear part of closed cavity flows

L/D = 14
L/D = 14.5
L/D = 15
L/D = 17.5
L/D = 20

Cp

x/D along centerline, rear wall aligned
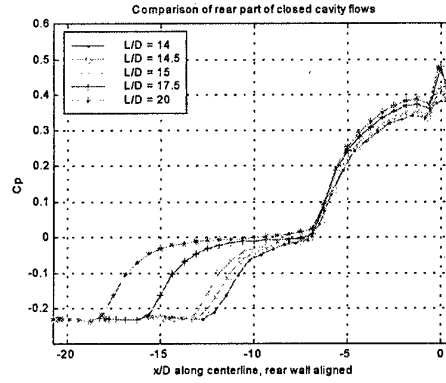
Fig. 5 Sketches of flow fields during the opening of the cavity flow

(1) At large value of L/D(>>13)

(2) At reduced value of L/D

(3) Transitional-closed cavity flow
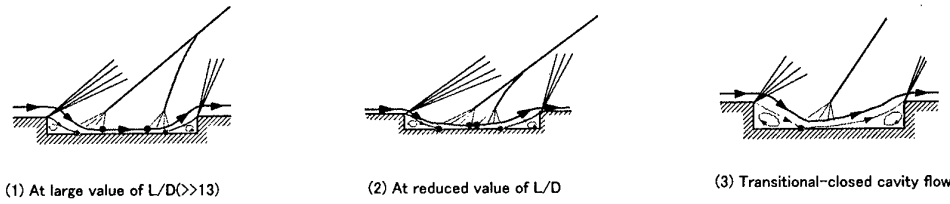
Fig. 6 Sketches of flow fields during the closing of the cavity flow

(a) At small value of L/D(<<10)

(b) At increased value of L/D

(c) For L/D near the critical value
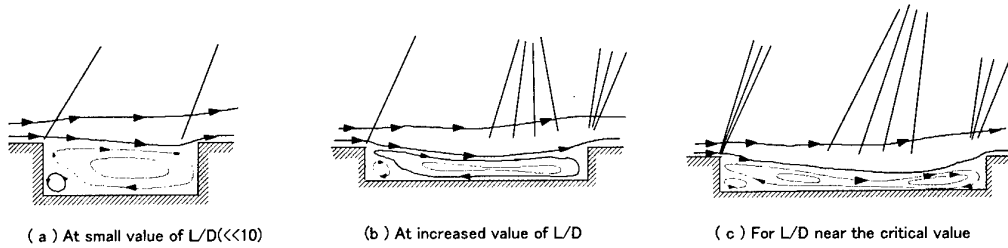
Fig. 7 Simulated effect of L/D on cavity
centerline pressure coefficient distributions

Cp along cavity centerline, Re_D = 3.4e+005 Mach = 1.94

L/D = 3
L/D = 5
L/D = 7.5
L/D = 10
L/D = 13
L/D = 13.5
L/D = 14
L/D = 15

Cp

x/L
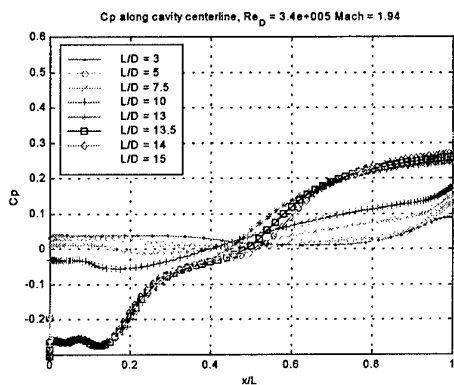
Fig. 8 Comparison of friction coefficient
distributions along cavity floor

rear wall aligned

L/D = 13
L/D = 13.5
L/D = 14
L/D = 14.5
L/D = 15

cf along floor

x/D
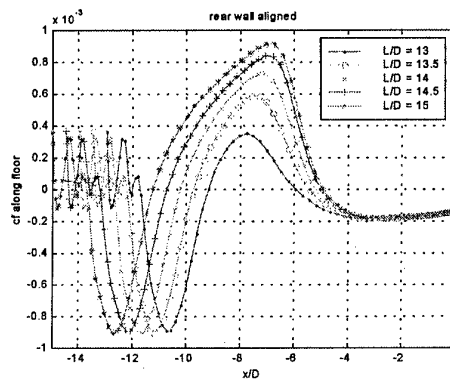
3F6   RESPONSE OF THE FLOW AROUND A CIRCULAR CYLINDER TO ITS ROTATIONAL OSCILLATION

Hessameddin Ebneddin Hamidi* and Yoshiaki Nakamura**
*Qadr Aerodynamic Research Center, Imam Hossein University,Tehran, Iran
**Department of Aerospace Engineering, Nagoya University, Nagoya, Japan

Key Words: Fluid dynamics, Unsteady Flows, Flow Control

ABSTRACT

The response of flow pattern and vortex shedding around a circular cylinder which is rotationally oscillating about its axis has been studied by numerical simulation. In this study, we can control the wake pattern by rotationally oscillating a cylinder around its axis. By doing this, the lift and drag of the cylinder is expected to be changed. The results show that over some range of frequency, the drag coefficient was reduced to 15 percent of the non-oscillatory case, and the amplitude of lift coefficient was also reduced to 15 percent. On the other hand, some other frequencies produced larger values of lift and drag coefficients than the stationary case. This oscillation is effective when the amplitude of oscillation is higher than a critical value. Furthermore, the relation between rotation angle and pressure distribution was analyzed by changing the frequency and amplitude of oscillation, and the frequency response between rotational oscillation and lift coefficient was obtained. It is found that there are phase lag and amplitude attenuation in low frequencies, while they vanish at high frequencies and very low frequencies.

1. INTRODUCTION

The flow around a circular cylinder has long been a basic subject for studying boundary layer separation and vortex

coefficient changes with time. These patterns are expected to be controlled by oscillating the cylinder about its axis[2].

In the current study we focus on the relation between rotation angle, pressure distribution, and forces in unsteady condition. This relation helps us model actual forces exerted on the object by flow in oscillatory or unsteady condition. Quasi-steady model, where unsteady response of the flow around an object is neglected, has been widely used by researchers and designers. However, this model has to be examined to make clear its limitations, because in a steady flow this quasi-steady model is valid but when the model is oscillating or moving unsteadily it is not applicable anymore. It was shown by our previous study that there exists hysteresis in flow characteristics, and that both amplitude attenuation and phase lag occur in the relation between rotation angle and pressure distribution at high frequency oscillations[3].

2. GOVERNING EQUATIONS AND FLOW SOLVER

In this study the two-dimensional incompressible Navier Stokes equations in non-dimensional form have been used. Furthermore, a generalized coordinate system has been employed to adapt the grid with the geometry. An O mesh with 130X81 grid points has been used around the cylinder with a diameter of 1 meter. The Reynolds number has been
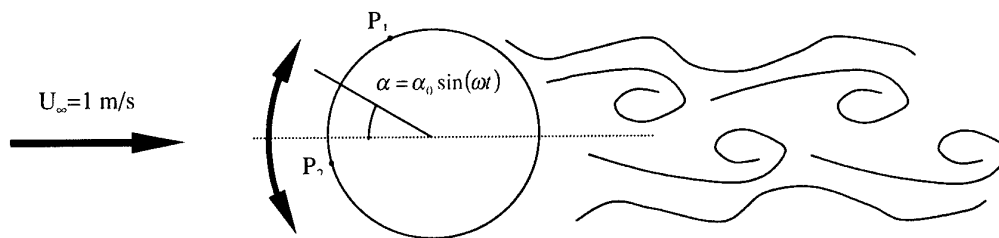

Fig. 1 Flow around a cicular cylinder with rotational oscillation

shedding. In the flow around a blunt body such as circular cylinder, the static pressure does not remain constant in the whole field of flow, so that separation and reverse flow occurs[1]. In the upstream half of the cylinder pressure decreases, the flow particles and the velocity increase, wheras in the downstream half due to viscosity the kinamatic energy is not enough large to resist the pressure increase, leading to the flow separation along with reverse flow. This causes alternate, clockwise and counterclockwise, Karman vortex shedding in the wake. Due to these vortices, the alternating circulation around the cylinder happens and the lift

set at 10^4 with a uniform flow velocity of 1.0 m/s. The SX-4 NEC super computer of National Institute for Fusion Science (NIFS) was used, and it took one hour for each run.

3. RESULTS AND DISCUSSION

Calculation was performed under various conditions such as variations in frequency and amplitude of cylinder oscillation about its axis, as shown in Fig. 1.

The frequency of the oscillation was changed over the range of $0 \leq \omega \leq 10$ with an increment of 0.5, and the
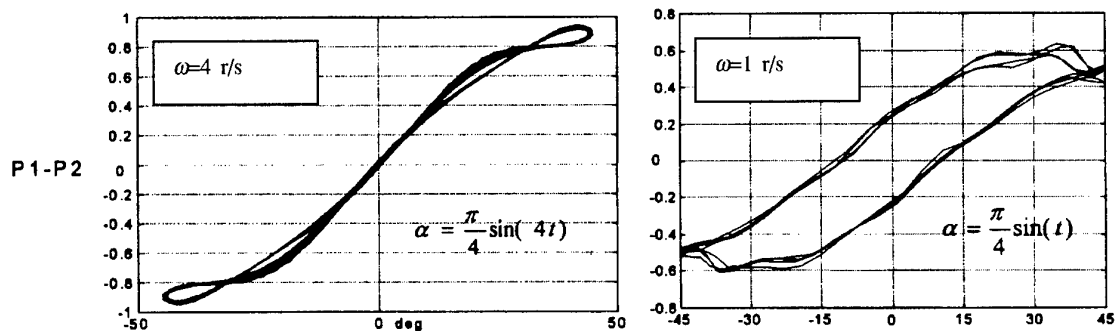
Fig. 2 Hysteresis in relation between attack angle and pressure differences

amplitude over the range of $0 \bullet \alpha_0 \bullet \pi/2$ with an increment of π. The data of time histories of pressure and velocity distribution and also the lift and drag coefitients were saved for further analysis. Analysis was done in three different category as follows:

• Effects of frequency and amplitude of oscillation on relation between rotation angle and pressure distribution.

• Effects of frequency and amplitude of oscillation on vortex shedding.

• Effects of frequency and amplitude of oscillation on exerted forces from fluid to circullar cylinder.

The relation between rotation angle and pressure difference $\Delta P = P_1 - P_2$ (see Fig. 1) is shown in Fig. 2 for frequencies equal to one and four. P_1 and P_2 are separated by 45 degrees from symmetric axis, so that when rotation angle is zero, $P_1 - P_2 = 0$. In steady flow, this relation is linear but as one can observe, hysteresis appears in this relation in frequency of about 1 r/s where it disappears again in higher frequencies as seen in Fig. 2. Hysteresis in this relation means that there is amplitude attenuation and phase lag. This is an important phenomenon which should be considered in the modeling of an unsteady flow.

The time history of the lift coefficient highly depends on vortex generation because these vortices change the circulation around the cylinder and its lift. From the time history of the lift coefficient we can see vortex generation pattern. Figure 3 shows the time history of the lift coefficient for three different oscillation frequencies: $\omega = 1$, 4, and 8. Based on this figure and observation of the flow field, flow pattern can be classified into the following three flow regimes:

• Flow pattern is similar to the case without oscillation $(\omega = 0 \sim 3)$

• Vortex generation frequency is equal to oscillation frequency $(\omega = 3 \sim 6)$

• Vortex generation is affected by both rotational oscillation and natural shedding $(\omega = 6 \sim 10)$

By looking at the pressure distribution for two different cases: a) $\omega = 1$ and b) $\omega = 4$. It is obvious that vortex shedding pattern is totally different mainly regarding generation frequency and size of the vortices. When $\omega = 1$ vortex shedding frequency is the same as its natural one when $\omega = 0$. However, when $\omega = 4$ its generation frequency is the same as oscillation frequency of the cylinder. This shows that at a certain frequency, vortex generation is totally different and it does not depend on its natural shedding frequency[4].

Figure 4 shows the relation between frequency and amplitude of the lift coefficient. It is shown that at frequencies of about 4 the amplitude of oscillation is very small and the circulation around cylinder becomes very slow. Figure 5 depicts the relation between frequency and drag coefficient. It is shown that this coefficient reduces to less than 15% of the non-oscillatory case at frequencies of about 4 r/s.

Figures 6a, 6b, and 6c show frequency responses of the cylinder lift coefficient to its rotational oscillation. In all cases amplitude of forced rotational oscillation is fixed to $\frac{\pi}{4}$.

As shown by this results we can also observe above three different patterns in frequency responses:

• Natural shedding is the same as the case without forced oscillation and its frequency is dominant for $\omega = 1$ and 2 (see Fig. 6a).

• Frequency of forced oscillation is dominant and vortex shedding is under influence of the forced oscillation for $\omega = 3 \sim 6$ (see Fig. 6b).

• Flow around the cylinder is influenced by both natural shedding and forced oscillation for $\omega = 7 \sim 10$ (see Fig. 6c).

It is difficult to find a specific transfer function between rotational oscillation and lift coefficient, because it is under influence of both natural shedding and forced oscillation. This cause the response to be highly nonlinear and difficult to estimate and analyze. Further investigation and analysis is required to predict the exact response of the flow to the rotational oscillation.

4. CONCLUSIONS

It was shown that the flow around a circular cylinder could be controlled by oscillating it about its longitudinal axis. This oscillation affects the pressure distribution, the force exerted from the flow on the object, and the vortex shedding. The results show that at a certain frequency, the drag coefficient was reduced to 15 percent of the non-oscillatory case, and the amplitude of lift coefficient was also reduced to 10 percent. On the other hand, some other frequencies produced larger values of the lift and drag coefficients than the stationary case. The flow pattern obtained here were classified into three categories: natural oscillation, forced oscillation, and their combination which are obvious from frequency response of lift coefficient. Furthermore, there are phase lag and amplitude attenuation at low frequencies, which vanish at

high frequencies and very low frequencies in the relation between rotation angle and pressure distribution.

REFERENCES

1. Schlichting H., "Boundary Layer Theory," McGraw-Hill, New York, 1960.
2. Tokumaru, P. T. and Dimotakis, P. E., "Rotary Oscillation Control of a Cylinder Wake," J. Fluid Mech. Vol. 224, pp. 77-90, 1991.
3. Hamidi, H. E. and Nakamura Y., "Control of Falling Body with Mathematical Model for Unsteady Force," Trans. Japan Soc. Aeronaut. Space Sci., Vol. 40, pp. 471-483, 1997.
4. Hamidi, H. E. and Nakamura Y., "Numerical Study on Unsteady Force Exerted on Circular Cylinder with Rotational Oscillation," The 30th Fluid Dynamics Conference, Okayama, Japan, 1998.
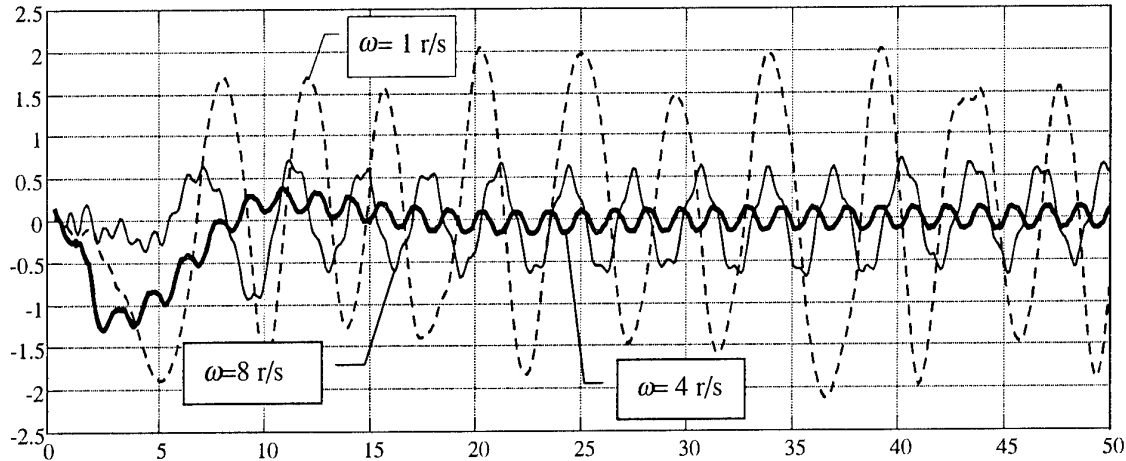
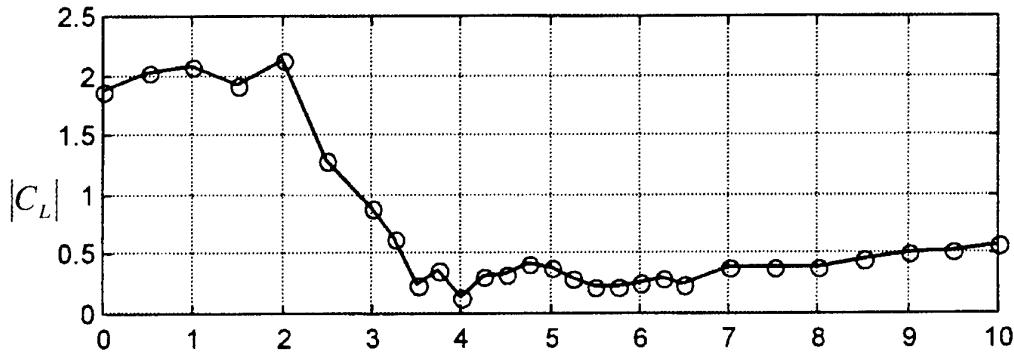Fig. 3 Time histories of lift coefficient in three different oscillation frequencies

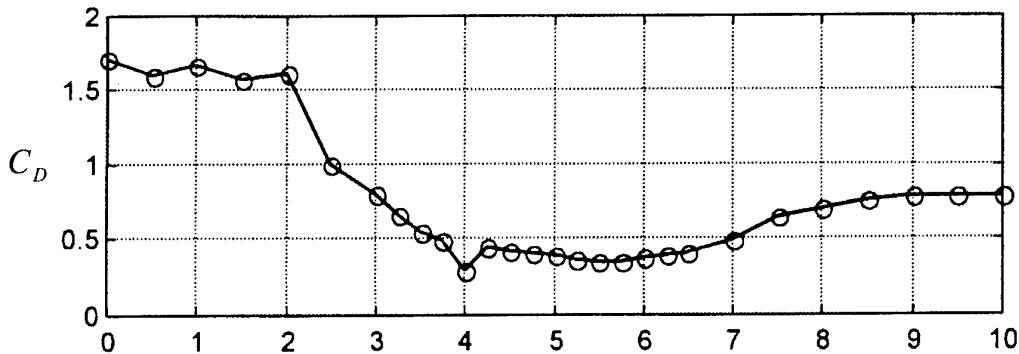Fig. 4 Relation between frequency and amplitude of lift coefficient

Fig. 5 Relation between frequency and drag coefficient

Fig. 6a Frequency Response of lift coefficient for ω=1 and 2

Dominant Natural Shedding in ω=1 and 2

Fig. 6b Frequency Response of lift coefficient for ω=3-6

Dominant Frequencies equal to forced oscillation frequencies for ω=3-6

Fig. 6c Frequency Response of lift coefficient for ω=7-10

Dominant Natural Shedding in ω=7-10

Peaks at Frequencies equal to forced oscillation for ω=7-10

3F7   INVISCID FLOW SIMULATION USING A CARTESIAN GRID METHOD

Paulus R. Lahur* and Yoshiaki Nakamura**

Nagoya University, Furo-cho. Chikusa-ku. Nagoya 464-8603, Japan

Key Words: Aerodynamics, Fluid Dynamics

ABSTRACT

A method to treat inviscid flow computation using Cartesian grid is being proposed in this study. The advantages of Cartesian grid methods include automatic and fast grid generation as well as the ability to treat realistic geometries. This means that for industrial applications, CFD-based analysis using Cartesian grid can be carried out in a time-efficient manner, without requiring the user to be an expert in grid generation. These merits are due to the non-body-fitted characteristic, that is, the grid intersects with solid surface. In comparison with Cartesian grid, more commonly used grids today are of body-fitted type, such as tetrahedral-based unstructured grid and block-structured grid. The present study is concerned with improving the Cartesian grid method and overcoming its weakness. One of the problems is the case with thin and sharp geometry, and the cell containing such geometry is split into two in this research. A solution-based grid adaptation using anisotropic Cartesian grid has also been developed in this study. The grid cells are either merged or refined in a certain direction such that their aspect ratios match local flow gradient. Thus a flow feature can be resolved using significantly fewer cells compared with the isotropic approach. Furthermore, a method to treat moving body using Cartesian grid is being developed.

1. INTRODUCTION

Today CFD has progressed into a versatile tool in analysis and design of any objects that make use of fluid dynamics. Significant contribution in making CFD a practical tool comes from the exponential progress in affordable computation power and advancement in computational algorithms. However, in many industrial applications, it becomes apparent that CFD needs much work to improve, especially in the field of grid generation. In many practices, not only grid generation is time consuming, but also it requires intensive manual labor. As in other manual operations, results will depend on the expertise of operator and the operation will tend to be costly. Moreover, the results may vary from one operator to the other, and in some cases, errors will be introduced. It is therefore highly desirable to have the method of automatic grid generation that can handle realistic geometry.

In recent years, the level of automation in grid generation has improved significantly, most notably in the cases of tetrahedral-based unstructured grid and Cartesian grid. The latter was chosen as the subject of the present research, because it is relatively unexplored.

Cartesian grid method is a non-body-fitted approach, that is, the grid intersects solid body surface. As a result, a grid cell that intersects the body surface has an irregular shape. Such cell is referred to as cut cell. A grid cell that does not intersect body surface has a regular rectangular shape. It is referred to as fluid cell if it contains fluid, and solid cell if it is inside body. This property allows for fully automatic treatment of complicated geometry. Furthermore, from the point of view of flow solver, the alignment of grid cells with Cartesian coordinate system leads to simplified and accurate flow computation.

This paper discusses three issues related to the effort to improve the Cartesian grid generation process within the framework of inviscid, compressible flow simulation. The first one is concerned with how to handle a type of geometry that may pose a problem in Cartesian grid generation, that is, thin and sharp geometry. It is important for the grid generation to be able to handle all types of geometry in order to be fully automatic. A cell-splitting method is thus proposed here to handle the problem efficiently.

The second part discusses grid adaptation in Cartesian grid, which is a method to improve grid and solution quality by regenerating the grid for a given initial solution. This is an important way to reduce human factor. The method proposed here is unique, because it combines some concepts of unstructured grid with Cartesian grid.

The third part is an attempt to automate grid for the treatment of moving body, that is, when there is a relative movement between solid body and grid.

2. THIN AND SHARP GEOMETRY

Thin geometry poses a problem in Cartesian grid, because there is a possibility that a grid cell contains more than two flow regions inside it. If not treated properly, this will result in erroneous solution. Although less severe, a sharp geometry may also pose a problem of reduced solution accuracy. As a method, we can continue to refine the problematic cell until the problems disappear, but it will produce a large number of cells.

In this research, cell-splitting approach was adopted instead, because of the small number of cells required. In the method developed here, the portion of body surface inside a cut cell is approximated as a flat panel to reduce data storage. However, this has a side effect: that is, a sharp edge will be effectively truncated. In order to restore the geometrical feature, the cell that contains such edge hsa to be split as well. The split cells are illustrated in Fig. 1. Using this method, it has been found that the problem can be solved effectively and efficiently [1].
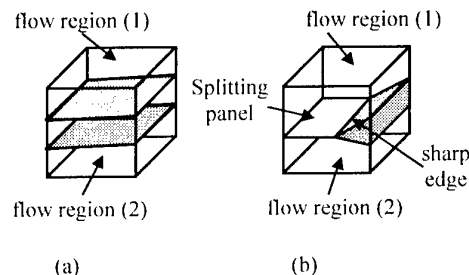

Fig. 1   Cell splitting for (a) thin geometry and (b) sharp geometry.

---

*   Research Associate. Dept. of Aerospace Engineering
** Professor, Dept. of Aerospace Engineering

A new grid refinement method has also been incorporated in order to increase the grid resolution around curved solid surface, leading to enhanced solution accuracy there.

An SST model is used to demonstrate the effect of treatment, because of its thin supersonic wing. Two computations were carried out. The first one does not perform any treatment, and the second one use both the cell-splitting method and grid refinement. The grid around the body is shown in Fig. 2.
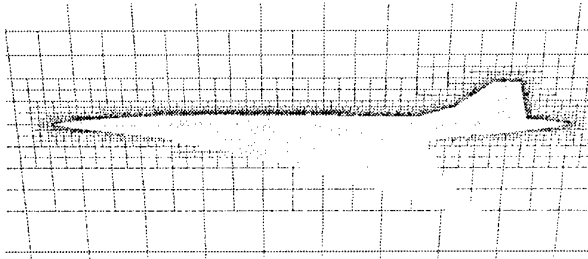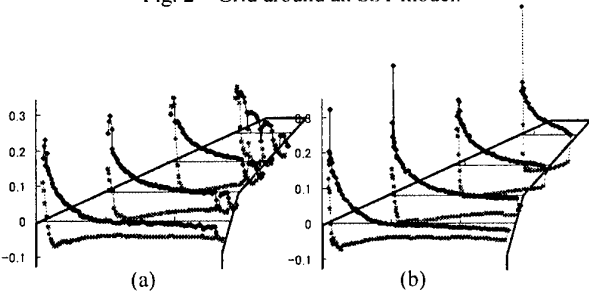

Fig. 2   Grid around an SST model.

Fig. 3   Pressure distribution around SST model. (a) baseline, and (b) cell splitting and geometry-based grid refinement.

The solutions for flight conditions with M=2.4 and α=1.5° are shown in Fig. 3, where it is apparent that the cell-splitting method performs much better. Furthermore, geometry-based grid refinement around the leading edge has reduced the number of cells from 262,056 in the baseline grid to 175,810.

3. ANISOTROPIC CARTESIAN GRID ADAPTATION

Grid adaptation can be regarded as a method to use grid cells efficiently. This can be done by first carrying out computation on an initial grid, and then improving the grid based on the flow solution. As a result, even if an operator made an initially low quality grid, high-quality solution will be obtained eventually.

Grid adaptation is an especially simple task in Cartesian grid, because it allows local grid refinement and coarsening. However, the number of produced cells can be quite large when a cell is refined isotropically, while many flow features such as shock are anisotropic. Such refinement is unavoidable when the data structure employed is octree, which is quite common in Cartesian grid method due to its simplicity and compactness.

In this research, anisotropic grid adaptation is employed instead; that is, the grid can be refined and coarsened in any Cartesian direction, and without any limit on the cell's aspect ratio. To attain such flexibility, an unstructured approach has been taken here.

The procedure usually starts with a rather rough grid, which is generated isotropically. Flow computation is carried out up to a certain degree of convergence, the results of which are used to improve the grid quality at the next cycle. The grid adaptation consists of three processes: grid coarsening, refinement, and smoothing [2].

A modified second finite difference is used to compute adaptation parameter G, as in Eq. 1, where only x direction is shown for simplicity.

$$(G_i)_x = (\Delta x_i)^L \left| (Q'_{ij})_{x,max} - (Q'_{ij})_{x,min} \right| / \Delta x_i \quad (1)$$

where Q'_{ij} is first difference of flow solution between cell i and its neighbor cell j sharing the common cell interface. Δx is the cell size, and L is a length scale to determine the balance of refinement between small and large cells.

Equation 1 is a modified version of the equation to compute second derivative. One of the modifications is the use of length scale L in order to control whether more refinement should be carried out for small cells or large cells. A larger value of L will result in more refinement of large cells, and tend to produce more cells. On the other hand, a smaller value of L will result in more refinement of small cells, which will tend to exhibit larger spatial variation in cell size. The other modification is the use of maximum difference instead of the difference between the right and left interfaces of a cell in a certain direction. Such modification is considered because a Cartesian grid cell in this study may have several neighbors on one face, which in general will have arbitrary locations and sizes. The use of maximum difference tends to enforce refinement on cells with many neighbors, which is a highly desirable property.

Having computed adaptation parameter G for all cells in all three directions, the threshold values for grid coarsening and refinement, T_{low} and T_{high}, respectively, are computed by using Eqs. 2 and 3.

$$T_{low} = MAX[0, (mean(G) - R_{low} \cdot sdev(G))] \quad (2)$$

$$T_{high} = mean(G) + R_{high} \cdot sdev(G) \quad (3)$$

where R_{low} and R_{high} are user-defined parameters regarding thresholds of coarsening and refinement. The mean and sdev in those equations are the mean value and standard deviation of G, respectively.

Grid coarsening is performed by removing the interface between cell i and its neighbor cell j if the values of parameter G for both cells are less than the lower threshold, as expressed in the following.

$$(G_i)_k < T_{low} \text{ and } (G_j)_k < T_{low} \quad (4)$$

where subscript k is the component in the direction normal to the interface.

Grid refinement is performed by dividing a cell into two equal parts in any direction of x, y, and z coordinates, when the value of adaptation parameter G is higher than the upper threshold value, T_{high}. Thus, it is possible to refine a cell in more than one direction, as shown in Fig. 4. For practical reasons, limitations are imposed on the minimum cell size and the maximum number of cells in the present method.

After a grid is coarsened and refined, grid-smoothing operation is applied to avoid degradation in grid quality. Here the criterion for grid smoothness is that there exist at most two neighboring cells along any of x, y, and z directions on a cell face. If this condition is violated, the cell is divided into two cells in the direction with too many neighbors. The division is carried out such that the resulting cells match their neighbor's boundaries.

A standard ONERA M6 test case is computed here. The flow condition is M=0.84 and α=3.06°. Two adaptations are carried out, and the initial and adapted grids are shown in Fig. 5 and the corresponding pressure distributions in Fig. 6, along with experimental data.
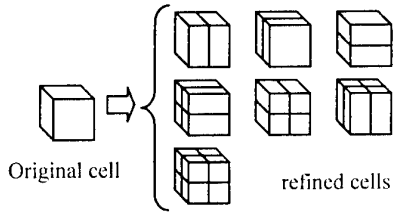

Fig. 4   Cell refinement.

It is evident from the results that the grid adaptation method successfully captures the flow features, including leading edge suction and the two shocks on the upper surface of the wing, as well as smoothly varying pressure distribution. The discrepancies in shock location and sharpness are acceptable, since the flow model used here is inviscid.

A measure of the method's efficiency is shown in Fig. 7, where the number of cells resulted from this method is compared to that of isotropic grid adaptation. Here it is shown that if the computation is carried out using isotropic grid adaptation, the cells needed would be 2.5 times as many.

In terms of computational storage, since the anisotropic adaptation method employs unstructured approach, it requires 400 bytes of memory per cell, whereas the isotropic adaptation 344 bytes. However, the total memory required by the anistropic adaptation method is still 2.2 times less than the isotropic one.
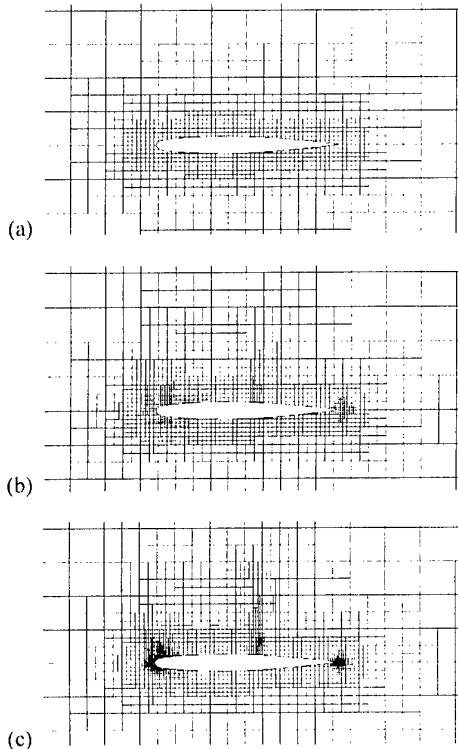

(a)

(b)

(c)

Fig. 5   Grid around ONERA M6 wing at 44% wing span:
(a) initial, (b) 1st adaptation cycle, (c) 2nd.
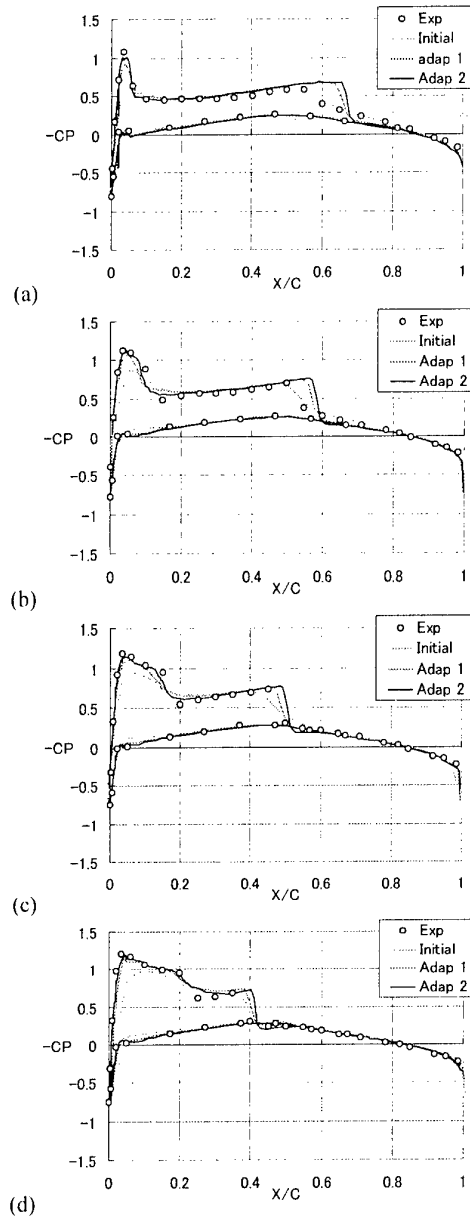

(a)

(b)

(c)

(d)

Fig. 6   Comparison of pressure distribution around ONERA M6 wing with experimental data: (a) 20% span, (b) 44%, (c) 65%, and (d) 80%.
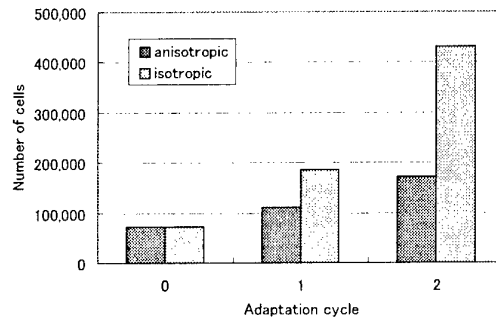

Fig. 7   The number of cells as a function of adaptation cycle.

3. TREATMENT OF MOVING BODY

In Cartesian grid method the grid remains stationary as a solid body moves across the grid. In contrast, for the case of body-fitted type of grid, such as tetrahedral-based unstructured grid and overlapped structured grid, body movement requires movement of grid cells in a region surrounding the body. Thus, for a given time step. Cartesian grid requires less amount of computation in order to update the geometrical data of grid cells, since only cells on the body surface are modified, while the rest of the grid cells are left unaltered.

In this research, we are attempting to extend the grid generation method for stationary body to handle moving body. At present, efficient computation on true 3D computation of moving body has not been carried out on Cartesian grid.

The problems Cartesian grid method has are unique when compared to those of body-fitted approach. The most obvious one is the problem of "appearing" or "disappearing" cell. The first case occurs when a solid cell becomes a cell that contains fluid at the next time step, and the second case is the reverse of the first one. This does not satisfy conservation of fluid mass, momentum and energy. In order to eliminate this problem, Bayyuk et al. has introduced a cell merging method [3]. In this method, potentially problematic cells are merged with their appropriate neighbor cells during a time step, such that the merged cells remain to be cut cells. After the time step is completed, the merged cells can be restored into their constituent cells. This approach is illustrated in Fig. 8.
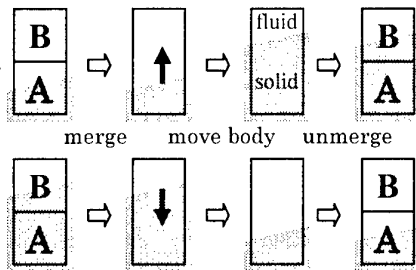

Fig. 8 Cell merging method to treat the problem of "appearing" and "disappearing" cells.

The problem now is how to find appropriate candidates for cell merging. Bayyuk et al. has implemented an approach in 2D. In this research, we are currently developing such implementation in 3D [4].

Shown in Fig. 9 is the density distribution for a 2D test case for two capsules moving in the opposite direction at M=2 in a tunnel. Although the test case is 2D, the flow computation itself is 3D. The computational domain is divided uniformly into 384x112x1 cells.

The flow solution shows that the flow features can be reasonably captured. However, the overall computational efficiency is still low. This is because the time step is limited by the size of cut cells, since the body is not allowed to move beyond merged cut cells. Further investigation is being underway to overcome this weakness.

4. CONCLUSIONS

Methods to improve inviscid, compressible flow computation on Cartesian grid have been proposed in this paper. Three issues have been discussed.

The first is a cell-splitting method, which is proposed to handle thin and sharp geometry. Together with local grid refinement, the method is shown to be effective and efficient in handling such problem.

The second is anisotropic Cartesian grid adaptation, which is shown to be significantly more efficient than isotropic Cartesian grid refinement, both in terms of the number of cells and the total memory required.

The last issue is concerned with moving body. Although the flow solution is quite reasonable, computational efficiency needs to be improved, particularly by reducing computation time.
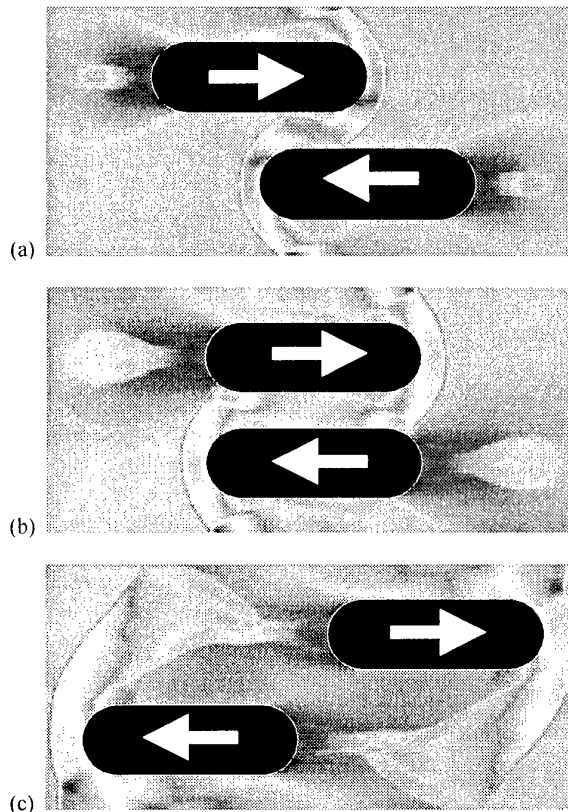

Fig. 9 Density distribution for the case of moving 2D capsules in a tunnel. (a) 1.1 time units, (b) 2.0, and (c) 3.7.

REFERENCES

1. Lahur, P.R. and Nakamura, Y., "A Cartesian Grid Generation Method Considering a Complicated Cell Geometry at the Body Surface," Trans. Japan Soc. Aero. Space Sci., Vol. 43, No. 139, pp. 8-15, 2000.
2. Lahur, P.R. and Nakamura, Y., "Anisotropic Cartesian Grid Adaptation," AIAA Paper 2000-2243, 2000.
3. Bayyuk, S.A., Powell, K.G., and van Leer, B., "A Simulation Technique for 2-D Unsteady Inviscid Flows around Arbitrarily Moving and Deforming Bodies of Arbitrary Geometry," AIAA Paper 93-2291-CP, 1993.
4. Lahur, P.R. and Nakamura, Y., "Simulation of Flow around Moving 3D Body on Unstructured Cartesian Grid," AIAA Paper 2001-2605, 2000.

3F8

Numerical Study of Stable Flame Holding During the acceleration of a Projectile in a Ram Accelerator

Ciheng Zhang *, Shiro Taki **

Division of Mechanical Engineering System, Hiroshima University
1-4-1 Kagamiyama Higashi-Hiroshima 739-8527 Japan
Email: zhang@mec.hiroshima-u.ac.jp

Key words: Flame holding, shock waves, boundary layer, ram acceleration

Abstract

The numerical simulation is carried out for the investigation of flame holding when the projectile moves with Mach number 4.6 in the ram accelerator. Finite difference method is used to get the solution of Navier-Stokes equations. The solution adaptive multilevel grid refinement method is used in present calculation and the highest-level grids ($37 \mu m$) are employed in the flame and the boundary layer area. The results of boundary layer, flame and shock waves are obtained. As the simulation shown, the separation of boundary layer on the front part of the projectile is observed to originate at the place where the reflected shock impinges on the surface. The flame propagates toward incoming flow along the boundary layer, depending on the choking at the back of the projectile. Then the flame front is stable at the place located 8mm distant from the shoulder. In the meantime the strong shock waves are formed near the wall where the fluid is expanded, but the pressure isn't so high near the projectile base to produce thrust

1. Introduction

A ram accelerator with a rectangular bore has been operated under low pressure (P<1.0MPa) in Hiroshima University named as HURAMAC, where the rail guides the projectile on the sidewall without fins, allowing two-dimensional flow over a projectile. This makes to simplify the computation model based on the condition of HURAMAC.

Generally a projectile moves faster than Mach 3 before it enters the combustible gas mixture in the ram acceleration tube. The thermally choking makes the pressure increase high when combustion takes place following the projectile. As it is known from the results of many experiments [1,2,3,4,5], the range of the start shot is very narrow, so the selection of the mixture composition is crucial. Obviously the location of flame front and the amount of heat release are the important factors to the ram acceleration performance. As our research before [6,7,8], we observed that the flame can be attached on the projectile surface and spreads widely, results in a thermal choke behind it.

According to the ram acceleration concept [9], the flame is expected to hold near the projectile base. Obtained from our simulation result [7] we found that the boundary layer on the projectile surface works as flame holding in the high-speed stream. If the flame front locates behind the shoulder of projectile, the ram accelerator is considered to run effectively. However it is also possible that the flame propagates to the front part along the boundary layer. In this situation the leading shock will be enhanced, so that leads to the reduction of thrust or even the ram acceleration unstart. The present simulation is carried to investigate the flame propagation, shock wave movement and the interference with the boundary layer. The flame stabilization is analyzed for the operation of ram accelerator in choking mode

2. Numerical model

The flow and geometric parameters are chosen to reproduce the experimental results of Hiroshima University ram accelerator, shown in Fig.1. The description of a two-dimensional flow field of HU ram accelerator is done corresponding to the distinguishing feature of the rectangular bore ram acceleration tube (15 × 20mm) and quasi
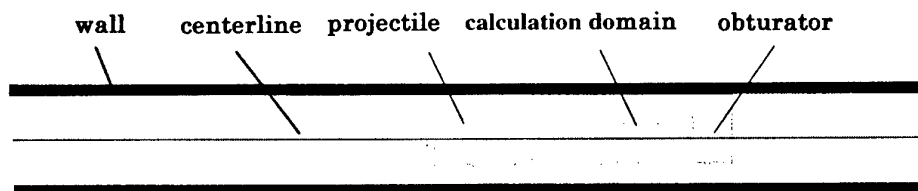

Fig.1　The present calculation domain

takes place following the projectile. As it is known

two-dimensional projectile. The domain on only

one side of the projectile of symmetry has been computed. The no-slip condition is employed at the interface between the fluid and the solid objects.

The initial condition is given considering a projectile flying (V=1400 m/s) in the ram acceleration tube. The projectile has 4 gram, 22.3 °, 33 mm long wedge, 53 mm long body. The composition of gas mixture is methane and oxygen diluted by CO2 (CH4+2O2+5.0CO2). The pressure and temperature of gas mixture filled in the ram acceleration tube are 3 atm and 293 K, respectively. A high temperature (2000K) region is assumed being formed near the projectile base at the beginning of simulation (t=0). A small obturator (height=8 mm) is employed in present simulation to perform the choking effect.

3. Governing equations

For the calculation of the combustion flow field around a projectile in the ram accelerator, the Navier-Stokes equations and species conservation equations are employed to supersonic flow with combustion. The conservation equations can be written in vector form as equations (1)-(4).

1) The conservation of mass

$$\frac{\partial \rho}{\partial t} + \nabla \cdot (\rho v) = 0 \tag{1}$$

2) The conservation of momentum

$$\frac{\partial v}{\partial t} + v \cdot \nabla v = -\frac{1}{\rho}(\nabla \cdot P) \tag{2}$$

3) The conservation of energy

$$\rho \frac{\partial e}{\partial t} + \rho v \cdot \nabla e = -\nabla \cdot q - P : (\nabla v) \tag{3}$$

4) The conservation of chemical species

$$\frac{\partial Y_i}{\partial t} + v \cdot \nabla Y_i = w_i - \frac{1}{\rho}[\nabla \cdot (\rho Y_i V_i)] \tag{4}$$

Where e, P, ρ and v denote the specific total energy, the pressure tensor, the density and the velocity vector, respectively. Y_i, V_i and w_i are the mass fraction, the diffusion velocity vector and the production velocity of species i, respectively.
The diffusion equation of species is

$$\sum_{j=1}^{N} \frac{X_j}{D_{ij}}(V_i - V_j) = -\frac{\nabla X_i}{X_i}, \quad (i = 1, \cdots, N) \tag{5}$$

The pressure tensor is

$$P = \left[p + \frac{2}{3}\mu \nabla \cdot v\right]U - \mu[(\nabla v) + (\nabla v)^T] \tag{6}$$

where, μ is the coefficient of viscosity and U is the unit tensor.
The heat flux is calculated by

$$q = -\lambda \nabla T + \rho \sum_{i=1}^{N} h_i Y_i V_i \tag{7}$$

The thermally perfect gas is assumed, then the state equation is written as

$$p = \rho R^o T / \overline{M} = \rho R^o T \sum_{i=1}^{N} Y_i / M_i \tag{8}$$

But the specific heat, the enthalpy and the entropy are approximated by polynomials of the temperature as follows:

$$c_{pi} = a_{i1} + a_{i2}T + a_{i3}T^2 + a_{i4}T^3 + a_{i5}T^4 \tag{9}$$

$$\frac{h_i}{RT} = \left[a_{i1} + \frac{a_{i2}}{2}T + \frac{a_{i3}}{3}T^2 + \frac{a_{i4}}{4}T^3 + \frac{a_{i5}}{5}T^4 + \frac{a_{i6}}{T}\right] \tag{10}$$

$$\frac{s_i}{R} = a_{i1} \ln T + a_{i2}T + \frac{a_{i3}}{2}T^2 + \frac{a_{i4}}{3}T^3 + \frac{a_{i5}}{4}T^4 + a_{i7} \tag{11}$$

The reaction kinetic model employed in present paper is the one proposed by Seshadri and Peters [10], which consist of thirty-five chain reaction steps and sixteen chemical species. The burning velocity of CH_4-O_2-CO_2 mixture is examined through the computation of the planar flame propagation [6] using this model. The accuracy is validated by comparison with experimental data.

4. Numerical methods and grid generation

Finite difference methods are used to get the solution of Navier-Stokes equations in the computational region. Time split method is used to integrate the terms in the conservation equations. The hyperbolic term is solved by the explicit MacCormack method, while the implicit Lomax-Baily method is employed to solve stiff chemical reaction equations. The viscosity term is integrated by the two-step method.

Square grids are employed on all computation regions. Because the combustion process is of very fast chemical reactions, the parameters vary greatly with time and space. Very fine mesh is approached to have a high order spatial accuracy. In present simulation, the solution adaptive multilevel grid refinement method is used; the elementary mesh size is 1 mm. The fine mesh (0.11 mm) is used to capture the shock wave and the highest-level grids (37 μm) are concentrated on the flame and boundary layer area. The array of the high-level grids is reformed every time after finishing the calculation of the next low-level grids, corresponding to the change of pressure, temperature and chemical species distribution in the computation region.

5. Results and analysis

The numerical simulation is performed for the flight velocity of 1400 m/s (Ma=4.6). The flame/boundary layer and shock/boundary layer

interactions are observed until the stable solution is achieved. The results are shown from 70 μ s to 140 μ s after the fluid begins to flow in.

against the wall and concentrate into one single shock. Behind the shoulder the strong shock is produced by the heat release. But high pressure is

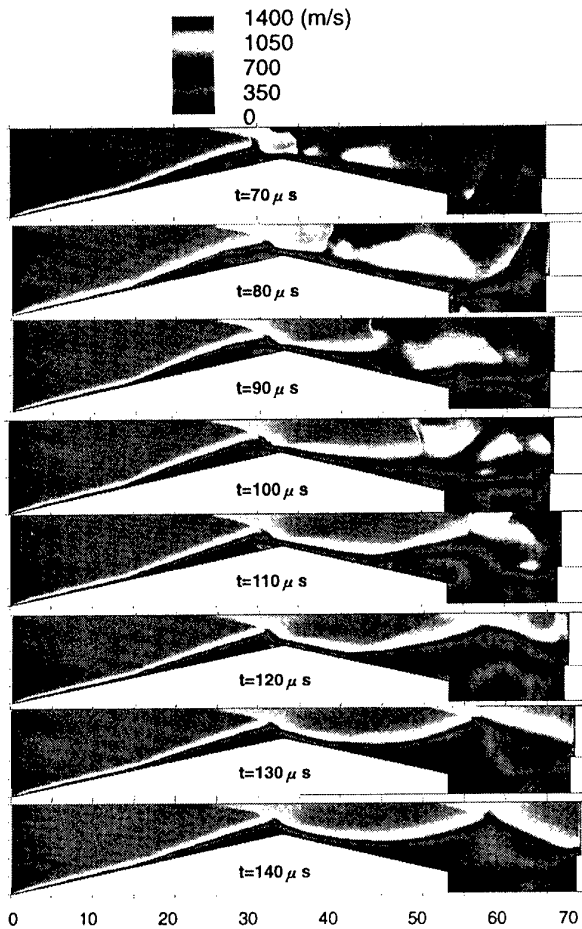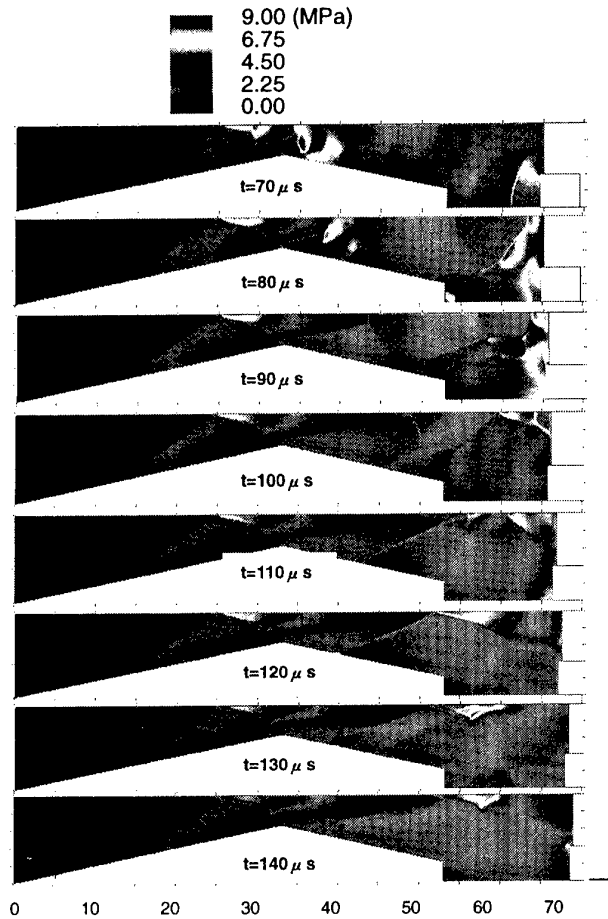Fig.2 Distribution of velocity in sequence of time.

Fig.3 Distribution of pressure in sequence of time.

The calculation result of velocity distribution is shown in Fig.2. The boundary layer near the projectile is formed when compressible gas passes over it. The separation of boundary layer on the front part of the projectile is observed to originate at the place where the reflected shock impinges on the surface. Although this may happen at the inlet of ram acceleration tube in the experiment, this problem is met in present simulation when the supersonic stream begins to flow in the diffuser. We also observed that the boundary layer would be reattached on the plane when the reflected shock moves farther downstream.

Because of the existence of the boundary layer separation on the projectile surface, two oblique shocks are induced: the first shock from the projectile head and the second one at the reattachment location of the boundary layer separation, as Fig.3 shown. These two shocks hit

only formed near the wall and it isn't utilized as thrust acting on the projectile.

The combustion field is shown by the distribution of the mass fraction of species OH in Fig.4. It is clearly seen that the flame is not only kept at the back of projectile but also attached on the projectile surface. The boundary layer becomes thick and the flow is disturbed in the burning state, as Fig.5 of flow line shown. With the advance of flame front toward incoming flow, the flame surface area increases, results in more heat release. Finally the shape of the flame front is stable at the place located 8 mm distant from the shoulder. It is also found that the vortices are produced in the boundary layer and the tail stream. The turbulent combustion takes place where the eddy stream is formed.
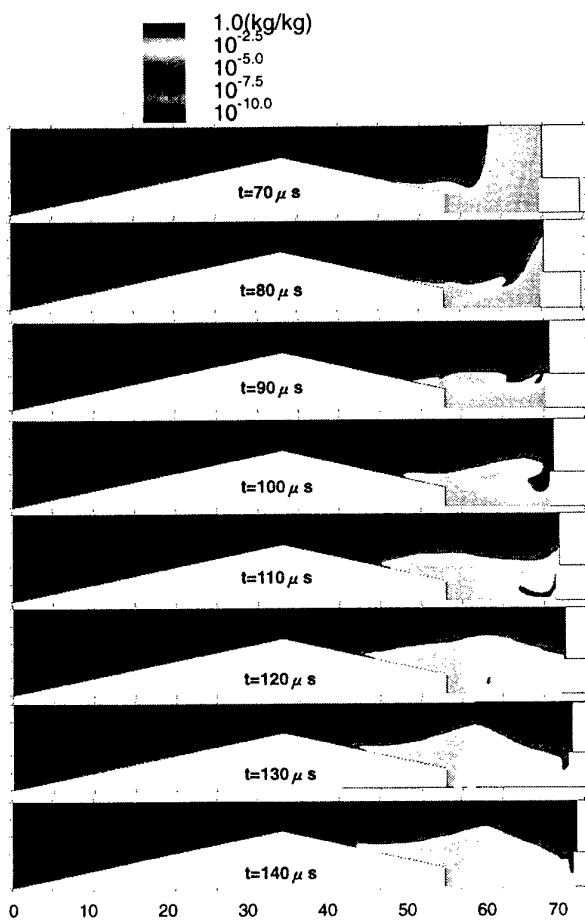
Fig.4 Distribution of mass fraction of radical OH in sequence of time.

6. Conclusion

The simulation of flame holding in the ram accelerator is carried to study the interference among the flame, the shock waves and the boundary layer. The separation of boundary layer on the front part of the projectile is observed at the initial time when the supersonic fluid begins to flow in. Oblique shock is formed at the reattachment location of the boundary layer separation. It is found that the flame front is stable

in the rear part of the projectile when it flies in the velocity of 1400 m/s. The strong shock waves are formed near the wall where the fluid is expanded. The turbulent combustion is observed as many vortices are formed in the boundary layer.

References

1. Higgins AJ, Knowlen C, Bruckner AP: An investigation of ram accelerator gas dynamic limits, AIAA paper 93-2181
2. Chang X, Higgins AJ, Schultz E, Bruckner AP: Operation of quasi two-dimensional projectiles in a ram accelerator, J. Prop Power 13:802-804
3. Giraud M, Legendre JF, Henner M: RAMAC in subdetonative propulsion mode-State of the ISL studies, Ram Accelerators, Springer-Verlag, Heidelberg, pp65-77
4. Sasoh A, Hirakata S, Ujigawa Y,Takayama K: Operation tests of a 25-mm-bore ram accelerator, AIAA paper 96-2677
5. Liu S, Bai ZY, Jian HX, Ping XH, Bu SQ: 37-mm bore ram accelerator of CARDC, Ram Accelerators, Springer-Verlag, Heidelberg, pp119-122
6. Zhang C, Taki S: Numerical Study of Shock Induced Ignition and Combustion in a Two Dimensional Ram Accelerator, Fourth International Workshop on Ram Accelerators, France, 1999
.. Zhang C, Taki S: Numerical Study of the usage of an ignition tube for successful starting of the ram accelerator, AIAA 2000-3237
8. Zhang C., Taki S: Numerical study of influence of boundary layer on the combustion flow field around a projectile in a ram accelerator, Proceedings of 77th Fluids Engineering Conference, Japan, 1999 (in Japanese)
9. Hertzberg A, Bruckner AP, Bogdanoff, DW: Ram accelerator: A new chemical method for accelerating projectiles to ultrahigh velocities, AIAA J 26:195-203
10. Seshadri K, Peters N: The Inner Structure of Methane-Air Flames, Combustion and Flame, 81, pp96-118(1990)
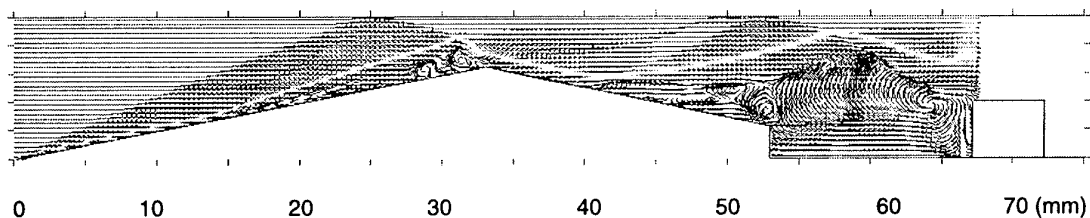
Fig. 5 Flow lines around the projectile (t=120 μ s)

3F9

Optimization of Flapping Wing Motion

Keiichi Ito* and Shinji Suzuki**

*University of Tokyo, Dept. of Aeronautics and Astronautics, 7-3-1Hongo, Bunkyoku, Tokyo

**University of Tokyo, Dept. of Aeronautics and Astronautics, 7-3-1Hongo, Bunkyoku, Tokyo

Key Words: Aerodynamics, Unsteady Flow

Abstract

This paper presents a design method for improving the performance of flapping wings. A Vortex Lattice Method is employed to model a finite-span flapping wing. The flapping wing model investigated in this paper is a rigid rectangular-planform plate with two degrees of freedom, i.e. pitching and heaving. An optimization is performed to find out an optimum combination of flapping frequency, flapping amplitudes, and coupling between pitching and heaving for maximum efficiency for a given thrust. Genetic Algorithms and Sequential Quadratic Programming codes were employed in the optimization. A function approximation using Neural Network is made to improve computational speed.

Nomenclature

A_{ij}, B_{ij}	= influence coefficient to the control point
$\tilde{A}_{ij}, \tilde{B}_{ij}$	= influence coefficient to the quarter chord
AR	= aspect ratio
c	= wing chord
ea	= elastic axis (center of pitch) location
h	= panel vertical distance
L	= lift as in wind tunnel coordinate
D	= drag as in wind tunnel coordinate
t	= time
U	= free-stream velocity

q	=pitch rate
S	= wing area
$\vec{V}$	= velocity vector
x, y, z	= wing coordinates with y along elastic axis
x_i	= x-coordinate of control point
Γ	= vortex or circulation
Γ_b	= bound vortex
Γ_w	= wake vortex
θ	= pitch angle
ρ	= air density
ϕ	= potential function

Introduction

Recently, flapping wing flight has attracted considerable attention partly due to the increase in interest towards Micro Air Vehicles (MAVs). In the past years, there has been a fairly good number of research concerning the mechanics and aerodynamics of flapping wings. However, few literatures have addressed the problem of designing an optimal flapping wing. Computational tools for designing a flapping wing with desired performance are needed. This paper will present advances towards such objectives. Here, Vortex Lattice Method was employed to model the aerodynamic force exerted to a rigid flapping wing. The coupling of heaving and pitching motion were optimized using a Genetic Algorithms code developed by Houck et al. Inertial forces due to the mass and geometry of the wing are not considered in this paper.

Vortex Lattice Method

The VLM represents the wing as a planar surface on which a grid of vortex lattices is superimposed. The velocities induced by each vortex lattice at a specified control

*Graduate Student, Department of Aeronautics and Astronautics

**Professor, Department of Aeronautics and Astronautics

point are calculated using the law of Biot-Savart. A summation is performed for all control points on the wing to produce a set of linear algebraic equations for the vortex strengths that satisfy the condition of no flow through the wing, i.e. the tangential condition (at the control points). A few governing equations are in order. For an irrotational flow, the velocity may be expressed in terms of potential function

$$\vec{V} = \nabla \phi \qquad (1)$$

In incompressible flow, the continuity equation is

$$\nabla \cdot \vec{V} = 0 \qquad (2)$$

Thus,

$$\nabla^2 \phi = 0 \qquad (3)$$

Another condition that has to be satisfied by the solution is Kevin's theorem, namely, that there is no net change in the circulation in the field at any time step, or

$$\frac{d\Gamma}{dt} = 0 \qquad (4)$$

In this research, the model, which satisfies these four equations, consists of panels having a constant bound vortex in each quarter chord of a rectangular cell. A control point is located in each cell at the three-quarter point of centerline. As stated previously, if the incident air velocity to the control points are known, a linear algebraic system of equation can be set up to solve for the unknown bound vortex strengths at every time step. The vortex strengths Γ s determined from the past time steps are shed behind the wing to form the wake. In the present model, one panel is used chordwise to represent the bound vortices and the wake is planar, and constrained in the same plane as that of the wing as shown in Fig. 1. The wing is a rigid rectangular-planform plate with two degrees of freedom, i.e. pitching with respect to y-axis and heaving along z-axis. The simplicity of the model works in favor of the optimization process discussed in the next section. The bound vortex strengths Γ_b s are determined from the following equation.
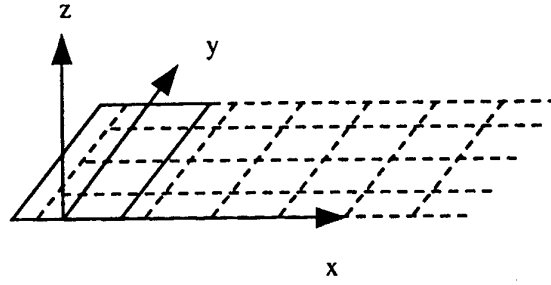

Fig. 1

$$-U \sin\theta - qx_i + \frac{\partial h_i}{\partial t}\cos\theta =$$

$$\left[A_{ij} \right] \begin{bmatrix} \Gamma_{b_1} \\ \vdots \\ \vdots \\ \Gamma_{b_n} \end{bmatrix} + \left[B_{ij} \right] \begin{bmatrix} \Gamma_{w_1} \\ \vdots \\ \vdots \\ \Gamma_{w_m} \end{bmatrix} \qquad (5)$$

Once Γ s are determined, the pressure difference can be determined using unsteady Bernoulli equation as derived by Katz. Then, lift and induced drag can be calculated from the following equations.

$$L = \rho U \sum_{k=1}^{n} \Gamma_{b_k} \Delta y + c \frac{d}{dt} \left(\sum_{k=1}^{n} \Gamma_{b_k} \right) \Delta y \qquad (6)$$

$$D = L\tan\theta + \frac{\rho \left(\sum_{k=1}^{n} W_k \Gamma_{b_k} \right) \Delta y}{\cos\theta} \qquad (7)$$

where

$$\begin{bmatrix} W_1 \\ \vdots \\ \vdots \\ W_n \end{bmatrix} = \left[\tilde{A}_{ij} \right] \begin{bmatrix} \Gamma_{b_1} \\ \vdots \\ \vdots \\ \Gamma_{b_n} \end{bmatrix} + \left[\tilde{B}_{ij} \right] \begin{bmatrix} \Gamma_{w_1} \\ \vdots \\ \vdots \\ \Gamma_{w_m} \end{bmatrix} \qquad (8)$$

$$+U \sin\theta + qx_i - \frac{\partial h_i}{\partial t}\cos\theta$$

When D is negative, it means the flapping is producing thrust. Power is computed from the following equation

$$P = L\dot{h} + M_p\dot{\theta} \qquad (9)$$

where M_p is pitching moment about ea.

Optimization procedure

Floating Point Genetic Algorithm was employed to find maximum efficiency (i.e. C_T/C_P) with respect to design variables such as flapping frequency, phase angle between heaving and pitching, and elastic axis location. By floating point, it is meant that the genes are not expressed in terms of binary codes but as decimal base real valued variables.

In order to save computational time, Radial Basis Function (which is a form of Artificial Neural Network) was employed to model the mapping between the design variables and the flapping efficiency. Instead of computing aerodynamic forces for every change in the design variables, RBF is trained with a set of data obtained by calculating the aerodynamic forces with respect to the design variables. Once the RBF was trained, it was used in the optimization procedure to obtain solution. This way one can reduce quite substantially the number of aerodynamic forces calculated and the saving in time.

Results

Numerical computation of thrust and efficiency was performed based on the simple model described previously. The following values were used in the calculation unless specified otherwise.

ea	= 0.25
h	= chord length
S	= 0.075 m^2
AR	= 3
U	= 1 m/s
ρ	= 1 kg/m^3

Fig. 2 to Fig.5 show the average thrust and average efficiency with respect to two design variables. Fig. 2 shows the thrust at various flapping frequencies and phase differences (here, denoted as phi1). Fig. 3 shows the flapping efficiency with respect to the flapping frequency and phase difference between heaving and pitching. Likewise, Fig. 4, and 5 show thrust and efficiency with respect to phase difference between heave and pitch and elastic axis location. Efficiency is defined as the ratio between thrust coefficient and power coefficient, i.e. C_T/C_P. Fig. 6 is a carpet plot version of Fig. 3 and Fig7 is the RBF reconstruction of Fig. 6. Five uniformly spaced data was taken along each axis. Therefore total of 25 combinations of

phase difference and flapping frequency were used to train the RBF. Using this RBF model, GA was employed to find the peak, i.e. the maximum of efficiency. Table 1 compares two methods of optimization. One is the method just described and the other is the benchmark where aerodynamic forces are calculated every time the fitness function (efficiency in this case) is called. For simplicity only one wing fixed panel was used in this comparison. As can be seen, there is a substantial reduction in computational time.
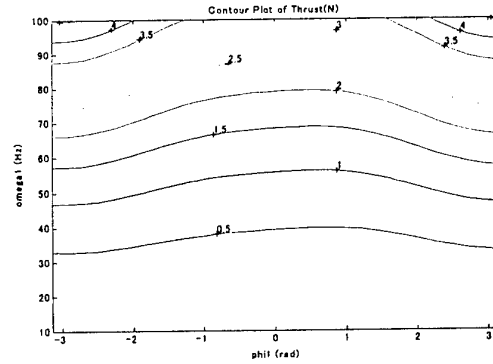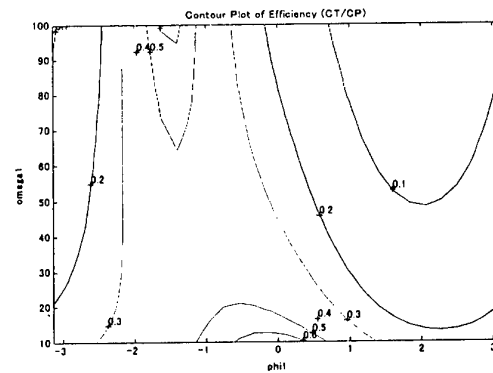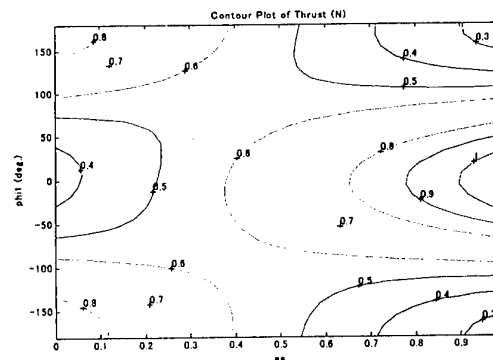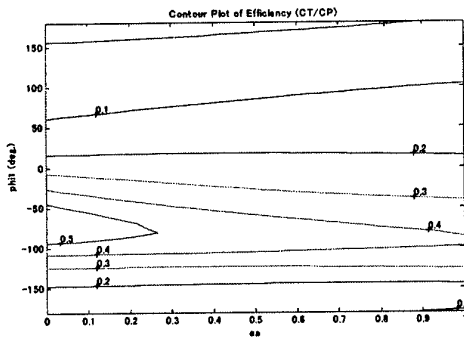

Fig. 2

Fig. 3

Fig. 4

Fig. 5
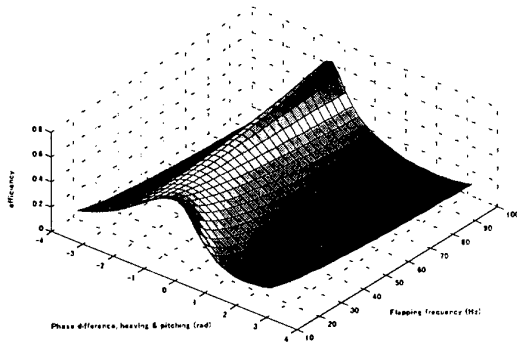
Fig. 6
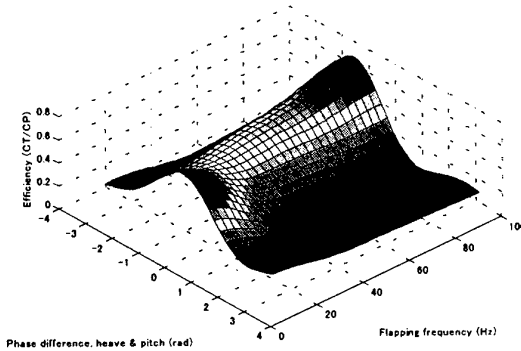
Fig. 7

optimization using RBF	direct optimization
elapsed time = 36 sec.	elapsed time = 377 sec.
solution: freq.=10Hz, phase=-0.111	solution: freq.=10Hz, phase= -0.0644
flapping efficiency= 0.685	flapping efficiency=0.686

Table 1

Conclusions

Optimization of flapping motion was conducted using Floating Point GA. A Neural Network was employed to model the mapping between the design variables and the flapping efficiency. It is observed that substantial reduction in computational time can be achieved using the Neural Network modeling of fitness function in the optimization procedure. In this paper, only the coupling of heaving and pitching were considered. Convergent optimal solutions were obtained with respect to flapping frequencies, phase differences and elastic axis location. A more sophisticated model can be developed to optimize not only the flapping motion but also the planform shape, inertia and elastic properties.

References

1. Azuma, A., "The Biokinetics of Flying and Swimming," Springer-Verlag, pp. 100 – 109.

2. Bisplinghoff, R. L., Ashley, H., and Halfman, R. L., "Aeroelasticity," Addison-Wesley, pp. 260 – 261, 274, 285, 393 – 394, 1955.

3. Haupt, R. L., and Haupt, S. E., "Practical Genetic Algorithms," John Wiley & Sons, pp. 1 – 64, 1998.

4. Houck, C. R., Joines A. J., and Kay, M. G., "A Genetic Algorithm for Function Optimization: A Matlab Implementation," Manual for GAOT (Genetic Algorithms Optimization Toolbox), North Calorina State University.

5. Katz, J., "Method for Calculating Wing Loading During Maneuvering Flight along a Three-Dimensional Curved Path," J. Aircraft, Vol. 16, November 1979, pp. 739 – 741.

6. Levin, D., and Katz, J., "Vortex-Lattice Method for the Calculation of the Nonsteady Separated Flow over Delta Wings," J. Aircraft, Vol. 18, December 1981, pp. 1032 – 1037.

7. Shyy, W., Berg, M., and Ljungqvist, D., "Flapping and Flexible Wings for Biological and Micro Air Vehicles," Prog. Aero. Sci., Vol. 35, 1999, pp. 455 – 505.

8. Vest, M. S., and Katz, J., "Unsteady Aerodynamic Model of Flapping Wings," AIAA J. Vol. 34, July 1996, pp. 1435 – 1440.

FURTHER EXAMINATION OF THE NONLINEAR MATH MODEL FOR TRANSONIC LIMIT CYCLE FLUTTER BY A CONTINUATION METHOD

Hiroshi Matsushita[*], Takafumi Miyata[**], Lasse Engbo Christiansen[***], and Tue Lehn-Schiøler[***]

[*,**] Fukui University, 3-9-1 Bunkyo, Fukui 910-8507, Japan
[***] Technical University of Denmark, Building 309, 2800 Kgs. Lyngby, Denmark

Key Words: Aeroelasticity, Wings and Airfoil Sections, Unsteady Flows

ABSTRACT

This examination improves the two-degrees-of-freedom, finite dimensional, nonlinear math model, which has been modeled and developed by the authors to explain qualitatively every feature of the transonic flutter data of the wind tunnel tests conducted at National Aerospace Laboratory in Japan for a high aspect ratio wing. It enables to explain the subcritical Hopf bifurcation of a limit cycle oscillation (LCO) of transonic flutter, saddle node bifurcation, and an unstable limit cycle. By making use of the continuation method for analyzing the bifurcation nature of the math model, quantitative matching is obtained for the LCO amplitude between the math model and the test results.

1. INTRODUCTION

In transonic regions flutter often takes the form of a limit cycle oscillation (LCO) caused by the nonlinearity of the transonic aerodynamics due to a shock wave moving on the wing surface coupled with the flow separation[1-3]. Recent tests in the transonic wind tunnel at National Aerospace Laboratory in Japan for a high aspect ratio wing have revealed a lot of bifurcation phenomena. Every flutter occurred suddenly as a subcritical Hopf bifurcation, jumping up to large amplitude LCO, while decreasing a dynamic pressure kept LCO continued until a saddle node bifurcation point where the wing stopped to oscillate. In such a way transonic flutter has a hysteresis in LCO occurrence. In between this range, stability boundary was identified which separates the regions into two groups: one going up to LCO and the other going down to equilibrium[4-6].

The authors have developed, by the nonlinear dynamics approach, a two-degrees-of-freedom nonlinear mathematical model, which has fourth order nonlinear terms in the diagonal components of the aerodynamics damping[7]. The nonlinear terms have two sets of free parameters to be determined to fit the test data.

With parameters chosen so far, the model can explain qualitatively the fundamental bifurcation phenomena listed above. Quantitative matching is not yet attained between the math model and the test results, however; mathematically predicted amplitude of LCO is rather smaller than the amplitude analyzed by the test data. Further examination to what extent this model can be improved by optimizing the parameters in the

model, therefore, is necessary. In the following chapters, the authors investigate this problem by conducting parametric study of changing the parameters in the math model making use of a continuation method for analysis of the bifurcation diagram.

2. EXPERIMENTAL OBSERVATION OF BIFURCATON IN TRANSONIC FLUTTER AND ITS NONLINEAR MATH MODEL

2.1 Experimental Observation

Figure 1 shows a wind tunnel model of a high aspect ratio wing. It has a leading edge and a trailing edge control surfaces. They are used for active flutter control research[10]. Basically the wing has a supercritical section
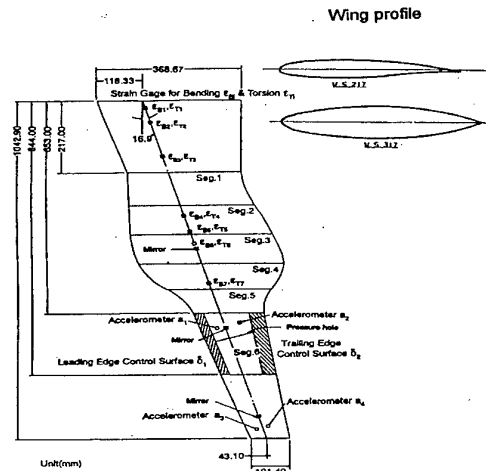

Fig. 1 High aspect ratio wing model

except at an inflated middle part where the wing section is symmetrical and two sets of electric motors are installed. For LCO investigation in the wind tunnel tests, a leading edge control surface is used as a source of excitation and wing response is measured by four accelerometers and seven sets of torsion and bending strain gages, which are fixed at an aluminum spar of the wing.

In the series of wind tunnel experiments at the transonic wind tunnel of the National Aerospace Laboratory in Japan, it was turned out that this wing behaves a typical transonic flutter. The wing has transonic dip phenomena and every flutter has the form of LCO. In each flutter, when the tunnel pressure is increased, the wing jumps up to LCO at a specified (nominal) dynamic pressure as shown at the top chart in Fig. 2. Successive investigation cleared that, even at lower dynamic pressure than the nominal pressure stated above, the wing can be brought into LCO state if it's excited above a certain energy level. Once LCO state is attained, it is kept continuing even after removing the excitation.
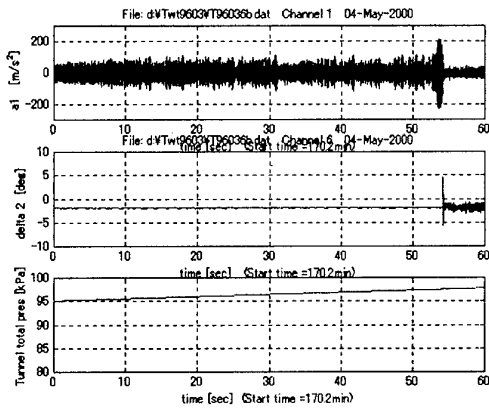
Fig. 2 Time history of nominal flutter occur-
rence during the increase of the wind tunnel
pressure.
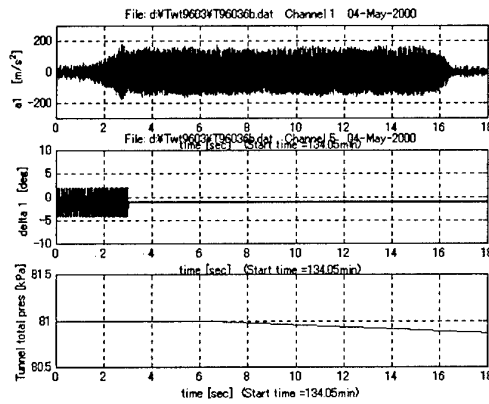
Fig. 3 Quasi-steady decrease of the dynamic
pressure at the saddle node bifurcation

Fig. 4 Bifurcation diagram obtained

Fig. 5 Bifurcation diagram of 2-DOF
nonlinear equation (1)

The LCO thus attained is stabilized again if the tunnel pressure is further decreased as shown in Fig. 3.

Figure 4 summarizes these phenomena found in the tests as a bifurcation diagram where the LCO amplitude is depicted against the dynamic pressure. In this figure the stability boundary, or unstable limit cycle expressed by the crosses, has a significant deviation and the stable region under the boundary is rather narrow. Disturbances around the wing such as turbulence in the wind tunnel flow, the flow separation occurred at the wing surface, etc., may decrease the stable region in the experimentally obtained diagram. This point will be discussed again in Chapter 3.

2.2 Nonlinear Mathematical Model

The first author *et al.* have developed a nonlinear math model in the form of a two-degrees-of-freedom, finite state nonlinear differential equation[7]. Introducing the fourth order nonlinearity in q_i, $i = 1,2$ to the generalized aerodynamic damping terms, they have obtained the following sixth order nonlinear differential equation,
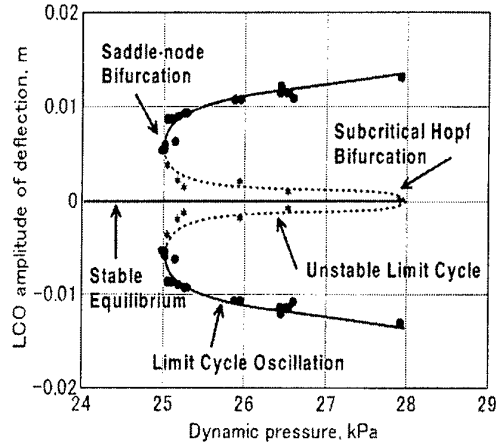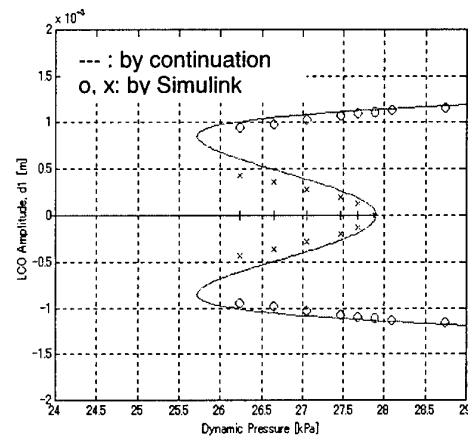
$$\dot{x} = \tilde{A}x; \quad x = [q, \dot{q}, z]^T \in R^6 \qquad (1)$$

where q is the generalized coordinates and z is the augmented variable expressing the unsteady aerodynamic delay. The system matrix comprises,

$$\tilde{A} = \{a_{ij}\} = \begin{bmatrix} 0 & I & 0 \\ -(M-A_0)^{-1}(K-A_2) & -(M-A_0)^{-1}(C-\tilde{A}_1) & -(M-A_0)^{-1} \\ B_a & 0 & -\Lambda \end{bmatrix} \in R^{6 \times 6} \qquad (2)$$

Here, the diagonal components of the aerodynamic damping part $(M-A_0)^{-1}\tilde{A}_1$ have fourth order nonlinear terms such as $(1 + \beta_1 q_1^2 + \gamma_1 q_1^4)a_{33_a}$ and $(1 + \beta_2 q_2^2 + \gamma_2 q_2^4)a_{44_a}$,

where a_{33_a} and a_{44_a} are the aerodynamic damping coefficients for torsion and bending deflection, respectively. The parameters β's and γ's are free parameters to be determined to fit the wind tunnel test data. When the parameters β's and γ's are set to be zero, the equation (1) is reduced to a normal linear flutter equation.

In order to make comparison with the test results, an output equation that relates the state variables in Eq. (1) with the output variables measured in the wind tunnel tests is necessary. Since two sets of measured

and derived variables, acceleration a_1, a_2, velocity v_1, v_2 and deflection d_1, d_2 at two accelerometer positions on the wing are enough for comparison, the output equation will take the form

$$y = Cx; y = [a_1, a_2, v_1, v_2, d_1, d_2]^T \in R^6 \qquad (3)$$

The set of equations (1) and (3) comprises the nonlinear 2DOF math model for transonic flutter.

Nonlinear simulation of solving the equations (1) and (3) was conducted by making use of MATLAB /Simulink software. The coefficients in the math model was set as $\beta_1 = \beta_2 = -0.5$, $\gamma_1 = \gamma_2 = 0.2$ since this set of values is reference one for a typical 1DOF nonlinear differential equation, which gives an LCO solution of a subcritical Hopf bifurcation. For each dynamic pressure the simulation was conducted by changing equal initial conditions for $x_1 (= q_1)$ and $x_2 (= q_2)$ with the other states equal to zero. In Fig. 5 the simulation results in term of the deflection at the accelerometer #1are displayed with circles (◯) and crosses (×). With this method of simulation it was difficult to get the smooth picture at the saddle node bifurcation as shown in the figure.

The Danish authors have applied the continuation method to the math model (1) modifying a computer program package of the method[8]. The package features a fourth order Runge-Kutta integrator with fixed size which is capable of making continuation of limit cycles using Poincaré sections. The continuation method can trace continuously the Poincaré section, even through the unstable limit cycle branch, once at the initial stage LCO amplitude has been captured. They could obtain

the smooth curve in the bifurcation diagram as shown as a solid line in Fig. 5. Both results are almost identical except with a small difference at the unstable limit cycle branch and the saddle node bifurcation area. The former difference will be discussed in the next chapter. Figure 5 has a good correspondence with the test results in Fig. 4 at least qualitatively in that it explains every feature of nonlinear phenomena such as the subcritical Hopf bifurcation, a saddle node bifurcation, and an unstable limit cycle. However figure 5 still has a large difference from Fig. 4 in amplitude of LCO. The math model has one-order small amplitude than the experimental results.

3. PARAMETER OPTIMIZATION BY CONTINUATION METHOD

Christiansen and Lehn-Schiøler studied the effect of the parameters β's and γ's on the bifurcation diagram. Particularly they got the amplitude and the velocity map at the saddle-node bifurcation for each bending parameters (β_1, γ_1) with torsion parameters neglected[8]. Decreasing β_1 gives larger amplitude near the saddle node and also moves it to a higher velocity. γ_1 can be used to adjust the amplitude.

Based on this study, parametric study has been executed to explore the proper values for the parameters in order that the analytical bifurcation diagram comes closer to the experimental one. The constraint of exploring is the condition that the bifurcation diagram should keep the distance of 10 % between the subcritical
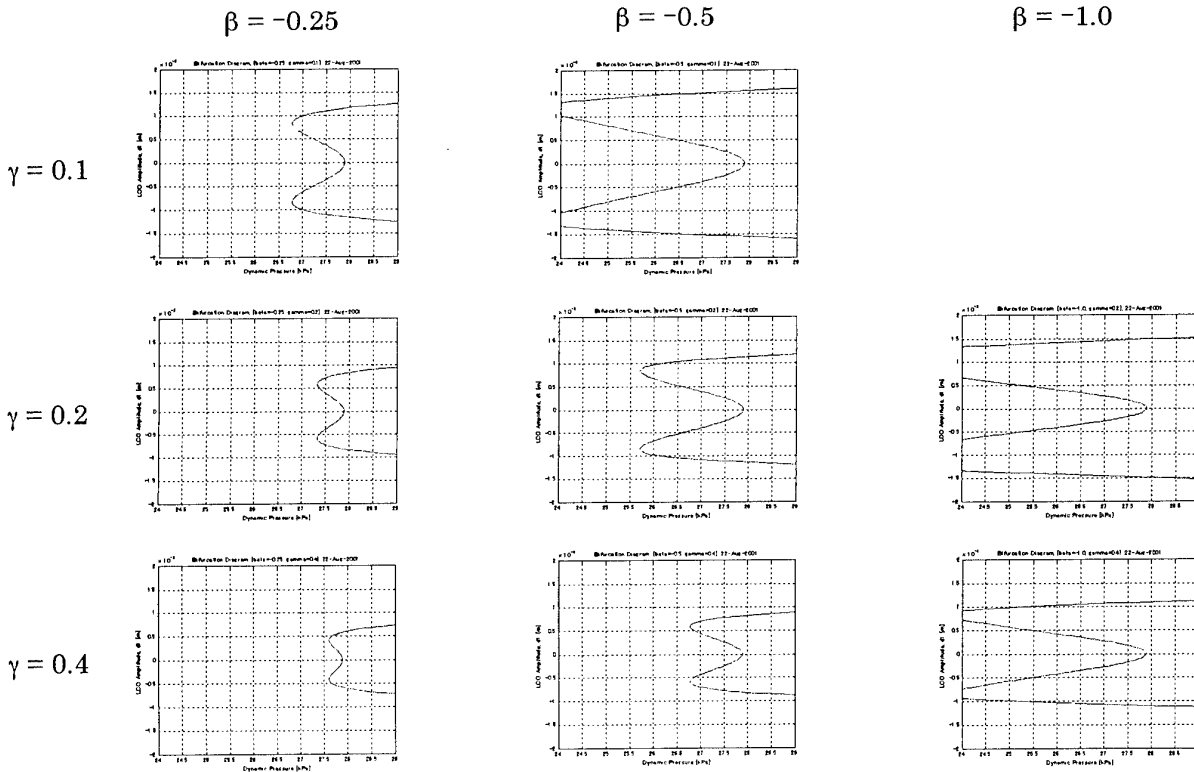

Fig. 6 Parameter sensitivity for increasing the amplitude of LCO

point and a saddle node point, which corresponds to the experimental results. We started to search the optimal direction of the set of parameters β's and γ's to change in order to increase the LCO amplitude. Applying the continuation method to Eq. (1) with the two parameters doubled and halved, we can get the sensitivity chart as shown in Figure 6. The figure shows that as γ is reduced, the amplitude of LCO increases but the saddle node bifurcation point greatly decreases, and as β is reduced in its absolute value, the saddle node point increases a little keeping the amplitude of LCO almost unchanged. Consequently the right direction we have to take may be upper left direction.

Making a lots of efforts to search an optimum combination of parameters, we have reached the values of β = -6.5e-3 and γ = 2.5e-5. Resulting bifurcation diagram is shown as a solid line in Fig. 7. In the figure experimental data are also plotted. The correspondence of the LCO between the math model and the experiment is quite good; the amplitude of LCO is almost coincident and the position of the saddle node bifurcation is exactly the same. There is a difference in unstable limit cycle; the mathematical model has a wide stable area under the unstable limit cycle, while the experimental data shows a limited region of stability. As stated earlier, the main reason of this discrepancy may exist in the noise effects. In real situation, even at the stable region disturbance may energize the wing to jump up to unstable region and push the wing to LCO state.

4. CONCLUSIONS

This investigation optimizes the free parameters in the two-degrees-of-freedom, finite dimensional, nonlinear math model. The model has been modeled and developed by the authors to explain qualitatively nonlinear features of the wind tunnel test data of the transonic flutter accumulated at National Aerospace Laboratory in Japan for a high aspect ratio wing. By making use of the continuation method of continuously tracking the bifurcation diagram of the math model, parameter optimization is tried and quantitative matching is obtained for the LCO amplitude between the math model and the test results. Resulting model enables to explain quantitatively the subcritical Hopf bifurcation of a limit cycle oscillation (LCO) of transonic flutter, saddle node bifurcation though there still has discrepancy for the unstable limit cycle with the wind tunnel tests.
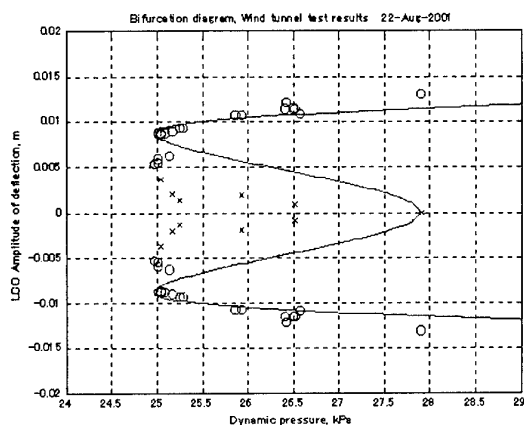
REFERENCES

1. Cunningham, A. M., Jr., "Practical Problem: Airplanes," Chapter 3, *Unsteady Transonic Aerodynamics*, Nixon, D., ed., Progress in Astronautics and Aeronautics, 120, AIAA, pp. 75-132, 1989.
2. Dowell, E. H., "Nonlinear Aeroelasticity," *Flight-Vehicle Materials, Structures and Dynamics*, 5, Part II, Chapter 4, ASME, pp. 213 – 239, 1993.
3. Schewe, G. and Deyhle, H., "Experiments on Transonic Flutter of a Two-Dimensional Supercritical Wing with Emphasis on the Non-Linear Effects," Proceedings of the Royal Aeronautical Society Conference on "UNSTEADY AERODYNAMICS", 1996.
4. Gránásy, P., Matsushita, H., and Saitoh, K., "Nonlinear Analysis of Transonic Flutter," Proceedings of the 10th International Sessions in Aircraft Symposium, JSASS, PP. 66-69, 1996.
5. Gránásy, P., Matsushita, H., and Saitoh, K., "Nonlinear Aeroelastic Phenomena at Transonic Region," Proceedings of CEAS International Forum on Aeroelasticity and Structural Dynamics 1997, Vol. III, Rome, pp. 379-385, 1997.
6. Matsushita, H., Saitoh, K., and Gránásy, P., "Nonlinear Characteristics of Transonic Flutter of a High Aspect Ratio Wing," Proceedings of 21st ICAS, Melbourne, pp. 1-7, 1998.
7. Matsushita, H., Saitoh, K., and Gránásy, "Two Degrees-of-Freedom Nonlinear Math Model with Fourth Order Nonlinear Aerodynamics for Transonic Limit Cycle Flutter," CEAS/AIAA/ICASE/NASA LaRC International Forum on Aeroelasticity and Structural Dynamics 1999, Williamsburg, US, June 1999.
8. Lasse Engbo Christiansen and Tue Lehn-Schiøler, "Stochastic Modeling of Transonic Flutter," Department of Physics, The Technical University of Denmark, Denmark, 2000.
9. Matsushita, H., Gránásy, p., Christiansen, L. E., Lehn-Schiøler, T., and Mosekilde, E., "Investigation of Nonlinear Phenomena in Transonic Flutter - wind Tunnel Tests and Nonlinear Dynamics Analysis," Proceedings of 3rd International Conference on Non-Linear Problems in Aviation and Aerospace, 2001, to appear.

Fig. 7 Bifurcation diagram of the math model with optimized parameters and the experimental results.

Vibration and Flutter Analysis of Composite Panels with Shape Memory Alloy Fibers at Elevated Temperatures

Jae-Sang Park* , Ji-Hwan Kim** and Sung-Hwan Moon***

Seoul National University

San 56-1, Shinrim-Dong, Kwanak-Ku, Seoul 151-742, Korea

Key Words : Stability and Control

Abstract

The vibration and flutter characteristics of composite panels with embedded shape memory alloy (SMA) fibers are investigated. The stress-strain relations for composite laminas with embedded SMA fibers are introduced for the first order shear deformation theory (FSDT) in this study, it is investigated the influence of the SMA fibers on the variations of the natural frequencies and flutter boundaries of the SMA fiber reinforced composite panels.

1. Introduction

The external skin panels of future high-speed civil transport (HSCT) and military aircraft may be experienced the significant aerodynamic and thermal loads. Such load conditions may be important since they change the characters of the static and dynamic behaviors of structures in supersonic regimes. On the other hand, shape memory alloy (SMA) of the recent smart materials is widely developed to be used with the shape memory effect (SME). The SME can be described as follows: an object in the low-temperature martensitic condition, when plastically deformed and the external stresses removed, will regain its original shape when heated. The class of material such as the SMA fiber-reinforced composites are simply a composite material that contains SMA fibers in such a way that the material can be stiffened or its behavior controlled by the heating. Generally, the SMA fibers are heated by applying an electrical current with some control device. In this study, the heat source is assumed to be due to the aerodynamic heating. Mechanical properties of shape memory alloys strongly depend on temperature and initial strain (Fig.1, Fig.2).

There have been many works of buckling analysis of SMA fiber-reinforced composites. Turner, et al. [1] analyze the thermal buckling problems and random response of SMA fiber reinforced composite plates. It is indicated that SMA increases the critical buckling temperature and reduce the thermal postbuckling deflection. Ostachowicz, et al. [2] show that SMA have influence on natural frequency and critical buckling temperature. Literature surveys show a limited number of papers on the vibration and flutter analysis of SMA fiber-reinforced composite panels. In the present work, the constitutive relations for a composite plate with embedded SMA fibers are introduced. The numerical results for the changes of natural frequencies and of flutter boundaries are studied by using the finite element method. The first-order shear deformation plate theory (FSDT) is used in the modeling of the SMA fiber reinforced composite panels.

2. Governing Equations

---

* Research Assistant, School of Mechanical and
  Aerospace Engineering
** Associate Professor, School of Mechanical and
  Aerospace Engineering
*** Post Doctor, School of Mechanical and Aerospace
  Engineering

The composite matrix has the principal material directions 1 and 2 the SMA fiber is embedded in the only 1 direction. Material properties of SMA fiber reinforced composites can be expressed as in Ref. [1].

For $T > T_s$ (T_s is the austenite start temperature),

$$E_1^* = E_{1m}\upsilon_m + E_s^*\upsilon_m \quad , \quad E_2^* = \frac{E_{2m}E_s^*}{\left(E_{2m}\upsilon_s + E_s^*\upsilon_m\right)}$$

$$G_{12}^* = \frac{G_{12m}G_s^*}{\left(G_{12m}\upsilon_s + G_s^*\upsilon_m\right)} \quad , \quad G_{23}^* = G_m\upsilon_m + G_s^*\upsilon_s$$

$$v_{12} = v_{12m}\upsilon_m + v_s\upsilon_s$$

$$\alpha_1^* = \frac{\left(E_{1m}\alpha_{1m}\upsilon_m + E_s^*\alpha_s\upsilon_s\right)}{\left(E_{1m}\upsilon_m + E_s^*\upsilon_s\right)} \quad , \quad \alpha_2 = \alpha_{2m}\upsilon_m + \alpha_s\upsilon_s$$

$$(1)$$

where subscripts m, s are represented composite matrix, SMA fiber, respectively. In addition, υ_s, υ_m are the volume fraction of SMA fiber and composite matrix, respectively.

The strain-displacement relations for FSDT are given as

$$\{\varepsilon\} = \{\varepsilon_m\} + \{\kappa\} = \begin{Bmatrix} u_{,x} \\ \upsilon_{,y} \\ u_{,y} + \upsilon_{,x} \end{Bmatrix} + z \begin{Bmatrix} \phi_{x,x} \\ \phi_{y,y} \\ \phi_{x,y} + \phi_{y,x} \end{Bmatrix}$$

$$\{\gamma\} = \begin{Bmatrix} \phi_y + w_{,y} \\ \phi_x + w_{,x} \end{Bmatrix} \qquad (2)$$

where u, υ and w are the displacements in the x, y and z directions, respectively; ϕ_x and ϕ_y are the rotation in the xz- and yz-planes, respectively.

For a k-th layer with an orientation angle θ, the stress-strain relations are given as in Ref.[1]

$$\{\sigma\}_k = \begin{Bmatrix} \sigma_{xx} \\ \sigma_{yy} \\ \tau_{xy} \end{Bmatrix}_k = \left[\overline{Q}^*\right]_k \begin{Bmatrix} \varepsilon_{xx} \\ \varepsilon_{yy} \\ \gamma_{xy} \end{Bmatrix}_k + \begin{Bmatrix} \sigma_x^* \\ \sigma_y^* \\ \tau_{xy}^* \end{Bmatrix}_k \upsilon_{s_k}$$

$$- \left(\left[\overline{Q}\right]_m \begin{Bmatrix} \alpha_x \\ \alpha_y \\ \alpha_{xy} \end{Bmatrix}_m \upsilon_m \right)_k \Delta T \qquad (T > T_s)$$

$$\{\tau\}_k = \begin{Bmatrix} \tau_{yz} \\ \tau_{xz} \end{Bmatrix}_k = \begin{bmatrix} \overline{Q_{44}^*} & \overline{Q_{45}^*} \\ \overline{Q_{45}^*} & \overline{Q_{55}^*} \end{bmatrix}_k \begin{Bmatrix} \gamma_{yz} \\ \gamma_{xz} \end{Bmatrix}_k \quad (T > T_s) \qquad (3)$$

where $\left[\overline{Q^*}\right]$ and $\left[\overline{Q}\right]_m$ are the transformed reduced stiffness matrices of the composite lamina and the composite matrix, respectively. In addition, σ_x^*, σ_y^* and τ_{xy}^* are recovery stresses for xy-plane.

For the anisotropic plate under the temperature change $\Delta T(x,y,z)$, the constitutive relations can be obtained by integrating the stress-strain relation through the thickness of plates as:

$$\begin{Bmatrix} N \\ M \end{Bmatrix} = \begin{bmatrix} A^* & B^* \\ B^* & D^* \end{bmatrix} \begin{Bmatrix} \varepsilon_m \\ \kappa \end{Bmatrix} + \begin{Bmatrix} N_\sigma^* \\ M_\sigma^* \end{Bmatrix} - \begin{Bmatrix} N_{\Delta T} \\ M_{\Delta T} \end{Bmatrix} \quad (T > T_s)$$

$$\{Q\} = \begin{Bmatrix} Q_{yz} \\ Q_{xz} \end{Bmatrix} = \begin{bmatrix} A_{44}^* & A_{45}^* \\ A_{45}^* & A_{55}^* \end{bmatrix} \{\gamma\} \qquad (4)$$

where the laminate stiffness are all temperature dependent, and the recovery in-plane and moment vectors are dependent on temperature and initial strain. In this study, the shear correction factors for FSDT are taken to be 5/6.

The equations of motion are derived using the principle of virtual work:

$$\delta W = \delta W_{\text{int}} - \delta W_{ext} = 0 \qquad (5)$$

The equation of motion for SMA fiber-reinforced composite plates is

$$[M]\{\ddot{d}\} + \left([K_l] + [K_r^*] - [K_{\Delta T}]\right)\{d\} = \{f\} + \{P_{\Delta T}\} \qquad (6)$$

where $\{d\} = \{\phi_x, \phi_y, u, \upsilon, w\}^T$ is the displacement vectors, $[M]$ is the mass matrix, $[K_l]$ is the linear stiffness matrix, $[K_r^*]$ and $[K_{\Delta T}]$ are the geometric stiffness matrices due to the recovery stress and thermal in-plane force vector, respectively. In addition, $\{f\}$ and $\{P_{\Delta T}\}$ are the aerodynamic and thermal load vector.

The aerodynamic load is described by the first order piston theory. Virtual work done by the aerodynamic load p is

$$\int_A p\delta w dA = \int_A \left(-\beta w_{,x} - g w_{,t}\right)\delta w dA \qquad (7)$$

where β is the aerodynamic pressure parameter, and g is the aerodynamic damping parameter.

$$\beta = \frac{\rho_a V_a^2}{\sqrt{(M^2 - 1)}} \quad , g = \frac{\beta}{V_a} \frac{M^2 - 2}{M^2 - 1} \qquad (8)$$

with ρ_a, V_a and M is the air density and the air flow speed, the Mach number, respectively.

By the finite element method, one can derive the following equations of motion for SMA fiber-reinforced composite plates subject to aerodynamic and thermal loads .

$$[M]\{\ddot{d}\} + g[AD]\{\dot{d}\} + ([K_l] + [K_r^*] - [K_{\Delta T}] + \beta[AF])\{d\} = \{P_{\Delta T}\}$$
$$(9)$$

where $[AF]$, $[AD]$ are the aerodynamic influence matrix and the aerodynamic damping matrix, respectively.

3.Numerical Results and Discussions

In this study, the isoparametic 9-node elements are used, and the reduced integration technique is chosen for the calculation of shear strain energy to prevent from shear locking. For the reduction of the number of degrees of freedom of system, the Guyan reduction is employed in the vibration and flutter analysis. In addition, the uniform temperature changes are considered in the present work.

The vibration and flutter of all edges are simply supported $[0/45/-45/90]_s$ quasi-isotropic square plates is analyzed. The thickness ratio (a/h) is chosen to be 150, and the plate is modeled with a 7×7 mesh.

The Material properties of Graphite/Epoxy composite matrix and SMA (Nitinol) are chosen as follows.

SMA-Nitinol		Graphite/Epoxy	
T_s	100°F	E_1	22.5 Msi
T_f	145°F	E_2	1.17 Msi
E^*	Fig.2	G_{12}	0.66 Msi
G^*	3.604 Msi $(T < T_s)$	G_{23}	0.47 Msi
	3.712 Msi $(T > T_s)$	v_{12}	0.22
v	0.3	ρ	0.1458×10^{-3}
ρ	0.6067×10^{-3}		
	$(lb - s^2 / in^4)$	$\alpha_1 = -0.04 \times 10^{-6}$	
α	5.7×10^{-6} /°F	$\alpha_2 = 16.7 \times 10^{-6}$	

(1) Vibration Analysis

The vibration equation at elevated temperatures is obtained by neglecting the aerodynamic influence matrix, aerodynamic damping matrix and thermal load vector of Eq. (9)

$$[M]\{\ddot{d}\} + ([K_l] + [K_r^*] - [K_{\Delta T}])\{d\} = \{0\} \qquad (10)$$

When the natural vibration of the system is concerned, the corresponding eigenvalue equation of the system is

$$[([\overline{K_l}] + [\overline{K_r^*}] - [\overline{K_{\Delta T}}]) - \omega^2[\overline{M}]]\{\Phi\} = \{0\} \qquad (11)$$

where $[\overline{K_l}]$, $[\overline{K_r^*}]$, $[\overline{K_{\Delta T}}]$, $[\overline{M}]$ are reduced matrices by the Guyan reduction.

(2) Flutter Analysis

For the flutter analysis, the Eq. (9) is reduced by the Guyan reduction with respect to in-plane and rotational DOFs as:

$$[\overline{M}]\{\ddot{w}\} + g[\overline{AD}]\{\dot{w}\} + ([\overline{K_l}] + [\overline{K_r^*}] - [\overline{K_{\Delta T}}] + \beta[\overline{AF}])\{w\} = \{0\}$$
$$(12)$$

By substituting $\{w\} = \{\Phi_c\}e^{\omega t}$ into Eq. (12), and formulating for state-variable equation, one obtains the following equations as :

$$\left[\begin{bmatrix} [0] & [\overline{M}] \\ [\overline{K}] & g[\overline{AD}] \end{bmatrix} - \omega \begin{bmatrix} [\overline{M}] & [0] \\ [0] & -[\overline{M}] \end{bmatrix} \right] \begin{Bmatrix} \{\Phi_c\} \\ \{\dot{\Phi}_c\} \end{Bmatrix} = \begin{Bmatrix} \{0\} \\ \{0\} \end{Bmatrix} \qquad (13)$$

where $[\overline{K}] = [\overline{K_l}] + [\overline{K_r^*}] - [\overline{K_{\Delta T}}] + \beta[\overline{AF}]$.

In addition, the following non-dimensional parameters are introduced.

$$\beta^* = \beta a^3 / D \quad , \quad \omega^* = \omega_i \sqrt{a^4 \rho h / D} \qquad (14)$$

where β^* and ω^* are non-dimensional dynamic pressure and frequency, in addition, a and h are side length and thickness of plates; D is rigidity of the plate ($D = E_2 h^3$ for anisotropic material). In this study, all the natural frequencies and flutter boundaries are calculated until the critical buckling temperature T_{cr}.

Fig.3 and Fig.4 show the natural frequencies and the flutter

boundaries of SMA fiber reinforced composite plates with temperature changes. The natural frequencies and flutter boundaries can be increased with the increase of temperature due to the aerodynamic heating, initial strain and the volume fraction of SMA fibers.

4. Acknowledgement

5. References

[1]   Travis L. Turner and Z. W. Zhong and Chuh Mei, "Finite Element Analysis of the Random Response Suppression of Composite Panels at Elevated Temperatures using Shape Memory Alloy Fibers", The 35th AIAA/ASME/ASCE/AHS /ASC Structures, Structural Dynamics and Materials Conference, AIAA-94-1324-CP, pp. 136-146,1994

[2]   W. Ostachowicz, M. Lrawczuk, A. Zak, "Dynamics and Buckling a Multilayer Composite Plate with Embedded SMA Wires", Composite Structures 48,   pp. 163-167, 2000

[3]   I. Lee, D.-M. Lee, and I.-K. Oh, "Supersonic Flutter Analysis of Stiffened Laminated Plates Subject to the Thermal Load", Journal of Sound and Vibration,   224(1), pp. 49-67,1999
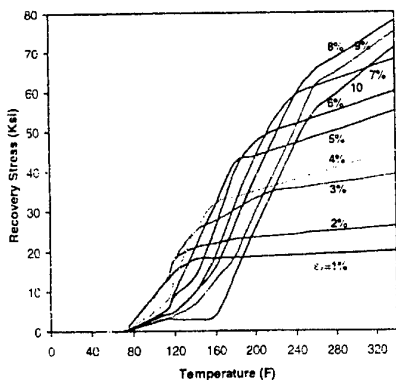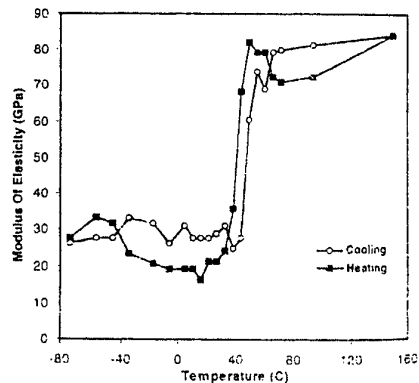

Fig.2   SMA Modulus v.s Temperature
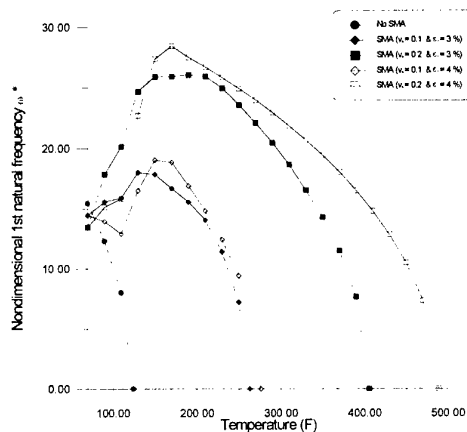
Fig.3   The First Natural Frequencies v.s Temperature
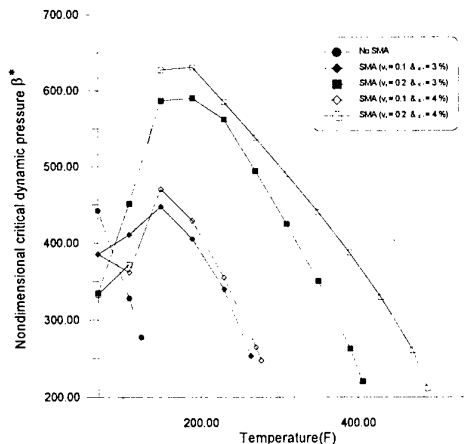
Fig.4   The Critical Dynamic Pressure v.s Temperature

Fig.1   SMA recovery stress v.s Temperature
with different initial strain

A Simplified Calendar Fatigue Life Prediction Approach for Aircraft Structures

Bintuan Wang*

Full-Scale Testing Group, Structures & Materials Research Center, National Aerospace Laboratory of Japan, 6-13-1 Osawa, Mitaka, Tokyo 181-0015 Japan (E-mail: wangb@nal.go.jp)

Keywords: Fatigue life, Atmospheric corrosion, Aircraft Structure

Abstract

Based on the fatigue property experiment of the aircraft structural materials pre-corroded in atmospheric environment, an approach is presented for predicting the calendar fatigue life of structures. The approach has the following features or advantages: (*i*) using the calendar fatigue loading spectrum which considers the real service calendar time as well as the flight time of the aircraft structures; (*ii*) adopting the modified Miner's Rule; (*iii*) providing a safe life for structure elements. An application example indicates that the approach is reasonable and practical.

1. Introduction

Calendar life is the necessary life criteria of structures (especially for aircraft structure) in service in atmospheric corrosion environment. Because of the complexity of the service environment of aircraft, there has not yet a practical approach to assess the calendar life. But some indirect approaches are used for considering the effect of the corrosion environment on the aircraft structures.

1.1 About corrosion maintenance

The U.S.Air Force(USAF) adopts a method of *environmental corrosion severity classification system*[1-3] to determine the calendar inspection periods. In Boeing's structural maintenance plan [4], the *environment damage rating*(EDR) system aims to insure the durability and integrity of airplane structure through inspection and maintenance. All these measures are through effective management to extend the service calendar life of aircraft structure.

1.2 Environment spectrum

---

* Science & Technology Agency Fellow

Considering the effect of corrosion environment on the service life of the aircraft structure, MIL-A-008866B(1975) and MIL-A-87221(1985) specify the requirement on aircraft's chemistry/heat/environment spectrum. The Air Force Advisory Group for Aeronautical Research and Development(AGARD) of NATO and the US Naval Air Development Center(NADC) establish the accelerated pre-corrosion simulative test method and the environment/loading spectrum[5-7]. Here two methods are worth being introduced.

(1) Crack propagation allowance value method

By transforming the complex working environment into a single crack propagation allowance value, the corrosion fatigue crack propagation life can be easily calculated. Boeing adopts a weighing environment method. The airplane's working environments are divided into four types which contain seven types of laboratory environments, and the latter's weighing percentages are specified for the former.

$$M = \sum_{i=1}^{n} M_{T_i} m_i \; ; \; M_{T_i} = M_B m_e m_f m_r \; ; \; N_F = 10^4 [\frac{M/G}{S}]^p$$

(1)

where M_{T_i} is the crack propagation parameter in *i*th laboratory environment; m_i is weighing factor of the flight environment; M_B is the crack propagation rating value in standard laboratory environment; m_e, m_f and m_r are modified coefficients for no-standard laboratory environment, loading frequency and stress ratio respectively. N_F is the crack propagation life; p, G and S are the crack propagation parameter, the geometry factor and rating stress respectively.

(2) *T-RH-α* Curved surface [8,9]

Temperature-Relative humidity-Conversion factor (T-RH-α)curved surface(Fig.1), that is an equivalent relationships between certain atmospheric corrosion environment and the
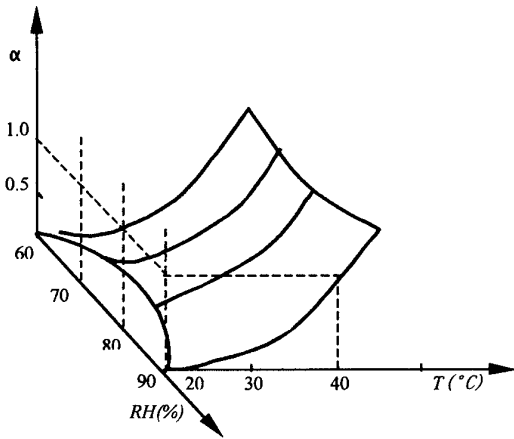

Fig.1 The equivalent conversion curve $T - RH - \alpha$

accelerated environment spectrum. By the conversion factor (α) of the equivalent corrosion time, the atmospheric corrosion environment spectrum of certain region can be converted to an accelerated environment spectrum. At present, this curved surface is only available for aluminum alloy and contains only two environment variables(T and RH).

With the T-RH-α curved surface, an accelerated corrosion spectrum can be obtained for the actual annual average environment spectrum $T_i - RH_j - h_{ij}$ ($i = 1,2,\cdots k_1, j = 1,2,\cdots k_2$) . For an aircraft serves in a region and exposed to a environment with k_1 levels temperature, k_2 levels relative humidity and exposure time h_{ij} , then the equivalent time h of the equivalent laboratory corrosion spectrum (here the equivalent temperature is T_0 and the humidity is RH_0):

$$h = \sum_{i=1}^{k_1}(\sum_{j=1}^{k_2} \alpha_{ij} h_{ij})$$ (2)

where α_{ij} is the converting factor corresponding to T_i and RH_j.

1.3 Corrosion fatigue model

The corrosion fatigue and corrosion fatigue crack propagation models are based on the accelerated laboratory corrosion fatigue test. Here three types of model are listed

(1) The stress-controlled corrosion fatigue crack initiation model, such as the local corrosion model and Kim model[10,11];
(2) The strain-controlled corrosion fatigue crack initiation model based on Manson-Coffin formula,

$\varepsilon_a = \dfrac{\sigma_f^{'}}{E}(2N_f)^b + \varepsilon_f^{'}(2N_f)^c$, such as the dual-strain(DS) model, strain range (SR)model, strain range frequency(SRF) model [12];
(3) The models based on local stress-strain method, that is suitable for typical mechanically-fastened joints [13]. Since these models combine the environment converting factor (ECF) with the fatigue life in dry air, they are practical in engineering.

1.4 Corrosion damage calendar life model

Zhang Fuze presents a calendar life model for corrosion damage of metal in multi-medium environment [14]. The basic hypothesis is: in the same corrosion medium and for the same corrosion
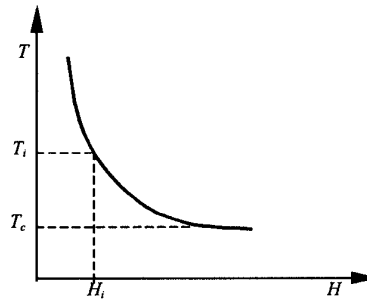

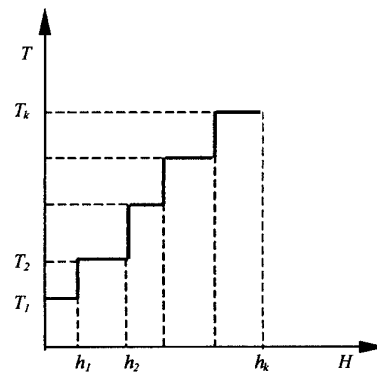Fig.2 The supposed $T-H$ curve for critical corrosion damage D_c

Fig.3 The supposed temperature(T)-time(H) spectrum

critical damage, the higher the temperature, the less the corrosion time. Within certain range of temperature, the relationship between the

temperature of corrosion medium(T) and the corrosion time(H) is supposed similar to that of fatigue stress-life curve(Fig.2). So the corrosion damage can be accumulated in a similar way as the Miner's Rule. This is a single corrosion damage model, so it can not be used in fatigue life prediction of the aircraft structures subjected to loading spectrum.

For a structure element subjected to the corrosion medium(T-H spectrum as Fig.3), the corrosion damage corresponding to the T_i- Δh_i is:

$$D_i = \frac{\Delta h_i}{H_i} \quad (i = 1,2,\cdots k) \tag{3}$$

where H_i is critical corrosion time. For m kinds of medium:

$$\lambda \sum_{j=1}^{m} (\sum_{i=1}^{k} \frac{\Delta h_i}{H_i})_j = 1 \tag{4}$$

where λ is the total number of blocks when the accumulated corrosion damage reaches to the critical damage.

Because of the lack of the necessary testing data as well as a practical quantitative methodology for assessing the calendar life of the airframe structure in the aircraft design standards and the design handbooks, the designers and users have to adopt some rough approaches such as the qualitative analysis, semi-quantitative analysis, the leading flight experience or the repairing experience at present. So, this paper tries to present a quantitative approach for predicting the calendar fatigue life for aircraft structures.

2. A simplified approach—real time fatigue characteristics

Based on the fatigue experiment of the aircraft structural materials pre-corroded in atmospheric environment, the modified Miner's rule and the dynamic probabilistic fatigue model, a new approach — real time fatigue damage model is presented to predict the calendar fatigue life of aircraft structural elements. The approach has the following features.

2.1 Calendar fatigue loading spectrum[15]

Upon the statistics the military aircraft in service its most percentage of service time are staying on ground, only a very small portion are flying in air. So we count the aging effect of the structure only when the aircraft parks on ground and the flying situation is omitted. Then we avoid many complex problems, such as how to simulate the air environment at various height, in different seasons and areas.
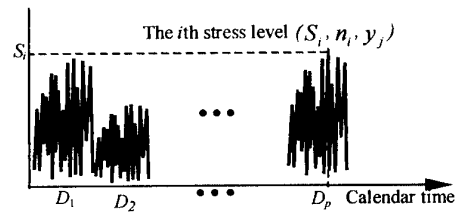

Fig.4 Calendar loading spectrum of aircraft

Consider a flight training period with number of flights m, flight hours T and calendar time Y(for example one year). At the kth flight, the ith loading state contains three parameters(Fig.4): S_i, n_i, y_j, that are stress level, the corresponding number of cycles and calendar time respectively, and y_j is as follow:

$$y_j = Y_1 + Y_2 + \cdots + Y_{k-1} \tag{5}$$

where Y_{k-1} equals the $(k-1)th$ flight time plus the ground parking time. Usually, an aircraft serves in several different regions (with different atmospheric corrosion environments), then the equivalent calendar time should be given:

$$y_i = y_{D_1}^* + y_{D_2}^* + \cdots + y_{D_{p-1}}^* + y_{D_p}^* \tag{6}$$

where $y_{D_1}^*$, $y_{D_2}^*$, $\ldots y_{D_p}^*$ are the equivalent service calendar time in different environment regions.

For high strength aluminium alloys, for four typical environment regions(A,B,C,D), from the empirical equivalent relationships between the atmospheric pre-exposure corrosion calendar time(year) and the laboratory accelerated corrosion environment[15], the equivalent calendar time relationships between these regions can be easily obtained (take region A as the reference):

$$y_B = 10^{[\lg(y_A+10)]^{1.141}} - 10 \tag{7}$$

$$y_C = 10^{[\lg(y_A+10)]^{1.227}} - 10 \tag{8}$$

$$y_D = 10^{[\lg(y_A+10)]^{1.407}} - 10 \tag{9}$$

By these formulas the equivalent calendar time in Equation (6) can be easily determined.

2.2 $y - S - N_f$ and R-y curves [15-18]

To investigate the decreasing of fatigue strength, a parameter 'life ratio' R is introduced. The ratio R means: at the same testing condition, the fatigue life of a treated material compares with the fatigue life of the original material at 0 year.

$$R = \frac{fatigue\ life\ of\ treated\ material\ at\ present}{fatigue\ life\ of\ original\ material\ at\ 0\ year}$$
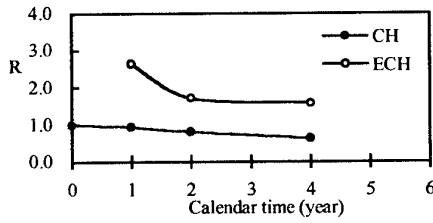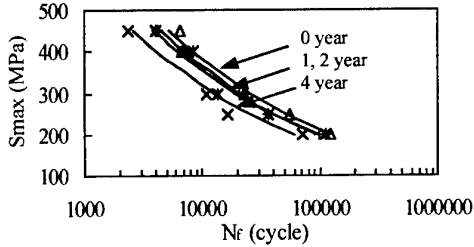
Fig.5 *R-y* curve for LC4CS specimen

Fig.6 S-N curve for LC4CS plain specimen

Some typical curves of R against calendar year are shown in Fig.5(CH: central hole specimen; ECH: cold worked central hole specimen)

Within the range of middle fatigue life, the $S - N_f$ curve can be fitted to:

$$N_f \cdot S^m = C \qquad (10)$$

Fig.6 shows the fitting $S - N_f$ curves at 0,1,2 and 4 year, from these curves the R-y curves for LC4CS at all stress levels can be fitted to one curve:

$$R = 1.0028e^{-0.1694 \cdot y} \qquad (11)$$

So, $y - S - N_f$ curve for LC4CS can be in the following form:

$$R = 1.0028e^{-0.1694 \cdot y} \cdot N_f(0) \cdot S^m = C \qquad (12)$$

where m and C are parameters at 0 year, $N_f(0)$ is the fatigue life at 0 year at stress level S .

2.3 The calendar fatigue life predicting approach[17]

When a structure of an aircraft subjects to a block of loading spectrum of k stress levels (T flight hours), according to the Miner's ruler, its predicted fatigue life is :

$$T \bigg/ \sum_{i=1}^{k} \frac{n_i}{N_{fi}} \quad \text{(flight hours)} \qquad (13)$$

where n_i and $\overline{N_{fi}}$ are loading cycles and fatigue life at the i th stress level S_i . When an aircraft serves in a corrosion environment, and it can accomplish a loading spectrum of T flight hours training within an elapse of calendar time Y , then :

$$\sum_{j=1}^{L} \left(\sum_{i=1}^{k} \frac{n_i}{\overline{N_{fi}}(jY - Y + y_i)} \right)_j = 1 \qquad (14)$$

where y_i is the corresponding calendar time at S_i , $\overline{N_{fi}}(jY - Y + y_i)$ is the fatigue life of material for the i th stress level at the calendar time $(jY - Y + y_i)$, and L is the number of loading blocks. So, the calendar fatigue life of the structure is $L \cdot Y$.

Usually, an aircraft structure serves in several different regions (with different atmospheric corrosion environment) such as D_1 , D_2 , $\cdots D_p$ (Fig.6), and the elapse of service calendar time in these regions are Y_1 , Y_2 , $\cdots Y_p$ respectively. The structure is subjected to k_1, k_2, $\ldots k_p$ stress levels of loading spectrum in the corresponding region. y_{1i} , y_{2i} , $\cdots y_{pi}$ are the calendar time at i stress level during the service time in each region. Then the modified Miner rule is:

$$\sum_{i=1}^{k_1} \frac{n_i}{\overline{N_{fi}}(y_{1i})} + \sum_{i=1}^{k_2} \frac{n_i}{\overline{N_{fi}}(y_{2i})} + \cdots +$$
$$\sum_{i=1}^{k_p} \frac{n_i}{\overline{N_{fi}}(y_{pi})} = 1 \qquad (15)$$

Suppose all the environment regions can be divided into four typical regions, then according to formula 6~9, formula (15) can be simplified as:

$$\sum_{i=1}^{k} \frac{n_i}{f_1(y_{1i}^*)\overline{N_{fi}}(0)} = 1 \qquad (16)$$

where y_{1i}^* are the equivalent calendar time in a new re-arranged sequence, $\overline{N_{fi}}(0)$ is the fatigue life at i stress level at 0 year.

3. Example of Predicting Calendar Fatigue Life

The LC4CS ear-shaped joint of an aircraft wing beam, with a stress concentration factor K_t=3.17, is subjected to the nominal stress

spectrum of a loading 'block' (200 flight hours) in Table 1.

Table 1. Nominal stress spectrum (200 flight hours)

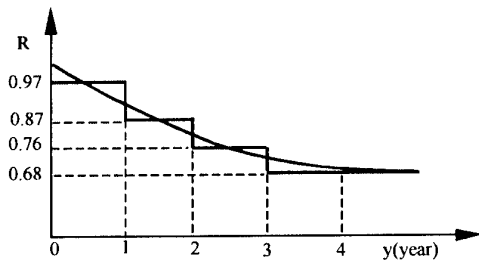| Loading sequence	1	2	3	4	5	6	7	8	
S_{max}(MPa)	92.1	196.0	33.4	423.7	383.5	274.6	191.2	161.	
S_{min}(MPa)	41.2	49.0	41.2	41.2	41.2	41.2	47.8	41.	
Cycles	145	146	59	1	13	234	137	40	

Fig.7 Approximately segmenting of the $R - y$ curve

Because the R-y curve drop down very slowly, it can be approximately replaced with straight line segment,and also the calculation can follow a very simple process:

Step I : Calculate the fatigue damage under the no-corrosion environment ;

Step II: Consider the corrosion damage modifying .

$$D_{bi}^* = \frac{1}{R_D(y = i-1,i)} D_{bi} \qquad (17)$$

according to Miner's Rule,let : $\sum D_{bi}^* = 1$

The predicted life result is 39.3 blocks. If the ordinary fatigue property of the material is used, the predicted life is 59 blocks (the test life is 65 blocks). Usually a training aircraft could accomplish 'a block'(200 flight hours) of training within a calendar year. The smallest life scatter factor for the aircraft structure is 4, so the safe service life is only 39.3/4≈10 years.(In fact, the corrosion fatigue life scatter factor could be larger than that without corrosion.)

4. Conclusion

On basis of above research, some conclusions can be made as following:

(1) It is practicable to apply the modified Miner rule as well as introducing calendar time for predicting the calendar fatigue life of aircraft structure.

(2) It is not correct to use the ordinary material fatigue strength (here is the '0-year' strength) without any deduction to predict fatigue life over a certain calendar time. Usually the predicted (by testing or by calculating) fatigue life should be divided by a safety coefficient 3~4 to obtain a much smaller service life. Such a coefficient could only be an empirical value, but as for considering the effect of corrosion and aging on aircraft structures it has no sound basis.

(3) The approach can be adopted in the preliminary design step of the aircraft structures and applied to assess the calendar fatigue life of the aging aircraft structures.

Reference

1. Summitt R. and Pacer lime, "An environmental corrosion severity classification system," ADA 100496,1980.
2. Miller R N., "Preventing aircraft corrosion by predictive corrosion modeling," ADA 189660.
3. Criscimagna N H., "The airforce corrosion program status report," ADA 073054,1978.
4. John Hall and Ulf.Goranson, "Principles of achieving damage tolerance with flexible maintenance program for new and aging aircraft," pp8-51,1982.
5. Cohen B., "Corrosion fatigue: chemistry, mechanics and microstructure," Eds McEvily and Staehle, NACE, 1972.
6. Wanhill R.J.H., Luccia J.J.De and Russo M.J., "The fatigue in aircraft corrosion testing program," AGARD Report, pp5-72, No.713, Feb. 1989.
7. Wanhill R.J.H., "Environment effect on fatigue of aluminium and titanium alloys," AGARD Report, No.659, 1977.
8. Zhou xiyuan, ACTA AERONAUTICA ET ASTRONAUTICA SINICA, Vol.17 No.5,1996. (In Chinese)
9. Y.L.Chen,P.Jin,C.M.Duan and X.H.Yang, "Study on local environmental spectrum and accelerated corrosion equivalent spectrum of aircraft structure," Proceedings of the seventh international fatigue congress, pp2353-2358,Beijing, P.R.China.
10. Kim Y. H, Speaker, S.M, Gordon, D.E, Manning, S.D and Wei, R.P., "Development of Fatigue and Crack Propagation Design and Analysis Methodology in a Corrosion Environment for Typical Mechanical Fastened Joints," Vol.1-Phase 1 Documentation, NADC-83126-60 Vol.1,1983.

11. Muller M., "Theoretical consideration on corrosion fatigue crack initiation," Metallurgical Transaction A, Vol.13A, Apr. 1982.
12. Bernstein H. and Loeby C., "Low-cycle Corrosion Fatigue of Three Engineering Alloys in Salt Water," J. Eng. Mats. & Tech.,1987.
13. Manning, S.D, Gordon, D.E and Wei, R.P., "Development of Fatigue and Crack Propagation Design and Analysis Methodology in a Corrosion Environment for Typical Mechanical Fastened Joints," Vol.3-Phase 2 Documentation, NADC-83126-60 Vol.III,1984.
14. Zhang Fuze, "A model of Predicting calendar life for corrosion damage of metal," ACTA AERONAUTICA ET ASTRONAUTICA SINICA, Vol.20 No.1,1999. (In Chinese)
15. Wang Bintuan(supervisor:Yang Qingxiong), "Study on structural fatigue calendar life and its probability," Ph.D dissertation, Northwestern Polytechnical University, P.R.China, 2000.
16. Wang Bintuan, Fan Jianhua and Yang Qingxiong, "Fatigue characteristics of metals pre-corroded in atmospheric environment," *ACTA METALLURGICA SINICA*, Vol.35, No.11 pp1163-1166, 1999.(In Chinese)
17. Wang Bintuan, Fan Jianhua, Sun Qin and Yang Qingxiong, "Calendar Fatigue Life of Airframe Materials," The 22nd Congress of the International Council of the Aeronautical Science, Harrogate,U.K., 2000.
18. Yang Qingxiong and Wang Bintuan, "The Fatigue strength decrease of structural materials caused by atmosphere corrosion and aging," The Fourth International Conference on Fracture and Strength of Solids, Pohang, Korea, 2000.